
# Development of Metal Matrix Composites suitable for hulls and ship decks

**by**

**ORITONDA MURIBWATHOHO**

**Thesis submitted in fulfillment of requirements for the degree**

**Doctor of Engineering: Mechanical Engineering**

**in the Faculty of Engineering and Built Environment**

**at the Cape Peninsula University of Technology**

**Supervisor: Prof. V. Msomi**

**Co-Supervisor: Dr. S. Mabuwa**

**Bellville**

**April 2025**

## DECLARATION

I, Oritonda Muribwathoho, declare that the contents of this dissertation/thesis represent my unaided work and that the dissertation/thesis has not previously been submitted for academic examination towards any qualification. Furthermore, it represents my own opinions and not necessarily those of the Cape Peninsula University of Technology.

**14 / April / 2025**

**Signed** **Date**

## ABSTRACT

Metal matrix composites (MMCs) have gained significant attention due to their enhanced mechanical and tribological properties, making them suitable for various industrial applications, particularly in the marine and aerospace sectors. However, challenges such as poor reinforcement dispersion, porosity, and limited optimization of processing parameters remain critical research gaps. While extensive studies have been conducted on aluminium-based MMCs, limited research exists on AA5083-H111 reinforced with coal, particularly in the context of friction stir processing (FSP) as a fabrication method. This study aimed to fabricate aluminium metal matrix composites (AMMCs) of AA5083-SiC and AA5083-Coal MMCs using FSP for potential application in ship hulls and decks, focusing on reinforcing the joint region rather than fabricating a bulk MMC sheet. The novelty of this research lies in the use of coal as an alternative reinforcement, offering a cost-effective and sustainable approach to MMC fabrication while maintaining high wear resistance and mechanical strength. Silicon carbide (SiC) was used as a benchmark reinforcement due to its well-documented ability to improve hardness, wear resistance, and thermal stability, providing a comparative reference for evaluating the effectiveness of coal as a reinforcement material.

In the fabrication process, AA5083-H111 was reinforced with silicon carbide and coal particles to create AMMCs, and their properties were compared to unreinforced AA5083-H111. To run the test on the AA5083-H111, AA5083/SiC composite joints and AA5083/Coal composite joints, the specimens were cut with a CNC milling machine. Among the tests performed were tensile testing, macrostructure and microstructure analysis, fractographic analysis (SEM), hardness tests, flexural tests, chemical composition analysis and X-ray diffraction (XRD) analysis. The described specimens for the composites were cut from various positions on the plates, including the plate's start, middle and end. This method enabled a thorough study of material characteristics and behavior by constantly analyzing material properties at these exact places across all testing. The following symbols were used to represent the cut positions on the processed plates to symbolise their positioning (S for the start, M for the middle and E for the end of the plate).

Conclusions were drawn based on the test findings. The test results of the mentioned AMMCs (AA5083/SiC composite and AA5083/Coal composites) joints produced with different reinforcements were evaluated and compared to those of AA5083-H111. The XRD analysis of the AA5083 base alloy and its composites revealed the presence of various phases, including Al-metallic, $Al_6Mn$, AlMnFe, $Al_3Mg_2$, $Al_3Si$, $Al_2O_3$, $Mg_2Si$, $Al_4C_3$ and amorphous carbon. These phases significantly influence the mechanical properties, thermal conductivity and corrosion resistance of the materials. The base alloy's intermetallic phases play a crucial role in its strength and corrosion resistance. In the composites, the formation of $Al_2O3$, $Al_3Si$, and $Mg_2Si$ enhances hardness, wear resistance and grain refinement. The presence of $Al_4C_3$ in the coal composite improves wear resistance and thermal stability. The amorphous carbon contributes to the overall properties of the composite. Microstructural analysis revealed a significant grain refinement in the composite joints. The AA5083/SiC composite exhibited an average mean grain size of 31.148 µm, representing a 50.819% reduction compared to the base material (61.292 µm). The AA5083/Coal composite exhibited an average mean grain size of 31.173 µm, a 50.8598% reduction. This grain refinement is attributed to dynamic recrystallisation induced by FSP.

The results of the flexural testing for the AA5083-H111 revealed a maximum ultimate flexural strength (UFS) of 415.20 MPa with an MFS of 26.82% for specimens. The face specimens of the AA5083/SiC composite exhibited superior flexural strength compared to the root specimens, with a maximum UFS of 765 MPa for the face and 632.78 MPa for the root, resulting in a difference of 132.22 MPa. Similarly, the AA5083/Coal composite showed a

significant difference in UFS between face and root specimens, with values of 747.53 MPa and 631.95 MPa, respectively, resulting in a difference of 115.58 MPa. This disparity highlights the variation in mechanical properties along the joint length. While the AA5083/Coal composite showed improved UFS compared to the base material, the AA5083/SiC composite demonstrated the most significant enhancement. The AA5083/SiC composite exhibited the highest ultimate flexural strength (UFS) for both face and root specimens. The base material demonstrated a higher strain rate compared to both composites. Additionally, the AA5083/SiC composite exhibited a higher strain rate within the composite joints than the AA5083/Coal composite.

Mechanical testing revealed that adding reinforcements did not significantly enhance the ultimate tensile strength (UTS) compared to the base material. The base material, AA5083-H111, exhibited a maximum UTS of 311 MPa, a yield strength of 248.8 MPa, and a strain rate of 58.65%. The AA5083/SiC composite achieved a maximum UTS of 281 MPa, yield strength of 224.8 MPa, and a strain rate of 31.49%, representing an 11.576% reduction compared to the base material. The AA5083/Coal composite reached a maximum UTS of 282 MPa, a yield strength of 225.6 MPa and a strain rate of 33.48%, showing a 21.318% reduction in UTS compared to the base material. The grain refinement induced by FSP contributed to improved mechanical properties. However, agglomerated reinforcement particles, particularly in the AA5083/Coal composite, negatively impacted the overall performance. The fracture surfaces of the AA5083/SiC and AA5083/Coal composites exhibited a mixed-mode fracture mechanism, characterised by microvoids, rough surfaces, dimples and particle clusters.

The base material, AA5083-H111, had an average hardness of 90.57 HV. The AA5083/SiC composite joints exhibited an average hardness of 92.57 HV, representing a slight increase. The AA5083/Coal composite joints had an average hardness of 91.42 HV, also showing a slight increase. The increased hardness in both composites can be attributed to microstructural refinement, particularly grain size reduction, induced by the FSP process. This refinement, coupled with dislocation pinning by reinforcement particles, contributes to the enhanced hardness. The Orowan mechanism and Hall-Petch relationship support this correlation between grain size and hardness.

This study successfully fabricated AA5083-based AMMCs using FSP with SiC and coal reinforcements. The addition of reinforcements significantly influenced the mechanical properties of the base material AA5083-H11. Both AA5083/SiC and AA5083/Coal composites exhibited refined grain structures and enhanced hardness compared to the unreinforced base material. While the UTS of the composites was slightly lower than the base material, they maintained respectable UTS values. The AA5083/SiC exhibited the best results compared to those of AA5083/Coal. The results provide valuable insights into the applicability of AA5083-based MMCs in marine and structural applications, addressing current industrial needs for lightweight, high-strength, and corrosion-resistant materials. By bridging the gap in the literature regarding coal-reinforced AA5083 composites and FSP optimization, this study contributes to the advancement of MMC fabrication techniques, offering a sustainable and efficient alternative for next-generation engineering applications.

## ACKNOWLEDGEMENTS

First and foremost, I want to thank the omnipotent God for helping me get this far since I could not have accomplished it on my own.

**My sincere gratitude to the following who made the completion of the study possible:**

My sincere gratitude goes to the Cape Peninsula University of Technology for paying my tuition through the Vice Chancellor's Prestigious Achievers Award.

I want to thank my supervisor, Prof. Velaphi Msomi, for his steadfast guidance, inspiration, encouragement, support, dedication, and patience during the whole thesis-writing process, as well as for being available to me during my postgraduate studies. His thoughts, advice, and guidance motivated me to continue with the research. To me, he was more like a parent who never gives up on their child. Thank you so much for believing in me even at the moments when I lost hope in myself and encouraging me to finish up my studies. I thank God we crossed paths. May God continue to generously bless you and your family. I hope you'll keep being a blessing to other students who would like to embark on this research adventure.

I want to thank my co-supervisor, Dr. Siphokazi Mabuwa, who supported me throughout my study and motivated me to finish my project. She has been much more to me than simply a supervisor; she never stopped encouraging me and wishing me success. Her ideas, advice, and guidance motivated me to carry on with the research. I thank God we crossed paths, and I appreciate your faith in me. May God continue to generously bless you and your family. I hope you'll keep being a blessing to other students who would like to embark on this research adventure.

I would like to extend my sincere gratitude to Prof. Tiyamike Ngonda, who, despite not being officially appointed as my supervisor, provided invaluable support and guidance throughout my studies. His encouragement, advice, and unwavering belief in my abilities were instrumental in my success. I am truly grateful for his mentorship.

To my mother, Ms. Stella Mutavhatsindi, for raising me and the foundation she laid, as well as for her love, support, advice, kindness, and encouragement while I pursued my education. Thank you so much. My siblings Rilinde and Hudivhaene Muribwathoho and my cousin Touch Junior Mutavhatsindi, I appreciate your kindness, support, motivation, and everlasting belief in me. I adore you so much and consider you to be a true blessing to me. I would also like to express my sincere gratitude to my close relatives, extended family, and friends for their unwavering support and encouragement throughout my educational journey. Despite the distance and busy schedule, their belief in me has been a constant source of motivation.

I would like to express my sincere gratitude to Prof. Kasongo Nyembwe, Head of the Department, Mr. Simphiwe Nqabisa, Former Head of the Department, and Mr. Abdul Jarnodien, the CPUT senior laboratory technician, for their invaluable assistance and for providing me with access to the CPUT Mechanical Engineering Department laboratory for conducting my practical work. I would like to express my sincere gratitude to Miss Shaheeda Petersen for her invaluable assistance in preparing specimens for microstructure and hardness testing, as well as for her support during mechanical property testing. Her advice on the metallurgical aspects of the research, coupled with her motivation, was invaluable in driving the project forward. I would also like to thank Mr. Zukile Cobothwana for his assistance in cutting aluminum plates, fabricating the FSW/FSP tool, and providing valuable advice throughout this research. I am also grateful to Mr. Menzeleli Mamane for assisting me with a basic crash course on how to operate, code, and cut the specimen using the CNC Mill machine, and for all the advice he gave. I am also grateful to Mr. Mthokozisi Radebe for his invaluable assistance in wiring and maintaining the FSW machine.

I would like to express my sincere gratitude to Mrs. Penny Louw, Nkopo Chaule, and Rachel Cupido from the University of Cape Town for their invaluable assistance in preparing samples for microstructural analysis and XRD analysis. Additionally, I would like to thank Dr. Kazeem Bello from the Durban University of Technology for their assistance with SEM analysis.

Last but not least I would like to express my sincere gratitude to my friends, some colleagues, and the entire workshop staff for their invaluable support and encouragement throughout my research journey. Special thanks to Ms. Imani Thavhana, Ms. Aviwe Magudu, Mr. Luvuyo Kakaza, Dr. Olukayode Ayodele, Mr. Paul Senda, Mr. Luyanda Millard Meyers, Mr. Trollip Zwelethu Ngewana, Mr. Tendai Chipanga, Mr. Abslom Maluleke, Mr. Selboutne Makhmo, Mr. Pitso Tebele, Mr. Cletus Magoda, Mr. Mark Ludick, Mr. Mark Jenkins, Mr. Mark Gillion, Mr. Dikwidi Gaone, Mr. Shane Charles, Mr. Adenan Abrahams, Mr. Monwabisi Fasi, Mr. Njabulo Mthembu, Mr. Muziwandile Mazibuko, Mr. Rafique Williams, Mrs. Eucretia Matyala, Mrs. Noxolo Ngqondela, and Mrs. Hazel Hobonwana for their willingness to assist and their positive influence on my work.

In memory of Mr. Edelbert Masekwana, whose invaluable expertise and tireless dedication in operating the FSP machine were instrumental in the preliminary studies for the fabrication of our AMMCs. His contributions will be deeply missed.

## DEDICATION

I dedicate this dissertation to my late uncle Tshimangadzo Touch Mutavhatsindi. He encouraged me, always had faith in me, and constantly wanted me to achieve more. I'll always acknowledge the motivation he provided while he was still alive for my accomplishments. I also dedicate this dissertation to my grandmother Nyadzanga Mutavhatsindi. She has always been our family's pillar of strength and has been significant in my life. She has always supported me and has done so since I was a young child. Grandma, you are extremely loved by me.

Last but not least, I would want to dedicate my dissertation to my beloved mother, my siblings, my nephew, my extended family (Ramaano's Family) and my friends. I love you deeply with all my heart. This work would not have been accomplished without your love and support. I appreciate your patience as I studied towards and earned this degree. To my nephews, Roanda and Thendokhae, always keep in mind that everything is possible. Never be frightened to go for your goals and dreams.

## LIST OF PAPERS

### *Supplement 1*

Muribwathoho, O., Msomi, V. and Mabuwa, S., 2022. Metal Matrix Composite Fabricated with 5000 Series Marine Grades of Aluminium Using FSP Technique: State of the Art Review. Applied Sciences, 12(24), p.12832. https://doi.org/10.3390/app122412832

### *Supplement 2*

Muribwathoho, O., Msomi, V. and Mabuwa, S., 2023, May. Metal Matrix Composite Developed with Marine Grades: A Review. In Materials Science Forum (Vol. 1085, pp. 77-89). Trans Tech Publications Ltd. https://doi.org/10.4028/p-jub91t

### *Supplement 3*

Muribwathoho, O., Msomi, V. and Mabuwa, S., 2024. Optimization of FSP parameters in fabricating AA5083/Coal composites using Taguchi method. *Engineering Research Express*. **DOI** 10.1088/2631-8695/ada41a

### *Supplement 4*

Muribwathoho, O., Msomi, V., and Mabuwa, S., 2025. Optimization of FSP parameters in fabricating AA5083/SiC composites using the Taguchi method. **Paper ID (MS2106: Second round of peer-review)**. *8th International Conference on Material Strength and Applied Mechanics*.

### *Supplement 5*

Muribwathoho, O., Msomi, V. and Mabuwa, S., 2024. An Analysis Comparing the Taguchi Method for Optimizing the Process Parameters of AA5083/Silicon Carbide and AA5083/Coal Composites That Are Fabricated via Friction Stir Processing. *Applied Sciences*, *14*(20), p.9616. https://doi.org/10.3390/app14209616

### *Supplement 6*

Muribwathoho, O., Msomi, V. and Mabuwa, S., 2024. Optimization and Regression Analysis of Friction Stir Processing Parameters of AA5083/Coal Composites for Marine Applications. Crystals, 15(1), p.34. https://doi.org/10.3390/cryst15010034

### *Supplement 7*

Muribwathoho, O., Msomi, V. and Mabuwa, S., 2025. Optimizing FSP Parameters for AA5083/SiC Composites: A Comparative Analysis of Taguchi and Regression. *Metals*, *15*(3), p.280. https://doi.org/10.3390/met15030280

### *Supplement 8*

Muribwathoho, O., Msomi, V. and Mabuwa, S., 2025. Microstructural Characterization and Mechanical Properties of AA5083/Coal Composites Fabricated by Friction Stir Processing. *Metals*, *15*(3), p.308. *https://doi.org/10.3390/met15030308*

### *Supplement 9*

Muribwathoho, O., Msomi, V., and Mabuwa, S., 2025. Microstructural Characterization and Mechanical Properties of AA5083/SiC Composites Fabricated by Friction Stir Processing. **Paper ID (10353: Under review).** *Engineering, Technology and Applied Science Research (ETASR).*

***Supplement 10***

Muribwathoho, O., Msomi, V., and Mabuwa, S., 2025. Comparative Study of AA5083/SiC and AA5083/Coal Composites Fabricated by Friction Stir Processing. **Paper ID (NXMATE-D-25-00182: Under review)**. *Next Materials*.

**TABLE OF CONTENT**

# Contents

## LIST OF FIGURES

## LIST OF TABLES

## GLOSSARY

| Terms/Acronyms/Abbreviations | Definition/Explanation |
|---|---|
| AA | Aluminium Alloy |
| AAs | Aluminium Alloys |
| ACW | Anti-Clockwise |
| Al | Aluminium |
| Al-Mg | Aluminium Magnesium |
| Al-SiC | Aluminium Silicon Carbide |
| AMMC | Aluminium Metal Matrix Composite |
| AMMCs | Aluminium Metal Matrix Composites |
| ANOVA | Analysis of Variance |
| ASTM | American Society for Testing and Materials |
| BM | Base Material |
| Br | Boron |
| C | Carbon |
| CNC | Computer numerical control |
| COF | Coefficient of friction |
| CPUT | Cape Peninsula University of Technology |
| Cu | Copper |
| Cr | Chromium |
| DDRX | Discontinuous Dynamic Recrystallization |
| DoE | Design of Experiment |
| DRV | Dynamic Recovery |
| DRX | Dynamic recrystallization |
| EBSD | Electron Backscatter Diffraction |
| EDM | Electrode Discharge Machining |
| EDX | Energy Dispersive X-Ray Spectroscopy |
| Fe | Iron |
| FESEM | Field Emission Scanning Electron Microscopy |
| FSP | Friction Stir Processing |
| FSPed | Friction Stir Processed |
| FSW | Friction Stir Welding |
| FSWed | Friction Stir Welded |
| FZ | Fusion Zone |
| GA | Genetic Algorithms |

| | |
|---|---|
| GDRX | Geometric Dynamic Recrystallization |
| HAZ | The Heat-Affected Zone |
| HcHCr | High carbon high chromium |
| HV | Hardness Vickers scale |
| $H_2O$ | Water |
| MFS | Maximum Flexural Strain |
| Mg | Magnesium |
| MMC | Metal matrix Composite |
| MMCs | Metal matrix Composites |
| Mn | Manganese |
| NAOH | Sodium Hydroxide |
| NZ | Nugget Zone |
| O | Oxygen |
| OM | Optical Microscopy |
| OP | Oxide Polish |
| PE | Percentage Elongation |
| PM | Powder Metallurgy |
| SA | Simulated Annealing |
| SEM | Scanning Electron Microscopy |
| Si | Silicon |
| S/N Ratio | Signal-to-Noise Ratio |
| SZ | Stir Zone |
| TEM | Transmission Electron Microscopy |
| TMAZ | Thermo-Mechanically Affected Zone |
| TS | Tabu Search |
| UFG | Ultrafine Grain |
| UFS | Ultimate Flexural Strength |
| UTS | Ultimate Tensile Strength |
| XRD | X-ray Diffraction |
| YS | Yield Strength |
| Zr | Zirconium |
| Zn | Zinc |

# NOTATIONS

## Greek letters

| | |
|---|---|
| Degree | ° |
| Degree Celsius | ℃ |
| Mg-Si Precipitates | $\beta$ |
| Mu | $\mu$ |
| Omega | $\omega$ |
| Percentage | % |
| Phi | $\varphi$ |
| Pressure | p |
| Sigma/stress | $\sigma$ |
| Theta | $\theta$ |

## Basic symbols

| | |
|---|---|
| Area | A |
| Angles | $\alpha, \beta, \gamma$ |
| Cartesian coordinates | x, y, z |
| Change | Δ |
| Force | F |
| Mass | m |
| Number of experiments | n |
| Pressure | P |
| Response factor | y |

## Units

| | |
|---|---|
| Centimetre cubed | $cm^3$ |
| Degree | ° |
| Degree Celsius | ℃ |
| Gram | G |
| Gigapascal | GPa |
| Kilogram | kg |
| Kilonewton | kN |
| Kilopascal | kPa |
| Meter | m |
| Minute | min |

| | |
|---|---|
| Millilitre | ml |
| Millimetre | Mm |
| Millimetre per minute | mm/min |
| Millimetre per second | mm/s |
| Newton | N |
| Megapascal | MPa |
| Nano meter | Nm |
| Pascal | Pa |
| Revolutions Per Minute | RPM |
| Seconds | S |

## Reinforcement particles abbreviations

| | |
|---|---|
| Aluminium oxide | $Al_2O_3$ |
| Br | Boron |
| Boron carbide | $B_4C$ |
| Boron nitride | BN |
| Carbon nanotube | CNT |
| Carbon nanotubes | CNTs |
| Cerium oxide | $CeO_2$ |
| Copper | Cu |
| Graphene | G |
| Graphene nano platelets | GNP |
| Graphene oxide | GO |
| Graphite | Gr |
| Magnesium Silicide | $Mg_2Si$ |
| Molybdenum | MO |
| Multi-wall carbon nanotube | MWCNT |
| Multi-wall carbon nanotubes | MWCNTs |
| Nickel | Ni |
| Nickel Titanium | NiTi |
| Rise hush ash | RHA |
| Silicon carbide | SiC |
| Silicon dioxide/ Silica/ Quartz | $SiO_2$ |
| Stainless steel | SS |
| Titanium | Ti |
| Titanium boride | TiB |

| | |
|---|---|
| Titanium diboride | $TiB_2$ |
| Titanium Carbide | TiC |
| Titanium dioxide | $TiO_2$ |
| Tungsten | W |
| Tungsten carbide | WC |
| Yttria/ Yttrium oxide | $Y_2O_3$ |
| Zirconia | $ZrO_2$ |

# CHAPTER ONE

# INTRODUCTION

## 1.1 Introduction

The importance of materials selection in the fabrication of products has long been recognised. The best material can be impacted by a range of factors that also affect the selection process, making it challenging to develop a systematic method for selecting material. To improve a current product's reliability, cost, performance and lightness, as well as to choose a material for a new product, materials selection is essential for these key purposes. The choice of materials greatly influences the performance of the product, making this task a crucial component of product design [1].

High strength-to-weight ratio materials are extremely significant and critical in today's applications, particularly in automotive and aerospace engineering, in which efficiency in performance and fuel consumption are essential. The maritime, automotive, aerospace, defence and recreation industries require materials with increased mechanical properties such as temperature-withstanding ability, fatigue resistance, wear resistance and fracture toughness. A complex blend of material qualities is necessary to meet the demands of advanced infrastructure and innovative machines [2]. Metal matrix composites (MMCs) have emerged as one of the most promising engineering materials and are making steady progress because of their excellent properties such as high strength, low density and high wear resistance.

The origins of modern composites are said to date back to the 1930s. The introduction of polymer-based composites in 1960 attracted commercial interest from a variety of industries. Since then, composites have been regarded as better materials and they have been designed and manufactured for a variety of industrial and non-industrial applications. In the late 1970s, efforts were made to fabricate MMCs materials using silicon carbide (SiC) whisker reinforcements, mostly from aluminium alloys (AAs). The major goal of these efforts was to significantly enhance the properties of AAs by achieving high specific modulus and specific strength. Particle reinforcements were developed as a result of the high expense of whiskers. The utilisation of inexpensive reinforcements was the main focus of study around the turn of the twentieth century. Because of their outstanding properties, composite materials (also known as composition materials or simply composites) are commonly used in many industries such as automotive, aerospace and marine [3].

MMCs comprise two or more unreactive materials that are mixed to create a new material system with superior properties. Non-metallic elements such as aluminium oxide, fly ash, graphite and silicon carbide are often utilised as reinforcing materials, while metals such as aluminium, titanium and magnesium are commonly used as substrates [4,5]. Metal matrix composites primarily come in three different forms: particle-reinforced MMCs, short fiber or whisker-reinforced MMCs, and continuous fiber or sheet-reinforced MMCs [6]. The most commonly utilised substrate to fabricate MMCs is aluminium and its alloys due to their ductility, low density and formability, which can be mixed with load-bearing capacity and high-stiffness reinforcements [7]. SiC is frequently utilised as a reinforcement material due to its specific advantages over other reinforcements, including exceptional hardness, high corrosion resistance and low cost [8].

### 1.1.1 Fabrication of MMCs

The goal of composite material fabrication is to create materials with better properties than the base material. According to the reviewed literature [5,9], MMCs are formed using many fabrication routes, some of which include squeeze casting, electroplating, in-situ method,

powder metallurgy, stir casting and deposition technique [10], each presents distinct advantages and limitations. Figure 1.1.1 depicts various MMCs fabrication techniques on an industrial scale.

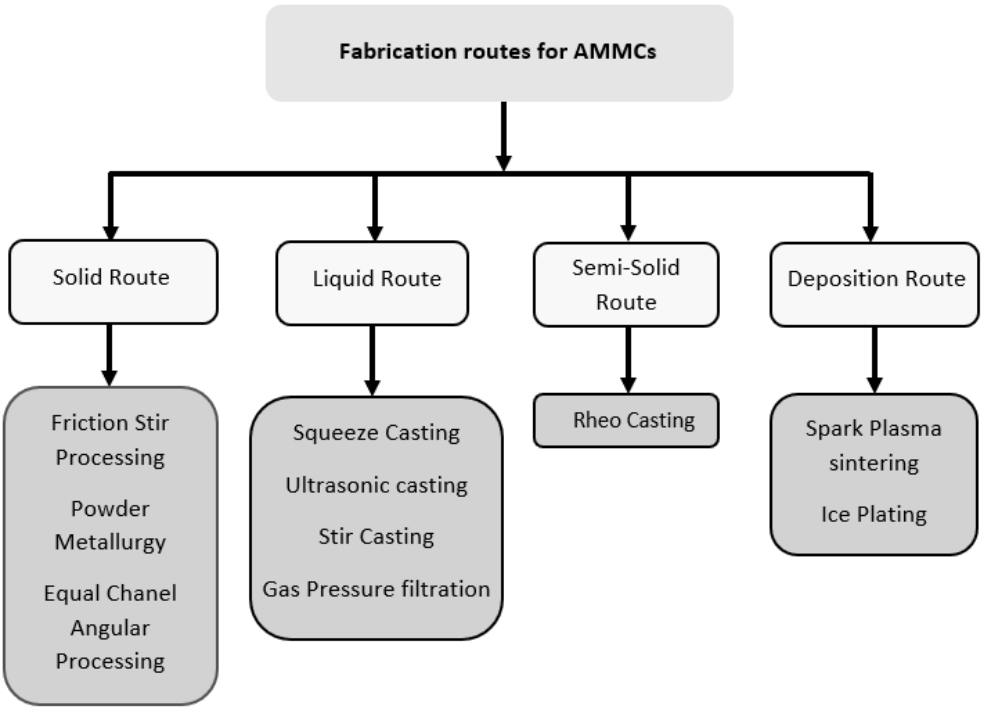


**Figure 1.1.1: Different MMCs fabrication techniques.**

Over the years, various fabrication techniques have been developed to produce aluminum metal matrix composites (AMMCs) as seen in Figure 1.1.1, each with its own set of advantages and limitations. Traditional casting techniques, such as stir casting [11] and squeeze casting [12], involve mixing reinforcement particles into molten metal before solidification. Stir casting, while cost-effective and simple, often results in non-uniform particle distribution [13], porosity [11], and weak interfacial bonding between the matrix and reinforcements. This non-uniformity can lead to localized variations in mechanical properties, compromising the overall performance of the composite. Squeeze casting, which applies pressure during solidification, reduces porosity and improves density, but is limited by high equipment costs and reinforcement size constraints, restricting its applicability to complex geometries and large-scale production [12].

Compo-casting [14], a variant of stir casting, aims to improve particle distribution by controlling the melt temperature and stirring parameters. However, it still faces challenges related to particle agglomeration and interfacial reactions. Spray forming [15] involves spraying molten metal and reinforcement particles onto a substrate, allowing for rapid solidification and fine microstructures. Nevertheless, it can lead to porosity and requires careful control of spray parameters to achieve uniform deposition. Liquid metal infiltration [16] offers an alternative by infiltrating a porous reinforcement preform with molten metal. This technique allows for the fabrication of complex shapes and high reinforcement volume fractions. However, it requires precise control of infiltration parameters and can be limited by wetting issues between the metal and reinforcement.

Powder metallurgy (PM) [17,18] involves blending metal powders with reinforcement materials, compacting them, and then sintering at high temperatures. Although this method offers good control over composition and microstructure, it is expensive, prone to oxidation, and often leads to weak interfacial bonding [13]. The high temperatures involved can also

result in grain growth and reduced mechanical properties. Mechanical alloying, a solid-state powder processing technique, involves high-energy milling of metal and reinforcement powders, leading to fine and homogeneous microstructures [19,20]. While it offers excellent control over particle distribution and grain size, it is time-consuming and can be expensive for large-scale production.

Deposition techniques [21], such as thermal and plasma spraying, create MMC coatings by depositing reinforcements onto a substrate surface. These processes allow for rapid fabrication and are suitable for surface modifications; however, they typically result in high porosity and weak adhesion between the coating and the substrate, limiting their use in structural applications [22]. Finally, in-situ processing [23] generates reinforcements through controlled chemical reactions during solidification, leading to strong interfacial bonding and improved properties. Despite this advantage, in-situ processing presents challenges in controlling reaction parameters and is limited in material selection, as it relies on specific chemical reactions to form the reinforcement phases.

Each of these techniques presents a trade-off between cost, process complexity, and the resulting composite properties. Therefore, the selection of an appropriate fabrication method depends on the specific application requirements, desired microstructure, and economic considerations. Given these limitations, friction stir processing (FSP) has emerged as the most suitable secondary processing technique, particularly for localized reinforcement and joint fabrication, offering the potential to overcome some of the limitations associated with traditional methods. Unlike casting methods, FSP is a solid-state process, eliminating defects such as porosity and segregation [24]. The severe plastic deformation and dynamic recrystallization during FSP result in grain refinement [25], enhancing mechanical properties such as strength, hardness, and wear resistance while maintaining ductility [26]. Additionally, FSP ensures a homogeneous distribution of reinforcement particles [25], preventing the clustering issues commonly observed in stir casting and powder metallurgy. Compared to deposition and in-situ techniques, FSP is also cost-effective and energy-efficient [27], as it does not require melting or additional alloying steps.

Overall, the use of FSP to prepare AMMCs is straightforward and up to date. Given these advantages, FSP has been selected as the fabrication method for this study to develop AA5083-based MMCs optimized for marine applications.

### 1.1.2 Techniques for MMCs fabrication via FSP

FSP is comparable to friction stir welding (FSW), the sole difference is the operating surfaces. In FSW, two materials are required, but in FSP, a single surface is a fundamental need [28-30]. Owing to the similarities between FSW and FSP many people find differentiating between the procedures a daunting task, particularly because FSP was created from the FSW approach. For the two approaches to work properly, they require a specifically developed tool and a stable backing plate [31-33]. The tilt angle of the tool, traverse speed, penetration measure and tool rotational speed all need to be modified to account for numerous value combinations of the FSW or FSP technique since different materials call for numerous sets of parameters [34,35]. The FSP approach was previously used to modify metallic materials without introducing any external material. Current studies exhibit that FSP may be employed to improve the microstructure of materials by adding foreign materials to generate AMMCs [36-39].

To develop MMCs using the FSP method, a reinforcement material and a metal matrix (base material) are required. The base metal is dimensioned and fastened to the FSP machine backing plate. Before implementing the FSP method, the precise size of grooves/holes for inserting the reinforcement is normally determined in the centre of the plate. The inserted reinforcements are usually covered by a tool with no pin during the FSP procedure to avoid

reinforcement scattering. The MMCs are produced using the FSP technique after all of these operations have been completed [40-42]. The fabrication process to develop MMCs is depicted in Figure 1.1.2.1.

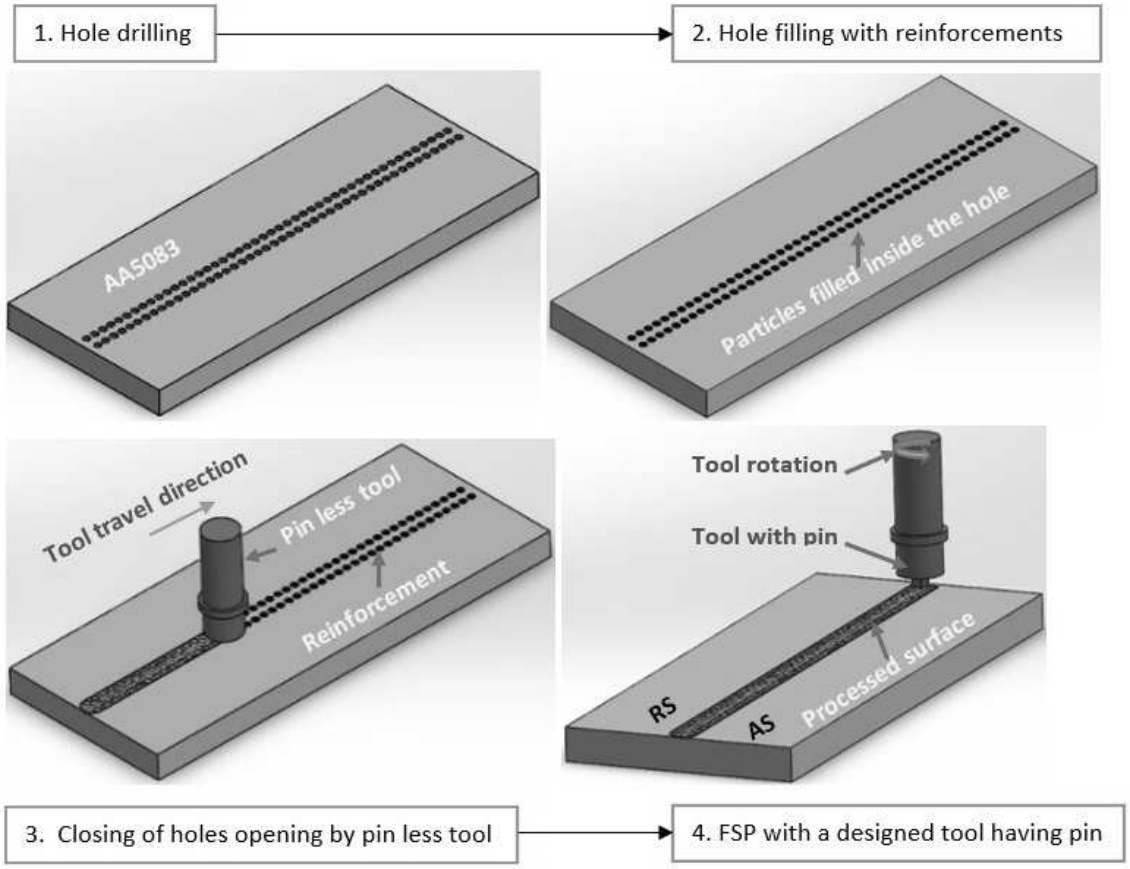


**Figure 1.1.2.1: Schematic diagrams of MMCs fabrication using the FSP technique.**

FSP is performed using a stirring and moving non-consumable tool with a pin and shoulder geometries of various geometries, the revolving non-consumable tool is fitted into the surface workpiece, after which the tool produces frictional heat and mixes the material. Tool plunging and traversing cause the material to dynamically recrystallise due to extreme plastic deformation, resulting in fine equiaxed grains in the processed area. In the FSP process, plastic deformation and material movement cause the formation of several zones, with the stir zone (SZ) being the region in which the material mixing occurs, followed by the thermomechanically affected region and the heat-impacted area. The most crucial of the three zones created by FSP is the change between the SZ and the thermomechanically impacted region since it defines the characteristics of the processed material in the FSP. Axial force sufficient to insert the rotating tool into the workpiece surface is needed to carry out FSP. Since there is no interaction between the base material and reinforced particle, as is the case in conventional procedures, the solid-state property of FSP is advantageous for the fabrication of surface composites [43]. Many types of input variables are used in FSP composite production and these variables have been discussed by many researchers [44-47]. Figure 1.1.2.2 depicts the parameters of the fabrication process.

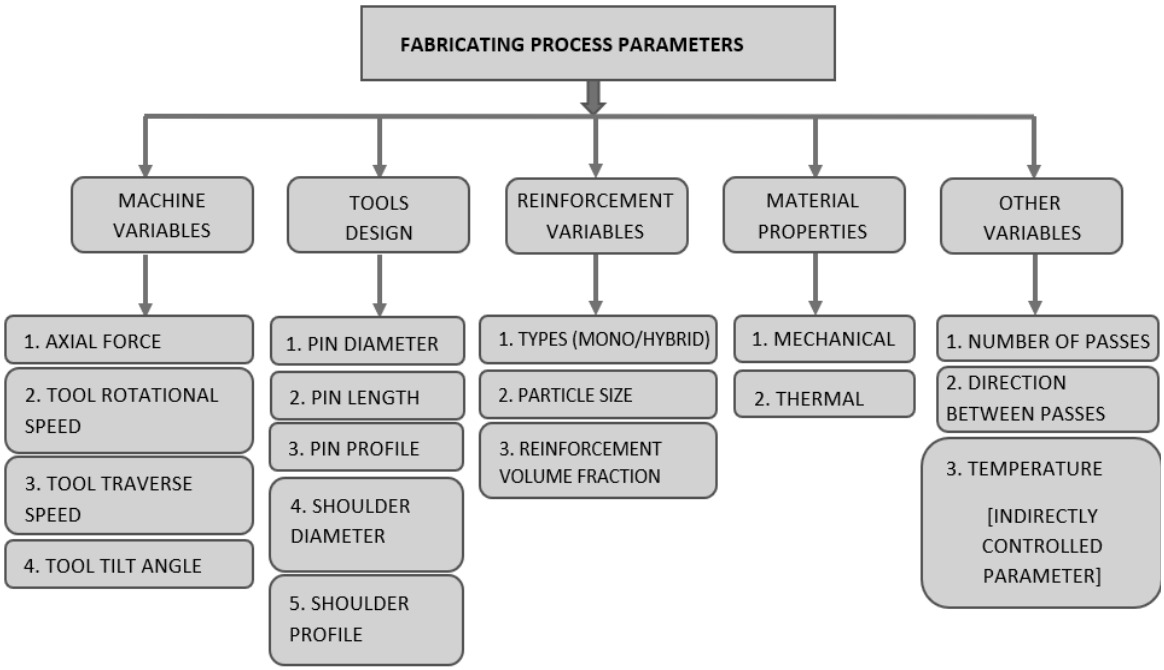


**Figure 1.1.2.2: Fabrication process parameters.**

## 1.2 Problem statement

The most challenging aspect of composite processing is homogenizing the distribution of reinforcement phases to form a sound microstructure, that can be either particles or fibres, depending on the geometry of the reinforcing phases in the composite [48]. This process demonstrates that a new approach must be used to intensify the microstructural and mechanical properties of metal products. One of the answers to the challenges stated is the use of FSP to improve the mechanical properties of metal alloys, including their formability, strength, ductility, hardness and fatigue life, without affecting bulk metal properties. FSP has gained a reputation for producing high-quality MMCs in solid form in a range of industries. The use of FSP to fabricate AMMCs is also straightforward, current and cost-effective [27]. FSP has several benefits, including homogenization of precipitates, densification, homogeneity of the processed region and grain refinement of composite materials and aluminium alloys [25]. This research study will focus on developing aluminium metal matrix composites suitable for hulls and ship decks using the FSP technique, specifically focusing on reinforcing the joint region rather than fabricating a bulk MMC sheet.

## 1.3 Research background

### 1.3.1 Introduction to Composite Materials

A composite material comprises two or more constituent materials, each of which has distinct physical or chemical properties. When combined, they form a material with characteristics different from the individual components. In composite materials, the matrix (also known as the substrate or base material) and the reinforcement are the two primary components. To fabricate a composite, the reinforcing material is incorporated into the matrix in various forms and sizes [49,50]. The interface between the matrix and the reinforcement plays a critical role in the overall performance of the composite, influencing load transfer and failure mechanisms [51].

### 1.3.2 Classification of Composite Materials

Composite materials are generally classified based on the physical or chemical properties of the matrix phase, including polymer matrix, metal matrix, and ceramic composites. Among these, metal matrix composites (MMCs) have gained significant attention due to their ability to integrate a strong metallic matrix with hard ceramic or soft reinforcements. Compared to traditional monolithic alloys, MMCs offer enhanced mechanical properties and have been studied extensively for various industrial applications particularly in aerospace, automotive, and marine industries [52]. Metal matrix composites may be divided into three categories: continuous fiber-reinforced MMCs, whisker-reinforced MMCs and particle-reinforced MMCs [53, 6].

### 1.3.3 Reinforcement materials selection in MMCs

Many types of reinforcement are utilised to produce MMCs. Therefore, the selection of reinforcement materials is crucial in tailoring the properties of MMCs. Reinforcements enhance properties such as hardness, tensile strength, and resistance to wear, heat, corrosion, and chemical degradation. They are broadly classified into three categories:

#### 1.3.3.1 Ceramic-Based Reinforcements

Ceramics are solid materials that, in general, display ionic and covalent connections that are quite durable [54]. These include aluminium oxide ($Al_2O_3$) 55-58], silicon carbide (SiC) [59-63], titanium diboride and zirconia ($ZrO_2$) [64,65]. These materials enhance wear resistance, hardness, and thermal stability due to their high melting points and mechanical strength. However, some ceramic reinforcements exhibit poor wettability with metal matrices, which can lead to weak interfacial bonding.

#### 1.3.3.2 Metallic-Based Reinforcements

Metallic-based reinforcements are materials used to strengthen a metallic matrix, where the reinforcement itself is also metallic, such as another metal, a metal alloy, or an intermetallic compound. Materials such as copper (Cu) [66], nickel (Ni) [67], nickel-titanium (NiTi) [68-69] and stainless steel (SS) [70] improve electrical conductivity, thermal properties, and toughness while maintaining good ductility. However, these reinforcements can increase density and may form undesirable intermetallic compounds that affect the composite's integrity.

#### 1.3.3.3 Carbon-Based Reinforcements

Carbon-based reinforcements are materials that utilize carbon in various forms to enhance the properties of a matrix. Materials such as Carbon nanotubes (CNTs) [71-73], graphene [74-75], graphite [76], rice husk ash (RHA) [77], and fly ash [78] enhance stiffness, strength, and tribological properties while maintaining a low weight. The primary challenge with carbon-based reinforcements is their tendency to form clusters, which can result in uneven mechanical performance.

### 1.3.4 Matrix selection for MMCs

In addition to reinforcement selection, the choice of the base metal also significantly influences the final composite properties. A variety of metals, including magnesium, titanium, cobalt, copper and aluminium, as well as their alloys, are frequently utilised as the substrate/base material. Aluminum and its alloys are favored as base materials for Metal Matrix Composites (MMCs) due to a compelling combination of advantageous properties [7]. While metals like

magnesium, titanium, cobalt, and copper offer unique strengths, aluminum strikes a valuable balance.

Magnesium, though exceptionally light, suffers from lower strength and corrosion resistance [79]. Titanium excels in strength and heat resistance but carries a higher cost [80]. Cobalt provides hardness and wear resistance, yet its density and expense limit broader application [81]. Copper's conductivity is valuable, but its strength is comparatively low. In contrast, aluminum's low density, ductility, formability, and cost-effectiveness make it highly versatile. Crucially, its properties can be effectively matched with various reinforcement materials, allowing for the creation of MMCs with tailored characteristics. Furthermore, aluminum offers reasonable corrosion resistance, enhancing its suitability for diverse applications [82]. This combination of factors establishes aluminum as a highly desirable substrate for MMCs across numerous industries.

#### 1.3.4.1 Aluminium Alloys in MMCs

Different alloys have varying degrees of compatibility with reinforcements. The most widely used aluminium grades for MMCs include:

1. Heat-Treatable Aluminium Alloys

These alloys allow for post-fabrication heat treatment, which can significantly enhance strength and hardness (e.g., AA6061, AA7075, AA2124) [83]. However, some, such as AA7075, contain high zinc content, making them prone to corrosion in certain environments.

- AA6061: Widely used in aerospace and automotive due to its good strength-to-weight ratio and corrosion resistance [84,85]. It is commonly reinforced with SiC particles for increased wear resistance.
- AA7075: Favored in the aircraft industry for its exceptional strength-to-weight ratio, AA7075 is crucial in high-stress structural components [86,87]. However, protective coatings are required for its longer service life because of its vulnerability to corrosion, particularly in a wide range of climatic conditions.
- AA2124: Also utilized in aircraft applications, AA2124 offers high strength but demands precise manufacturing techniques to prevent cracking [86,87]. Because fatigue resistance of the material is an essential component in aircraft engineering, AA212 is frequently strengthened with fibers.

2. Non-Heat-Treatable Aluminium Alloys

These alloys rely on strain hardening and grain refinement for strength enhancement, making them more suitable for marine and aerospace applications (e.g., AA5083, AA6351, A356, A359) [88]. Their mechanical properties are generally lower compared to heat-treatable alloys, necessitating reinforcement to improve strength and durability [82,89].

- AA5083: Excellent corrosion resistance and weldability, making it ideal for marine applications [90]. It is often reinforced with ceramic particles for increased strength and wear resistance in harsh environments.
- AA6351: Good extrudability and corrosion resistance, used in structural applications [91]. To further enhance the mechanical properties, silicon carbide (SiC) particles are commonly incorporated as reinforcement.
- Al A356/A359: Commonly used in casting applications due to their good castability [92,93]. They are often reinforced with ceramic particles for increased strength and wear resistance in cast components.

#### 1.3.4.2 Aluminium-based composites

Aluminium Metal Matrix Composites (AMMCs) represent a significant advancement in materials science, offering enhanced mechanical properties compared to conventional aluminium alloys. The inherent strength and lightness of aluminium make AMMCs ideal for high-performance applications. These composites consist of an aluminium matrix reinforced with a secondary material, which can be metallic, ceramic, or organic, designed to improve the material's physical, mechanical, and tribological characteristics [94]. The advantages of aluminium over the other metal matrix composites currently on the market are that aluminium is lightweight and readily available, together with its ease of handling, excellent electrical conductivity, thermal properties, energy conservation and environmental friendliness. Aluminium metal matrix composites offer improved mechanical properties and electrical and thermal conductivities, and can withstand high temperatures, radiation and moisture [95].

Furthermore, aluminium-based composites are increasingly utilized across diverse sectors, including automotive, aerospace, marine, and mineral processing, where their enhanced specific strength, superior wear resistance, increased thermal conductivity, and lower coefficient of thermal expansion are highly valued. Driven by the need for lightweight materials in automotive and aviation industries due to finite fossil fuel and energy resources, AMMCs are finding applications in bicycles, medical equipment, electronic packaging, home appliances, and spacecraft. Notably, AMMCs are replacing monolithic alloys in automotive, marine, and aviation engineering due to their superior tribological properties, high strength-to-weight ratio, and corrosion resistance [52, 96-101].

### 1.3.5 Fabrication Methods for MMCs and Their Limitations

Achieving a defect-free microstructure with uniform reinforcement distribution is crucial in Metal Matrix Composite (MMC) fabrication. Many different methods are available, each of which has its own set of benefits and drawbacks:

#### 1.3.5.1 Stir Casting

Stir casting, a widely used method for fabricating Metal Matrix Composites (MMCs), involves the direct mechanical stirring of reinforcement particles into a molten metal matrix [11]. This process is favored for its simplicity, cost-effectiveness, and suitability for large-scale production [13]. However, it suffers from several limitations. The resulting composite is often prone to porosity, which can degrade mechanical properties [11]. Achieving a uniform distribution of reinforcement particles is challenging, leading to potential particle agglomeration and inconsistent material performance [13]. Furthermore, weak interfacial bonding between the reinforcement and the matrix, due to poor wettability and the formation of undesirable reaction products, can compromise the composite's integrity. Finally, stir casting offers limited control over the final microstructure, which can restrict its application in high-performance scenarios.

#### 1.3.5.2 Powder Metallurgy

Powder Metallurgy (PM) offers a distinct approach to MMC fabrication, centered on the meticulous blending of metal and reinforcement powders [17,18]. This mixture is subsequently compacted into a desired shape and sintered, a process that fuses the particles. A significant advantage of PM is the exceptional control it affords over the composite's composition and microstructure, facilitating the creation of intricate and complex shapes. However, this method is not without its drawbacks. The process is inherently expensive, largely due to the cost of powders and specialized equipment. Additionally, the fine powders are highly susceptible to

oxidation during processing, potentially degrading material properties [13]. Achieving strong bonding between the particles can be challenging, leading to weak interfaces. Finally, residual porosity can persist within the sintered material, negatively impacting its mechanical performance.

#### 1.3.5.3 Squeeze Casting

Squeeze casting, a method employed in MMC fabrication, involves the injection of molten metal into a mold containing reinforcement performed under significant pressure. This process offers distinct advantages, notably improved reinforcement dispersion, which leads to a more homogeneous composite [12]. The application of high pressure effectively reduces porosity, enhancing the material's density and mechanical properties [12]. Furthermore, it promotes better interfacial bonding between the matrix and reinforcement, improving the overall composite integrity. However, squeeze casting necessitates the use of specialized high-pressure equipment, which significantly increases production costs. Additionally, the process is limited in its application to specific shapes, restricting its versatility for complex geometries.

#### 1.3.5.4 Deposition Techniques (Thermal/Plasma Spraying)

Deposition techniques, such as thermal and plasma spraying, offer a unique approach to MMC fabrication by spraying molten metal and reinforcement particles onto a substrate [21]. This method is particularly advantageous for coating applications and the creation of functionally graded materials, where material properties vary across the component. However, these techniques are not without their limitations. The resulting coatings often exhibit high porosity, which can compromise their mechanical integrity [22]. Furthermore, achieving strong adhesion between the coating and the substrate can be challenging, leading to potential delamination. The processing itself is complex, requiring precise control of numerous parameters. Finally, the application of these techniques is primarily limited to surface modifications, restricting their use for bulk composite production.

#### 1.3.5.5 Compo-casting

Compo-casting, a variant of stir casting, aims to improve particle distribution by controlling the melt temperature and stirring parameters [14]. This method involves introducing reinforcement particles into a semi-solid metal matrix, followed by mechanical stirring [102, 103]. A key advantage of compo-casting is the potential for enhanced particle distribution compared to traditional stir casting, achieved through precise control of melt conditions. However, it still faces challenges related to particle agglomeration, especially with high reinforcement volume fractions, leading to non-uniform composite properties. Interfacial reactions between the reinforcement and matrix can also occur, compromising the composite's integrity. Furthermore, scaling up compo-casting for large-scale production can be complex, requiring sophisticated temperature and stirring control systems.

#### 1.3.5.6 Spray Forming

Spray forming involves spraying molten metal and reinforcement particles onto a substrate, allowing for rapid solidification and fine microstructures [15,104]. This technique offers the advantage of rapid solidification, which results in refined microstructures and potentially improved mechanical properties [104,105]. It also makes it possible to fabricate components with a near-net form, which reduces the amount of significant machining that is required for the component. However, spray forming can lead to porosity within the deposited material, reducing its density and mechanical strength. Achieving uniform deposition and consistent particle distribution across the substrate is also challenging, requiring precise control of spray

parameters. Additionally, the high processing temperatures and velocities can result in oxidation and other unwanted reactions.

#### 1.3.5.7 Liquid Metal Infiltration

Liquid metal infiltration offers an alternative by infiltrating a porous reinforcement preform with molten metal [16, 106]. This technique allows for the fabrication of complex shapes and high reinforcement volume fractions, enabling the creation of components with tailored properties [16]. In addition to this, it makes it easier to manufacture composites with near-net forms, which reduces the amount of post-processing that is necessary. However, liquid metal infiltration requires precise control of infiltration parameters, such as pressure and temperature, to ensure complete filling of the preform [107]. Wetting issues between the metal and reinforcement can also limit the quality of the interface, affecting the composite's mechanical properties. Furthermore, the fabrication can be challenging and costly.

#### 1.3.5.8 In-situ Processing

In-situ processing generates reinforcements through controlled chemical reactions during solidification, leading to strong interfacial bonding and improved properties [23]. This method results in excellent interfacial bonding due to the formation of reinforcements directly within the matrix, enhancing the composite's strength and toughness. It also offers the potential for fine and uniform reinforcement distribution [108]. However, in-situ processing presents challenges in controlling reaction parameters [109,110], such as temperature and reaction kinetics, to achieve desired reinforcement characteristics. It is also limited in material selection, as it relies on specific chemical reactions to form the reinforcement phases, restricting its versatility.

#### 1.3.5.9 Mechanical Alloying

Mechanical alloying, a solid-state powder processing technique, involves high-energy milling of metal and reinforcement powders [19], leading to fine and homogeneous microstructures [19,20]. This method offers excellent control over particle distribution and grain size, resulting in composites with superior homogeneity [111] and mechanical properties. It also allows for the fabrication of composites with a wide range of reinforcement materials and volume fractions [112,113]. However, mechanical alloying is time-consuming and can be expensive for large-scale production, limiting its economic viability. The utilization of fine powders introduces a heightened risk of oxidation during processing, which may adversely affect the material's resultant properties. Additionally, achieving complete densification during subsequent consolidation processes can be challenging, leading to residual porosity.

#### 1.3.5.10 Friction stir processing (FSP)

Friction Stir Processing (FSP) presents a distinct solid-state approach to MMCs fabrication, utilizing a rotating tool to plastically deform and intimately mix reinforcement particles into the metal matrix. This method offers several key advantages. It ensures a remarkably homogeneous distribution of reinforcement, leading to consistent material properties [25]. Grain refinement is significantly enhanced [25], contributing to increased strength and toughness [26]. By operating in the solid state, FSP effectively eliminates defects such as porosity and segregation, which are common in melt-based processes [24]. Furthermore, the solid-state nature of the process promotes improved interfacial bonding between the reinforcement and the matrix. However, FSP is not without its limitations. Its application is primarily confined to surface or near-surface modifications, restricting its use for producing bulk composites. The process also demands specialized tooling and requires meticulous

control of processing parameters, such as tool rotation speed, traverse speed, and plunge depth, to achieve desired results.

### 1.3.6 Justification for using friction stir processing

In the pursuit of high-performance Metal Matrix Composites (MMCs), the inherent limitations of traditional fabrication methods necessitate the exploration of alternative techniques that ensure homogeneous reinforcement distribution and superior mechanical properties. Friction Stir Processing (FSP) has emerged as a particularly promising method, demonstrating a unique ability to achieve these critical objectives. In comparison to conventional processes such as stir casting and powder metallurgy, FSP consistently produces more refined and defect-free microstructures, ultimately leading to enhanced mechanical performance. The precise control over FSP parameters, including tool speed, plunge depth, and traverse speed, allows for the meticulous tailoring of the composite's properties to meet specific application requirements. Beyond bulk properties, FSP can significantly improve mechanical properties, particularly wear resistance [114-117]. Furthermore, FSP's remarkable versatility enables the incorporation of a wide range of reinforcement particle types, regardless of their chemical and physical characteristics, making it a highly adaptable technique for diverse MMC applications.

### 1.3.7 Justification for AA5083 as a Base Material

Various aluminum alloys, including Al 6061 [118], AA 2124 [119], AA 7039 [120], AA 7075 [121], Al A359 [122], Al A356 [123] and AA 6351 [124] have been used as base materials in the fabrication of AMMCs. However, AA5083 stands out as a crucial alloy, particularly in automotive, marine, and aerospace applications, due to its favorable deformation behavior and exceptional resistance to seawater corrosion [114]. Regarded as one of the most important aluminum alloys, AA5083 is widely employed in structural applications, notably in ship and building construction, owing to its high strength, excellent weldability, and superior corrosion resistance [125]. These mechanical properties make it ideally suited for marine environments where durability and resistance to harsh conditions are paramount. Notably, AA5083 is not heat-treatable as it relies on strain hardening and grain refinement for mechanical property enhancement, limiting the options for strength and hardness enhancement. Therefore, reinforcing it presents a viable alternative to further improve its mechanical properties (e.g strength and hardness) while maintaining its inherent ductility making it a prime candidate for MMC fabrication.

### 1.3.8 Justification for Coal and Silicon Carbide (SiC) as Reinforcements

Aluminium Metal Matrix Composites (AMMCs) are fabricated with a diverse range of reinforcements, utilizing various processing methods to tailor material properties. Materials such as $Al_2O_3$ [56-58], $B_4C$ [126-128], Cu [60], CNT [71-73], fly ash [78], graphene [74-75], graphite [76], $Mg_2Si$ [129], Ni powder [67], NiTi [68-69], RHA [77], SiC [60-63], SS [70], Ti [130], TiB [131], $TiB_2$ [132], TiC [133], WC [134], $Y_2O_3$ [135], $ZrO_2$ [65] and fibers [136] have all been incorporated to enhance properties like hardness, tensile strength, wear resistance, thermal stability, corrosion resistance, and chemical stability. Among these, silicon carbide, alumina, and boron carbide are the most frequently used. Silicon carbide, particularly, imparts excellent mechanical properties, including low weight, high tensile strength, stiffness, fatigue strength, corrosion resistance, and low thermal expansion [137-139]. Aluminium oxide reinforcement contributes high compressive and wear resistance, while boron carbide primarily enhances hardness but does not increase wear resistance [140].

#### 1.3.8.1 Coal as a Novel Reinforcement

Coal has been chosen as a novel reinforcement due to its abundance, cost-effectiveness, and potential to improve wear resistance and mechanical properties while promoting environmental sustainability. Primarily composed of carbon, coal can enhance hardness, self-lubrication, and wear resistance. Compared to expensive carbon-based reinforcements like graphene or CNTs, coal offers a significantly more affordable and readily available alternative. Its utilization also supports sustainable material use and waste reduction, aligning with environmental concerns.

#### 1.3.8.2 Silicon Carbide (SiC) as a Benchmark Reinforcement

Silicon carbide (SiC) serves as a benchmark reinforcement due to its proven ability to enhance hardness, wear resistance, and thermal stability in MMCs. With its high strength, excellent thermal conductivity, and corrosion resistance, SiC is widely employed in structural and marine applications [141,142]. Its extensive research and application history make it an ideal reference material for evaluating the performance of novel reinforcements like coal.

### 1.3.9 Conclusion

This study introduces a novel approach to enhancing AA5083 composites by incorporating coal as a reinforcement via Friction Stir Processing (FSP), with a comparative analysis against AA5083-SiC composites. The research aims to expand the current understanding of AMMCs fabrication by exploring a sustainable and cost-effective reinforcement alternative, while simultaneously evaluating its suitability for demanding marine and structural applications. While extensive research has focused on enhancing AA5083's mechanical properties through ceramic and hard particle reinforcement using FSP [143-145], the existing literature reveals a significant gap regarding the use of coal as a reinforcement in AA5083. The reviewed literature confirms FSP as a highly effective technique for producing AMMCs with superior composite characteristics, demonstrating that unreinforced aluminum alloys cannot match the mechanical properties of reinforced composites. Therefore, given coal's abundance, affordability, and potential to enhance wear resistance and mechanical properties while promoting environmental sustainability, it has been chosen as a novel reinforcement. Silicon carbide (SiC) serves as a benchmark reinforcement due to its well-established ability to improve hardness, wear resistance, and thermal stability. AA5083, selected for its excellent corrosion resistance, weldability, and high strength, is particularly suitable for marine applications. Addressing a gap in current knowledge, this study investigates the use of coal as a reinforcement material in AA5083 composites processed using FSP. The mechanical properties of the resulting AA5083-Coal composites will be compared with those of AA5083-SiC composites.

## 1.4 Research aim and objectives

The research aims to create an aluminium metal matrix composite (AA5083-SiC and AA5083-Coal) that can be used in the marine industry using the FSP technique. To fulfil this aim, the following objectives have been established:

- Optimisation of process parameters using the Taguchi method to determine the best conditions for fabricating the required aluminium metal matrix composites.
- Manufacturing a material (AMMCs) using an AA5083 as the parental/base material and SiC, as well as Coal, as reinforcement suitable for hull and ship decks using the FSP technique, with a specific focus on reinforcing the joint region rather than creating bulk AMMC sheets.
- Cutting of the joints on the surface of FSPed regions.

- Conducting mechanical and tribological tests on the reinforced AMMCs to analyze the characteristics of the composite and compare the results.

### 1.5 Thesis outline

Chapter one of the study contains an introduction to MMCs, background and fabrication of AMMCs, as well as the study's aims and objectives. The second chapter summarizes the evaluated literature and provides detailed information relevant to the current study. Chapter Three provides a comprehensive presentation of the experimental setup and performances that were carried out. The results of the tests conducted on the produced aluminum metal matrix composites (AA5083-SiC and AA5083-Coal) are reported in Chapter Four, along with the explanations that follow for each of the experiments. This chapter also includes a comparative study conducted between the AA5083-SiC and AA5083-Coal results. Chapter Five presents the study's conclusions based on the findings and recommendations are made for further work. Figure 1.5 depicts the thesis outline.

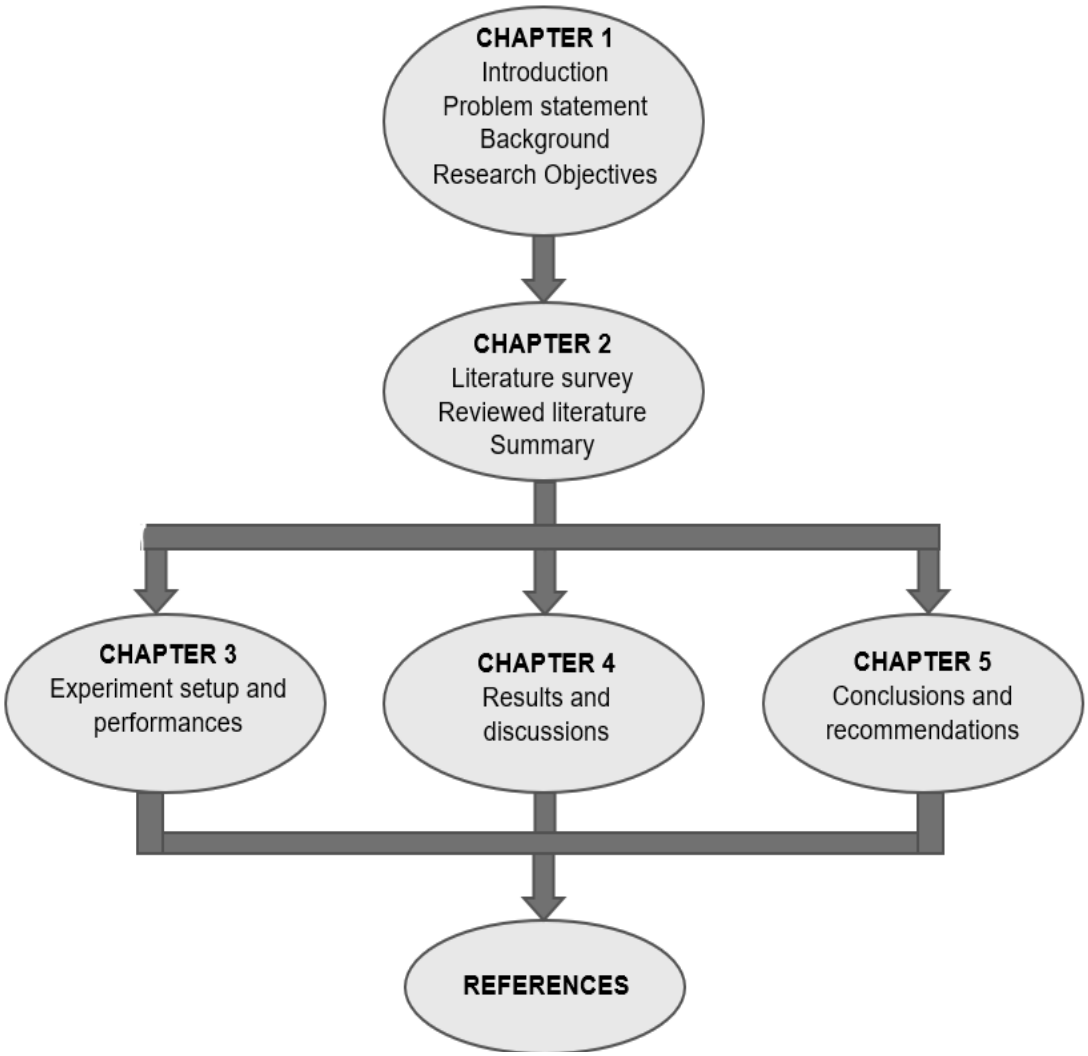


**Figure 1.5: Thesis outline**

# CHAPTER TWO

# LITERATURE REVIEW

This chapter presents an in-depth literature review focused on the fabrication of Aluminum Metal Matrix Composites (AMMCs) using Friction Stir Processing (FSP), with a particular emphasis on marine-grade aluminum alloys. To ensure a logical and coherent flow, the following sections will be discussed. First, a brief overview of aluminum alloys (AAs) used in marine applications will be provided, detailing the characteristics and applications of various aluminum alloy series relevant to marine environments. Second, the fabrication of AMMCs via FSP using a range of aluminum grades will be examined, highlighting the process parameters and resulting properties. Third, a detailed analysis of AMMCs fabricated via FSP using marine-grade aluminum alloys will be conducted, focusing on their microstructural and mechanical properties. Finally, a summary of the key findings from the literature review will be presented, identifying research gaps and justifying the necessity of the current study. The primary focus of this review is on FSP-fabricated AMMCs produced from marine-grade aluminum alloys, as these materials hold significant potential for enhancing the durability and performance of marine structures. The discussion will also include a broader overview of aluminum alloys (AAs) used in marine applications, including the characteristics of various aluminum alloy series and their uses, to provide context for the selection of AA5083 in this research.

## 2.1 A brief overview of aluminium alloys (AAs) used in marine application

Due to its high mechanical strength and low production cost, steel has been used in shipbuilding for about 150 years [146,147]. With the increasing need for larger ships, AAs have become the best alternative because of their strong corrosion resistance and reasonable weight savings due to their low density (2.71 grams per cubic centimetre) compared to that of steel (7.84 grams per cubic centimetre). Innovative technologies have been used to make several AAs with mechanical properties similar to those of steel that are necessary for shipbuilding and maritime applications for improved ship performance. The choice of AAs aluminium alloys over steel for maritime applications was based on their low weight and enhanced mechanical properties.

Aluminium is a non-ferrous metal that is lightweight and AAs have exceptional flexibility and applicability, along with multiple benefits (corrosion resistance, strength and workability), making them suitable for various goods and markets [148]. Naval architects and ocean engineers have recognised aluminium and its alloys as being very favourable materials for marine and offshore structures [149]. Many of these uses have been made possible by AAs' lighter weight, improved mechanical properties and corrosion resistance. Naval architects can use AAs to build boats with higher payloads and high-speed capability, a longer life, minimal maintenance costs and a high recycling value [150]. Aluminium and its alloys also provide significant benefits in terms of hull maintenance and structural weight reduction [151]. AAs from the 5xxx and 6xxx series have appropriate corrosion resistance properties and strength making them popular materials for maritime constructions such as decks, hulls and superstructures for boats, ships, cargo carriers and ferries [152, 153].

### 2.1.1 Aluminium alloy selection for marine applications

5xxx and 6xxx AAs have valuable uses in various marine structures, such as the fabrication and maintenance of offshore platforms, shipbuilding and submarines. The key features and applications of AAs are summarised below. A detailed list of aluminium alloys, their metallurgical grades and uses in marine structures is listed in Table 2.1.1.

#### 2.1.1.1 Properties and uses of AA 5xxx

Strain-hardened Al-Mg 5xxx AAs provide excellent corrosion resistance in salty water. Even at low temperatures, these alloys achieve exceptional strength and hardness. They can be easily welded up to a thickness of 20 mm utilising a variety of welding processes. AA 5xxx offers a fantastic balance of strength and corrosion resistance when compared to other AAs. The addition of Mg as a main alloying element is responsible for this alloy's high strength. AAs are often identified by distinct temper conditions. The inclusion of Mg as the primary alloying element is responsible for the alloy's exceptional strength. Different temper conditions are used to categorise AAs. The alloy's particular temper condition has a direct impact on the properties needed for marine applications. Specific temper grades H321 and H116 have been approved by the Aluminium Association for use in maritime applications for 5xxx AA with an Mg content that is greater or equal to three percent by weight [154]. Work hardening, annealing and stretching are for the H116 temper alloys and strain hardening and thermally stabilising for the H321 products. Similar mechanical properties and the desired corrosion resistance are attained at both temper settings. AA 5083 [152, 155, 156] is the most frequently used 5xxx series alloy in shipbuilding. It has high corrosion resistance and strength, as well as being easily formable when tempered. As the usage of aluminium and related alloys in maritime industries increased, so did the need for manufacturing new AAs with higher properties (formability, corrosion resistance and strength). The alloy's desired properties are enhanced by changing the chemical composition of the identified alloy. By making minor changes to the alloy composition, Pechiney Marine Group was able to obtain a significant improvement over AA 5083 [157]. In comparison to the traditional AA 5083, they produced AA 5383, that has a reduced Iron (Fe) and Silicon (Si) content and a higher Zirconium (Zr), Magnesium (Mg), Zinc (Zn), Copper (Cu) and Manganese (Mn) content. This alloy (AA 5383) outperformed AA 5083 in terms of formability, corrosion resistance and strength. Further alterations to alloy chemistry led to the creation of AA 5383NG [158], that contains slightly less Cr and Cu but more Zr, Mn and Mg than AA 5083. Other AAs (5059, 5052, 5086, 5454, 5456 and so on) have also been developed and are widely employed in maritime applications.

AAs are commonly employed in bulkheads, commercial ships' hulls, deck panels, doors, keel gratings, hatch covers, ladders, railings, stiffeners and windows [152]. Aluminium alloy 5083 is often used in marine applications [159-161] such as pressure vessels, drilling rigs and other applications [152]. Proserio ships (single hull with high speed) utilise AA 5083-H113/H321 for their decks, superstructure and stiffeners. Other AAs used in the construction of marine hulls for different boats include 5059 and 5383 [162]; while 5086, 5454 and 5456 are used for sheet and plate forms. Strain-hardened conditions (H temper) such as H 111, H132, H116, and H32 are employed when higher strength is required, while other alloys are commonly used in the annealed condition (O temper) for common uses [163, 164]. AA 5086-H 32, with a thickness of 4.5 to 12.7 mm, is currently an extensively used hull material. Although 5052 can also be utilised, bulkheads, cabins and fuel tanks are constructed from the same material as the hull [124]. Hull plating with AA 5086 is also common [161]. Smaller boats are also constructed from the AAs 5xxx series of metals. Privately owned aluminium boats are produced using AA 5456-H321 in thicknesses ranging from 4.8 to 9.5 mm. This alloy is also used in the construction of Hydrofoils' hulls, cabins and bulkheads. In marine frames, AA 5754 is utilised. AA 5083 and AA 5454 are also used in high-speed ferries for single or multiple hulls [154].

#### 2.1.1.2 Properties and uses of AA 6xxx

These alloy series has high strength, corrosion resistance and may be heat treated. Extrudability is one of the most essential characteristics of AA 6xxx. It is readily welded and

frequently utilised in shipbuilding in the extruded form [165]. The strong alloying elements of this alloy series, as compared to the AAs 5xxx series, are Mg and Si, that have almost identical strengths but significantly lower corrosion resistance. Extruded 6xxx alloys are frequently utilised in crossbars, deck furniture with complex cross-sectional shapes, hull stringers and ribs, radar towers, railings, stairways, sailboat masts, tracks and walkways [125]. Many small boats are created using the 6xxx alloy [161]. AA 6061, 6063 and 6082 are the most often utilised 6xxx alloys in the marine sector. In cases in which stretch forming is not required, AA 6061-T6 is a popular material employed for small hull ships. The alloy AA 6061-T4 is also utilised when stretch forming is necessary [161]. AA 6061 is used in bulkheads, deck plating, deck panels and marine frames [155, 161]. Extruded AA 6061-T6 shapes are also extensively utilised in the manufacture of privately owned boats. AA6063 alloys are also mostly utilised in boat and ship construction and is employed to make the superstructure of high-speed ferries stable. AA 6063//6061 extrusions are often used for ornamental and structural components such as gunwales, spray rails and keels. The "fish room" system, a lightweight structural framing system frequently employed in construction, makes use of AA 6063/6061-T6 aluminum, which can be found in both rolled and extruded forms [161]. The high-strength alloy AA 6082 is utilised in maritime frames and stiffened deck panels for strongly loaded structural applications. Most strengthened deck panels are constructed from AA 6xxx, and this material ultimately will find its way into the manufacture of hull structures.

**Table 2.1.1: Aluminium alloys, metallurgical grades, and marine structural applications.**

| AA | Metallurgical classification grades | The use in different marine structures |
|---|---|---|
| 5052 | H321 | Bulkheads, cabins, fuel tanks, cabins [160] and small hulls |
| 5059 | H116, H321 | Ship’s hulls [162,164] |
| 5083 | H116, H321, H323 | High-speed ship superstructures [155], hull stiffeners, and ship decks and hulls [159,160,161, 163,164] |
| 5086 | H116, H321 | Bulkheads, cabins [161], hulls [164] and hull plating |
| 5383 | O, H111, H116, H321 | Hulls [161,164] |
| 5454 | O, H112, H32, H34 | Ship's upper decks [163] and stack enclosures |
| 5456 | O, H112, H116, H32, H321 | High-speed ferry hulls [155,163] |
| 6005 | T6 | Deck panels with a built-in stiffener [149] |
| 6061 | T6 | Cabin and bulkheads, deck plating and marine frames [155,161], and fish room system [161]. Gunwales, hull, keels, integrally stiffened deck panels [149] and spray rails (decorative sections) |
| 6063 | T6 | Chines, fish room system [161], gunwales and spray rails (decorative parts) [161], integrally strengthened deck panels [149] and keels |
| 6082 | T6 | Deck panels with a built-in stiffener [149] |

## 2.2 Fabrication of AMMCs via FSP using different aluminium grades

This section details the fabrication of AMMCs using FSP with oxide and carbide reinforcements. It covers studies on AA1050 with TiC, AA2024 with SiC, AA2014 with $Al_2O_3$, and AA7075-T651 with $B_4C$ and TiC.

### 2.2.1 Oxide and Carbide Reinforcements

Sanusi and Akinlabi [25] explored the fabrication of an AA1050-Titanium carbide (TiC) surface composite using FSP. The FSP approach was employed in this work to fabricate surface composites of AA 1050 reinforced with TiC powder having particle sizes less than 60 μm squeezed into the groove. For this process, rotational speeds of 1200 and 1600 rpm and travel rates of 100, 200 and 300 mm/min were used. The effect of processing factors on the microstructure of FSPed Al-TiC composites was then examined. Microstructural characterisation was performed using optical microscopes and scanning electron microscope (SEM) in conjunction with Oxford energy-dispersion spectrometry. The results showed that the processing variables had an impact on the TiC particle dispersion. The influence of processing variables on the microhardness of FSPed Al-TiC composites was also investigated using microhardness profiling. According to the findings, the microhardness profile of the processed samples exhibited a rise in hardness value when compared to the parent material. The FSP technique increased surface engineering properties, according to the wear-resistance test findings.

Ghanbari et al. [61] employed the two-pass and four-pass FSP procedures to produce AA2024-Silicon carbide (SiC) composites. An H13 steel tool with a square pin shape was used for the FSP procedure. For the entire FSP operation, the rotational and traverse speeds were held at 1000 revolutions per minute and 25 millimetres per minute, respectively. It was noted that at higher FSP passes, regardless of post-treatment, the microstructural examination indicated refined grains and homogeneous particle dispersion. The heat-treated FSP specimens had a microhardness that was 70 Vickers hardness greater than the non-heat-treated samples. The dissolution of coarse S-section precipitates and the re-precipitation of refined S-phase precipitates have been connected to the growth in microhardness. The improvement in wear resistance was further improved by using the re-precipitation of fine S-phase precipitates.

Sharma et al. [166] used the four-pass FSP approach to reinforce the AA2014-T6 plate with a thickness of 6.35 millimetres with 38 μm silicon carbide particles. The rotating rate was kept constant at 710 revolutions per minute during the fabrication process, while the traverse speed was kept constant at 100 millimetres per minute. A hot die metallic tool with a conical pin form and concave shoulder was used for the FSP technique. Consequent to the 4-pass FSP technique, microstructural examination revealed a considerable reduction in grain size (from 120 micrometres to 8 micrometres) in the stir region, as well as the dissolving of several precipitates because of the high-temperature exhibition. AMMCs were discovered to have a slightly greater microhardness than the base metal. Owing to the occurrence of dynamic recrystallisation during FSP, a recrystallised equiaxed microstructure occurred. A crack-free surface composite with a homogenous distribution of SiC particles was created and preserved. The size of the reinforcing particles was lowered during processing. However, the microhardness of the FSPed alloy is less than that of the parental alloy, indicating that precipitation hardening is more important than grain refining. The inclusion of harder ceramic particles enhances the surface composite's hardness. However, this reviewed study [166] does not mention the other mechanical properties of the fabricated surface composite.

Ramesh and Murugan [167] examined FSP for producing and characterising an AA7075-T651-Boron carbide ($B_4C$) surface composite. During the FSP process, the tool rotational

speeds were changed from 425 to 575 rpm, the traverse rate from 40 to 60 mm/min and the number of passes from 1 to 3. The researchers discovered that an acceptable processed surface composite could be created with a rotating speed of 500 revolutions per minute and a traverse speed of 60 millimetres in 3 passes. Furthermore, increasing the rotating speed lowered the grain size in the NZ for a given traversal speed. The average microhardness of the FSPed surface composite was 1.5 times that of the parental metal. Garca-Vázquez et al [168] studied the effect of FSP parameters on AA7075-T651-TiC. The influence of FSP parameters on microstructure, such as whether the groove is sealed or unsealed, the direction of each pass, and the number of passes, was examined. To create a functional surface, TiC nanoparticles (2 percent weight) were incorporated into AA7075-T651. Fixed parameters employed for this were: 1000 rpm rotation, 300 mm/min travel speed, and 2.8 mm pin penetration. The selected FSP parameters, according to the findings, impacted the distribution of TiC particles, the micro-hardness of the surface composites and the area of the surface composite. In addition, the microhardness value was shown to be decreasing.

Hamdollahzadeh et al. [169] investigated the impact of second-pass processing on the evolution of the microstructural and mechanical properties of AA7075 friction stir weldment strengthened with nano-SiC. FSP was conducted at 1250 revolutions per minute and 40 millimetres per minute when the groove was filled with SiC particles. The researchers used single and double-pass FSP in the investigation and discovered uniform dispersion as well as grain refinement in double-pass FSPed AMMCs. The connection between the reinforcements and the base metal was strong in each specimen. The 1-pass processed specimen, however, had a less uniform particle dispersion than the 2-pass processed material. During tensile testing, all tensile specimens were fractured beyond the SZ. Surprisingly, SEM examination of cracked surfaces matched the ductility results perfectly.

Bharti et al. [170] used a one-pass FSP procedure to reinforce 15 μm Aluminum oxide ($Al_2O_3$) particles into an AA2014 plate five millimetres thick. An H13 steel tool profile with a tapered cylindrical pin was used for the one-pass FSP technique. To achieve the desired results, the two different rotational speeds of 1000 revolutions per minute and 1400 revolutions per minute, respectively, were paired with a 40-millimetre per minute constant traverse speed. A rotating speed of 1000 revolutions per minute exhibited a 9.2 μm average grain size, whereas a rotational speed of 1400 revolutions per minute exhibited a 3.2 μm average grain size. The specimen developed at 1000 revolutions per minute had a microhardness of 154 HV, whereas the specimen manufactured at 1400 revolutions per minute had a somewhat lower microhardness of 142 HV. Surface roughness was established to be decreasing when rotational speed was increased, and wear behaviour followed a similar trend. However, the information concerning the other mechanical properties was not found during the literature reviewed conducted for this paper.

Moustafa [171] investigated the effect of overlapping FSP on the mechanical properties of AA2024-$Al_2O_3$ nanocomposites. As a surface composite sheet, AMMCs reinforced with aluminium oxide nanoparticles were created via FSP. Three travel rates of 10 millimetres per minute, 15 millimetres per minute and 20 millimetres per minute, were used with the tool rotating at 900, 1120, 1400 and 1800 rpm, respectively. A 2-degree tool tilt angle was used. 0.5 mm/s tool plunge speed and 2 s dwell duration were maintained at the same levels. In the procedure, three multi-passes were used. Mechanical properties, hardness and microstructure grain were studied for processing parameters. According to this reviewed study's findings, multiple FSP passes create a good dispersion of aluminium oxide in surface composite and homogeneous distribution. The microstructure inspection reveals finer grain in specimens subjected to two and three passes of FSP. When compared to the base metal, grain refining had increased by 80%. Processing factors, particularly rotary tool rates and FSP passes, have a significant effect on UTS and surface microhardness. Owing to the presence of reinforcement $Al_2O_3$ nanoparticles, the average UTS improved by 25%, and the average microhardness improved by 46%. Multi-pass FSP increases the hardness of matrix composites, according to the study's findings [171].

Yang et al. [172] produced the 4-pass AA2024-$Al_2O_3$ composites using FSP. An H13 steel tool with a concave shoulder and a threaded pin shape was used to fabricate the MMCs. The tool rotational rates remained constant at 900 rpm during the FSP process, and the traverse rate was adjusted to 50 mm/min. The tool was tilted at a 2.5° angle to avoid surface defects. Before employing the FSP approach, the 2.5 mm thick AA2024 plate was cold sprayed with $Al_2O_3$ to generate a 4 mm thick AA2024-$Al_2O_3$ layer. Post the FSP technique, the microstructural examination revealed excellent particle dispersion and refined grains. Low FSP passes, however, demonstrated good corrosion resistance, with two pass FSP specimens demonstrating remarkable corrosion resistance. The specimens that went through the four-pass FSP process showed poor corrosion resistance due to a loss of good surface quality and damaged inner coating interfaces.

2.2.2 Analysis and Discussion

Table 2.2.2 summarizes the composites produced from different aluminum base materials with various reinforcements using the FSP process.

**Table 2.2.2: Aluminium metal matrix composite developed with FSP outside the marine grades.**

| AA+ Reinforcement | Parameters | | Results | Reference |
|---|---|---|---|---|
| | Tool rotational speed (rpm) | Traverse speed (mm/min) | | |
| 1050+TiC | Varying | Varying | The processing parameters had an impact on the TiC particle distribution.<br>The hardness value increased when compared to the parent material. | 25 |
| 2024-T351+ SiC | 1000 | 25 | In the SZ, nanoparticles with a uniform dispersion were formed.<br>The heat-treated sample's results revealed an improvement in hardness and wear resistance. | 61 |
| 2014-T4+ $Al_2O_3$ | Varying | 40 | After FSP, there was a uniform distribution of $Al_2O_3$ reinforcement particles in AA2014.<br>After FSP, adding $Al_2O_3$ resulted in a 30% increase in hardness.<br>In FSPed samples, the coefficient of friction (COF) improved from 0.27461 in base material to 0.22570. | 170 |
| 2014-T6+ SiC | 710 | 100 | A surface composite with no defects and a uniform distribution of SiC particles was produced.<br>Due to the addition of harder ceramic particles, the surface composite exhibited an increase in hardness. | 166 |
| 2024+ $Al_2O_3$ | Varying | Varying | Compared to base metal, grain refinement had improved by 80%.<br>The presence of the reinforcement $Al_2O_3$ in the nanoparticles improved the ultimate tensile strength and average hardness by 25% and 46%, respectively. | 171 |

| | | | | |
|---|---|---|---|---|
| 2024-T3+ $Al_2O_3$ | 900 | 50 | The AA2024/$Al_2O_3$ coatings' corrosion resistance improved with the best corrosion performance happening at 2-pass FSP.<br>At four passes, there was a decrease in corrosion resistance. | 172 |
| 7075-T651+ $B_4C$ | Varying | Varying | FSP composite had an average hardness that was 1.5 times more than that of the base metal AA7075-T651.<br>Hardness was increased due to the fine dispersion of $B_4C$ particles and the tiny grain size of the aluminum matrix. | 167 |
| 7075-T651+ TiC | 1000 | 300 | The findings showed that the chosen FSP parameters had an impact on the surface composites' micro-hardness, TiC particle dispersion and surface area. | 168 |
| 7075-O+ SiC | 1200 | 40 | Each specimen had a strong bond between the reinforcements and the matrix.<br>The microstructure of the 2-pass processed specimen was coarser than that of the 1-pass processed one.<br>During tensile testing, every tensile specimen broke outside the SZ. | 169 |

The influence of processing parameters is significant in TiC-reinforced AA1050 composites, affecting the distribution of TiC particles and resulting in increased hardness. In AA2024-T351, the introduction of SiC leads to a uniform dispersion of nanoparticles and enhances both hardness and wear resistance, with heat treatment further improving these properties. Silicon carbide reinforcement in AA2014-T6 refines the grain size of the aluminum matrix and consequently increases hardness. The addition of $B_4C$ to AA7075-T651 increases hardness, attributed to the fine dispersion of particles and the resulting small grain size. For TiC-reinforced AA7075-T651, friction stir processing (FSP) parameters play a crucial role in determining microhardness, particle dispersion, and surface area. Finally, the incorporation of $Al_2O_3$ in AA2024 improves grain refinement, ultimate tensile strength (UTS), and hardness, although it's important to note that corrosion resistance can vary depending on the number of FSP passes.

### 2.3 Detailed review of fabricated AMMCs via FSP using marine aluminium alloys

In shipbuilding, several marine AAs are used to fabricate various sections such as hulls, superstructures, decks and bulkheads. MMCs that use FSP have a distinct advantage over MMCs that use other manufacturing techniques. When compared with most other strategies, FSP has several distinct benefits. This part of the study examines the impact of reinforcing particles, process parameters, multiple passes and active cooling on mechanical characteristics during the fabrication of aluminium MMCs using available literature. The review focused on marine-grade AAs.

#### 2.3.1 AA5052- based MMCs

This section details AA5052 composites with oxide/carbide ($Al_2O_3$, TiO2, SiC) and carbonaceous (Carbon fiber) reinforcements.

2.3.1.1 Oxide and Carbide Reinforcements in AA5052

Sharifitabar et al. [173] employed FSP to create the AA5052-$Al_2O_3$ nano-ceramic particle reinforced composite. After multiple FSP passes, the microstructural and mechanical properties of AA5052-$Al_2O_3$ surface composites were studied. FSP was performed with varying tool rotation speed to travel rate ratios (ω/υ) that ranged from 8 revolutions per minute to 100 revolutions per minute and a pin tilting angle (φ) ranging from 2.5° to 5° to identify optimum FSP conditions for the fabrication of NZ without macroscopic flaws. It was observed that as the number of FSP passes increased, the grain size of the NZ reduced, and the surface composite produced by 4 passes had a submicron mean grain size. The increasing of the FSP passes also resulted in homogenous $Al_2O_3$ particle dispersion in the base material and the formation of a nanocomposite after four passes with a mean cluster size of 70 nm. Tensile tests revealed that composites made in 3 and 4 passes had greater UTS and yield strengths and lower elongation than FSPed materials made without powder under similar circumstances and that all FSP samples had greater elongation than the parental metal. In perfect parameters, UTS and percentage elongation of parental material improved to 118% and 165% respectively, in a composite formed by 4 FSP passes.

Mathur et al. [174] investigated the impact of reinforcement titanium dioxide nano-particles, on the AA5052 using FSP. Variable parameters such as spindle rotating speed of 700 rpm, 1000 rpm and 1300 rpm, as well as traverse rate of 50 mm/min, 65 mm/min and 80 mm/min, respectively, were employed with the 6 mm square pin tool. The maximum hardness value of 78 ± 1 Vickers hardness and tensile strength value of 193.1 ± 3 megapascals were obtained at rotational and traverse speeds of 1000 rpm and 65 mm/min, respectively. Micro-voids were noted at the grain boundaries of the casted aluminium alloy 5052. Micro-voids were removed after FSP because of dynamic recrystallisation caused by tool movement throughout the process. The AMMCs saw grain size decrease because of dynamic recrystallisation during the process. Hardness was improved up to 1000 rpm tool rotating speed due to grain refinement and homogenous reinforcement distribution. However, after 1000 rpm, there was a decrease in hardness. According to the authors [174], excessive centrifugal force caused the reinforcement to be thrown away from the SZ, resulting in a drop in hardness. During the specimen's tensile test, a ductile fracture was discovered.

Dolatkhah et al. [175] investigated how process factors affected the mechanical properties and microstructure of an AA5052-SiC composite made using FSP. An MMCs was created on the surface of 5052 aluminium sheets using FSP and 5 μm and 50 nm SiC particles. Between passes, the impact of traverse speed and rotational direction shifts was investigated. Experiments were conducted using all combinations of three traverse speeds of 40 mm/min, 80 mm/min and 125 mm/min and three rotational speeds of 700 revolutions per minute, 1120 revolutions per minute and 1400 revolutions per minute, respectively, to discover the tool rotational and traverse speeds that resulted in the greatest powder dispersion. The effects of tool rotational speed and particle size on SiC particle distribution, FSP passes and microstructure, wear and microhardness parameters of specimens were investigated. The results show that decreasing the size of the SiC particles, changing the rotating direction of the tool between FSP passes, decreasing the size of the SiC particles and increasing the number of passes, enhanced the hardness and wear characteristics. An ultrafine microstructure was created using FSP and nano-sized SiC particles. The inclusion of SiC powder increased the hardness substantially. In comparison to the parental material, the value microhardness improved by up to 55%, with a 9.7 times reduction in wear rate. Another study [176] found that AA5052-SiC particle composites may be produced satisfactorily using FSP. In the same study, the hardness of the resulting AMMC increased by up to 140%.

2.3.1.2 Carbonaceous Reinforcements in AA5052

Cao et al. [177] studied AA5052-Carbon fiber composites' microstructural, tribological and mechanical properties. In this work, multi-pass FSP was used to successfully produce carbon fiber-reinforced AA5052 bulk composites to improve AA5052 wear resistance. FSP was carried out using a 1000 rpm constant rotation speed and traverse rates of 50, 75 and 100 mm/min. The tool's tilt angle was 2.5° and the depth of the plunge was 0.2 mm. For comparison, the same processes were used to process unreinforced AA5052 at a traverse speed of 100 mm/min and a rotating speed of 1000 rpm. It was discovered that carbon fibers were homogeneously spread in considerable volume in the composites, with no visible $Al_4C_3$ layer between the carbon fibers and the parent material, according to microstructure investigations. Owing to the substantial plastic deformation caused by FSP, the orientation of carbon fibers in the composites was random. Further mechanical testing revealed that the hardness of the composite improved by 46.8% when compared to the parental metal, and the composite produced at 1000 revolutions per minute and 75 millimetres per minute had an 18.6% higher UTS and 13.0% greater elongation than the parental material. The wear tests revealed that the composite's wear process was more stable, with wear volume loss reduced by more than 70%. GNDs, fracture deflection and load transmission of carbon fibres have all been linked with improved mechanical properties.

2.3.1.3 Analysis and Discussion

Table 2.3.1.3 summarises the composites fabricated from AA5052 base material with various reinforcements using the FSP process.

**Table 2.3.1.3: AA5052- based MMCs fabricated with FSP.**

| AA+ Reinforcement | Parameters | | Results | Reference |
|---|---|---|---|---|
| | Tool rotational speed (rpm) | Traverse speed (mm/min) | | |
| 5052-H30+ $Al_2O_3$ | Varying | Varying | The SZ's grain size reduced as the number of FSP passes increased, and the composite produced by the four passes had an average grain size of less than one micron.<br>The increase in FSP passes caused an equal distribution of $Al_2O_3$ particles in the matrix.<br>Tensile and yield strengths were higher, and elongation was lower for three and four-pass composites compared to friction stir processed materials without powder. | 173 |
| 5052+ $TiO_2$ | Varying | Varying | When compared to the aluminium alloy without FSP, the reinforced material had improved mechanical properties.<br>Titanium dioxide nanoparticles were discovered in the grain structure of the aluminium alloy, that improved the surface properties of the material. | 174 |
| 5052+ SiC | Varying | Varying | The incorporation of the silicon carbide powder considerably increased hardness. | 175 |

| | | | | |
|---|---|---|---|---|
| | | | The wear rate of the nanocomposite layer was nine times lower than that of the base material. | |
| 5052+ SiC | Varying | Varying | The addition of SiC nanoparticles had a significant effect on grain distribution and orientation.<br>Compared to the annealed Al-Mg alloy, the processed UFGed nanocomposite improved hardness, yield stress and ultimate tensile strength by up to 140%, 75% and 60%, respectively.<br>The fracture features revealed a mixed ductile-brittle rupture pattern. | 176 |
| 5052-H32+ Carbon fibre | 1000 | Varying | The hardness of the composites improved by 46.8% when compared to the base metal, with 18.6% higher UTS and 13.0% greater elongation.<br>The composites experienced abrasive wear, but the base metal and FSPed matrix also had adhesive wear. | 177 |

The studies on AA5052-based MMCs demonstrate the versatility of FSP in fabricating composites with various reinforcements. The addition of $Al_2O_3$ to AA5052 refines the grain size and enhances both ultimate tensile strength (UTS) and yield strength, particularly when employing multi-pass friction stir processing (FSP). $TiO_2$ reinforcement is effective in improving the mechanical and surface properties of the composite material. Furthermore, the inclusion of SiC leads to increased hardness and a reduction in the wear rate. Carbon fiber reinforcement contributes to improvements in hardness, UTS, and wear resistance. Across these composites, it is crucial to recognize that processing parameters play a vital role in achieving optimal particle dispersion and, consequently, desired composite properties.

### 2.3.2 AA5083- based MMCs

This section discusses AA5083 composites with various reinforcements: oxides/carbides ($ZrO_2$, Graphene Oxide, SiC, $B_4C$), carbonaceous (MWCNTs, CNTs), metallic (Cu, Ni, W), and hybrid (CNTs/$CeO_2$, $B_4C$/CNTs, $B_4C$/MWCNTs, CNTs with SiC).

#### 2.3.2.1 Oxide and Carbide Reinforcements in AA5083

Mirjavadi et al. [65] studied the wear and mechanical properties of an AA5083-$ZrO_2$ composite made using FSP. This investigation used multi-pass FSP with zirconia nanoparticles to fabricate surface nanocomposites on AA5083 sheets. The impact of increasing the number of passes on the microhardness, microstructural, wear parameters and tensile of the specimens was investigated. After a series of trial and test runs of FSP, it was determined that a traverse speed of 50 mm/min and a rotating rate of 800 rpm were the most ideal in terms of possible flaws, that was also in agreement with reference [178], and that these speeds were employed for all FSP passes. For all samples, the tool tilt angle concerning the workpieces was approximately 3°. As a result, it was discovered that FSP iteration consistently increases the material's tensile properties and microhardness. This result was mostly due to microstructural modification using FSP, which included improved powder dispersion, finer grain size and reduced clustered particles. In the 8-pass friction stir processed nanocomposite, EBSD and TEM investigation revealed a substantial number of high-angle grain boundaries and continuous dynamic recrystallisation. According to wear tests, the wear rate of the further processed sample was also much lower than that of its counterparts. Furthermore, the fracture

surface of the 8-pass treated material, in common with the base material, displayed ductile fracture consisting mainly of dimples and voids. The composite with eight passes had the most grain-refined structure, with a microhardness of 140 Vickers microhardness. The wear rate of composites produced in eight passes was also reduced.

Naghshekesh et al. [179] used graphene oxide as the reinforcing material to evaluate the impact of FSP on the surface of AA5083. To enhance the microstructural and mechanical properties of the AA5083, a surface nanocomposite comprising graphene oxide was created utilising FSP in a liquid-cooled condition. For this aim, FSP was utilised to produce up to three passes on a parental material with and without reinforcing particles. The resulting surface–nanocomposite, friction stir processed AA5083, and base material were studied for microstructural characteristics and mechanical properties. For this study, the processing was carried out at a 315 rpm rotational speed and a 16 mm/min traverse speed. The microstructure was studied using electron backscatter diffraction and it was observed that after the processing, the grain size of the nanocomposite was approximately 1 μm. The grain size of the specimen without reinforcement was 6 ± 1.1 μm, whereas the base material grain size was 23 ± 2.3 μm. The main cause for this discrepancy was the considerable impact of the reinforcing particles on grain growth in the nanocomposite specimen. According to research on the mechanical properties of the parental material, nanocomposite and FSPed specimen, using a chilling environment while executing the procedure increases the microhardness of the NZ compared to that of the parental material. In the presence of graphene oxide particles, the rise was increased to 123 ± 1.7 HV. In terms of tensile properties, the nanocomposite outperformed the parent material and the FSPed sample.

Mishra et al. [180] were the first to work on composite manufacturing utilising FSP. Composites containing AA5083 alloy as base material and SiC as reinforcement were created in this study. The development of AA5083-SiC surface composites with various particle volume fractions was successful. The surface of AA5083 plates was cleaned before processing. A small amount of silicon carbide powder was mixed with a small amount of methanol and then put on the plates' surface to generate a thin silicon carbide particle coating. The procedure is identical to tape casting, except there is no binder in the mixture. After drying in the air, the aluminium plates with a pre-placed SiC particle coating were exposed to FSP. The pin height of the tacking tool used was 1.0 mm. The tool was spun at a constant speed of 300 rpm while the shoulder depth and traverse rate were varied. The tool spindle angle was adjusted at 2.5°, that assisted the forging action at the shoulder's trailing edge. According to the study's findings, the thickness of the surface composite layer varied from 50 μm to 200 μm. The silicon carbide particles were equally distributed in the aluminium base material. The surface composite, which is reinforced with 27 volume percent silicon carbide of 0.7 μm average particle size, has a microhardness of 173 HV, that is approximately twice that of the base material. As a result of the solid-state fabrication, high-performance surface composites with very fine microstructures were created. When compared to the base material, there was a 51% increase in microhardness and wear resistance.

Deepak et al. [181] evaluated the mechanical properties of an AA5083-SiC surface composite prepared by FSP. The FSP tool was installed in the spindle of a CNC milling machine, that was configured to rotate at 1200 rpm with a traverse speed of 40 millimetres on the machine bed. The results showed that doping AA5083 with hard SiC particles, using FSP significantly increases the surface composite's microhardness generated on the friction stir processed sample layer. The microhardness is highest in the middle of the FSPed zone at 155 HV and drops to roughly 84 HV at a distance of approximately 2 millimetres from the middle of the FSPed zone on each side. Despite its enhanced hardness, the FSPed sample had a poorer wear resistance than AA5083. During wear testing, the FSPed sample had a higher friction force and a higher coefficient of friction. This result could have been due to the greater friction force and coefficient of friction reported during wear testing in the FSPed sample.

Yuvaraj et al. [182] used FSP to create an AA5083-$B_4C$ nanocomposite and tribologically characterise it. FSP was used to produce an AA5083 incorporated with boron carbide as a reinforced layer. As reinforcements, nano-sized and micro-sized $B_4C$ particles were utilised. Optical microscopy and SEM examinations were used to examine the friction-processed surface composite layer. In the creation of surface composites by FSP, the number of passes and the amount of reinforcement are critical. Before fabrication, a series of trials were undertaken, and the constant rotational and transverse speeds were determined to be 1000 revolutions per minute and 25 millimetres per minute, respectively. Microhardness tests and tensile tests were used to evaluate the mechanical properties of the FSPed surface composites. The results were compared to the base metal properties. The impact of reinforcement and the number of passes on properties were also examined. The pin-on-disk test was used to assess the surface composite's tribological performance. Compared to the base metal's performance, the surface composite layer created in 3 passes with nanoparticle reinforcement improved wear resistance, tensile behaviour and hardness. The dispersion of nanoparticles in the base material became more uniform compared to a single-pass FSP nanocomposite, resulting in increased hardness. After three passes, the microhardness of the nanocomposite was raised to 122 HV. The hard $B_4C$ particles placed on the surface of the AA5083 improved the wear resistance of the nanocomposite. In the one-pass method, some substantial reductions in yield and ultimate tensile strength values of surface composites were found when compared to non-reinforced samples. Despite these reductions, the surface composites' microhardness was greater than that of the non-reinforced samples and the wear rate was also reduced.

Jain et al. [183] investigated the mechanical properties, sliding wear behaviour and microstructure of AA5083-$B_4C$/SiC/TiC surface composites produced via FSP. In this work, FSP was used to make three dissimilar AA5083 surface composites reinforced with TiC, $B_4C$ and SiC particles. The mechanical properties of reinforced particles and three sequential FSP passes were examined. Based on experimental trials, a tool tilt angle of 3°, a transverse rate of 25 mm/min, several passes and a rotational speed of 1600 rpm were chosen to generate a sound FSP area and homogenous particle dispersion in the stirred zone. The FSPed sample's mechanical properties were assessed and compared to the parental material. There was substantial grain refinement in the microstructure, with dense particulate distribution on both the advancing and retreating sides of the stir region, particle-free zones and strong particle-matrix bonding in some areas. FSP induces significant plastic deformation in the materials, allowing the constituent phase to mix and refine. The FSPed sample's wear resistance was assessed and compared to the parental material. According to the findings, including TiC, $B_4C$, and silicon carbide particles in the parental material (AA5083) enhances wear characteristics. According to the data, when a pin-on-disc tribometer was used to evaluate the wear mechanism, findings revealed that the wear mode changed from abrasive to delamination. Furthermore, the findings show that adding TiC, $B_4C$ and SiC particles to the parental material improves the tensile properties while also enhancing its hardness. The fracture mode of SiC and TiC particle-reinforced surface composites was ductile, whereas the fracture mode of B4C reinforced surface composites was bimodal. The UTS and microhardness of the AA5083-$B_4C$ composite were found to be 349 MPa and 132.56 ± 2.52 HV, respectively, when compared to the AA5083-SiC/ TiC composite. The AA 5083-$B_4C$ composite has a minimum wear rate of 18x10-5 $mm^3$/Nm.

2.3.2.2 Carbonaceous Reinforcements in AA5083

Owa and Shimizu [184] explored the fabrication and strength behaviour of MWCNT-reinforced AA5083 composite through FSP. The inclusion of MWCNTs into AA5083 via FSP was researched to increase the strength of the alloy, which is utilised in various industries. The following FSP parameters were used to fabricate surface composite (AA5083-MWCNT), a 3° tilt angle, a traverse speed of 25 mm/min, a rotational speed of 880 rpm and a traverse length of 90 L/min. Compared to the base material, the composite grain size was greatly

refined. With the FSP-optimised conditions, the composites contained no voids or other flaws. The use of a composite powder comprised of MWCNTs and AA5083 resulted in the grain refinement and uniform distribution of MWCNTs. When compared to the base material, the composite's proof stresses ranged from 53% to 61% higher and the UTS increased from 13% to 16%.

Prabhakar et al. [185] used FSP to make AA5083-CNT composites and studied the effects of grain refinement and carbon nanotubes on corrosion and mechanical properties. In the current investigation, FSP was used to integrate CNT into AA5083 to produce a metal matrix composite. The processing was performed at a rotational speed of 1800 rpm and a feed rate of 25 mm/min, that is based on the results of the preliminary experiments. Microstructural analysis revealed smaller grains and nonuniform CNT dispersion in the SZ. The fine grains and presence of CNT in the composite resulted in a 25% improvement in hardness when compared to unprocessed aluminium alloy, that is attributable to the fine grains and presence of CNT in the composite. The electrochemical tests revealed that the FSPed composite had somewhat greater corrosion resistance. The findings reveal that the addition of CNT, in combination with the grain size effect, has a considerable impact on the corrosion resistance of AA5083. As a result of the findings, it can be concluded that adding CNT to AA5083 through FSP can increase mechanical performance. However, attention must be taken to enhance CNT dispersion since the presence of CNT has a significant impact on corrosion resistance. It was found that by using FSP to fabricate AA5083-CNT composites, lightweight energy-efficient structures with superior mechanical properties and corrosion resistance may be constructed.

2.3.2.3 Metal Reinforcements in AA5083

Zohoor et al. [186] studied the influence of processing variables on the formation of Al-Mg/Cu composites using FSP. This study examined the fabrication of AA5083-Cu surface composite layer using aluminium alloy 5083 with copper particles via FSP. The FSP settings were 25 mm/min traverse speeds, 750 rpm and 1900 rpm tool rotational speeds with a tilted angle of 3°. SEM and optical microscopy were used to characterise the microstructure. Particle distribution pattern, microstructure and microhardness were studied as a function of FSP pass numbers, rotational speed and copper particle size. According to the findings, the samples with micro and nano-sized particles showed tiny grains and a greater level of microhardness. The nano-sized particle composite surpassed the AA5083 in terms of tensile strength and ductility. X-ray diffraction (XRD) studies were performed on the specimens FSPed with Cu particles to discover the phases present in the NZ. Some reactions between the alloying elements are seen in XRD observations. After four passes using Cu-reinforcing particles, a considerable increase in strength and hardness was noted. The chemical interaction between Cu particles and the aluminium material was also observed to increase with rotational speed.

Bauri et al. [187] investigated the influence of process variables and tool geometry on the fabrication of AA5083-Ni composites using FSP. For FSP, a traditional cylindrical tool was originally employed, and numerous processing parameters such as rotational and tool traverse speeds were investigated to obtain a defect-free SZ and uniform particle dispersion. Another tool with particular characteristics on the pin and shoulder was used to investigate the influence of tool geometry. For producing a defect-free SZ, a traverse speed of 24 mm/min and a tool rotation speed of 1200 rpm were determined to be effective. Regardless of whether the SZ was flawed or sound, the distribution of Ni particles was inhomogeneous for all the parameters utilised with the basic cylindrical tool. The tool with the unique features of threads on the pin and spiral grooves on the shoulder was found to be extremely successful in both establishing a sound SZ and dispersing Ni particles. In comparison to coarse particles received as-is, ball-milled tiny particles were found to be distributed more evenly in the SZ. The grain size of the aluminium base material was similarly reduced from 25 microns to 3 microns using FSP. The microstructure was characterised by equiaxed fine grains with a large

proportion of high-angle grain boundaries and a narrow grain size distribution. The impact of particle inclusion on the alloy's mechanical properties was also studied. When comparing the base material, the composite's strength enhanced dramatically, and it also attained a high level of ductility.

Kumar et al. [188] studied the effect of ball milling and particle size on the surface composite FSPed AA5083-Ni. To produce a metal particle-reinforced composite, FSP was employed to integrate Ni particles into an AA5083 material. To achieve a flawless NZ and uniform particle distribution, a range of rotation rates tools from 1000 revolutions per minute to 1800 revolutions per minute and a range of traverse rates from 6 millimetres per minute to 24 millimetres per minute were investigated. Results revealed that finer particles of 10 μm for the ball-milled were distributed more consistently in the composite than base material during the optimisation of process parameters for uniform particle distribution. Before being included in the AA5083, the particles were ball-milled. The finer ball-milled particles were evenly spread and a thin intermetallic layer was created. AA5083–Ni composite intermetallic was discovered in the layer. No such layer was seen in the processed composite when tiny particles of similar size (10 μm) were integrated using the same FSP parameters. The study findings showed that the microstructure of the composite was modified by particle ball-milling. The creation of the interfacial layer is responsible for the high energy state of the ball-milled particles. When compared to the unreinforced AA5083, both composites had greater strength. FSP also reduced the grain size of the parental material from 25 to 3.5 μm, an action that improved the composites' strength. Due to the existence of the interfacial reaction layer, the strength and ductility of the ball-milled composite were lower than the composite with as-received tiny Ni particles, as predicted.

Kumar et al. [189] investigated the wear properties of an AA5083-tungsten composite made using the FSP technique. FSP was employed to integrate tungsten particles in an AA5083 material to create metal particle-reinforced surface composites. On an AA5083 plate with a thickness of 10 mm, a groove of 60×2×1.5 mm was created. Tungsten particles of 10 μm were retained in the groove. The FSP tool revolved at 1,200 revolutions per minute with a 24 mm/min transverse speed. Wear test samples with a diameter of 8 millimetres and a height of 10 millimetres were cut using electrical discharge machining (EDM). Results revealed that the microstructure was found to have a uniform distribution. The particles were equally scattered in the base material and FSP refined the grain size. The tungsten particles remained in their elemental state after X-ray diffraction and investigation revealed no intermetallic peak. Compared to the base and FSPed alloys, the composite surface layer displayed much greater wear resistance. The worn surface inspection of the base and FSPed samples revealed that the composite undergoes oxidative mild and adhesive wear at all 3 loads, shifting to an abrasive and delamination type of severe wear at higher loads.

Papantoniou et al. [190] investigated a new technology in the hardening and surface modification of AAs using a FSP: AA5083-Cu. FSP was performed on thick AA5083 plates in this investigation. The parameters used for this study are a traverse speed of 13 mm/min and a rotational speed of 1000 rpm, that were based on preliminary experiments. The pinless FSP pass's parameters were 1000 rpm rotational speed and 120 mm/min transverse speed. A thin sheet of pure copper with a cross-section of 4 mm × 0.8 mm was FSPed into a machined groove on the upper side of the aluminium plate. The samples were made with 1, 2 and 3 FSP passes, respectively. The metallurgical and mechanical effects of the AA5083-Cu composite were then examined. The results indicated that the Cu thin sheet was successfully integrated into the AA5083 NZ, with non-integrated Cu disappearing after further FSP passes. The reinforcement was divided into small particles, blended and spread throughout the SZ. There were various intermetallic phases detected after FSP overlapping, as well as the particles dimensionally concerned in the material flow direction because of the rotating action. Owing to the intense plastic deformation caused by heat generation and material movement near the tool, particles of Cu became enriched with aluminium atoms as a result of the interplanar

diffusion–interfacial migration effect. The production of intermetallics such as $AlCu_4$, $Al_2Cu$ and $MgCu_2$ was proposed by XRD. Cu diffusion and the production of diverse hard intermetallics increased the hardness of the surface composite. Almost all the Cu was incorporated in the nugget region, primarily in the form of Cu-based micron-sized intermetallic particles and, secondly, by Cu diffusion in the AA5083 material when the FSP passes were increased. The microhardness inside the NZ was found to have risen from 77 HV to 138 HV because of the presence of complex intermetallic compounds generated by the high heat input and severe plastic deformation.

2.3.2.4 Hybrid Reinforcements in AA5083

Hossieni et al. [73] used FSP to create AA5083 surface composites reinforced with CNTs and cerium oxide nanoparticles. FSP was used to integrate MWCNT and nanosized cerium oxide particles into the AA5083 base material to generate surface-reinforced composites in this study. The effect of different nanosized reinforcements on the microstructure, corrosion resistance and mechanical properties of FSPed surface composites was studied Individually and in combination. FSP was conducted with a traverse speed of 35 mm/min and 45 mm/min, rotation speeds of 600 rpm and 800 rpm, and a tilt angle of 5°, respectively. A threaded cylindrical hardened steel tool was utilised. FSPed samples were examined and compared to the parent material regarding mechanical properties and corrosion resistance. The hybrid composite, having a mixture of carbon nanotubes and cerium oxide in a volume ratio of 75–25, attained the highest tensile strength and hardness, respectively, whereas cerium oxide alone resulted in a considerable improvement in the pitting resistance of the base material. Potential dynamic polarisation experiments were used to analyse the samples' corrosion behaviour, that was evaluated regarding pitting potential and passivation range. Microstructural examination employing optical microscopes and electron microscopes revealed that reinforcements are well scattered throughout the SZ and that significant grain refining was achieved. The mechanical properties of produced composites incorporating cerium oxides or CNTs were enhanced. The hybrid composite with 75% carbon nanotubes and 25% cerium oxide exhibited the best properties. The hardness is 118% greater, and the UTS is 42% higher than the parent aluminium alloy. Grain refinement, improved reinforcement distribution and microstructural modification are all achievable in SZ.

Khan et al. [191] examined the cold formability of boron carbide particles and carbon nanotubes in friction-stir processed aluminium composites. The base materials AA5083 and MWCNTs, as well as $B_4C$ reinforcements, were used. A single pass of FSP was carried out to prepare composites at a 750 rpm rotational speed, a 16 mm/min traverse speed and a 2° tilt angle. FSPed aluminium metal matrix composites' cold formability was evaluated using the bend-ductility test. Carbon nanotube-containing composites fractured under bending, whereas boron carbide-containing composites survived; hybrid composites cracked, but the crack was less than nanotube-only composites. Potential reasons for these results include poor interfacial nanotube or aluminium bonding and inadequate nanotube dispersion. The mechanical and microstructural features of the composites determine cold formability. The $B_4C$-reinforced composite enhanced tensile strength and hardness by 28% and 12%, respectively and passed the bend ductility test with no surface fractures. The MWCNT-composite demonstrated a 50% decrease in fracture strain, as well as improved hardness and tensile properties. However, the bend ductility test exhibited fractures because of clusters of CNTs developed in the TMAZ since it is a single-pass FSP. The hybrid composite increased tensile strength and hardness by 10% and 5%, respectively, while decreasing fracture strain by 16%. This specimen failed the bend-ductility test due to the weak interfacial bonding of MWCNTs and aluminium alloy, as well as inadequate MWCNT dispersion in the composite.

Khan et al. [192] used FSP to evaluate the impact of FSP spacing on the growth of $B_4C$ and MWCNTs reinforced AA5083 composite. In this study, FSP was used to add boron carbide and carbon nanotube particles into AA5083 to create hybrid surface composites. The impact

of metal loss in cavities generated to incorporate reinforcements at 8-millimetre and 10-millimetre inter-cavity spacings using a single-pass approach was examined. To prepare surface composites, a single pass of FSP was performed at a 2° tilt angle, 16 mm/min traverse speed and a rotational speed of 750 rpm. Surface composites with individually reinforced $B_4C$ and MWCNTs particles, as well as a hybrid composite with both reinforcements, were created. Microstructural analysis and the existence of any flaws were carried out using optical microscopy and SEM. Mechanical tests found that composites with 10-millimetre inter-cavity spacing and boron carbide particles increased their UTS and microhardness by up to 38% and 18%, respectively. The cold formability of FSPed composites was then evaluated using the U-bend ductility test. Carbon nanotube composites with an inter-cavity spacing of 8 mm failed because of severe cracking generated by clustering and insufficient compensation for material loss, that had a substantial influence on the final mechanical properties. It was determined that sinking reinforcement in the parental material was required to compensate for material loss. If the material loss in the form of a cavity for reinforcements is not compensated for, a higher empty volume causes mechanical properties to degrade. A 10 mm inter-cavity separation permitted maximum reinforcement sinking and minimum clustering using carbon nanotubes in single-pass FSP. The FSP and tribological characterisation of AA5083-$B_4C$ surface composites were also investigated [182]. According to the findings, the constant mixing of nano $B_4C$ boosted the material's tensile strength.

Jain et al. [193] employed FSP to develop and analyse AA5083-CNTs/SiC composites. Through FSP, CNT and micron sized SiC particles were reinforced with an AA5083 base material to create hybrid and mono composites. The influence of CNTs/SiC on texture, mechanical properties and microstructural development texture of FSPed AA5083 composites was investigated, both in individual and aggregate form. With a transverse speed of 20 mm/min and a rotational speed of 1600 rpm, all the samples were exposed to three passes for homogenous reinforcement dispersion. FSP was compared on a parental material without reinforcement under similar experimental conditions. After dynamic recrystallisation, TEM and EBSD investigations showed a dislocation rearranged to create high-angle grain boundaries, and equiaxed recrystallised microstructure, respectively. Multiple passes resulted in a generally poor texture intensity over the SZ of FSPed samples. By incorporating carbon nanotubes/silicon carbide particles into the AA5083 base material, the Zener-Holloman and particle-stimulated nucleation mechanisms were activated, resulting in the formation of randomly oriented grains. Silicon carbide particles are uniformly disseminated with good interfacial bonding in FSPed composites while carbon nanotubes are partly reacted with an AA5083 material to generate an in-situ $Al_4C_3$ intermetallic compound. The AA5083-CNTs/SiC hybrid composite has a maximum UTS of 361 MPa, whereas the base material has a tensile strength of 298 MPa. The void initiation at the matrix-particle interface areas was exhibited on the fracture surface of the SiC-reinforced composite. Hardness testing revealed that AA5083/SiCasSiCs had the highest difference in hardness, namely: 1.5 times that of the base material. AA5083/SiCasSiCs also had a greater hardness and elastic modulus. The hybrid composite increases hardness by 1.4 times.

2.3.2.5 Analysis and Discussion

Table 2.3.2.5 provides a comprehensive overview of the composites fabricated from AA5083 base material with various reinforcements using the FSP process.

**Table 2.3.2.5: AA5083 - based MMCs fabricated with FSP.**

| AA+ Reinforcement | Parameters | | Results | Reference |
|---|---|---|---|---|
| | Tool rotational speed (rpm) | Traverse speed (mm/min) | | |

| | | | | |
|---|---|---|---|---|
| 5083-H111+ $ZrO_2$ | 800 | 50 | In the 8-pass FSPed nanocomposite, EBSD and TEM examination revealed a substantial number of high-angle grain boundaries as well as the presence of CDRX.<br>The wear rate of the further processed specimens was lower than that of their counterparts.<br>The fracture surface of the eight-pass processed material displayed ductile fracture with dimples and voids, similar to the base material. | 65 |
| 5083+$CeO_2$ and CNTs | Varying | Varying | The hybrid composite with a volume ratio of 75-25 of CNTs and cerium oxide attained the highest tensile strength and hardness value.<br>The addition of a CNTs-$CeO_2$ mixture in a volume ratio of 75-25 enhanced the strength of Al5083 by 42%, decreased the matrix grain size by five times, and doubled the hardness. | 73 |
| 5083+ GO | 315 | 20 | The nanocomposite's grain size was approxiately 1 μm.<br>Compared to the base alloy, adding graphene oxide enhanced the hardness at the stir zone.<br>Compared to the base alloy and the FSPed specimen, the nanocomposite was observed to have improved tensile behaviour. | 179 |
| 5083+ SiC | 300 | Varying | The SiC particles were evenly dispersed throughout the aluminium matrix. The surface composites bonded well with the aluminium alloy substrate.<br>The surface composite reinforced with 27vol.% SiC of 0.7m average particle size had a microhardness of 173 HV, about twice that of the AA5083 base material (85 HV). | 180 |
| 5083+ SiC | 1200 | 40 | The use of FSP to dope AA5083 with hard SiC particles greatly enhance the microhardness of the surface composite fabricated on the FSPed sample layer.<br>The wear resistance of the surface composite is much lower than that of the AA5083 base material. | 181 |
| 5083-O+ $B_4C$ | 1000 | 25 | The surface composite layer created in three passes with nanoparticle reinforcement outperformed the base metal in terms of hardness, tensile behaviour and wear resistance. | 182 |

| | | | | |
|---|---|---|---|---|
| 5083+ $B_4C$, SiC, and TiC | 1600 | 25 | FSP causes extreme plastic deformation in the materials, encouraging mixing and refinement of the constituent phase.<br>The addition of $B_4C$, SiC and TiC particles to the matrix enhances its hardness, tensile strength and wear resistance.<br>TiC and SiC particles reinforced surface composites exhibit ductile fracture, while $B_4C$ reinforced surface composites exhibit bimodal fracture. | 183 |
| 5083+ MWCNTs | 880 | 25 | With the best possible FSP conditions, the composites contain no voids or other defects.<br>MWCNT grain refinement and uniform dispersion were accomplished. The composite contained nanoparticles of MWCNTs as well as submicron particles.<br>In comparison to the basis material, the proof stresses of the composites increased by between 53% and 61%.<br>Tensile strengths increased by between 13% and 16%. | 184 |
| 5083+ CNT | 1800 | 25 | Microstructural analysis showed smaller grains and non-uniform CNT dispersion in the stir zone.<br>Compared to unprocessed Al alloy, microhardness testing revealed a 25% improvement in hardness.<br>The corrosion resistance of the FSPed composite was marginally higher. The results indicate that the addition of CNT, in addition to the grain size effect, has a considerable influence on the corrosion resistance of Al5083. | 185 |
| 5083+Ni | 1200 | 24 | The distribution of Ni particles was inhomogeneous.<br>FSP reduced the grain size of the aluminium matrix from 25 μm to 3 μm.<br>In comparison to the base alloy, the strength improved dramatically.<br>The composite also has a significant amount of ductility. | 187 |
| 5083+Ni | Varying | Varying | Ball-milled tiny particles (10 μm) dispersed more equally in the matrix than as-received coarse particles (70 μm).<br>FSP reduced the grain size of the aluminium matrix from 25 μm to 3.5 μm.<br>The strength of the composites was greater than that of the unreinforced AA5083. | 188 |
| 5083-O+ W | 1200 | 24 | The particles were equally distributed in the matrix, and FSP refined the grain size.<br>The absence of an intermetallic peak in X-ray diffraction examination confirmed | 189 |

| | | | | |
|---|---|---|---|---|
| | | | that the tungsten particles remained in their elemental state.<br>The composite surface layer outperformed the base and FSPed alloys in terms of wear resistance. | |
| 5083+ Cu | 1000 | Varying | By increasing the number of FSP passes, nearly all the copper was incorporated in the stir zone, mostly as copper-based micron-sized intermetallic particles, followed by copper diffusion in the AA5083 matrix.<br>The presence of complex intermetallic compounds generated by the high heat input and severe plastic deformation increased the hardness inside the stir-zone from 77 to 138 HV. | 190 |
| 5083+ $B_4C$ and MWCNTs | 750 | 16 | Tensile strength and hardness have been improved by 28% and 12%, respectively, in the $B_4C$-reinforced composite.<br>The MWCNT-composite reduced fracture strain by 50% while improving the hardness and tensile properties.<br>Tensile strength and hardness increased by 10% and 5%, respectively, while fracture strain was reduced by 16%.<br>Composites containing carbon nanotubes broke after bending, but those containing boron carbide particles did not break.<br>Cracking was seen in hybrid composites, although it was less severe than in those containing just nanotubes. | 191 |
| 5083+ $B_4C$, and MWCNTs | 750 | 16 | Mechanical characterisation revealed that 10 mm inter-cavity spacing composites containing boron carbide particles increased tensile strength and hardness by up to 38% and 18%, respectively. Carbon nanotube composites with 8 mm inter-cavity spacing failed due to severe cracking induced by clustering and lower compensation to compensate for material loss, that played a critical role in final mechanical properties. | 192 |
| 5083+CNTs and SiC | 1600 | 20 | In FSPed composites, the Al5083 matrix and CNTs are partially reacted to generate an in-situ Al4C3 intermetallic compound. SiC particles dispersed uniformly with good interfacial bonding.<br>The crystallographic texture was degraded by the addition of CNT/SiC particles.<br>A composite made of Al5083-CNTs and SiC reached a maximum tensile strength of 361 MPa. | 193 |

The incorporation of $ZrO_2$ in aluminum matrix composites enhances tensile properties, microhardness, and wear resistance, particularly when processed with multi-pass friction stir

processing (FSP). Graphene oxide reinforcement refines the grain size of the composite material, leading to improvements in both microhardness and tensile properties. Similarly, the addition of SiC increases microhardness and wear resistance. $B_4C$ reinforcement is effective in improving wear resistance, tensile behavior, and hardness. The introduction of multi-walled carbon nanotubes (MWCNTs) and carbon nanotubes (CNTs) refines grain size and enhances strength and hardness, although the dispersion of CNTs can influence corrosion resistance. Additions of Cu and Ni influence the microstructure and mechanical properties of the composite, with particle size and distribution being critical factors. Hybrid reinforcements also play a significant role; for instance, combining CNTs with cerium oxide nanoparticles results in enhanced tensile strength and hardness, while cerium oxide improves pitting resistance. However, achieving a balance in hybrid reinforcements is crucial, as seen in composites with boron carbide particles and CNTs, where cracking occurred due to poor interfacial bonding and dispersion despite boron carbide's benefits. Similarly, AA5083 composites reinforced with CNTs and silicon carbide particles can achieve higher UTS than the base material. Therefore, careful consideration of reinforcements is essential to optimize the composite's overall performance.

### 2.3.3 AA6061- based MMCs

This section discusses AA6061 composites with oxides/carbides (SiC), carbonaceous (Graphite, CNTs, GNPs, RHA), and hybrid (Graphite/GNP/CNT with SiC, SiC-graphite, $Gr/Al_2O_3$ with SiC, GNP/CNT with SiC, $Al_2O_3$-BN) reinforcements.

#### 2.3.3.1 Oxide and Carbide Reinforcements in AA6061

Rathee et al. [194] studied the impact of tool plunge depth on the distribution of reinforcing particles in friction stir surface composite processing. This study investigated the influence of tool plunge depth on the pattern of reinforcement particle dispersion in the metal matrix using AA6061-Silicon carbide surface composites. Six different tool plunge depths were chosen at fixed levels of tool tilt angle and shoulder diameter to examine the sole impact of plunge variation. The experiment's rotational speed, tool tilt angle and travel speed were all set at 1400 revolutions per minute, 2.5° and 40 millimetres per minute, respectively. A stereo zoom and optical microscope were used for macro and microstructural studies, respectively. According to the findings, lower plunge depth levels result in inadequate heat generation and cavity formation at the NZ centre. Higher plunge depths, however, cause the ejection of reinforcing particles and the material to adhere to the tool shoulder. It was discovered that an ideal plunge depth is necessary to produce defect-free surface composites. The dispersion of SiC particles alters as the plunge depth increases. A 0.25 mm plunge depth was the most successful in creating a refined and homogeneous SiC particle dispersion.

#### 2.3.3.2 Carbon Fiber Reinforcements in AA6061

Maurya et al. [195] studied the influence of carbonaceous reinforcements on the tribological and mechanical parameters of FSPed Al6061 alloy. To see how carbonaceous particles affected the tribological and mechanical characteristics of FSP Al6061, researchers used carbonaceous particles (graphite, carbon nanotubes and graphene) as reinforcement. FSP was performed with continuously optimised process parameters at a rotating speed of 1100 revolutions per minute, a traverse speed of 0.2 millimetres per minute and a plunge depth of 1.2 millimetres. Raman spectroscopy demonstrated the preservation of damaged carbonaceous products in the NZ due to the significant plastic deformation and shear strains involved in the FSP. Transmission electron microscopy was utilised to confirm carbonaceous particle damage. The surface peak hardness of the graphene-reinforced composite increased to 1.3 GPa due to grain refinement as compared to untreated Al6061 of 0.5 GPa. When compared to untreated Al6061 stick-slip wear damage, the self-lubricating nature of carbonaceous materials suggests lower frictional force and dominance of the gross-slip

regime with graphene reinforcement in FSP Al6061. Due to substantial plastic deformation, the XRD spectrums of the generated AMMCs exhibited a decrease in crystallite size from 42 nm to 27 nm.

Dinaharan et al. [196] studied the impact of rice husk ash particles on the microstructure and tensile behaviour of FSPed AA6061 AMMCs. The study used the innovative FSP technique to produce and characterise AA6061/18 vol percent RHA AMC. The tool rotated at 1600 rpm, the traverse was 60 mm, the axial force was 10 kilo newtons and the FSP was performed in a single pass. SEM, optical microscopy and an electron-backscattered diagram were used to investigate the microstructure. In the composite, a homogeneous dispersion of RHA particles was achieved. There was no evidence of segregation or agglomeration. The resulting composite had a fine and evenly distributed grain structure. During FSP, rice husk ash particles fractured. After the incorporation of RHA particles, the UTS of the material improved and fragmented RHA particles were scattered across the fracture surface, indicating strong interfacial bonding with the aluminium matrix. The findings revealed the substrate was evenly dispersed with fine equiaxed granules. On AA6061/RHA, significant grain refining (from 31.6 μm to 6.8 μm) was reported. The AA6061/RHA was found to have a greater ultimate tensile strength than the base metal.

Sharma et al. [197] investigated the impact of reinforcement addition on the tribological and mechanical qualities of an AA6061-CNT nanocomposite produced using the FSP method. The goal of this research was to see how reinforcement addition affects the mechanical characteristics, tribological properties and microstructure of Al-CNT nanocomposite manufactured via FSP. The FSP was performed at a 2° tool tilt angle, 40 mm/min traverse rate, 1400 rpm tool rotational speed and plunge depth of 0.2 mm. The proposed multiple micro-sized channel reinforcement filling technique achieves a significant grain refinement of 23% when compared to the traditional single macro-sized channel reinforcement filling approach. The sandwiched aluminium matrix's better consolidation between the sequential reinforcing grooves is attributed to substantial grain refinement. When compared to the un-reinforced treated alloy, the UTS of the multiple micro-sized channel reinforcement-produced composites went up by 22% with a 3% elongation decrease. Better wear overall performance is connected with the formation of a carbon-rich tribo layer, that prevents direct contact of the composite with the counter surface. Grain refinement, Orowan looping, interface load transfer and thermal mismatch among CNTs and Al matrix are all factors that contribute to the strength of Al-CNT composites.

Marini et al. [198] examined the wear behaviours of FSPed aluminium metal matrix composites. The base materials utilised in this study were AA6061 Al alloy. As a result, the FSP of AA AA6061 was introduced to increase the wear performance. Rice husk ash with a volume percentage of 6% was added to FSPed AA6061. The FSP manufacturing settings were 1000 rpm, 1400 rpm and 1600 rpm rotation speeds with a constant traversal speed of 25 millimetres per minute. A pin-on-disc tribometer was utilised to examine the wear properties. The final results were the mass loss and wear rate of the specimen materials. When FSPed AA6061/6Vol.% RHA was compared to FSPed AA6061, the wear characteristics of FSPed AA6061/6Vol.% RHA were found to be better. The best result was obtained with FSPed AA6061/6Vol.% RHA, that was produced at 1600 rpm and 25 mm/min, with a mass loss of 0.02 g and a rate of wear of $0.97 \times 10\text{-}3\ mm^3/Nm$. The AA6061's wear performance has increased as a consequence of the FSP and the inclusion of RHA particles. Archard's wear rule states that the relationship between hardness and wear rate is inversely proportional. The rate of wear decreases as the hardness of the material increases. It was also discovered that raising the hardness of the composite minimises material loss during sliding. The wear rate was lowered because of the presence of hard reinforced particles.

Reddy et al [199] studied the microstructural and damping capabilities of FSP-generated AA6061-graphite surface composites. The goal of this research was to enhance the damping

qualities of the AA6061-T6 alloy using FSP by adding graphite flakes. The rotational speed of the tool was set to 1120 revolutions per minute, the traverse speed of the tool was set to 30 mm/min, and the axial force was set to 10-kilo Newtons. The graphite content ranged from 5% to 15% by volume. Electron and optical microscopy were used to examine the distribution of graphite particles and the microstructure refinement. Results revealed that in the stirred zone, the grains were unidentifiable. The hardness of the surface composites decreased when the graphite component was increased. The damping capability of samples obtained from the stir zone was tested using a dynamic mechanical analyser. The damping ability of FSPed AA6061 and the surface composites was found to be superior to the parental metal in terms of frequency and temperature-dependent tests. At 250°C, the damping capability of the composite containing 15Vol.% graphite was 3.5 times that of the base metal. The results revealed that fine equiaxed grains were spread evenly across the substrate. Significant grain refinement was found on composites with varying graphite concentrations (from 45 μm to 4.25 μm). Microhardness decreased when the reinforcing content was increased while composites' damping capacity increased as reinforcement content increased.

2.3.3.3 Hybrid Reinforcements in AA6061

Sharma et al. [60] investigated the tribological properties of an Al6061-SiC surface composite with carbon nanotubes, graphite and graphene impregnated by FSP. Various characterisation methodologies, such as SEM microstructural characterisation, TEM interfacial investigation and XRD phase analysis, were studied. As detailed in this study, the wear mechanism of an Al-SiC surface composite was altered by the impregnation of carbon nanotubes, graphite and graphene with FSP. Based on the previous study [157], the traverse speed of 25 mm/min with a 2° tool tilt angle, 0.2 mm plunge depth and optimal rotational speed of 2200 rpm was revised for the current investigation. With silicon carbide and GNP reinforcements, the specific wear rate and friction coefficient were lowered by 34% and 50%, respectively, when compared to the base Al6061 alloy. When SiC and CNT reinforcements are mixed, the wear resistance of the composite considerably decreased. The higher wear resistance was connected to the layered structure, large specific surface area and wrinkled form of graphene flakes. Exfoliation of GNP to few-layered graphene during FSP significantly improved surface properties. Abrasion was shown to be the dominant wear mechanism in Al-SiC-Graphite and Aluminium-Silicon carbide-GNP hybrid composites, whereas delamination was found to be the most dominant in Aluminium-Silicon carbide-CNT hybrid composites owing to counter surface adhesion. For enhancing the wear resistance of Al6061-SiC surface composites, GNP is the optimal carbon family reinforcement.

Sharma et al. [200] investigated the FSP of hybrid surface composites of aluminium alloy 6061/SiC-graphite. FSP was used to mix AA6061 alloy with SiC reinforcement to produce a hybrid composite weld material. A robust weld was achieved by using a high rotating speed of 2200 rpm, and a traverse rate of 25 mm/min. When compared to a standard FSPed weld, the strength of the weld with reinforced SiC was dramatically enhanced. Indentation, microstructural, spectroscopic and force analysis experiments were used to investigate FSPed Al6061-SiC-Graphite hybrid composites. The impact of different tool rotating speeds was also evaluated, with the axial force fluctuation being observed. The variation in microstructure at various tool rotating speeds was investigated using a scanning electron microscope. The tool rotational speed affects the area of the FSP region, particle fragmentation and depth of penetration, agglomeration dispersion and grain refinement of the matrix material. X-ray diffraction and Raman analysis investigations were used to characterise the processed samples spectroscopically. The strength of the Raman peaks changed significantly, indicating residual stresses and diverse abnormalities in the crystal structure of the reinforced particles. The impact of rpm and the presence of SiC and Graphite particles on mechanical properties were investigated using nanoindentation testing. At an ideal set of processing conditions, the Al6061-SiC-graphite composite demonstrated the combination of best and uniform mechanical characteristics. When compared to a standard FSPed weld, the

strength of the weld with reinforced SiC was dramatically enhanced. Microstructural tests validated the reinforcing particles' homogeneous distribution. The stirring speed was observed to be a key influencing factor and the cause of changes in hybrid composite weld mechanical properties.

Devaraju et al. [201] investigated the impact of combining Gr/$Al_2O_3$ with SiC on the wear characteristics of AA6061-T6 hybrid composites via FSP. FSP was used to create AA base surface hybrid composites by mixing silicon carbide+graphite and silicon carbide+aluminium oxide particles with an average size of 20 m on an AA 6061-T6 plate. During the processing process, the tool was rotated at 900 revolutions per minute, traversed at 40 millimetres per minute, tilted at 2.5° along the centre line and a vertical force of 5 kN applied. Both surface hybrid composites' NZs were observed to have evenly distributed SiC, Gr and Al2O3 microstructures. The combination of Gr particles with SiC particles, rather than $Al_2O_3$ particles, decreased the microhardness of the AA 6061-T6 surface hybrid composite but greatly increased the dry sliding wear resistance. Microstructures and worn micrographs are used to link microhardness and wear characteristics. The microhardness values of both AlSiC/Gr (approximately 108 HV) and AlSiC/$Al_2O_3$ (approximately 120 HV) surface hybrid composites were increased due to the presence of hard reinforcement particles when compared to the average microhardness of the aluminium matrix (approximately 104 HV). The AlSiC/Gr hybrid composite had a lower hardness value owing to the soft graphite phase, whereas the AlSiC/$Al_2O_3$ composite had a higher hardness value due to the inclusion of both tougher phase particles. The AlSiC/Gr surface hybrid composite had a lower coefficient of friction than the AlSiC/$Al_2O_3$ surface hybrid composite. In terms of wear resistance, the AlSiC/Gr surface hybrid composite outperformed the AlSiC/$Al_2O_3$ surface hybrid composite because of the formation of a thin and tough mechanically combined layer containing Gr, that had a greater solid lubricating impact than $Al_2O_3$.

Sharma et al. [202] presented a study on the surface characteristics of hybrid composites manufactured using FSP whereby AlSiC multi-walled carbon nanotubes and AlSiC graphene nanoplatelets were compared. Based on the findings of from earlier research [18], a recommended rotational speed of 2200 r/min with a traverse speed of 25 mm/min, a plunge depth of 0.2 mm and a tool tilt angle of 2° are revised for the current investigation. The results indicated that the GNPs had a much more homogenous dispersion in the Al matrix than CNTs, according to microstructural analysis. A flawless-free interface between the reinforcements and matrix was discovered, as well as dislocation blocking by silicon carbide and GNP particles. The surface nano-hardness of AlSiCGNP and AlSiCCNT hybrid composites increased by 207% and 27%, respectively, compared to the base metal Al6061 alloy in a nanoindentation investigation. The microhardness values of AlSiCCNT and AlSiCGNP, however, are increased by 17% and 36%, respectively, when compared to the parental metal of Al6061 alloy. According to a tribological investigation, the specific wear rate of the AlSiCGNP hybrid composite is lowered by 56%, whereas it is raised by 122% in the AlSiCCNT composite. The increased strength of the AlSiCGNP composite is associated with the mechanical exfoliation of GNPs to few-layered graphene in the presence of SiC. Furthermore, different factors such as Orowan looping, grain refinement and thermal mismatch all contribute to the strength of the composites. Furthermore, the improved tribological performance of the composites is due to the squeezed-out GNP creating a tribo layer on the surface.

Moustafa et al. [203] examined at the mechanical, microstructural and thermal characteristics of the AA6061/$Al_2O_3$-BN hybrid and mono nanocomposite surfaces. The basic matrix in both hybrid and mono composite surfaces was an aluminium alloy 6061 wrought alloy reinforced with BN and $Al_2O_3$ ceramic nanoparticles. The mechanical characteristics of the AA6061/$Al_2O_3$-BN hybrid nanocomposite were studied using compression and microhardness tests, with the AA6061/$Al_2O_3$-BN hybrid nanocomposite having the best mechanical properties. A hybrid composite surface was created using the FSP method at a tool travel speed of 60 mm/min and 1080 rpm tool rotation speed. According to the stress-strain curve,

the ultimate stress of the hybrid nanocomposite was greater than that of the parental alloy. Scanning electron and optical microscopy were used to examine the produced composite's microstructure. The FSP has a significant impact on grain refinement, reducing the grain size of the AA6061 receiving alloy by 29 times. Furthermore, equiaxial grains were formed because of the stirring action and the FSP pin tool thread design, leading to a 400% increase in grain aspect ratio. As seen in the SEM inspection analysis, the dispersion of BN and $Al_2O_3$ nanoparticles was effectively obtained throughout the current experiment. Thermal expansion and electric conductivity parameters of the hybrid nanocomposite were noted to be at their lowest value. Thermal expansion and electrical conductivity were lowered by adding reinforcement to the parental metal. Despite the elongation loss, the UTS and yield strength of AA6061/$Al_2O_3$-BN were greater than that of all other composites and parental metals.

2.3.3.4 Analysis and Discussion

Table 2.3.3.4 summarises the composites fabricated from AA6061 base material with various reinforcements using the FSP process.

**Table 2.3.3.4: AA6061 - based MMCs fabricated with FSP.**

| AA+ Reinforcement | Parameters | | Results | Reference |
|---|---|---|---|---|
| | Tool rotational speed (rpm) | Traverse speed (mm/min) | | |
| 6061-T6+SiC | 1400 | 40 | Lower plunge depth levels result in insufficient heat generation and cavity creation towards the stir zone centre, according to the results.<br>Higher levels of plunge depth result in the ejection of reinforcing particles and even the material sticking to the tool shoulder. | 194 |
| 6061+ Gr+CNT+G | 1100 | 0.2 | The XRD spectrums of the produced AMMCs showed a drop in crystallite size to 27 nm from 42 nm due to significant plastic deformation.<br>Surface peak-hardness for graphene-reinforced composite increased to 1.3 GPa as compared to untreated Al6061 with 0.5 GPa due to grain refinement of 50-100 nm. | 195 |
| 6061+ RHA | 1600 | 60 | The fabricated composite had a fine and equiaxed grain structure.<br>Rice husk ash particles were dispersed homogeneously and the addition of RHA particles increased the tensile strength.<br>The fracture surface was distributed with fragmented RHA particles and exhibited strong interfacial bonding with the aluminum matrix. | 196 |
| 6061+CNTs | 1400 | 40 | When compared to the un-damping capacity reinforced processed alloy, the tensile strength of the micro-sized channel reinforcement filling (MCRF) produced composite improved by 22% at the cost of only a 3% drop in elongation. | 197 |

| | | | | |
|---|---|---|---|---|
| | | | When compared to unreinforced processed alloy, the specific wear rate of Al-CNT composites made by MCRF is lowered by approximately 20%. | |
| 6061+ RHA | Varying | 25 | Compared to FSPed AA6061 followed by AA6061, it was discovered that the wear properties of FSPed AA6061/6Vol.% RHA composite had improved. | 198 |
| 6061-T6+ Gr | 1120 | 30 | In the stirred zone, the grains were indistinguishable.<br>As the amount of graphite increased, the hardness of the surface composites decreased.<br>FSPed AA6061 and the surface composites were shown to possess better frequency and temperature dependence than the base metal.<br>At 250°C, the composite with 15Vol.% graphite had a dampening capability that was 3.5 times more than that of base metal. | 199 |
| 6061+ SiC and Gr | 2200 | 25 | The Raman peak strength changed significantly, revealing residual stresses and different discrepancies in the crystal structure of the reinforced particles.<br>The Al6061-SiC-Gr composite displayed the best and most consistent mechanical properties under optimal processing conditions.<br>The strength of the weld with reinforced SiC was significantly increased when compared to a regular FSPed weld. | 200 |
| 6061-SiC+ Gr/ $Al_2O_3$ | 900 | 40 | The microstructures of both surface hybrid composites showed that SiC, Gr and $Al_2O_3$ are distributed uniformly in the SZ.<br>The combination of Gr particles rather than $Al_2O_3$ particles with SiC particles reduces the microhardness but greatly boosts the dry slide wear resistance of aluminium alloy 6061-T6 surface hybrid composite. | 201 |
| 6061-SiC+ CNT/ GNP | 2200 | 25 | The microhardness values of the Al-SiC-GNP composite and Al-SiC-CNT composite are raised by 36% and 17%, respectively, when compared to the as-received Al6061 alloy.<br>The specific wear rate of the Al-SiC-GNP hybrid composite is reduced by 56%, but it is increased by 122% in the Al-SiC-CNT composite.<br>Microstructural analysis showed that GNPs are distributed more uniformly in the Al matrix than CNTs. | 20 |
| 6061+$Al_2O_3$ and BN ceramic Particles | 1080 | 60 | The stress-strain curve revealed that the hybrid nanocomposite had a more | 203 |

| | | | | | |
|---|---|---|---|---|---|
| | | | | enhanced ultimate stress than the base alloy.<br>The dispersion of $Al_2O_3$ and BN nanoparticles was accomplished satisfactorily.<br>Thermal expansion and electrical conductivity were reduced by reinforcing the metal matrix with ceramic nanoparticles $Al_2O_3$ and BN. | |
| 6061-SiC+ Gr/ GNP/ CNTs | | 2200 | 25 | The combination of SiC and CNT reinforcements significantly reduces the wear resistance of the composite.<br>In Al-SiC-Gr and Al-SiC-GNP hybrid composites, abrasion is revealed as the dominant wear mechanism and GNP has been discovered as the optimum carbon family reinforcement for improving the wear resistance of Al6061-SiC surface composites. | 60 |

SiC reinforcements improve strength and wear resistance, with processing parameters significantly affecting the composite's properties. Graphite addition can enhance damping capacity but may reduce hardness. GNPs show promise for improving wear resistance and achieving uniform particle distribution. RHA reinforcements for AA6061 composites, several studies highlight their potential. Combining Gr/Al2O3 with SiC in AA6061-T6 via FSP decreased microhardness but greatly increased dry sliding wear resistance. Comparing multi-walled carbon nanotubes and AlSiC graphene nanoplatelets, it was noted that GNPs dispersed more homogeneously in the Al matrix and increased surface nano-hardness compared to CNTs. AA6061/Al2O3-BN hybrid nanocomposite surfaces exhibited the best mechanical properties, with FSP effectively reducing the grain size of the AA6061 alloy. These studies underscore that while individual reinforcements offer specific advantages, however, careful control of processing parameters is essential to optimize performance.

### 2.3.4 AA6063- based MMCs

Sections 2.3.4.1 and 2.3.4.2 discuss AA6063 composites with oxide/carbide ($TiB_2$, $SiO_2$, SiC) and hybrid (SiC-Gr, $B_4C$-$TiB_2$) reinforcements.

#### 2.3.4.1 Oxide and Carbide Reinforcements in AA6063

Chen et al. [204] studied the impact of nanosized particles on the microstructural development of an Al6063-$TiB_2$ composite made by FSP in situ. Neutron diffraction, synchrotron X-ray line analysis profile and SEM with electron backscatter diffraction was used to quantitatively evaluate the influence of $TiB_2$ particles on the thermal stability after additional T6 heat treatment, as well as the as-deformed structure in the stir zone. The traverse speed was set at 200 mm/min and the rotation speed was set to 600 rpm. Only a four-pass FSP process was shown to considerably increase the strength and ductility of the FSPed 6063-$TiB_2$ composite in our prior study [205]. The findings in comparison to those produced from a FSPed AA6063 alloy reveal that the FSPed AA6063-$TiB_2$ composite has a lower average grain size than the FSPed AA6063 alloy, as well as a more uniform grain size distribution. Second, the FSPed AA6063-$TiB_2$ composite has a greater estimated dislocation density than the FSPed AA6063 alloy. Third, compared to its alloy counterpart, the FSPed AA6063-$TiB_2$ composite dynamically recrystallises a small number of grains, indicating that the presence of nanosized $TiB_2$ particles effectively inhibits grain growth during FSP and T6 heat treatment and recrystallisation. Finally,

the microhardness was improved because of reduced grain size and increased dislocation density.

Joyson et al. [206] studied the FSP of quartz particle reinforced AA6063 aluminium matrix composites. The study focuses on the application of FSP to generate AMCs reinforced with quartz/$SiO_2$ particles. A one-pass FSP was performed in this investigation employing a combination of optimal process parameters. The traverse speed was 60 mm/min, the tool rotational speed was 1600 rpm, the tool tilt angle was 0° and the axial force was 10 kN. The volume proportion of quartz particles in the AMMCs was changed in six Vol.% increments from 0 to 18 Vol.%. Transmission, scanning electron and optical microscopy were used to examine the created AA6063-Quartz AMCs. The $SiO_2$ particles were evenly dispersed throughout the Al matrix, regardless of where they were in the stir zone. The combination of the pinning effect of quartz particles and the thermomechanical impact of FSP greatly refined the grains of the AA6063. The wear resistance and microhardness of the AMMCs were enhanced by the quartz particle dispersion.

Rathee et al. [207] investigated the microstructure alterations of FSP-fabricated SiC reinforced AA6063 matrix composites. Three different tool rotational rates of 900 rpm, 1120 rpm, and 1400 rpm were used to perform single-pass FSP on AA 6063 sheets. The traverse speed was kept constant at 40 mm/min and was preserved at 2 degrees tool tilt angle. The microstructure of produced composites was then examined using optical microscopy. It was possible to establish a uniform dispersion of silicon carbide particles in the base metal. The processing conditions of 1120 rpm and 40 mm/min 2˚ produced the most homogenous distribution of SiC and the highest microhardness of 87 Hv. The aluminum matrix and the SiC particles had no interfacial contact.

Gangil et al. [208] investigated the combined impact of tool shoulder and pin profile on FSPed AA6063-SiC composites. The first method employed square, triangular, tapered cylindrical and plain cylindrical tool pin profiles with a flat shoulder design. Cylindrical pin and square profiles, as well as clockwise and anti-clockwise scrolling shoulder designs, were utilised in the second method. The composites were produced using a single-pass processing method. Based on prior studies from the same field, a rotating speed of 900 revolutions per minute, 40 millimetres per minute traverse speed and a 2.5° tilt angle were chosen. For AA6063 base material, the HCHCr tool was utilised over slots filled with 17 nanometres SiC reinforcement. In the course of the research, it was discovered that utilising an anti-clockwise scrolled shoulder square pin profile resulted in a larger area of the agglomerated zone, but using an ACW scrolled cylindrical pin resulted in no such band of agglomeration. The cylindrical pin ensured that the SiC in the AMMCs was distributed evenly, depending on the tool's rotating orientation, the scrolling shoulder feed material from the tool's outer perimeter to the tool's axis or vice versa. The authors discovered that SC manufactured using an FSP tool with a cylindrical pin and an ACW scrolling shoulder may give improved reinforcing distribution with no flaws.

Gangil et al. [209] investigated a strategy for fabricating AA6063-T6 Al surface composites using multi-pass FSP. Using silicon carbide reinforcement particles, FSP was utilised to create surface composites on AA6063-T6 base metal. The effect of processed zone dimensions, the microhardness of manufactured composites and multiple FSP passes on SiC particle distribution was examined. The traverse speed, tool tilt and rotating speed were all maintained at a constant level, but the number of passes was changed between two, four, six and eight. The rotational speed, traverse rate, tool tilt and shoulder plunge were set at 1120 rpm, 63 mm/min, 2.5° and 0.35 mm throughout all processing runs. This set of parameters was determined after extensive testing. After FSP, particle distribution in the processed zone was examined using OM and SEM and microhardness was determined using the Vickers indentation test. The results show that increasing the number of passes in the processed zone size can eliminate defects such as particle aggregation and void. The microhardness of the reinforced zone improved evenly with increasing passes due to the homogeneous dispersion

of reinforcement particles. In a sample that was processed with eight FSP passes, a peak Vickers microhardness value of 81.9 was found. The processed zone showed strong substrate bonding and grain refinement. A finer recrystallised grain structure was seen as the passes were increased.

2.3.4.2 Hybrid Reinforcements in AA6063

Dhayalan et al. [210] investigated AA6063/SiC-Gr surface composites' characterisation when generated by FSP. The microstructural characteristics of the AA 6063-SiC/Gr composite were studied using the FSP technique. As reinforcement SiC and Gr were utilised. The FSP parameters used included an axial load of 10 KN, tool rotating speed of 1000 rpm and 30 mm/min traverse speed. The HcHCr FSP tool was utilised, with a cylindrical threaded profile pin with a pin diameter of 6 mm, a 5.8 mm pin length and a shoulder diameter of 18 mm. The FSP was performed with the aid of a FSW machine. Surface composites of Al/0.4Vol.%, SiC-0.4Vol.%, Al/0.8Vol.% Gr and Al/0.8Vol.% SiC Gr were made in three different combinations. The microstructural alterations were studied using an SEM and optical microscope. Optical microscopy results showed that the SZ had the most refined grain structure when compared to HAZ. In the FSPed zone, the recrystallised grain structure was seen. The microhardness of FSPed plates was determined using an HV tester. The silicon carbide-reinforced Al alloy surface composite had a greater microhardness. The maximum microhardness of the aluminium alloy 6063-SiC surface composite was increased to 62 Vickers hardness.

Narimani et al. [211] investigated the microstructural and wear behavior of AA6063-B4C/TiB2 hybrid and mono composite layers produced by FSP. FSP was employed to create hybrid, and mono surface composite layers of aluminum matrix with TiB2 and B4C particles in this work. The base material chosen for this project was AA6063. FSP integrated different percentages of in situ TiB2–10 wt% and milled B4C Al composite powder generated by mechanical alloying into the matrix. For the first three passes, the tool rotated at 1000 rpm, and for the last pass, it rotated at 710 rpm. The angle of tilt was 2 degrees and the tool traverse speed was 40 mm/min. The wear resistance and microstructure of surface layers were studied using varying ratios of TiB2 and B4C reinforcing particles. FESEM /Field emission scanning electron microscopy and cross-sections of surface composite layers by optical microscopy were used to assess the samples' microstructure. Hardness testing was done throughout the cross-sections of FSPed materials, as well as a pin on the disk dry sliding wear test on FSPed samples, to provide hardness profiles. The inclusion of B4C and TiB2 reinforcing particles at the surface improved wear resistance, and the microhardness of composite layers when compared to the FSPed AA6063 alloy. Furthermore, when compared to other fractions, the surface composite layer made of 100 percent TiB2 exhibited the highest hardness and the best wear behavior. According to a microstructure study, increasing the fraction of TiB2 particles resulted in a reduction in the space between tiny reinforcing particles. The development of mechanically mixed layers lowered the wear rate of mono surface composite layers.

2.3.4.3 Analysis and Discussion

Table 2.3.4.3 summarises the composites fabricated from AA6063 base material with various reinforcements using the FSP process.

**Table 2.3.4.3: AA6063 - based MMCs fabricated with FSP.**

| AA+ Reinforcement | Parameters | | Results | Reference |
|---|---|---|---|---|
| | Tool rotational speed (rpm) | Traverse speed (mm/min) | | |

| | | | | |
|---|---|---|---|---|
| 6063+ $TiB_2$ | 600 | 200 | The average grain size of the FSPed AA6063-$TiB_2$ composite is less than that of the FSPed AA6063.<br>A small number of grains dynamically recrystallise in the FSPed AA6063-$TiB_2$ composite.<br>The estimated dislocation density in the FSPed AA6063/$TiB_2$ composite is greater than that in the FSPed AA6063 alloy. | 204 |
| 6063+ $SiO_2$ | 1600 | 60 | Regardless of location within the stir zone, the quartz particles were distributed equally throughout the aluminium matrix.<br>The AA6063 grains were extensively refined by combining the pinning effect of quartz particles with the thermomechanical effect of FSP.<br>The quartz particle dispersion increased the microhardness and wear resistance of the AMCs. | 206 |
| 6063+ SiC | Varying | 40 | The SiC particles were distributed uniformly in the metal matrix.<br>1120 rpm, 40 mm/min and 2˚ produced the most homogenous distribution and the maximum microhardness of 87 Hv.<br>There was no interfacial interaction between the aluminium matrix and the SiC particles. | 207 |
| 6063+ SiC | 900 | 40 | Among various shoulder profiles, the ACW scrolling shoulder produced a pancake-shaped stir zone and significantly improved stir zone grain size.<br>The cylindrical pin ensured that SiC was dispersed equally in the AMMCs. | 208 |
| 6063+SiC | 1120 | 63 | Owing to the uniform distribution of reinforcement particles, the microhardness of the reinforced zone increased uniformly with increasing passes.<br>In a sample processed with eight FSP passes, a peak microhardness value of 81.9 Hv was found.<br>The processed zone shows adequate bonding of substrate and grain refinement. | 209 |
| 6063+ SiC and Gr | 1000 | 30 | Recrystallised grain structure was observed.<br>When compared to HAZ of the SiC-reinforced Al alloy surface composite, the SZ possessed the most refined grain structure, resulting in a higher microhardness. | 210 |
| 6063+ $B_4C$ and $TiB_2$ | Varying | 40 | In comparison to the FSPed AA6063 alloy, the addition of $B_4C$ and $TiB_2$ reinforcing particles to the surface enhanced the microhardness and wear resistance of composite layers. | 211 |

When compared to other fractions, the 100% $TiB_2$ surface composite layer had the greatest hardness and best wear behaviour.

---

$TiB_2$ reinforcement refines the grain size of the aluminum matrix and increases microhardness. The dispersion of $SiO_2$ particles within the composite enhances both wear resistance and microhardness. The distribution of SiC particles and the selection of tool parameters during processing significantly influence the resulting microhardness and grain size of the material. Hybrid reinforcements offer the capability to tailor composite properties; for example, combining SiC and Gr affects wear resistance, while combining $B_4C$ and $TiB_2$ improves microhardness.

### 2.3.5 AA6082- based MMCs

This section discusses AA6082 composites with various ceramic reinforcements ($B_4C$, $Al_2O_3$, SiC, WC, TiC).

#### 2.3.5.1 Oxide and Carbide Reinforcements in AA6082

Dinaharan [27] studied the impact of ceramic particle type on the microstructural and UTS of FSPed AMMCs. AMMCs were fabricated utilising AA6082 as the base metal and different ceramic particles such as $B_4C$, $Al_2O_3$, SiC, WC and TiC as reinforcement particles. The process parameters for FSP were 1600 revolutions per minute tool rotating speed, 60 millimetres per minute travel speed and 10 kN axial force. The parameters were determined based on previous work and experimental experiments by the researchers. The findings showed that the microstructure was unchanged by the ceramic particle used. Each type of ceramic particle offered a homogeneous dispersion in the stir region and good interfacial bonding regardless of location. The observed microstructure is connected to the strengthening mechanisms and property variations. The hardness results showed that the AA6082-TiC composite was harder than the other AMMCs developed in this study under the same testing circumstances. The AA6082-TiC composites showed good wear resistance, according to the findings. $Al_2O_3$ did not fracture as much as other reinforcements, such as TiC, WC, SiC and $B_4C$, as a result of severe plastic deformation due to its smaller size.

Thangarasu et al. [212] examined the fabrication and wear characterisation of AA6082-TiC surface composites when combining TiC and AA6082 base metal to generate AMMCs via FSP. The FSP method was used to create surface AMMCs and the impact of titanium carbide particles on the microstructural and dry sliding wear behaviour was investigated. The FSP was performed using an FSW machine that was constructed in-house. The following parameters used for this technique were: 1200 revolutions per minute tool rotating speed, 60 millimetres per minute traverse speed and 60 millimetres per minute axial speed. Five plates were FSPed with a force of 10 kN by changing the diameter of the groove to achieve five levels of TiC particle volume fraction which are 0, 6, 12, 18 and 24 vol. percent. The AA6082-TiC composite microstructure was next examined using optical microscopy and SEM. The findings demonstrated that TiC particles had a substantial impact on TiC particle dispersion. The researchers observed that the grain size of the fabricated AMMCs in the NZ was decreased, as was the uniform dispersion of TiC particles. The sliding wear behaviour was investigated using pin-on-disk equipment. According to the findings, the TiC particles had a significant impact on the sliding wear behaviour of the AA6082-TiC composite. There was an increase in TiC quantity fraction as well as a decrease in wear.

#### 2.3.5.2 Analysis and Discussion

Table 2.3.5.2 summarizes the composites fabricated from AA6082 base material with various reinforcements using the FSP process.

**Table 2.3.5.2: AA6082-based MMCs fabricated with FSP.**

| AA+ Reinforcement | Parameters | | Results | Reference |
|---|---|---|---|---|
| | Tool rotational speed (rpm) | Traverse speed (mm/min) | | |
| 6082+ SiC, TiC, WC, $B_4C$, and $Al_2O_3$ | 1600 | 60 | The microstructure remained unaltered, but excellent interfacial bonding promoted homogenous dispersion in the stir region. In comparison to other AMCs fabricated in this work under the same set of experimental conditions, the AA6082/TiC composite demonstrated higher hardness and wear resistance. $Al_2O_3$ did not fracture as much compared to other reinforcements such as TiC, WC, SiC and $B_4C$. | 27 |
| 6082+ TiC, | 1200 | 60 | TiC particles had a significant impact on the AA6082/TiC AMCs' sliding wear behaviour and TiC particle distribution. In the NZ, grain sizes were reduced and TiC particles were evenly distributed. Wear was reduced because of the addition of TiC. | 212 |

The research indicates that, generally, the type of ceramic particle reinforcement does not significantly alter the overall microstructure of the composite. However, the specific type of ceramic does influence certain mechanical properties. Notably, TiC reinforcement results in the highest hardness among the studied ceramic reinforcements. While the microstructure remains relatively consistent across different ceramic additions, each reinforcement contributes unique characteristics, allowing for tailoring the composite's properties to suit specific application requirements.

## 2.4 Summary

It is undeniable that Aluminum Metal Matrix Composites (AMMCs) are capable of exhibiting tailored microstructures, excellent damping capacity, high strength-to-weight ratio, enhanced wear resistance, increased hardness, and reduced thermal expansion. This combination of properties makes them highly desirable and suitable for a wide range of demanding applications across various sectors. These sectors include aerospace (e.g., aircraft structural components, engine parts), consumer electronics (e.g., heat sinks, housings), cutting tools (for improved tool life and performance), defense (e.g., armor, structural elements), marine applications (e.g., ship components, underwater structures), packaging industries (for lightweight and rigid containers), transportation (e.g., automotive parts for weight reduction and fuel efficiency), and space (e.g., satellite structures, spacecraft components).
Friction Stir Processing (FSP) has been acknowledged as a relatively new and effective secondary processing approach for significantly enhancing the microstructure and, consequently, the mechanical and physical properties of AMMCs. By employing FSP, it's possible to achieve grain refinement, improve the uniformity of the processed zone, promote densification, and achieve a more homogeneous distribution of reinforcement precipitates within the metal matrix composites. While the benefits of FSP in developing AMMCs have been widely recognized, the current body of research reveals a disparity. A relatively limited number of studies specifically address the production and optimization of AMMCs tailored for the harsh demands of marine applications.

The existing reviewed literature on AMMCs predominantly indicates that researchers have focused their efforts on fundamental aspects such as grain refinement mechanisms, achieving uniformity within the FSP-affected zone, increasing the density of the composite, and ensuring the homogeneous distribution of reinforcement phases (precipitates) within the metal matrix. This focus is crucial for improving the overall quality and performance of metal matrix composites developed using FSP. However, there is a noticeable lack of detailed information and systematic studies concerning the specific fabrication, characterization, and performance evaluation of AMMCs designed to withstand the unique challenges presented by marine environments.

This relative scarcity of research dedicated to marine-grade AMMCs, therefore, represents a significant gap in the current knowledge base. Addressing this gap is crucial for advancing the potential use of these materials in the marine industry. The development of AMMCs optimized and validated for marine applications is still an area that requires substantial research and development. It is critical to pay close attention to the impact of key performance indicators, including bending strength (to assess structural integrity under load), and X-ray diffraction (XRD) analysis (to characterize the material's microstructure and phase composition) of fabricated MMCs intended for marine structures. This heightened attention is necessary due to the increasing interest and trend in marine engineering towards utilizing aluminum alloys (AAs) and their composites for producing various components in marine vessels and offshore structures.

This study, therefore, aims to contribute to filling this knowledge gap by developing aluminum metal matrix composites using the FSP technique, with a specific focus on tailoring properties and performance characteristics to meet the demanding requirements of marine structures.

# CHAPTER THREE

# EXPERIMENTAL SETUP AND PERFORMANCE

The primary goal of this chapter is to outline and describe every instrument utilized in the experiment related to this study. It also discusses how to use the FSP technique to create an aluminum metal matrix composite joint rather than a bulk composite material. The processing conditions used, which were discovered during optimisation using the Taguchi technique, are also described in depth in this chapter. Finally, all of the investigations and testing performed on the aluminum metal matrix composite joint are detailed in this chapter.

## 3.1 Welding and processing setup

The following equipment was used in producing the welds:

- GEKA cutting machine and
- Friction Stir welding/processing machine.

### 3.1.1 GEKA cutting machine

A GEKA cutting machine was used to cut out all the required plates. A GEKA machine includes flat bar cutting equipment that produces exact cuts without wasting any material and is very easy to use. The equipment for flat bar cutting includes a guided table for directing the flat bar into the shearing station at various angles. It should be noted that while cutting the same material width, the guide does not need to be adjusted. For exact measurement of the material

to be cut, it is recommended to utilise an electric stop. A GEKA cutting machine and its cutting setup are shown in Figure 3.1.1.

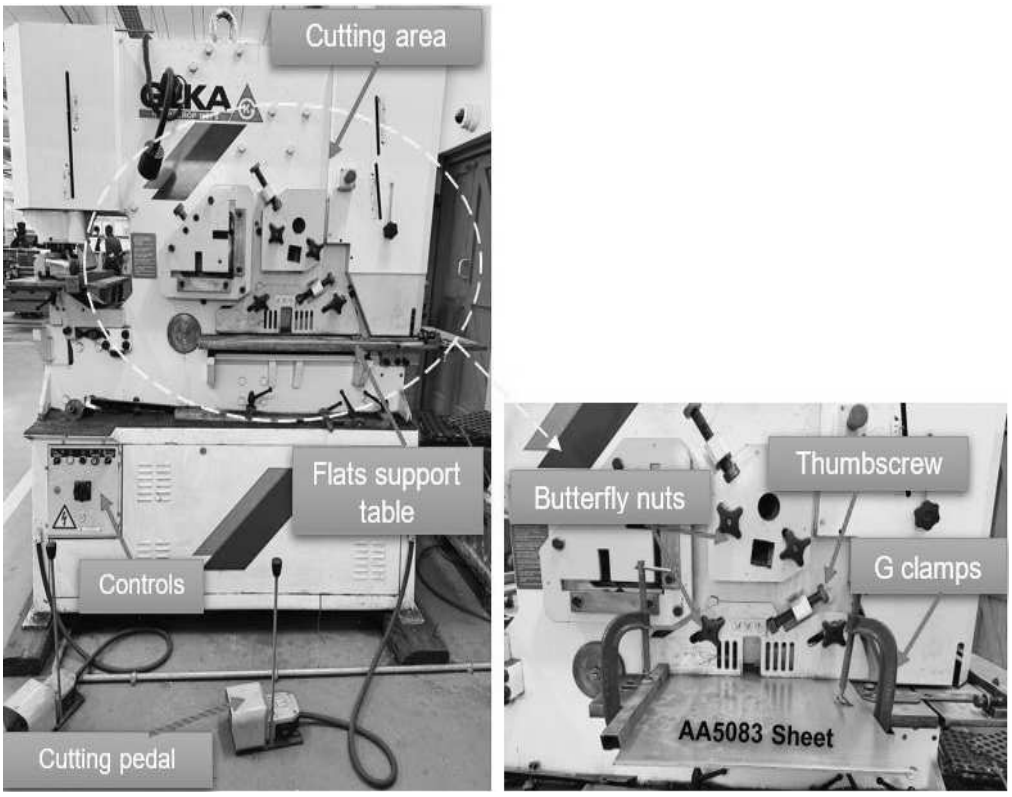


**Figure 3.1.1: GEKA cutting machine.**

The setup involves several sequential actions: Unscrew the butterfly nuts, raise the stop by twisting the thumbscrew to introduce the workpiece, and then place the aluminium sheet on the guided table. The aluminium sheet must then be pushed up until it touches the electric stopper. Turn the thumbscrew to lower the stop until the entire bearing leans against the workpiece. Ensure the plate is square and tighten the butterfly nuts that hold it in place to keep it from shifting while being cut. Afterwards, clamp the plate with two G-clamps, one on each side. Start the machine and push the pedal once everything is set up. The fixed knives or blades on the machine frame will then cut the required plate.

3.1.1.1 How does the electric stopper operate?

These instructions need to be followed when adjusting the electric stop. Position the end of the cross-stop bar so that it is facing the cutting station that will be utilised, by activating the clamping levers on the crankpin. Ensure that the bar end, which is in contact with the workpiece, is angled sufficiently to allow the cuts to fall freely. Determine the preferred cutting length, which is established by the intersection of the millimetre rule and the adjustable thumbscrew. Position the selector. Insert the workpiece until it reaches the electronic stop head. The device will then begin to function.

3.1.2 Friction stir welding/processing machine

The friction stir welding/processing and fabrication of the aluminium metal matrix composites were all carried out on an FSW/FSP machine (see Figure 3.1.2.1). The FSW/FSP machine consists of X, Y and Z movement controls, the bed and the head. A shoulder and a pin, which

is also known as a probe, are the two components of the tool that are inserted into the head. Figure 3.1.2.2 depicts the tool that was utilised for friction stir welding/processing and the pinless tool used for closing the holes during the AMMCs composite fabrication. To position the workpiece and stop movement during the performance, a backplate with a clamping fixture was built and installed into the FSW/FSP machine bed, as shown in Figure 3.1.2.3. The mechanical clamps and bolts are used to fasten the backing plate and the plate to be processed in place.

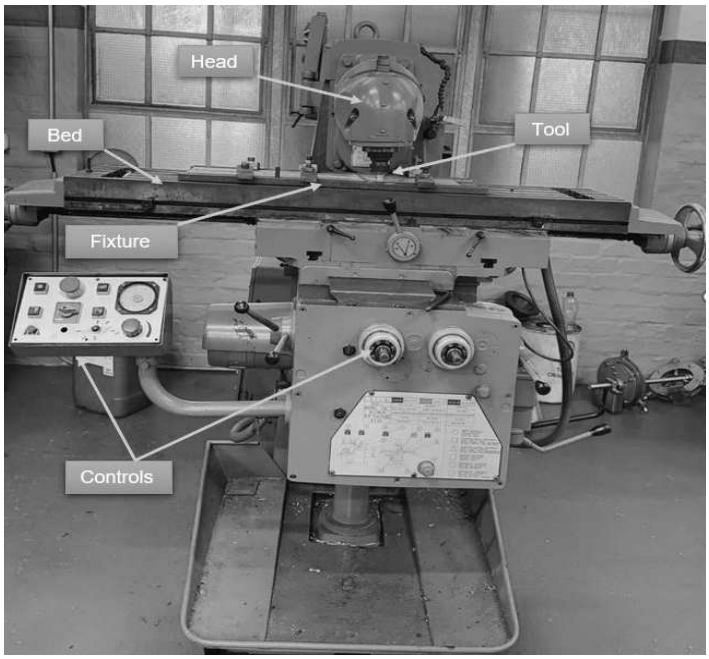


**Figure 3.1.2.1: FSW/FSP machine**

It should be noted that two tools were utilised for this study, one with a pin and the other without a pin. The sample of the two pins utilised is shown in Figure 3.1.2.2(a). Figure 3.1.2.2(b) displays the tool with a pin used for both FSW and FSP performance, and Figure 3.1.2.2(c) displays the pin-less tool used to close holes with reinforcement during the production of the AMMCs. There were two backplates made of EN8 steel used in the fabrication of AMMCs. Figure 3.1.2.3(a) displays the larger back plate, and Figure 3.1.2.3(b) displays the smaller back plate. The smaller backplate was for optimisation to conserve material during preliminary tests, and the larger backplate was used to fabricate the AMMCs for the actual study to enable the assessment of properties in different regions of the composite, such as the start, middle, and end. Detailed schematics of the plates can be found in Appendices A and B, and tool schematics in Appendices C-F.

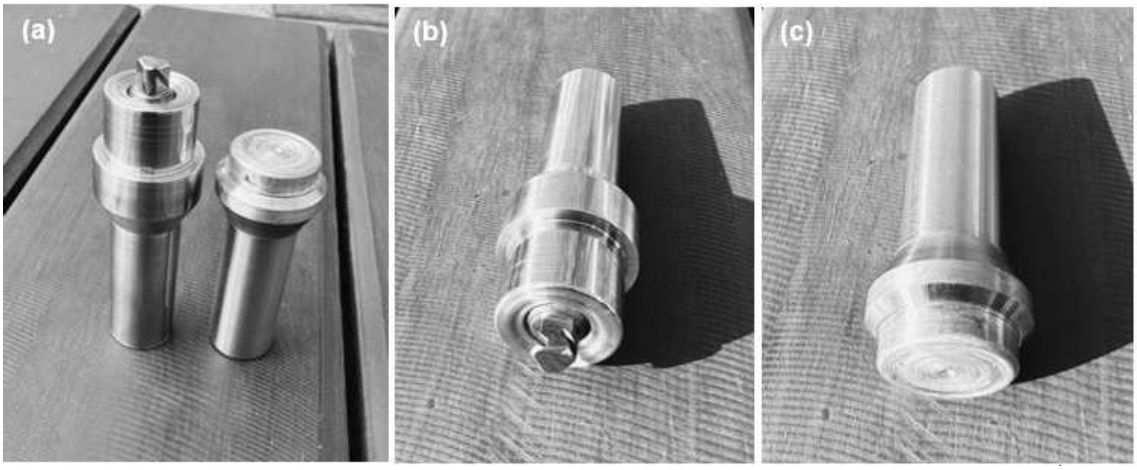


**Figure 3.1.2.2(a): Tools for fabrication; (b) Tool with a pin; (c) Pinless tool.**

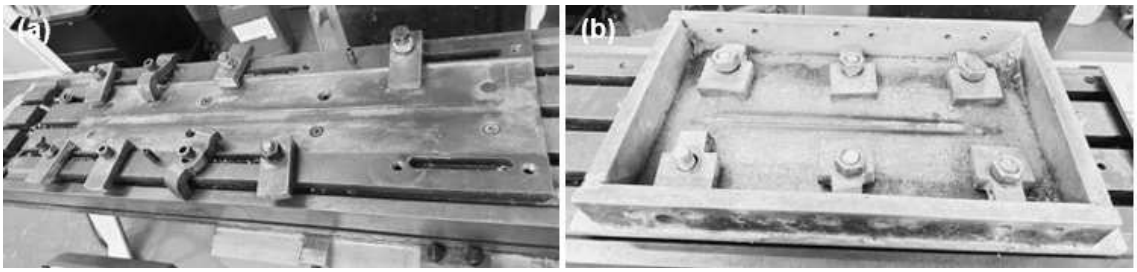


**Figure 3.1.2.3(a): Large back plate; (b) Small back plate.**

## 3.2 Optimization of composite fabrication parameters

This section covers the ideal parameters previously determined and reported in published optimisation studies to fabricate the AMMCs. The published work provides a detailed experimental investigation and analysis, leading to the identification of the optimal processing conditions for the composites [90,213,214,215].

### 3.2.1 Introduction

The optimisation of process parameters is crucial for achieving optimal material properties in FSP-fabricated AMMCs. Process parameters significantly influence NZ characteristics, particle distribution and overall composite quality. Extensive experimentation is required to identify optimal parameter combinations. Approaches to optimisation issues range from traditional to unconventional [216]. Conventional optimisation techniques can be broadly divided into two categories: mathematical search techniques (e.g., linear programming, nonlinear programming, dynamic programming) and experimental techniques such as statistical design of experiments (e.g., Taguchi method, response surface design methodology (RSM)). Non-conventional metaheuristic search methods, such as simulated annealing (SA), tabu search (TS), and genetic algorithms (GA), have become more and more popular among scholars in recent years.

While conventional optimization methods offer certain advantages, they also present limitations that can hinder their practical application in FSP optimization. For example, mathematical iterative search techniques often concentrate on specific machining aspects, such as cutting force, temperature, or tool wear. However, due to the numerous interdependent variables and their inherent stochastic nature, these techniques can struggle to fully capture the complexities of the overall cutting process [217]. Response Surface Methodology (RSM) techniques, which rely on a series of experiments, may not be feasible or cost-effective for many manufacturing scenarios [218]. Furthermore, the application of RSM

requires a continuously differentiable objective function to determine optimal cutting conditions, a requirement that may not be met by complex physical processes [216].

In contrast, metaheuristic methods provide a robust approach to optimization problems, as they do not necessitate derivative information or explicit functional relationships. Genetic Algorithms (GAs), a widely used metaheuristic technique, have demonstrated effectiveness in various applications. Nevertheless, GAs is subject to limitations, including uncertain convergence, sensitivity to parameter settings, substantial computational cost, and the potential for inconsistent results. Although GAs have proven valuable, it is important to acknowledge these drawbacks and consider alternative techniques or hybrid optimization strategies to address these limitations [216].

The Taguchi method, a robust engineering approach developed by Genichi Taguchi, aims to enhance product and process quality through structured experimentation. This method employs orthogonal array designs, signal-to-noise (S/N) ratio analysis, and analysis of variance (ANOVA) to optimize factor settings and minimize variability. This leads to improved product performance and enhanced manufacturing efficiency, all while requiring fewer experimental runs, offering a more practical and efficient approach for industrial applications [218,219]. Moreover, Analysis of Variance (ANOVA) helps identify the input parameters that significantly influence the output quality or characteristics by analyzing variations in the average performance across tested groups [220]

#### 3.2.1.1 Orthogonal array design

In robust engineering, engineers can assess product designs for cost and noise resistance using orthogonal arrays. Orthogonal arrays are designed to discover significant variables using the fewest possible combinations while estimating the effects of several factors and their interactions, hence minimising the number of trials needed. The array's construction intelligently distributes these variables [221, 222].

#### 3.2.1.2 Analysis of variance

Analysis of variance (ANOVA) is used to assess the significance of different parameters and their interactions on the output. By comparing performance variations across different experimental conditions, ANOVA helps identify parameters that significantly impact quality [220]. In an experiment, the percentage of contribution, which is determined by squaring the significance items, indicates the proportion of the overall variance attributed to each significant factor. It shows the relative contribution of a factor to variation reduction. The percentage of contribution indicates the amount that may be lowered from the overall variance by properly controlling the factor levels [223]. The quality of the properties and the significance of parameter effects are evaluated using the frequency-test (F-test) [224].

#### 3.2.1.3 Signal-to-noise ratio

The Taguchi method employs a signal-to-noise (S/N) ratio to quantify the desired output (signal) relative to process variability (noise). The aim is to identify parameter combinations that minimise noise effects and produce consistent, high-quality results [225]. Standard SN ratios come in three main types of noise factors.

##### 3.2.1.3.1. Smaller is better:

The smaller-the-better type is used when the objective is to minimize the output value and there are no negative values. The squared response is the magnitude that must be minimized in this specific case. The following formula is used to get the S/N ratio [226]:

(1)

$$\frac{S}{N} = -10 \log \left( \frac{1}{n} \sum_{i=1}^{n} {y_i}^2 \right)$$

3.2.1.3.2. Nominal is best:

The nominal-is-best type is used when one wishes the output value to be as near to a target value as possible. The squared deviation from the target value is the magnitude that must be reduced in this specific case. The following formula is used to calculate the S/N ratio [226]:

$$\frac{S}{N} = 10 \log \left( \frac{Mean\ squared\ response}{Varience} \right) = 10 \log \left( \frac{\overline{y^2}}{s^2} \right) \quad (2)$$

3.2.1.3.3. Larger is better:

The larger-is-better type is used when the objective is to maximise the output value and there are no negative values. The squared response is the magnitude that must be maximised in this specific case. The following formula is used to calculate the S/N ratio [226-227]:

$$\frac{S}{N} = -10 \log \left( \frac{1}{n} \sum_{i=1}^{n} \frac{1}{{y_i}^2} \right) \quad (3)$$

n is the number of experiments and y represents the response factor. The signal (S) denotes the desired output, while noise (N) represents undesirable variations.

Using S/N analysis, the S/N ratio for each level of process parameters is determined. The primary strategy is to select settings with a high S/N ratio, that indicates a relatively powerful signal, to obtain the appropriate mean value. The mean can then be fine-tuned by adjusting other factors. A higher S/N ratio indicates better performance, regardless of the category in which the performance characteristic is classified. When optimising single-response situations, this S/N ratio value may be considered [221].

3.2.2 Detailed optimization process using the Taguchi method

The Taguchi methodology involves a systematic approach comprising problem definition, parameter selection, level determination, Orthogonal Array selection, experimentation, data analysis and picking of optimal parameters. A detailed explanation of these steps is provided below.

3.2.2.1 Problem definition

The primary goal of this optimisation study is to identify the optimal process parameters for fabricating AMMCs with superior tensile strength, elongation and hardness. This goal will be achieved through the following procedures:

- Designing a Taguchi experimental array,
- Conducting experiments based on the array,
- Analysing output parameters to predict optimal conditions and
- Determining the parameter combination that maximises tensile strength and hardness.

3.2.2.2 Parameter selection

The selection of process parameters plays a critical role in determining the final properties of MMCs. Critical parameters influencing FSW/FSP outcomes include tool rotation speed, traverse speed, tool geometry, tilt angle, axial load, plunge depth and backing plate [228].

1. Tool Rotation Speed:

The rotational speed of the FSP tool plays a critical role in determining both the heat generation and material flow. An increase in rotation speed promotes enhanced dissolution of soluble particles and increased fragmentation of insoluble particles [229]. Furthermore, higher rotational speeds can lead to grain refinement and a substantial temperature rise within the stir zone [230]. However, exceeding a certain rotational threshold can induce excessive heat accumulation, potentially resulting in defects or unwanted phase changes [231]. It is important to note that the microstructural evolution of the material can be affected by the direction in which the tool rotates [232].

2. Traverse Speed:

Traverse speed dictates material flow along the workpiece, controlling deformation rate and grain refinement. Lower traverse speeds lengthen tool-material interaction times, leading to greater plastic deformation and finer grains; higher traverse speeds may compromise mixing and reinforcement distribution. While lower speeds can sometimes increase grain size in the processed zone, tool wear is minimally affected. Conversely, higher speeds can improve surface composite microhardness by enhancing reinforcement particle dispersion [233].

3. Tilt Angle:

The tool's tilt angle during Friction Stir Processing (FSP) is crucial for maintaining the stirred material within the tool shoulder and directing it rearward. This tilt angle directly impacts the downward force applied to the material, thereby affecting material flow and the retention of reinforcement particles within the stirred zone (SZ). Correctly chosen tilt angles are necessary to achieve adequate mixing and avoid surface imperfections. Higher tilt angles can result in coarser grains and larger particles, whereas lower tilt angles may produce defects within the processed zone [234]. Furthermore, it's worth noting that increasing the tool's tilt angle can contribute to an increase in processing temperature [235].

4. Plunge Depth and Tool Design:

Tool plunge depth and design collectively define material mixing and reinforcement integration. Tool geometry, including pin and shoulder, controls material flow and temperature, impacting microstructure [236-239]. Plunge depth significantly influences peak process temperature, with increased plunge depth yielding higher temperatures due to increased contact and friction. Insertion depth is a key determinant of maximum process temperature, with deeper insertions leading to higher temperatures due to increased tool-workpiece contact and friction [239]. Variations in pin profile also alter temperature distribution; pentagonal pins, for example, produce more heat during insertion than alternative shapes [237]. However, the tool shoulder has a more pronounced effect on workpiece temperature than the pin [237].

5. Number of Processing Passes:

To achieve a uniform composite with refined microstructure, the number of processing passes is a critical factor. Increasing the number of passes often promotes better homogeneity, resulting in improved reinforcement distribution, fine grains, and enhanced mechanical performance [171,240,241,242]. However, this increases processing time and heat input. While multiple passes tend to improve the composite's properties, the optimal number of passes is not universal and varies based on the material system and target results [242-243].

6. Axial Force:

Axial force in FSP dictates heat generation and material flow. If the force is too low, heat and mixing will be insufficient; conversely, excessive force can result in overheating and tool failure. Therefore, the optimal axial force must be adjusted based on the specific reinforcement materials and their properties [244].

7. Backing Plate:

A backing plate is essential for supporting the workpiece during FSP, minimizing excessive deformation and promoting uniform heat dissipation. The backing plate's material and thickness are key factors affecting heat transfer and material movement.

Overall, among the various FSP parameters, tool rotation speed and traverse speed are recognized to have a substantial effect on the homogeneous distribution of reinforcing particles, grain refinement, and heat generation during composite production [245], while tool tilt angle plays a significant role in the dispersion of these reinforcing particles. This study focuses on optimizing tool rotation speed, traverse speed, and tilt angle, as these parameters are primarily responsible for heat generation and significantly impact the quality of the resulting joint.

3.2.2.3 Level determination

For this study, three levels were established for each processing parameter (rotational speed, traverse speed, and tilt angle). Table 3.2.2.3 presents these parameters and their corresponding levels. The chosen parameters were selected based on their recognized effects on composite microstructure and mechanical properties within FSP [245]. Parameter levels were established by reviewing prior research. This methodology facilitated the identification of ranges that provided an appropriate balance between processing time and the resulting mechanical attributes [246-249].

**Table 3.2.2.3: Processing parameters with their levels.**

| Parameters | Units | Level | | |
|---|---|---|---|---|
| | | 1 | 2 | 3 |
| Rotational speed | [rpm] | 600 | 900 | 1200 |
| Tilt angle | [°] | 1 | 1.75 | 2 |
| Traverse speed | [mm/min] | 30 | 45 | 60 |

3.2.2.4 Orthogonal array selection

To minimize the required number of experimental trials, a Taguchi $L_9$ orthogonal array was implemented. A complete factorial design would have necessitated 27 separate experiments, but the Taguchi method effectively reduced this by 18 Friction Stir Processing (FSP) runs. This resulted in significant savings in both cost and time. It should be noted that MINITAB18 generated a design matrix, shown in Table 3.2.2.4, specifying the three parameter combinations and levels, resulting in nine experiments per composite.

**Table 3.2.2.4: Taguchi L9 design matrix.**

| No of experiments | Rotational speed [rpm] | Traverse speed [mm/min] | Tilt angle [°] |
|---|---|---|---|
| 1. | 600 | 30 | 1 |
| 2. | 600 | 45 | 1.75 |
| 3. | 600 | 60 | 2 |
| 4. | 900 | 30 | 1.75 |
| 5. | 900 | 45 | 2 |
| 6. | 900 | 60 | 1 |
| 7. | 1200 | 30 | 2 |
| 8. | 1200 | 45 | 1 |
| 9. | 1200 | 60 | 1.75 |

3.2.2.5 Experimentation

AMMCs fabrication requires a base material and a reinforcing phase. This study employed AA5083-H111 aluminium alloy plates (250 x 55 x 6 mm) as the base material. Silicon carbide and coal were used as reinforcement particles. Figure 3.2.2.5.1 displays a similar plate combination sample. Figure 3.2.2.5.2 presents the schematic of the dimensioned plate.


**Figure 3.2.2.5.1: Plate combination sample.**

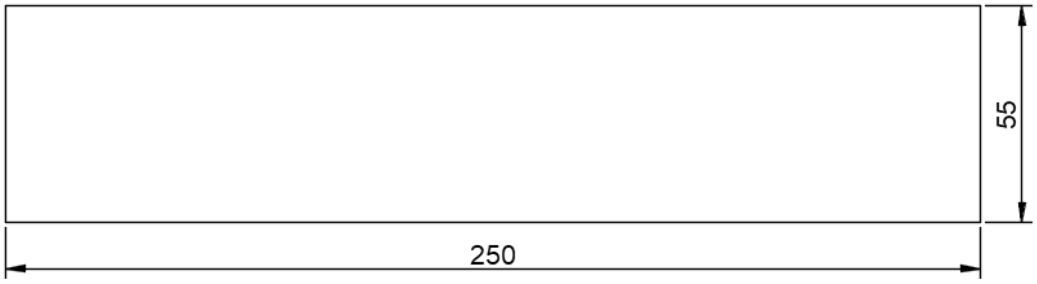


**Figure 3.2.2.5.2: Plate with dimensions in mm.**

To fabricate the AMMCs, two AA5083 plates were initially friction-stir welded (FSWed) to form a joint. The FSW performance is shown in Figure 3.2.2.5.3(a). Figure 3.2.2.5.3(b) displays a sample of the AA5083/AA5083 FSWed joint. Following this, holes with a 2.5 mm diameter were created at 15 mm intervals, reaching a depth of 4 mm, along the weld line. The drilled holes were then filled with a SiC/Coal reinforcement powder, comprising 5% volume fraction. Figures 3.2.2.5.3(c) and (d) illustrate the plate before and after the drilling process, respectively. Figure 3.2.2.5.3(e) presents a sample of the holes filled with the reinforcement particles. It should be noted that the selection of these hole dimensions was based on prior research, which highlighted the significance of optimizing these parameters to achieve consistent particle distribution and sufficient reinforcement concentration within the stirred zone [152,250-255]. Furthermore, the dimensions were chosen to accommodate the size of the reinforcement particles while maintaining the material's structural stability during the processing phase.

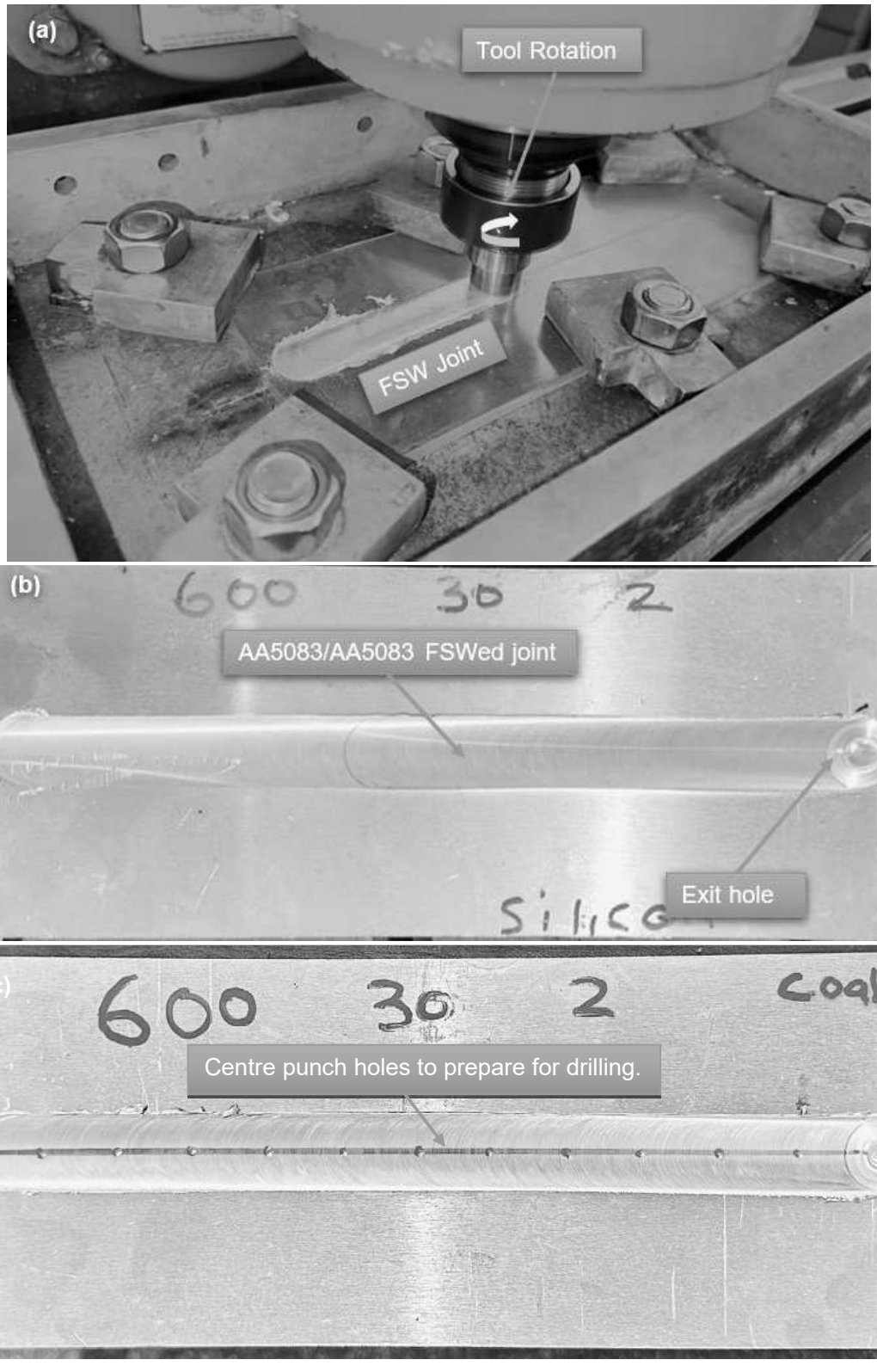
(a)
Tool Rotation
FSW Joint
(b)
600 30 2
AA5083/AA5083 FSWed joint
Exit hole
(c)
600 30 2 Coal
Centre punch holes to prepare for drilling.

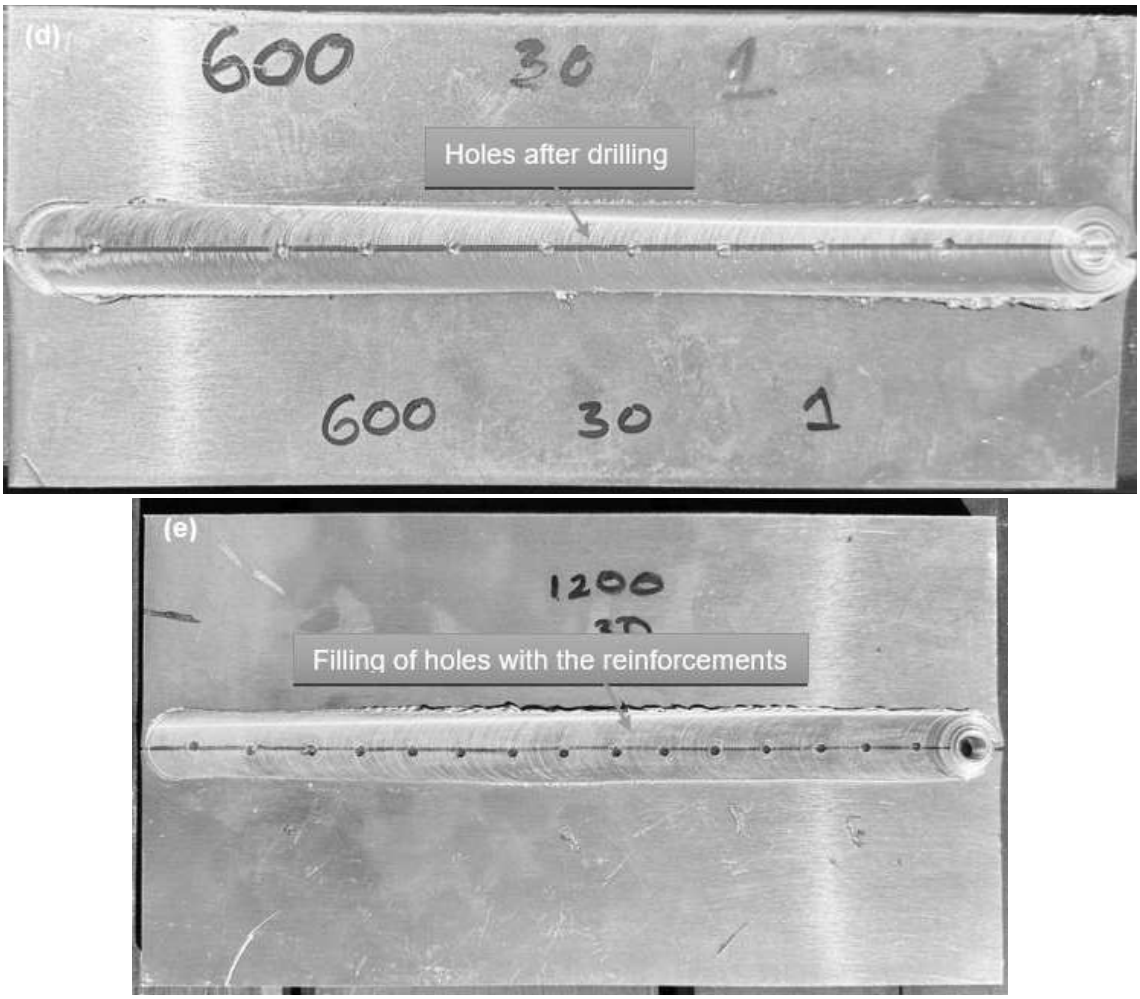


**Figure 3.2.2.5.3:(a) FSW Performance; (b) AA5083/AA5083 FSWed joint sample; (c) Plate before drilling; (d) Plate after drilling; (e) Holes filled with reinforcement particles.**

Reinforcement-filled holes were then sealed using a pinless FSP tool to prevent particle dispersion. Figure 3.2.2.5.4(a) depicts the process of using the pinless tool to close holes. Figure 3.2.2.5.4(b) shows a sample plate after the hole-closing process. Lastly, a single-pass FSP process is conducted at room temperature. Figure 3.2.2.5.4(c) shows the FSP performance during the fabrication of the composite. A sample of the fabricated composite joint is shown in Figure 3.2.2.5.4(d).


(a)
Closing of holes using a pin less tool
1200


(b)
1200
3D
2


(c)
FSP Pass
600
6


**Figure 3.2.2.5.4:(a) Closing of holes using a pinless tool; (b) Sample plate after the hole closing process; (c) FSP Performance for fabricating the composite using a tool with a pin; (d) Sample of AMMCs composite joint.**

Post FSP, Tensile and microhardness specimens were extracted from the fabricated AA5083/Silicon carbide and AA5083/Coal composite joints by cutting the joints perpendicular to the processing direction. Tensile testing adhered to American Society for Testing and Materials (ASTM E-8M-04 standards), while microhardness was evaluated using the ASTM E384 standard for Vickers microhardness. Figures 3.2.2.5.5 and 3.2.2.5.6 illustrate the tensile and microhardness test specimens.

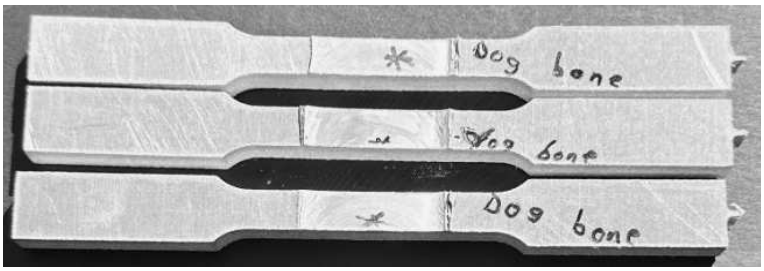


**Figure 3.2.2.5.5: Tensile specimen.**

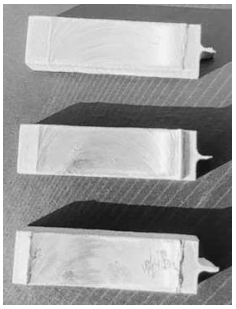

**Figure 3.2.2.5.6: Hardness specimen.**

3.2.2.6 Analysis of data

To optimise AMMCs parameters, the ultimate tensile strength (UTS), percentage elongation, and microhardness of the fabricated AA5083/Silicon carbide and AA5083/Coal composite joints were analysed using the Taguchi method. This technique focuses on single-response optimisation, assessing parameter influence through the S/N ratio. The larger-is-better S/N ratio criterion was employed to maximise desired responses for each response since a parameter combination that maximises tensile strength and hardness is required using equation.

$$\frac{S}{N} = -10 \log\left(\frac{1}{n}\sum_{i-1}^{3}\frac{1}{y^2}\right) \quad (3)$$

Where *n* is the number of experiments and *y* represents the response factor (UTS, HV, or PE). The signal (S) denotes the desired output, while noise (N) represents undesirable variations.

The Taguchi approach based on the S/N ratio demonstrated that:

- Analysis using the Taguchi Signal-to-Noise (S/N) ratio method revealed the following optimal parameter settings: For AA5083/Silicon carbide composites, the highest UTS and percentage elongation are obtained by setting the rotational speed to level 2, traverse speed to level 1, and tilt angle to level 3. The optimal microhardness for these composites was achieved with a tilt angle at level 3, traversal speed at level 2, and rotational speed at level 2. In the case of AA5083/Coal composite joints, the best Friction Stir Processing (FSP) parameters for maximizing UTS, percentage elongation, and microhardness were rotation speed at level 2, traversal speed at level 3, and tilt angle at level 3.

An ANOVA was conducted to determine each factor's percentage contribution and its statistical significance (F-value) on the output responses.

The Taguchi approach based on the ANOVA demonstrated that:

- An analysis of variance (ANOVA) indicated that rotational speed exerts a greater influence on both percentage elongation and microhardness in AA5083/Silicon carbide and AA5083/Coal composite joints. For AA5083/Silicon carbide, ultimate tensile strength is primarily influenced by rotational speed, while for AA5083/Coal, tilt angle is the dominant factor. The observed variations highlight the distinct impact of different reinforcements on process parameters, underscoring the necessity for tailored optimization approaches depending on the reinforcement type. These differences in parameter ranking are significant, as they reflect the unique material responses of the reinforcements during Friction Stir Processing (FSP). Harder reinforcements, such as SiC, rely heavily on heat generation and plastic deformation for effective distribution and bonding, hence the dominance of rotational speed. Conversely, more softer reinforcements, like coal, benefit more from controlled material flow and uniform particle dispersion, making tilt angle a crucial parameter.

Based on the results the conclusion was drawn that:

- For the fabrication of AA5083/Coal composites, optimal processing parameters were determined to be a tilt angle of 2 degrees, a traverse speed of 60 mm/min, and a rotation speed of 900 rpm.
- When fabricating AA5083/Silicon carbide composites, the highest microhardness was achieved with a rotational speed of 900 rpm, a traverse speed of 45 mm/min, and a tilt angle of 2 degrees. The maximum ultimate tensile strength and percentage elongation for these composites were obtained with a rotation speed of 900 rpm, a traverse speed of 30 mm/min, and a tilt angle of 2 degrees. The validity of these optimal parameters was subsequently confirmed through a series of validation tests. Specifically, average response values indicated that a tool tilt angle of 2°, a traverse speed of 30 mm/min, and a rotation speed of 900 rpm were optimal for AA5083/SiC composites. These validation tests supported the initial experimental findings, indicating improved mechanical characteristics with the optimized parameters.

Complete optimization details, including AMMCs fabrication, mechanical and microstructural analyses, and statistical evaluations (S/N ratio, ANOVA, normal probability plots, regression analysis plots), are available in Appendices H–K.

3.2.2.7 Picking the optimal parameters

The optimal parameter combinations for AA5083/Silicon carbide and AA5083/Coal composites were determined based on the S/N ratio and ANOVA results. These optimal conditions are presented in Tables 3.2.2.7(a) and (b), respectively.

**Table 3.2.2.7:(a) FSW/FSP optimal process parameters when using silicon carbide [213,215].**

| Process parameters | Condition |
|---|---|
| Rotational speed | 900 rpm |
| Traverse speed | 30 mm/min |
| Tool tilt angle | 2 ° |

**Table 3.2.2.7:(b) FSW/FSP optimal process parameters when using coal [90,213,214].**

| Process parameters | Condition |
|---|---|
| Rotational speed | 900 rpm |
| Traverse speed | 60 mm/min |
| Tool tilt angle | 2 ° |

From the optimised parameters obtained, it was observed that the parameter combinations for fabricating AA5083/Silicon carbide composite were different from the combination found for fabricating AA5083/Coal composite. These optimised parameters are the ones to be used to fabricate the actual AMMCs using the FSP technique discussed in section 3.3.

3.2.3 Justification for using optimal parameters

The decision to use the optimal parameters for fabricating the AA5083/SiC and AA5083/Coal composite is based on their proven effectiveness in enhancing composite properties. The application of these parameters ensures research consistency, reproducibility and comparability with previous studies.

3.2.4 Conclusion

The parameters used to fabricate the composites for this thesis were taken from well-substantiated optimisation studies conducted earlier for fabricating such ideal composites. These particular parameters were applied to achieve the required properties of the composites manufactured in this research, as indicated in the previous optimisation research paper. By implementing these proven parameters, this research seeks to build on existing studies and continue the exploration of the performance of the composites under conditions defined by the parameters.

### 3.3 Fabrication of aluminium metal matrix composites using the FSP technique

A base material and reinforcement are required to fabricate AMMCs. The simple process for fabricating an AMMC using FSP techniques requires the following steps: FSW to create a weld joint, drilling of holes to incorporate reinforcement, filling/incorporating reinforcement

particles into the holes, closing the holes using a pinless tool and, finally, using a tool with pin for FSP. The fabrication process is explained in depth in the following section.

3.3.1. AMMCs fabrication preparation

A base material and reinforcement are required to fabricate AMMCs. The base material used for this study was an AA 5083 plate that was 6mm thick. Before the welding performance, the plates were first cut with a GEKA cutting machine to a size of 530×70×6 mm. The dimensions were chosen based on the dimensions of the FSW backplate. Figure 3.3.1(a) displays a similar plate combination sample. The schematic of the dimensioned plate is shown in Figure 3.3.1(b). Silicon carbide and coal were the reinforcements utilised in the study and each reinforcement was used separately to create an AMMCs. Figures (c) and (d) show scanning electron microscope (SEM) micrographs that depict the morphology of the powder particles used as reinforcement. Tables 3.3.1(a), 3.3.1(b), 3.3.1(c), and 3.3.1(d) provide detailed information regarding the base material chemical composition, base material mechanical properties, reinforcement chemical composition and reinforcement particle size used in this study. This information is crucial for understanding the material behaviour and the impact of reinforcement on the mechanical properties of the composites.

**Table 3.3.1:(a) The base material chemical composition of the materials is wt %.**

| BM | Cu | Cr | Fe | Mg | Mn | Si | Ti | Zn | Al |
|---|---|---|---|---|---|---|---|---|---|
| AA5083-H111 | 0.010 | 0.040 | 0.153 | 4.339 | 0.649 | 0.139 | 0.011 | 0.013 | Bal |

**Table 3.3.1:(b) AA5083-H111 base material mechanical properties of the materials.**

| Tensile Strength (MPa) | Yield Strength (MPa) | Elongation (%) | Hardness (HV) |
|---|---|---|---|
| 311 | 248.8 | 58.65 | 90.57 |

**Table 3.3.1:(c) Reinforcement's chemical composition of the materials wt %.**

| Reinforcement | O | Br | C | Si |
|---|---|---|---|---|
| Silicon carbide | 3.7 | 0 | 28.8 | 67.4 |
| Coal | 5.4 | 1.3 | 91.7 | 1.6 |

**Table 3.3.1:(d) Reinforcement's particle size.**

| Particle size | |
|---|---|
| Silicon carbide | 13.155 µm |
| Coal | 11.765 µm |

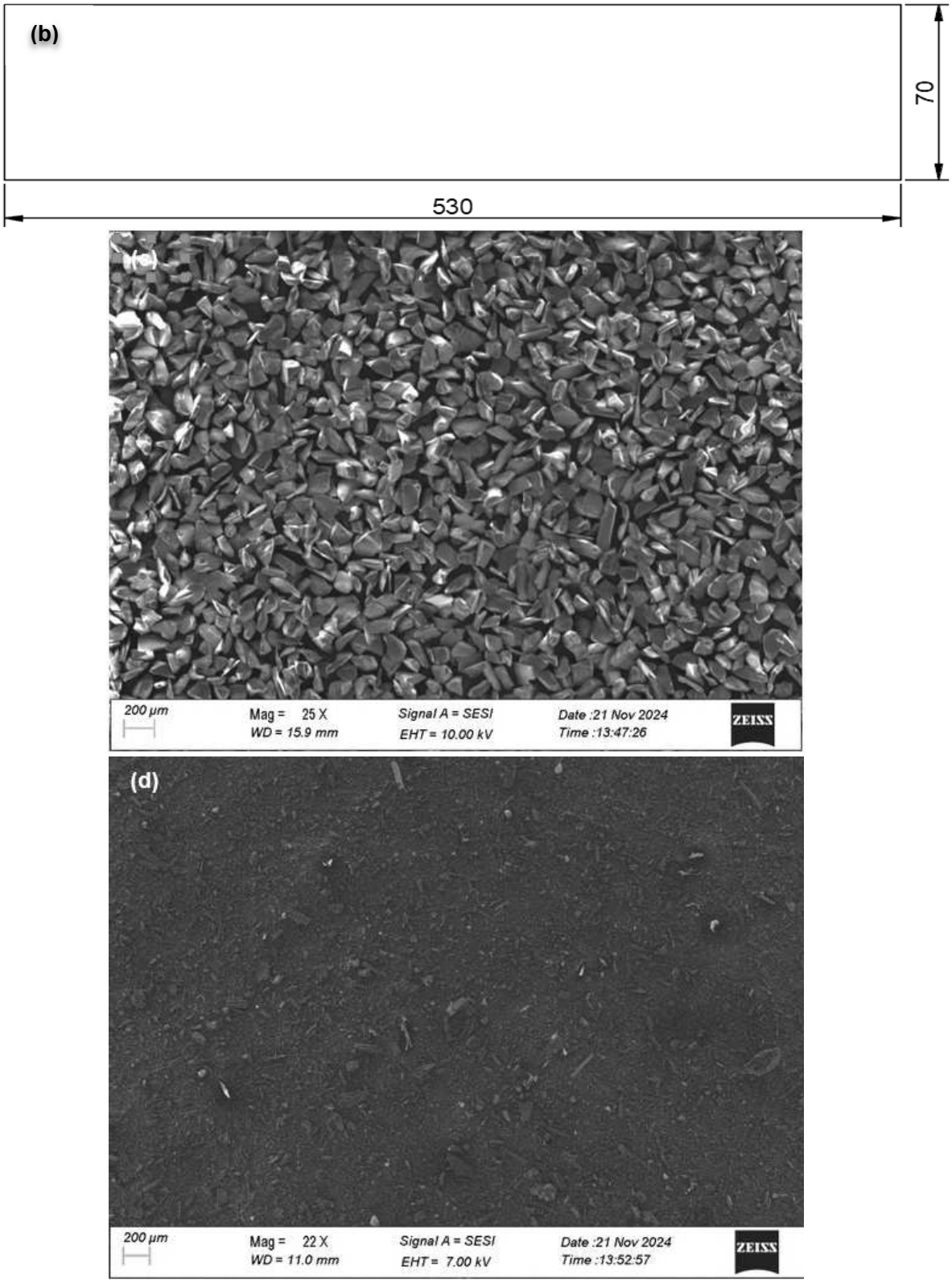


**Figure 3.3.1: (a) Plate combination sample; (b) Plate with dimensions in mm; (c) SEM micrograph illustrating the morphology of the SiC powder particles employed as reinforcement. (d) SEM micrograph showing the morphology of the Coal powder particles employed as reinforcement.**

3.3.1.1 Friction stir welding performance

FSW was performed on the FSW machine in this study using two similar aluminium alloy plates that were mounted on the backplate and then tightly secured onto the FSW machine's back plate. The plates were secured to the machine's backplate using eight clamps, preventing the plates from separating during the FSW performance. To perform FSW, the head holding the tool was lowered until the rotating tool pin was at the centre of the two plates, as shown in Figure 3.3.1.1.1, and the tool shoulder face made contact with the edges. The rotating tool was then plunged into the material. As a result, it melted the material plastically because of the heat generated by the friction. Once there was sufficient heat produced, the rotating tool traversed forward, resulting in a continuous joint until it reached the end of the plates. The optimized process parameters, determined via the Taguchi $L_9$ method as detailed in section 3.2, were employed to execute the Friction Stir Welding (FSW) and Friction Stir Processing (FSP) procedures [90,213,214,215]. Tables 3.3.1.1(a) and (b) present the specific optimized parameters for silicon carbide and coal, respectively. The performance of FSW is shown in Figure 3.3.1.1.2(a). The produced samples of the FSWed plates are shown in Figure 3.3.1.1.2(b). It should be noted that both of the process parameters were used to create a one FSWed plate which was used to create the required AMMCs using the FSP method.

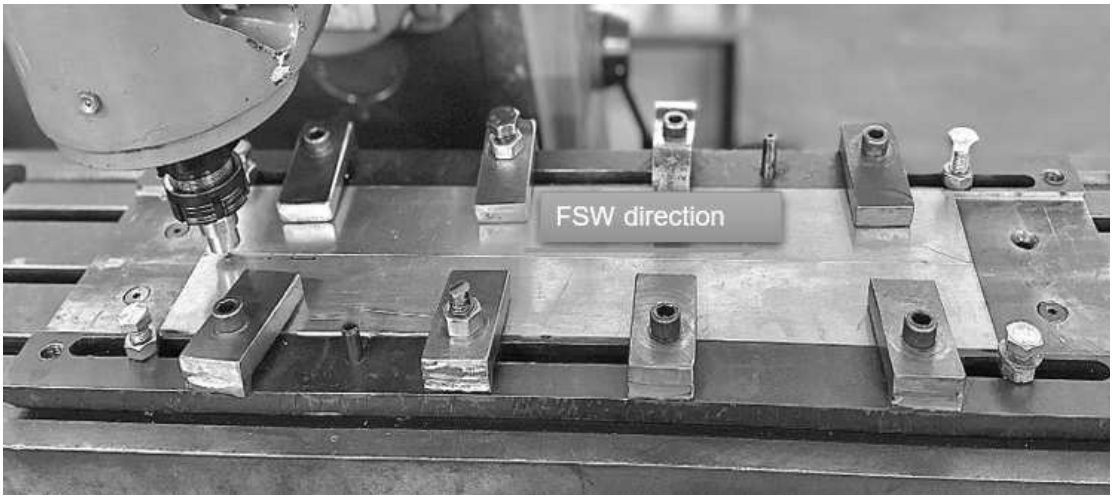


**Figure 3.3.1.1.1: FSW setup preparation.**

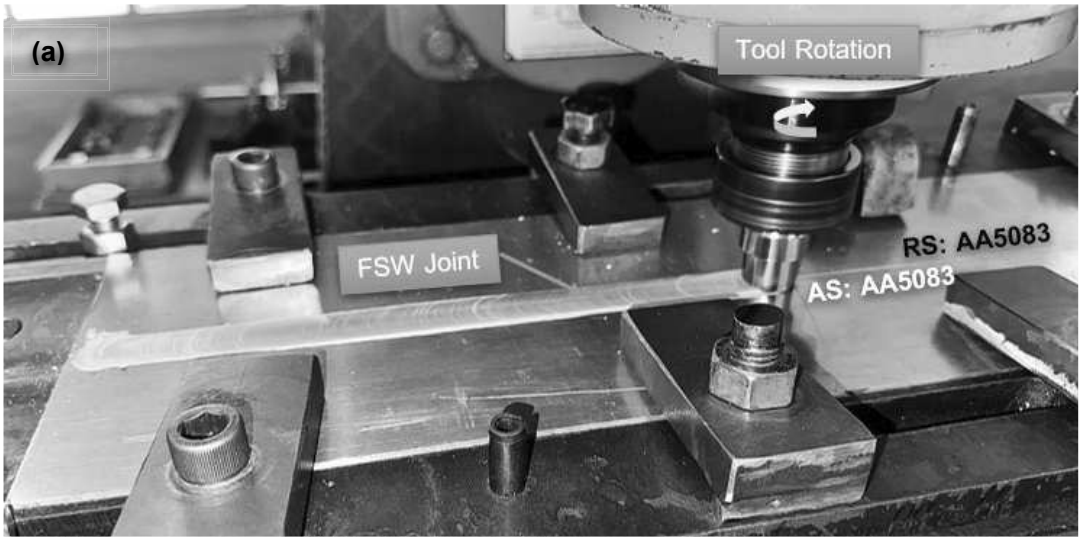

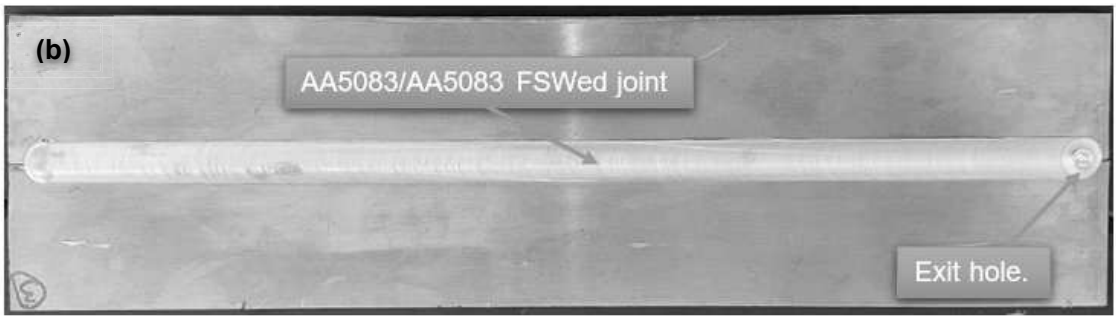


**Figure 3.3.1.1.2:(a) FSW performance; (b) AA5083/AA5083 FSWed joint.**

**Table 3.3.1.1:(a) FSW/FSP parameters when using Silicon carbide.**

| Parameter | Condition |
|---|---|
| Tool shoulder diameter | 20 mm |
| Tool probe diameter | 7 mm |
| Tool pin length | 5.8 mm |
| Tool plunge depth | 5.8 mm |
| Tool tilt angle | 2 ° |
| Traverse speed | 30 mm/min |
| Rotational speed | 900 rpm |
| Dwell time | 20 s |
| Axial force | 4 KN |
| Vertical feed | 20 tan (2) = 0.698 |

**Table 3.3.1.1:(b) FSW/FSP parameters when using Coal.**

| Parameter | Condition |
|---|---|
| Tool shoulder diameter | 20 mm |
| Tool probe diameter | 7 mm |
| Tool pin length | 5.8 mm |
| Tool plunge depth | 5.8 mm |
| Tool tilt angle | 2 ° |
| Traverse speed | 60 mm/min |
| Rotational speed | 900 rpm |
| Dwell time | 20 s |
| Axial force | 4 KN |
| Vertical feed | 20 tan (2) =0.698 |

3.3.1.2 Adding and confining reinforcement

To add the reinforcement to the FSWed joints, holes had to be drilled. In preparation for drilling the holes, a line was drawn in the centre of the AA5083/AA5083 FSWed joint, and then the centres of the holes that needed to be drilled were marked using a centre punch. The holes were drilled with an electric drill press with a 15mm distance between the centres. The holes were cut 4mm deep, with a drill bit that was 2.5mm in diameter. Figures 3.3.1.2(a) and (b) show the prepared plate before and after drilling, respectively. After the holes were drilled, the reinforcing particles (5% volume) were inserted into the hole. Owing to silicon carbide and coal being used as reinforcement particles in this study, the process had to be conducted twice. As a result, two plates were required: one for incorporating silicon carbide particles and the other for adding coal particles. It is important to point out that the reinforcing particles were inserted until the holes were filled. Figure 3.3.1.2(c) shows a sample of plate holes filled with reinforcement. To restrict the reinforcing powder particles from scattering during FSP performance, the necessary hole-closing process was carried out with a pinless tool. Figure 3.3.1.2(d) depicts the pinless tool's process used to close holes. Figure 3.3.1.2(e) shows the plate engaging in the hole-closing process.

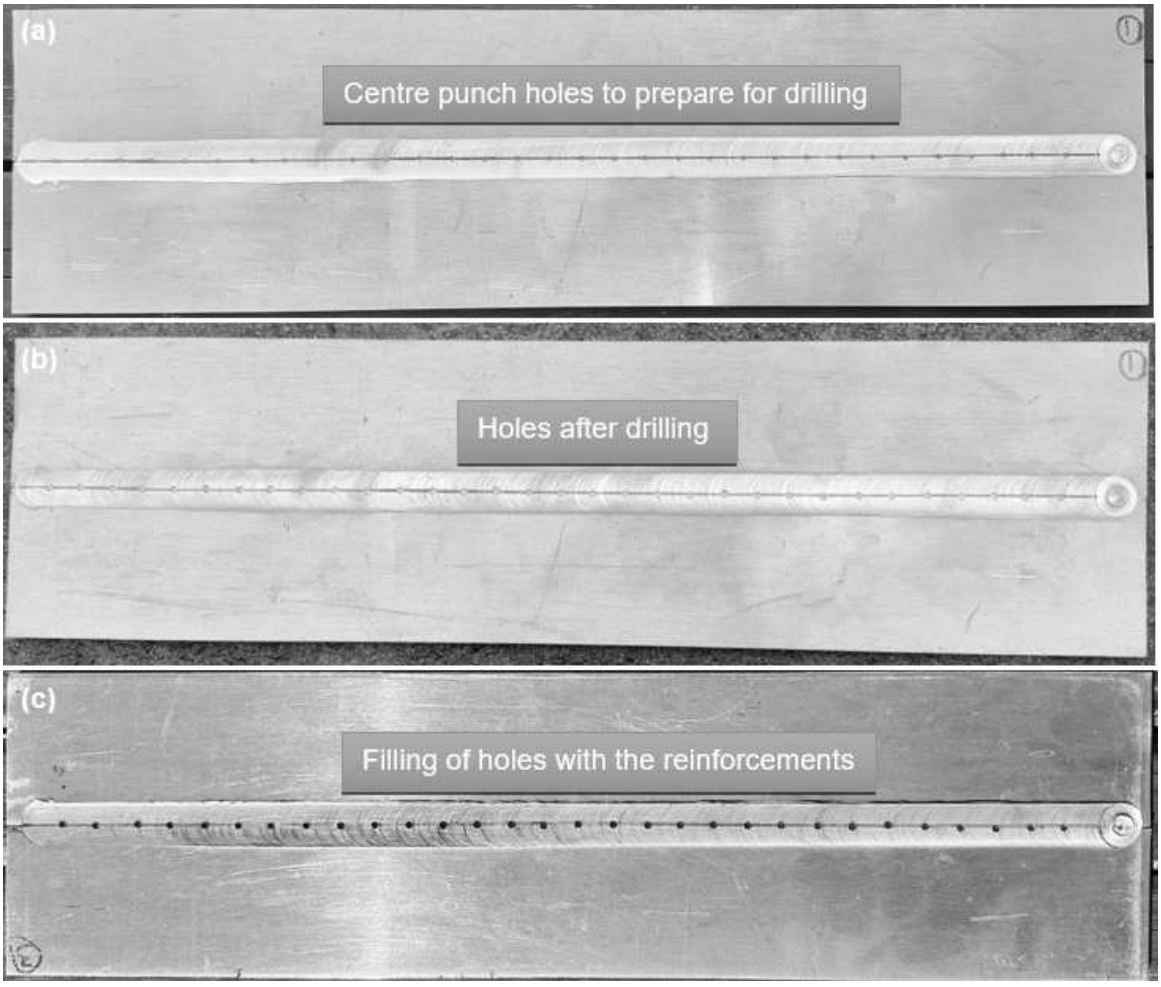


**Figure 3.3.1.2: (a) Prepared plate before drilling; (b); Plate after drilling (c); Sample of holes filled with reinforcement particles; (d) Closing of holes using pinless tool; (e) Sample plate after the hole closing process.**

3.3.1.3 Friction stir processing

Finally, a single FSP was performed using a tool with a pin to fabricate an AMMCS on the joints. The same tool used to produce the FSWed joint was also used to perform the FSP. To begin the FSP procedure, the head holding the tool was lowered until the rotating tool pin was placed at the centre of the joint and the tool's shoulder face made contact with the surface. The material then softens because of the frictional heat produced by the rotary action. This procedure promotes the metallurgical bonding between the reinforcing material and the FSWed joint. When sufficient heat is created, the rotating tool traverses forward and forms a plasticised zone, resulting in a continuous joint. This plasticised zone allows the reinforcing material to be integrated and transferred from the holes into the FSWed joint, resulting in the fabrication of AMMCs. The stirring action aids in achieving the uniform dispersion of the reinforcement material within the FSWed joint. It should be noted that the process parameters used to achieve a defect-free NZ and uniform particle distribution were established during optimisation. The parameters used to fabricate the AA5083/SiC composite are presented in Table 3.3.1.1: (a) above and the parameters used to fabricate the AA5083/Coal composite are presented in Table 3.3.1.1: (b) above. Figure 3.3.1.3: (a) shows the FSP performance during the fabrication of the composite. Figure 3.3.1.3: (b) shows samples of fabricated composite joints.

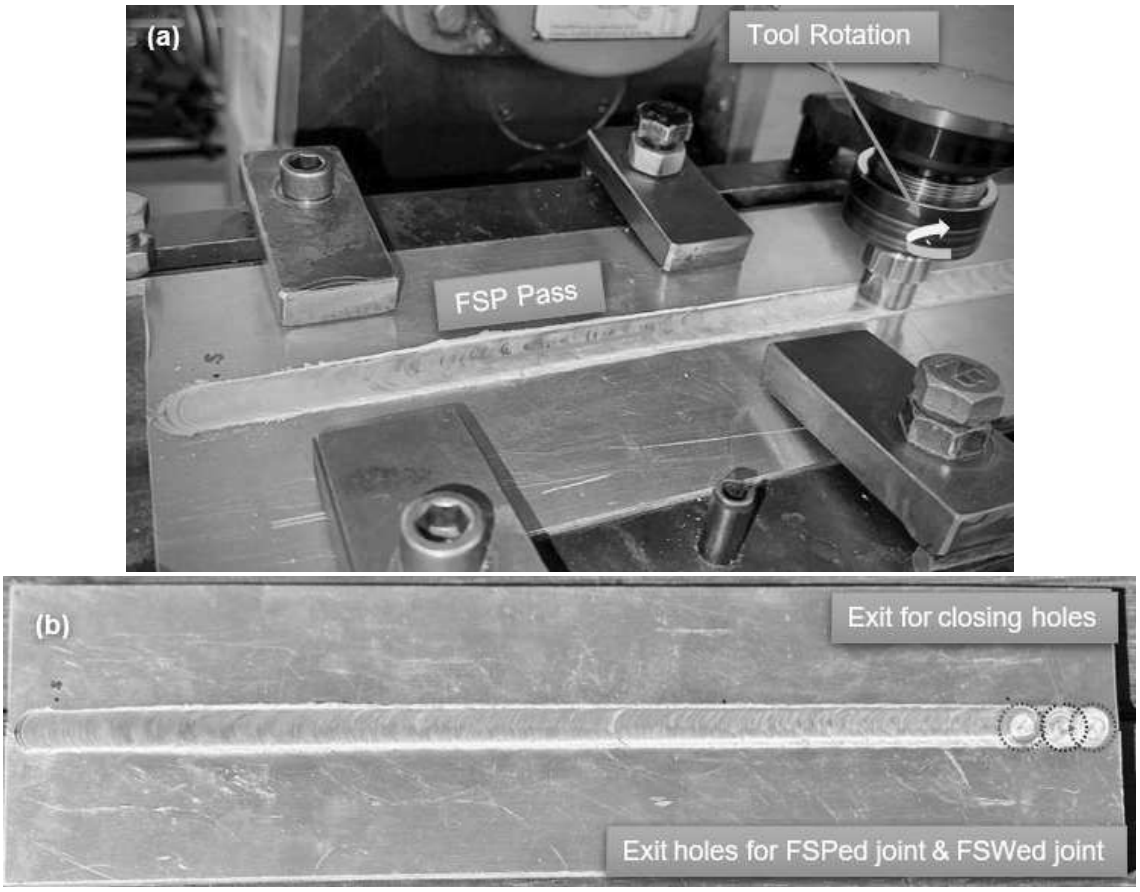


**Figure 3.3.1.3: (a) FSP Performance for fabricating AA5083/SiC composite using a tool with a pin; (b) Sample of fabricated composite joint.**

### 3.4 Performance of specimen preparation

The preparation of the specimens for all the tests, including the tensile, microstructural analysis, hardness, bending, chemical analysis and X-ray diffraction analytical tests, are explained in this section.

3.4.1 Tensile test specimen preparation

The American Society for Testing and Materials (ASTM E8-04) standard was used to create the tensile test specimen design and shape. The sketch of the dimensioned specimen is shown in Figure 3.4.1. The drawing was created using SolidWorks design software and all the measurements are in millimetres. The specimen is in the shape of a dog's bone. The tensile test specimen was cut using the waterjet cutting machine.

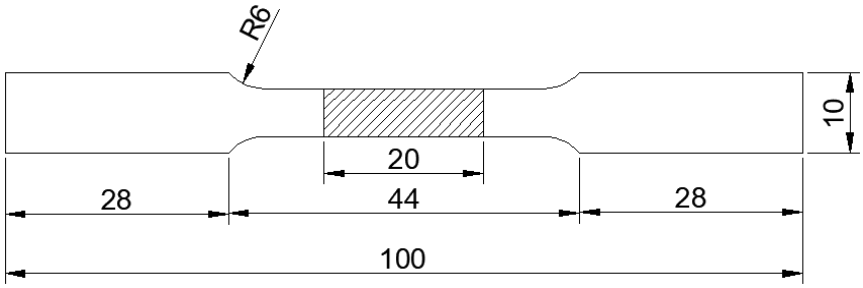


**Figure 3.4.1: Tensile test specimen.**

3.4.2 Microstructural analysis test specimen

SolidWorks was used to create the microstructural analysis specimen (see Figure 3.4.2). The waterjet cutting equipment was used to cut the test specimens for microstructural examination of the designed specimen.

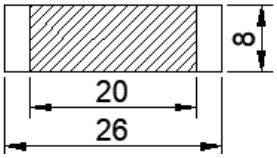


**Figure 3.4.2: Microstructure test specimen with dimensions in mm.**

3.4.3 Microhardness test specimen

The dimensions and shape of the specimens used for hardness testing are the same as those for microstructural analysis (see Figure 3.4.2 above). The specimen was duplicated, one pair was used for microstructure and the second pair was used for hardness testing.

3.4.4 X-ray diffraction test specimen

The X-ray diffraction test specimen's shape and design followed ASTM D5380. The X-ray diffraction (XRD) specimen's dimensioned design was created in SolidWorks, with all measurements being in millimetres, is shown in Figure 3.4.4. The waterjet cutting machine was used to cut the X-ray diffraction test specimen.

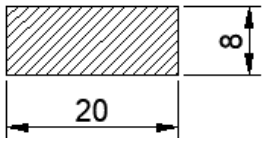


**Figure 3.4.3: XRD specimen with dimensions in mm.**

3.4.5 Chemical composition/analysis specimen

The XRD and chemical analysis experiments both utilised similar specimens with the same dimensions and geometries (see Figure 3.4.4).

3.4.6 Bending test specimen preparation

The ASTM E290 standard was followed in terms of specimen design and geometry for the bending specimen. The dimensioned bending specimen from SolidWorks is shown in Figure 3.4.6, with all measurements shown in mm. The bending test specimen was cut using the waterjet cutting machine.

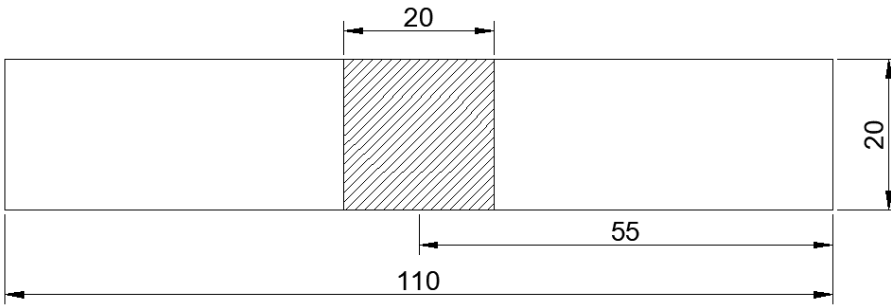


**Figure 3.4.4: Bending test specimen with dimensions in mm.**

### 3.5 Cutting of specimen

This section describes the cutting out of all the designed specimens mentioned in section 3.4 above. The computer numerical control (CNC) milling machine (see Figure 3.5) was used to cut out the specimens. In this section, the procedure for cutting using a CNC milling machine is explained. Before cutting, the process begins by creating a drawing of the plate containing all the specimens to be machined using AUTOCAD (Computer-aided design and drafting software application), outlining all the features, cutting paths and dimensions that will be useful for coding. Notepad is then used to create the CNC program by converting the AUTOCAD model into G & M codes that the CNC milling machine can understand. Before fabricating or producing a material, it is essential to optimise the materials to determine the optimum best process parameters. These measurements were simulated with CNCMillSim to ensure the code would not develope any problems. The G&M code is then transferred to the computer that is linked to the CNC milling machine. Clamps are used to hold the plate to the worktable of the CNC milling machine, and to ensure that it is correctly aligned and tightly secured to avoid movement during cutting. The machined is then switched to manual mode and it is verified that the G on the codes match the G on the machine. The zero-reference point of the tool is set to align with the set zero of the workpiece. It is necessary to ensure that X, Y and Z are set at absolute zero. Next, the CNC milling machine is set to receive the code from the PC by opening the CNC send software option and sending the CNC program to the machine. The spindle speed and feed rate are set, the coolant turned on and the start button pressed to commence the cutting process. The CNC milling machine automatically moves the cutting tool along the pre-programmed tool paths, removing material following the design specifications and continues to do so until the program is complete. Once the program is finished, the workpiece should be carefully removed from the CNC milling machine. During cutting, it is necessary to carefully watch the cutting process to observe any vibrations or improper cutting by the machine.

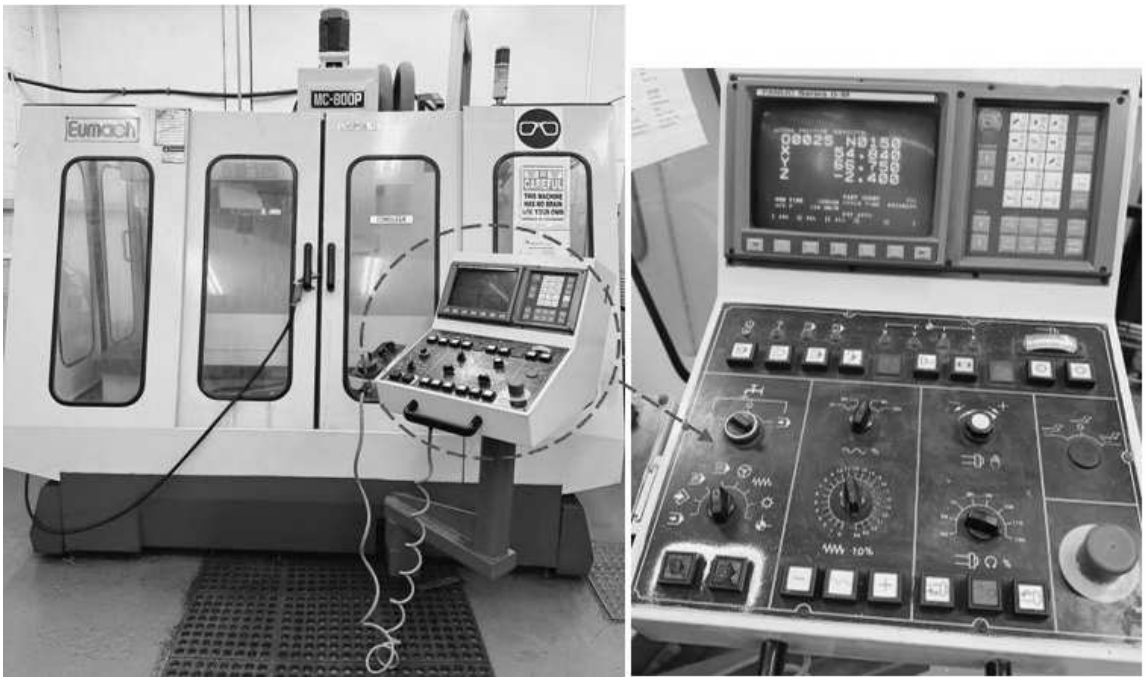


**Figure 3.4: CNC Mill machine**

### 3.6 Preparation of weldments analysis

This section covers weldment analysis preparation of the microstructural and microhardness specimen. Below is a list of the equipment and techniques used for analysing the weld joints that were produced through the steps described in section 3.3 above.

- Struers Lapopress-3 mounting press machine and
- Struers LapoPol-5 polishing machine

3.6.1. Struers Lapopress-3 mounting press machine

Prior to the mounting process, the designed specimens were cut using the CNC milling machine. The cut cross-sectional surfaces (see Figure 3.6.1.1) of the AMMCs joints specimens were then mounted using a Struers labopress-3 machine and a multi-fast Aka-Resin phenolic (see Figure 3.6.1.2). The mounting procedure includes the following actions: brushing the ram with Aka-no-stick powder to stop the hardness specimen from sticking, positioning the specimen on the ram ensuring the viewing surface is facing down and lowering the ram to its lowest point (specified depth). Once the ram is lowered to the desired depth, approximately one scoop of the chosen resin is poured using a funnel on top of the specimen until the inside cylinder depth is filled, and then the ram is closed off with the lid. The parameters, including force, heating time, temperature and cooling time, are set after the lid is secured. When the start button is pressed, the procedure begins automatically. The mounting is then operated according to the predetermined parameters until it is removed from the machine. Figure 3.6.1.3 displays a sample of the mounted specimen. The predetermined parameters are shown in Table 3.6.1.

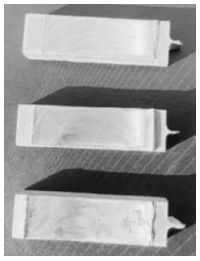

**Figure 3.6.1.1: Sample of cut cross-sectional surface joints for microstructure or microhardness specimen.**


**Figure 3.6.1.2: Mounting press machine.**

**Figure 3.6.1.3: Mounted microstructure test specimen sample.**

**Table 3.6.1: Mounting Processing Parameters**

| **AKA- Resin Phenolic mounting processing parameters** | |
|---|---|
| Force | 20 kN |
| Heating time | 7 minutes |
| Cooling time | 7 minutes |

3.6.2 Struers LapoPol-25 grinding machine

The Struers Labopol-25, shown in Figure 3.6.2.1, is a device that grinds, laps and removes the surface damage that occured during the cutting of any type of metal. The machine operates by mounting a chosen grinding disc onto the turntable and choosing a suitable rotational speed (between 50 and 500 rpm). The grinding process is started by pressing the start button and continued until the desired surface finish is achieved. The material preparation process involves using different grinding discs with suitable lubrication. Figure 3.6.2.2 illustrates the various grinding discs employed. The P800, P1200 and P4000 grit discs are used with regular tap water or distilled water as a lubricant for aluminium specimens. Before the final polishing step, the specimen is cleaned with ethanol and dried.

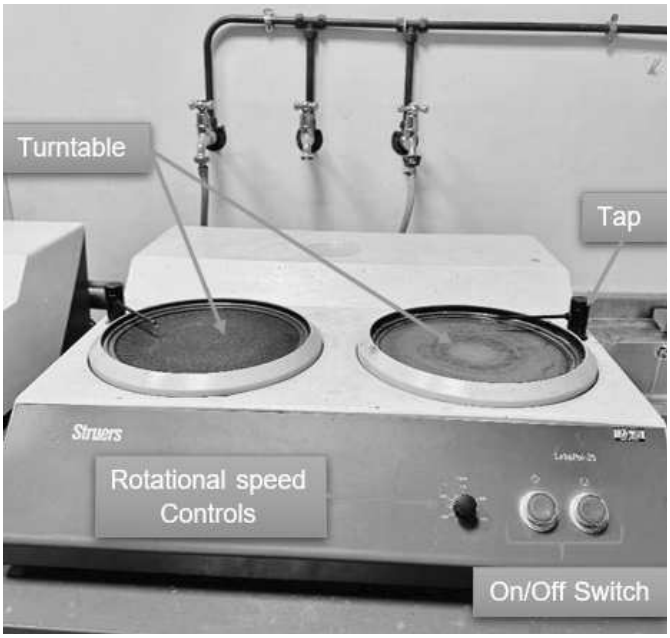


**Figure 3.6.2.1: Grinding machine.**

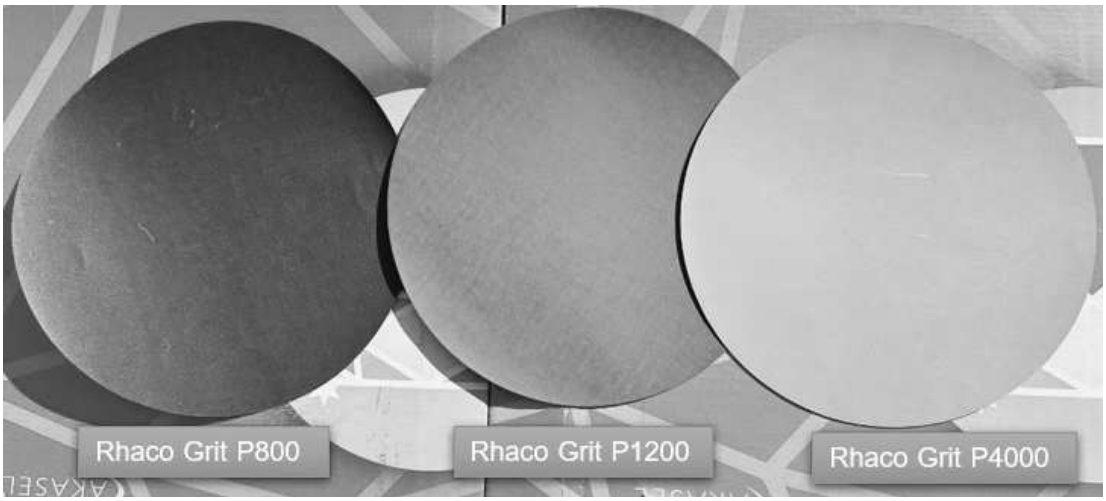


**Figure 3.6.2.2: Akasel grinding paper- Rhaco Grit discs.**

3.6.3 Struers Tegramin 25 polishing machine

The Struers Tegramin 25, shown in Figures 3.6.3.1: (a) and (b), is a polishing machine used to remove surface damage on various metals caused during the cutting processes. The Struers Tegramin 25 shown in Figure 3.6.3.1: (a) is a standard model that operates without the use of oxide polishing (OP) suspension. In contrast, the Struers Tegramin 25 shown in Figure 3.6.3.1: (b) is a model equipped for OP suspension, allowing for a more advanced polishing process. To operate the machine, the desired polishing disc is mounted on the turntable. A suitable lubricant, rotational speed and time are then selected. The polishing process is initiated by pressing the start button and continues until the selected time period has elapsed. During the polishing process, different types of polishing discs are used, depending on the material being prepared. Figures 3.6.3.2 and 3.6.3.3 illustrate the various polishing discs and the different polishing agents, respectively. The Aka-Chemal polishing disc is water-based, whereas the Aka-Daran and Aka-Napal discs require Blue Aka-Lube as a lubricant. As mentioned above, before the final polishing step, the specimen is cleaned with ethanol and dried. Figure 3.6.3.4 displays an example of a polished specimen after completion of the polishing process.


**Figure 3.6.3.1: (a) Polishing machine – no OP Suspension.**


**Figure 1: (b) Polishing machine – with OP Suspension.**

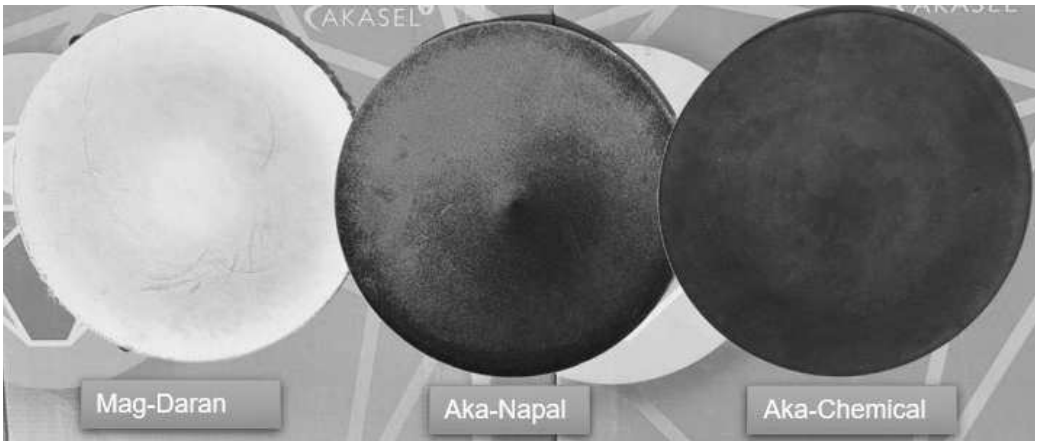


**Figure 3.6.3.2: Polishing discs.**

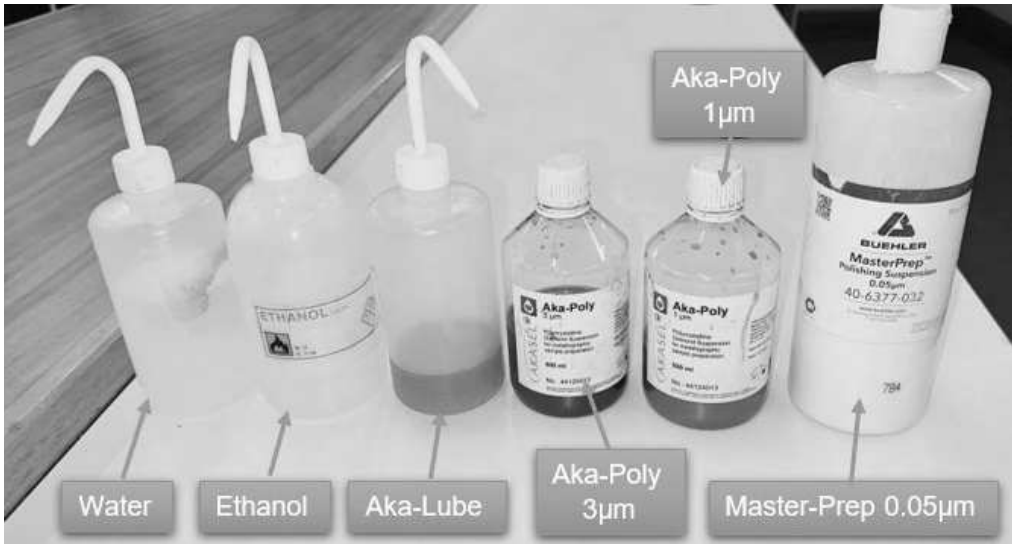


**Figure 3.6.3.3: Metallographic polishing agents.**

**Figure 3.6.3.4: Polished specimen samples.**

3.6.3.1 Using the Zeiss Stemi DV4 Stereo microscope during the polishing.

To provide quality control while polishing microstructure and hardness specimens, the use of the Zeiss Stemi DV4 Stereo microscope (see Figure 3.6.3.1.1) is crucial. The device's magnification range (8x–32x) and 3D viewing capabilities allow for a thorough examination of surface characteristics such as cracks and other deformations.

Instructions on how to use the Zeiss Stemi DV4 Stereo microscope effectively:

1. Pre-polishing inspection: Examine the specimen's initial surface for irregularities (such as scratches, pits or contamination).
2. Process monitoring: Use the microscope periodically to track polishing progress and ensure that the surface is being prepared correctly.
3. Post-polishing verification: Verify the surface is totally smooth before moving on to the hardness and microstructure analysis.

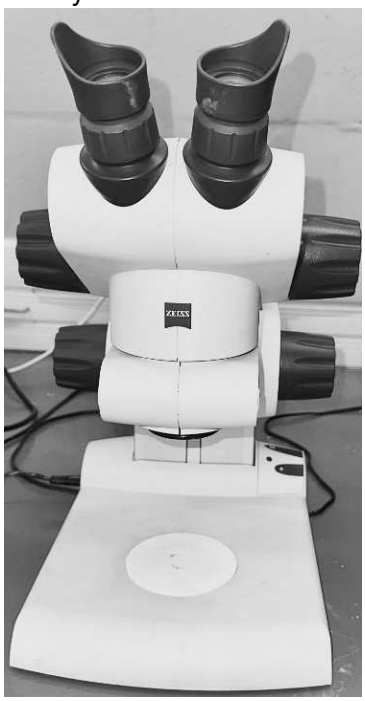


**Figure 3.6.3.1.1: Zeiss Stemi DV4 Stereo Microscope.**

3.6.3.2 Using ultrasonic cleaning during polishing

Ultrasonic cleaning during the polishing process is essential for achieving accurate hardness test results on aluminium specimens. Ultrasonic cleaning effectively removes contaminants such as oils, greases, polishing residues and fine particles, thereby ensuring optimal surface conditions. Ultrasonic cavitation, generated by high-frequency sound waves, dislodges contaminants from the most inaccessible areas without damaging the delicate specimen. Compared to manual cleaning, ultrasonic cleaning is more efficient, consistent and gentle, ultimately enhancing the reliability of the hardness test results. Figure 3.6.3.2.1 depicts an ultrasonic cleaning tank.


**Figure 3.6.3.2.1: Ultrasonic cleaning tank.**

**3.7 Etching of specimen for microstructural analysis**

To prepare the specimens for etching and subsequent microstructural analysis, the specimens were first mounted using a Struers Labopress-3 machine in section 3.6.1. The mounted specimens were then ground using a Struers Labopol-25 machine in section 3.6.2 followed by polishing using a Struers Tegramin 25 machine in section 3.6.3 to achieve a mirror finish. Before the microstructural analysis test, the specimens were first etched. Sodium hydroxide (NaOH) is the etching agent used in this study. The solutions used in NaOH etchant composition include distilled water ($H_2O$) and sodium hydroxide (NaOH). During the etching procedure, the specimen was immersed for five minutes and then immediately rinsed with distilled water. The specimen was thereafter cleaned with an ultrasonic bath, rinsed with ethanol, and then dried using a hot hairdryer. Once etched, the specimens are ready for microstructural analysis analysis. Figure 3.7. shows a fully prepared (etched) specimen. The same approach was used on all of the specimens for microstructural analysis. Tables 3.7 indicate the quantity used for NaOH etchant solution.

**Table 3.7: NaOH 2% Aq solution etchant**

| Quantity (g) | Solution |
|---|---|
| 2 g | NaOH |
| 100 g | $H_2O$ |

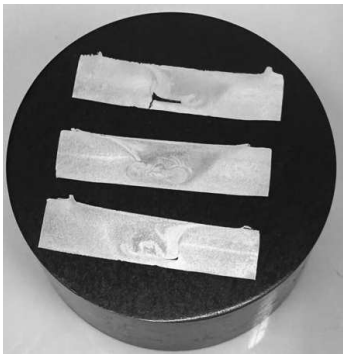

**Figure 3.7: Etched specimen samples.**

### 3.8 List of tests performed

To make a clear comparison, analysis of the FSPed and AMMCS joints (AA5083/SiC and AA5083/Coal Composites) was conducted. The following tests were run:

- Tensile tests
- Microstructural analysis
- Hardness tests
- Bending tests
- SEM analysis
- XRD tests
- Chemical composition/analysis

### 3.9 Mechanical test

The mechanical tests that were conducted are discussed in this section. To perform the test, different sets of specimens from the FSPed joints and AMMCS joints (AA5083/SiC and AA5083/Coal Composites) were cut out. The prepared specimens were subject to bending testing, tensile tests, microstructural analysis, hardness tests, XRD and chemical analysis. The start, middle and end of the plate were the three areas from which all the specimens were extracted. For each test, a total of three specimens were prepared. This method enabled a thorough study of material characteristics and behavior by constantly analyzing material properties at these exact places across all testing. Figure 3.9 represents the specimen positioning sample, where "S" denotes the start, "M" the middle, and "E" the end.

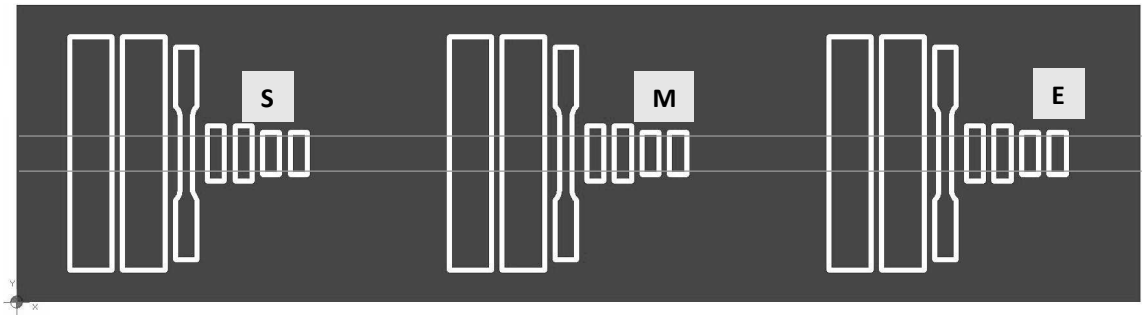


**Figure 3.9: Specimen positioning sample.**

#### 3.9.1 Tensile tests

For the tensile test, a specimen cut into the form of a dog's bone was utilised. Tensile tests were performed following ASTM E8-04 standards for metallic materials. The test was

conducted using a computer-controlled Hounsfield 25 K-type machine (see Figure 3.9.1.1). Before installing the specimens in the jaws, the tensile specimen measurements (gauge length, width and thickness) were first measured and recorded. After that, the flat clamping jaws were adjusted to fit the tensile specimen for gripping. The screws are tightened to prevent sliding or slippage while the test is being conducted. Figure 3.9.1.2: (a) depicts the flat clamping jaws used to install the tensile specimen.

The tensile test is performed on each specimen individually until the specimen breaks (see Figure 3.9.1.2: (b)). Horizon software is then used to log the data of the applied tensile load (N) and extension (mm). After the test is completed, the software's results are exported from the computer and analysed to determine the tensile properties, including yield strength, ultimate tensile strength, percentage elongation, engineering stress and engineering strain. The graph of stress vs strain is created using the determined data and the results are discussed in Chapter Four that follows. The tensile test parameters are listed in Table 3.9.1.

**Table 3.9.1: Tensile test parameters.**

| Speed (mm/min) | Extension range (mm) | Load range (kN) | Load cell (kN) |
|---|---|---|---|
| 3 | 0-15 | 0-10 | 25 |


**Figure 3.9.1.1: Hounsfield tensile test machine.**

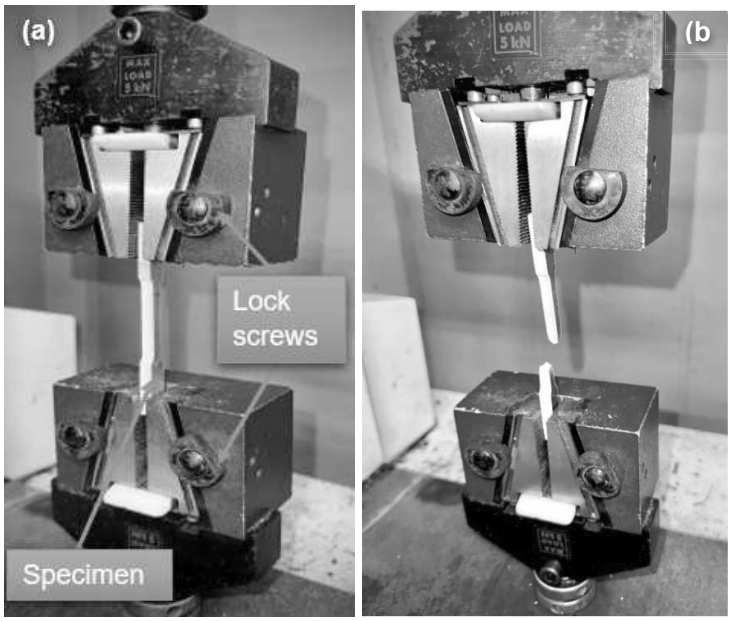


**Figure 3.9.1.2: (a) Tensile testing flat clamping jaws; (b) Completed tensile testing on the specimen.**

The ultimate tensile stress was calculated using the following formula:

$$\sigma = \frac{F}{A} \quad (4)$$

Where F is the maximum force, A is the cross-sectional area, and $\sigma$ is the ultimate tensile stress.

The following equation was used to determine percentage elongation:

$$\%\ Elongation = \frac{Final\ lenth - Original\ length}{Original\ length} \quad (5)$$

For a sample of calculations using these equations, refer to Appendix G.

3.9.2 Bending tests

A bending test, also known as flex or flexural testing, was conducted to measure the flexural strength of each joint on the bending specimen. The Hounsfield testing machine with a 3-point bend fixture was used to perform the bending test. A rectangular-shaped specimen was used for the bending test. One specimen was used for the face test (the side of the plate that was processed), while the other specimen was used for the root test (the side of the plate underneath the welded side) as shown in Figure 3.9.2.1. Before the bending test, the specimen was measured to confirm its dimensions. The specimen was then flat mounted against the rolling supports and a centre mark line was put on the joint's centre to ensure alignment with the exact centre of the loading pin as seen in Figure 3.9.2.2. The loading pin was lowered until it made contact with the top surface of the specimen. The ASTM E290 standard incorporated into the Horizon software program was chosen and it provided a screen upon which the specimen dimensions were entered. After that, the machine was zeroed before the test started. The test was carried out up until the specimen was broken or fractured and the data was automatically logged from the start until the specimen failed.

Chapter Four presents the findings from the obtained data that were utilised to determine the material's maximum stress at the moment of failure of all joints. The parameters for the bending test were the same as those for the tensile test (see Table 3.9.1 above), and data were recorded using the same method as for tensile testing. Each specimen was indivually subjected to the test. Figure 3.9.2.3 provide the schematic diagram for the bending test.

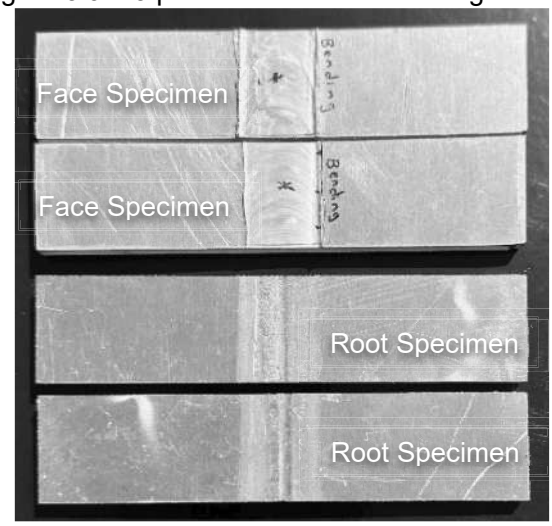


**Figure 3.9.2.1: Sample of bending specimen.**

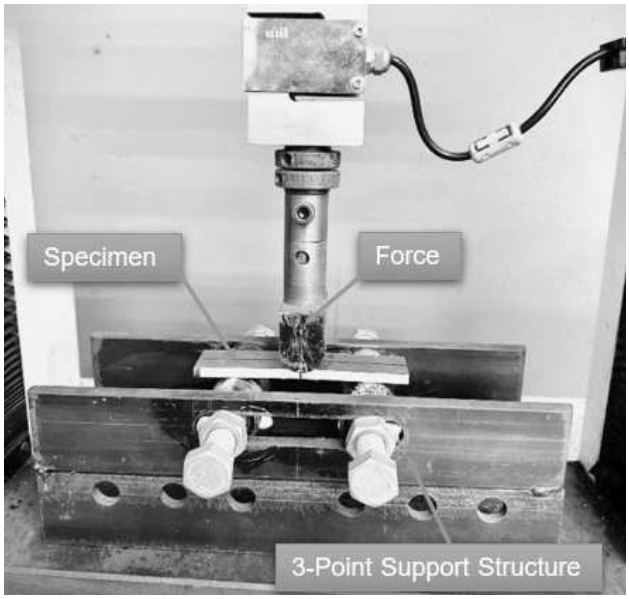


**Figure 3.9.2.2: Bending test setup with specimen alignment.**

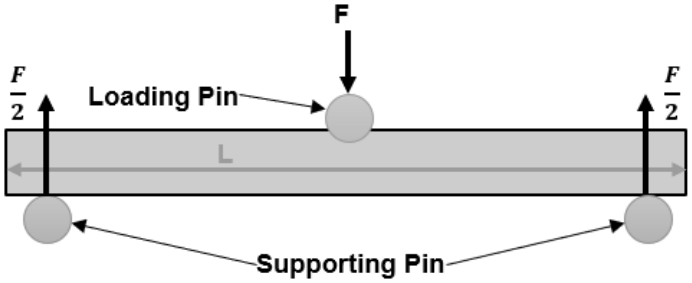


**Figure 3.9.2.3: Schematic diagram of a bending test.**

The following formula was used to calculate the maximum stress:

$$\sigma = \frac{3FL}{2bd^2} \quad (6)$$

Where F is the applied force, b is the specimen's width, L is its length, and d is its thickness. For a sample of calculations using these equations, refer to Appendix G.

3.9.3 Microstructural analysis

Microstructure analysis was conducted to analyse the grain sizes of the produced joints using a microscope. The Motic AE2000 metallurgical microscope (see Figure 3.9.3) facilitated the obtaining of the microstructural images for analysis. After placing the specimen on the specimen bed, the Moticam software was opened to begin the process of obtaining the required microstructure grain images. The specimen's image was then focussed using the zoom-in and out control switch. The software's scale was then set to 100 µm and the objective indication or stamp was to be visible on the image for further analysis. The preferred image was selected using different magnifications, including 5×,10×, 20×, 50× and 100×. The 5× magnification was utilised for larger imaging to show the different microstructural zones desired. It should be noted that the larger the objective size, the greater the zoomed-in imagery provided. Once the desired images were obtained, they were transferred to a memory stick from the desktop folder created by the software that records each image as it is taken. ImageJ software was then used to determine the average grain sizes and grain distribution curves according to the ASTM E112-13 standard for the linear intercept method.

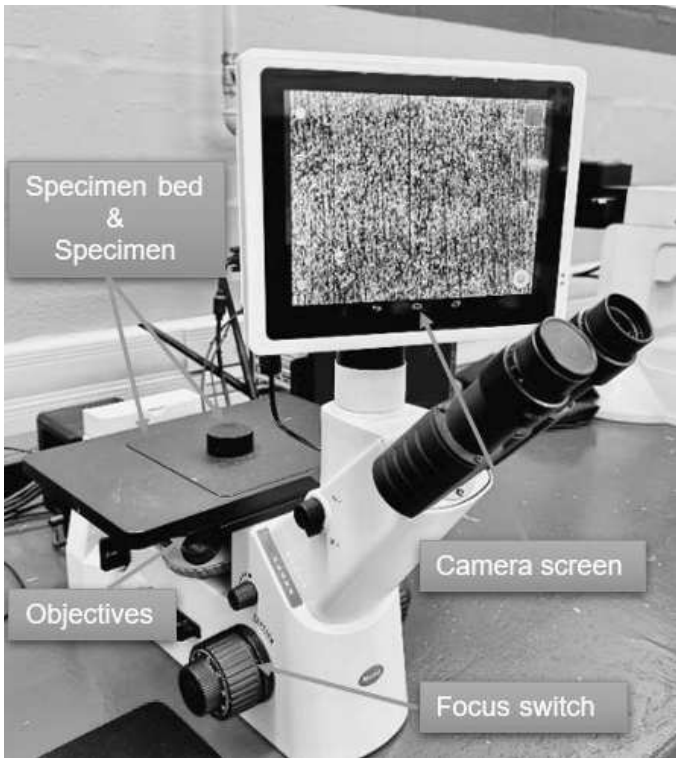


**Figure 3.9.3: Microstructure analysis apparatus.**

3.9.4 Hardness test

The Innova Test Falcon 500 hardness testing machine was used to carry out the hardness tests to estimate the Vicker's hardness of the produced joints (see Figure 3.9.4). The ASTM E384-11 standard was followed when conducting the hardness tests. For this purpose, the machine was first set in an appropriate condition for starting the tests. For specimen focussing during setup, the 10× and 20× objectives were used. A load of 0.5 kg and a space of 1 mm were applied from the centre of the specimen to each side (either advancing or retreating). The falcon IMPRESSIONS software program was opened on the screen before the hardness test was started and the specimen was placed in the middle of the machine bed. The specimen was then focused using the objectives and a test pattern was selected. Next the number of points (indents) in each line, the distance between the points and the distance between the lines were all set. A 3-line pattern was employed for this study, with the distance between the lines being 2 mm and that between the points being 1mm. Next the auto-focusing button was activated and the software program automatically snapped a photograph of the specimens – the process resumed when the start button was selected. At the end of the test, the obtained Vicker's hardness data was generated into a PDF document and saved to the memory stick and desktop folder. The generated data was used to produce the graphs displayed in the Chapter Four. The snapshots of the specimens were also used later for macrostructural analysis.

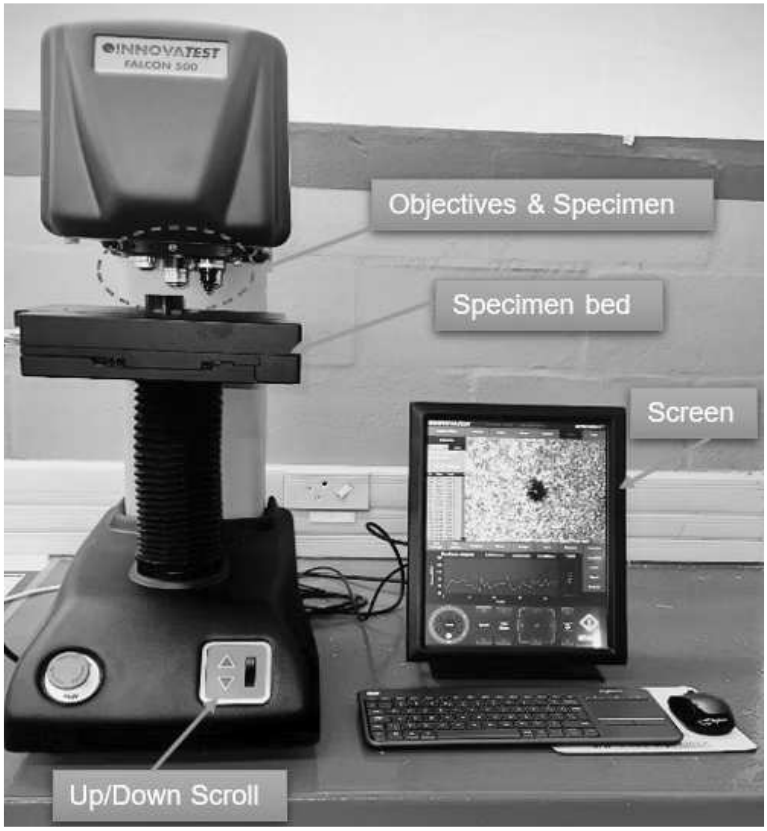


**Figure 3.9.4: Hardness testing machine.**

3.9.5 Chemical analysis

A spectrometer, like the Belec Compact Spectrometer HLC, is a device used to identify the elements present in a material and determine their concentrations. It operates on the principle of emission spectroscopy. To determine the elemental composition of the fabricated joints, chemical analysis was conducted using a Belec Compact Spectrometer HLC (Figure 3.9.5). Before analysis, the spectrometer was prepared by turning on the machine and initiating a purge with high-purity argon gas. Specimens were positioned on a flat surface and introduced to the spectrometer. The Belec WIN 21 software was activated to initiate the aluminium analysis, requiring specific sample details. The setup process continued when the spark button and then the machine's screen display was switched on and the Belec WIN 21 software located on the desktop of the machine's built-in computer subsequently activated. After the program was opened, the option for the aluminium test was selected, and all the correct details regarding the specimen being tested were entered. When the procedure was ready to be carried out, it was conducted by pressing the Belec probe's face on the specimen with sufficient pressure to prevent air from penetrating between the probe and the specimen. When the start button on the probe was pressed, the probe sparked on the workpiece for a few seconds. The probe was kept in position until the yellow indicator on the screen flashed to show that the measurement was complete. The yellow flashing was accompanied by the findings being displayed in table form on the computer screen. The memory disk was used to store the projected results table.

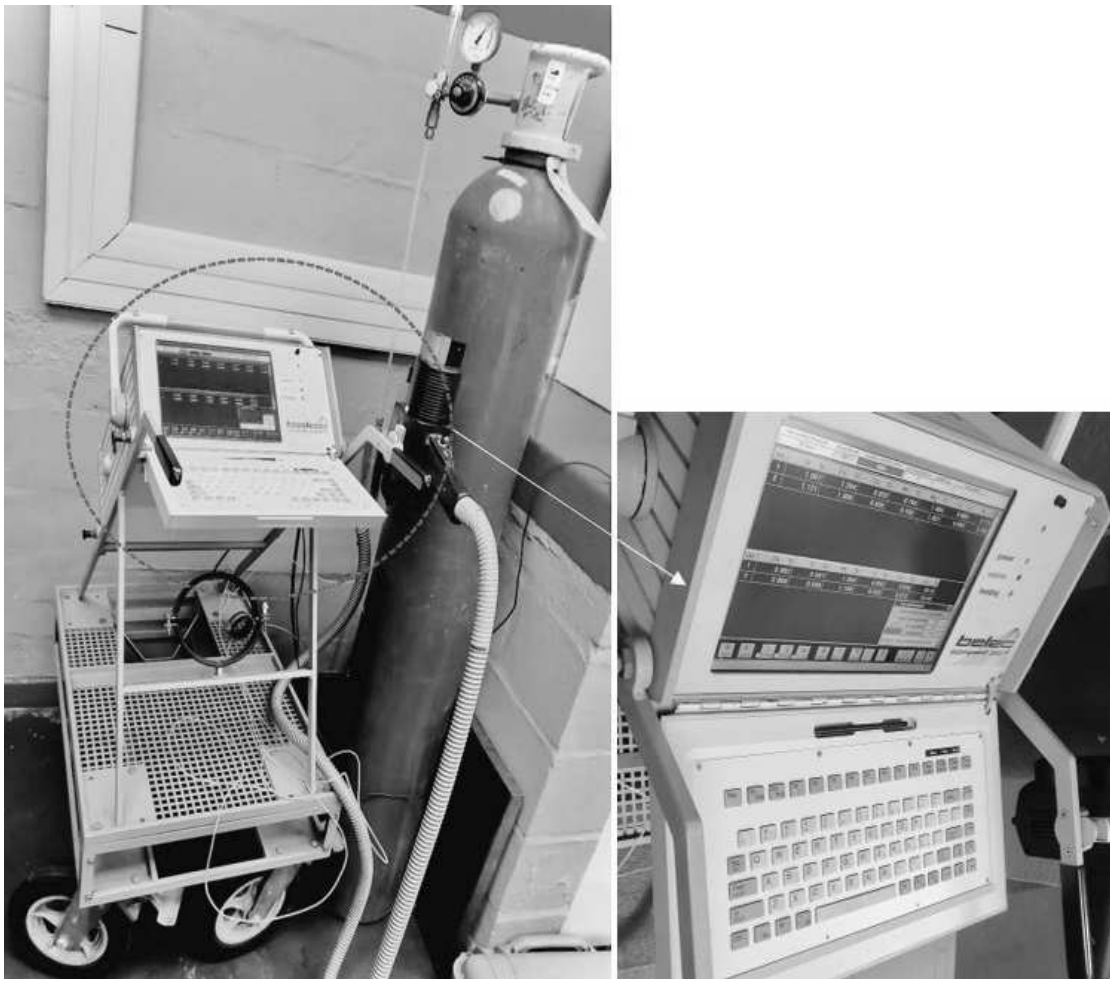

**Figure 3.9.5: Belec compact spectrometer machine.**

3.9.6 SEM

SEM (scanning electron microscope) is a method to examine specimen topographies at incredibly high magnifications (Figure 3.9.6). SEM inspection is often used to examine die/package cracks and fracture surfaces, bond failures and physical detects on the die or package surface. In this study, SEM analysis was conducted on post-tensile test specimens to investigate fracture surfaces and identify potential failure mechanisms**.** The SEM technique utilises a focused electron beam to generate high-resolution images of sample topographies. To facilitate analysis, specimens were prepared and mounted on the sample holder, that must be electrically coupled to avoid the electron beam from "charging" the sample and distorting the image using a conductive tape. The resulting images provided valuable insights into the fracture behaviour of the materials, as detailed in subsequent sections. The results of each test that was performed are presented in the sections that follow. It is should be noted that the SEM machine was outsourced.


**Figure 3.9.6: Scanning electron machine.**

3.9.7 XRD analysis

XRD analysis was conducted using a Bruker D8-Advance diffractometer (Figure 3.9.7). The instrument employed a Cu-Kα radiation source and a continuous θ-θ scan mode. Sample preparation involved mounting the specimen on a glass slide and levelling it to the appropriate height before analysis. Data acquisition utilised a Lyn-Eye detector with a step size of 0.034° within the user-defined range of 2θ and a scan speed of 0.5 seconds per step that is equivalent to a scintillation counter's effective time of 92 seconds per step. Background subtraction was applied to the diffraction patterns to enhance peak visibility. Phase identification was performed by comparing the experimental data to a reference database. Potential phases were determined through peak matching, considering the instrument's resolution limitations. (It is important to remember that the XRD machine was outsourced.)

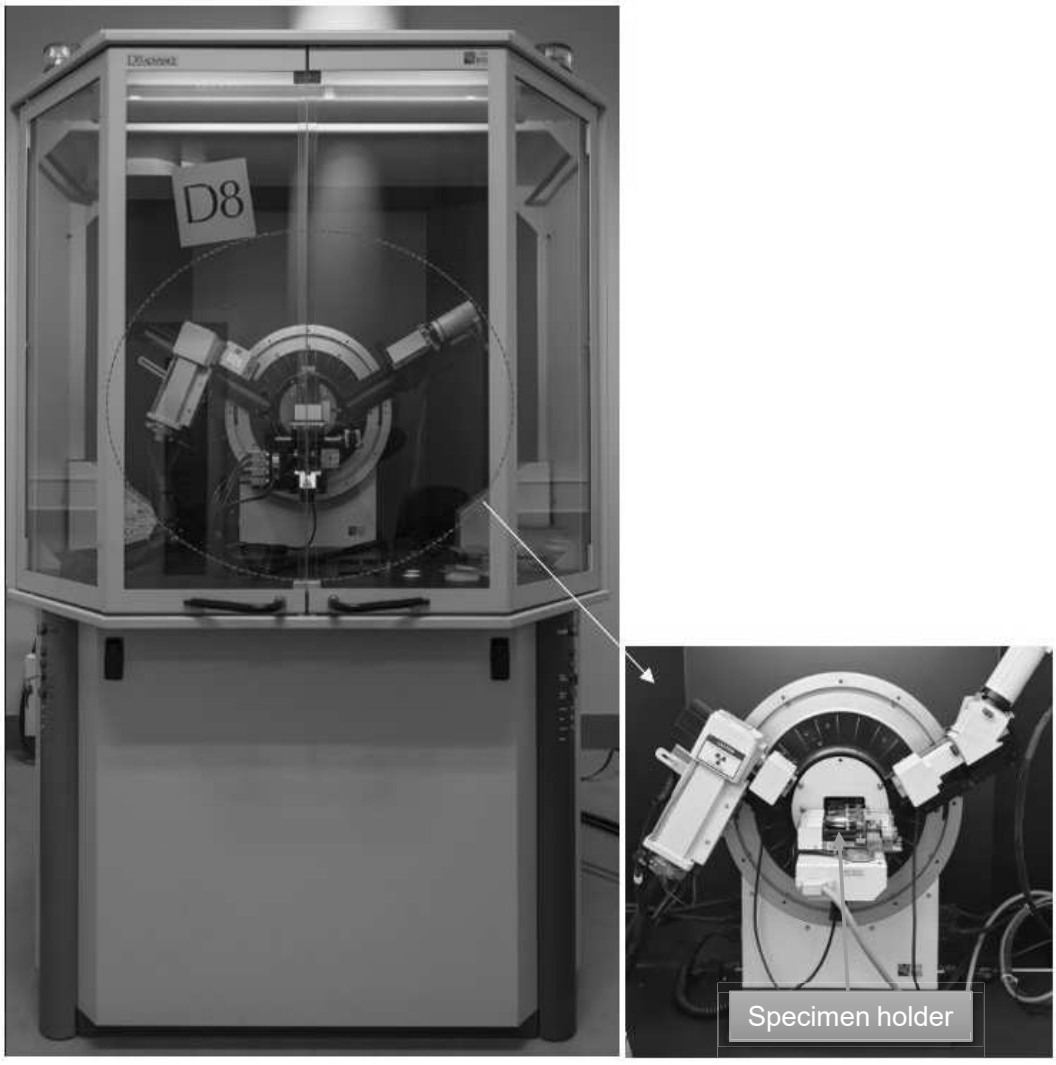


**Figure 3.9.7: Bruker AXS D8-Advance diffractometer.**

# CHAPTER FOUR

# RESULTS AND DISCUSSION

This chapter provides a detailed explanation of the results and findings from all of the experiments conducted in the previous chapter. Data was collected for scanning electron microscopy (SEM), tensile testing, hardness testing, bending testing, chemical analysis, macrostructure, microstructure and X-ray diffraction (XRD). The obtained data from AA5083/SiC composite joints and data obtained from AA5083/Coal composite joints was then compared. The AA5083 data provided a point of reference to help make the research activities more understandable.

## 4.1 AA5083-H111 base material

This section presents the detailed results and discussions concerning the AA5083-H111 base material.

### 4.1.1 X-ray diffraction analysis and chemical analysis of the joints

In mechanical engineering, XRD analysis is essential since it provides a variety of approaches for investigating and understanding material characterisation. X-ray methods offer crucial information that supports the development, testing and quality control of mechanical systems and components, whether used to determine phase compositions, verify material purity or examine internal structures. The base material AA5083-H111 (shown in Figure 4.1.1) was examined to identify newly generated phases during the fabrication of the aluminium metal matrix composite. The XRD pattern reveals four phases present in the base alloy AA5083-H111, namely the Al-metallic phase, $Al_6Mn$, AlMnFe intermetallic phase and $Al_3Mg_2$ phase.

The Al-metallic Phase is a prominent peak at approximately 38.5° 2-theta, corresponding to the diffraction from the (111) planes of the aluminium metal lattice. This peak's intensity indicates that aluminium is the primary constituent of the AA5083-H111 alloy [256-257]. The presence of additional peaks at around 44° and 50° 2-theta suggests the existence of $Al_6Mn$ and AlMnFe intermetallic phases, respectively. These phases often form during the solidification and heat treatment processes and contribute to the alloy's mechanical properties [257]. The $Al_6Mn$ and AlMnFe intermetallic phases play a significant role in the mechanical properties and corrosion resistance of AA5083 aluminium alloy. These phases can act as strengthening agents, enhancing the alloy's hardness and yield strength. However, they can also contribute to localised corrosion, particularly in aggressive environments. Recent research by Wang et al. [258] has highlighted the influence of these phases on the corrosion resistance of the alloy. A thorough understanding the formation, distribution and electrochemical behaviour of these intermetallic phases is essential for optimising the performance of AA5083 in various applications.

The $Al_3Mg_2$ phase is a very weak peak around 42° 2-theta, that is typically present in low concentrations in AA5083 and has a limited impact on the overall properties. The $Al_3Mg_2$ phase, also known as the β-phase, is a key factor in the susceptibility of AA5083 aluminium alloy to intergranular corrosion (IGC) and stress corrosion cracking (SCC) [257-258]. Magnesium (Mg) atoms diffuse to grain boundaries during heat treatment or exposure to elevated temperatures, forming $Al_3Mg_2$ precipitates. These precipitates act as anodic sites, leading to galvanic corrosion and localised attack at the grain boundaries. In the presence of tensile stress and a corrosive environment, these precipitates can further accelerate crack

initiation and propagation, resulting in IGC and SCC [258-259]. Appropriate heat treatment, careful alloy composition control and protective coatings or corrosion inhibitors are essential to mitigate these issues.

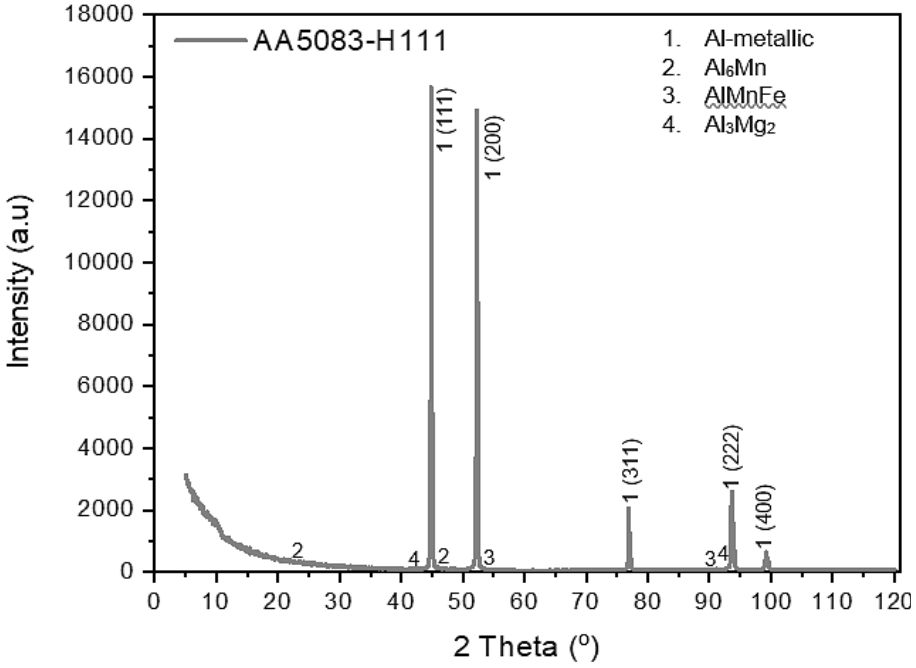


**Figure 4.1.1: Base materials XRD patterns: AA5083-H111.**

**Table 4.1.1: Chemical composition of the base material (wt %).**

| BM | Cu | Cr | Fe | Mg | Mn | Si | Ti | Zn | Al |
|---|---|---|---|---|---|---|---|---|---|
| AA5083-H111 | 0.010 | 0.040 | 0.153 | 4.339 | 0.649 | 0.139 | 0.011 | 0.013 | Bal |

4.1.2 Macrostructural analysis

Macrographs, that provide crucial data to enable in-depth microstructural research, are essential in the fields of material science and engineering. In metallurgy, macrographs are used to study the grain structure, welds and surface conditions of metals and alloys. Macrographs exhibit large-scale imperfections such as inclusions, voids, defects or cracks that might affect the material's performance during welding or other production processes. The macrograph of the AA5083-H111 is shown in Figure 4.1.2 and reveals a defect-free microstructure in the base material, free of voids or cracks.

**Figure 4.1.2: Macrograph: AA5083-H111.**

4.1.3 Microstructural analysis

Optical microstructure analysis is a vital method to provide a thorough understanding of the internal structure of materials. This information is essential for identifying phases, improving material performance, analysing failures (defect detection) and understanding material properties through the usage of grain size and shape. Figure 4.1.3.1 displays the optical micrographs of the AA5083-H111 base material, revealing a relatively uniform distribution of equiaxed. The measured grain sizes and their standard deviation are tabulated in Table 4.1.3, with the grain size distribution displayed in Figure 4.1.3.2. The AA5083 base material exhibited a mean grain size of 61.292 μm with a standard deviation of 10.8674 μm, ranging from a minimum of 36.061 μm to a maximum of 79.714 μm.

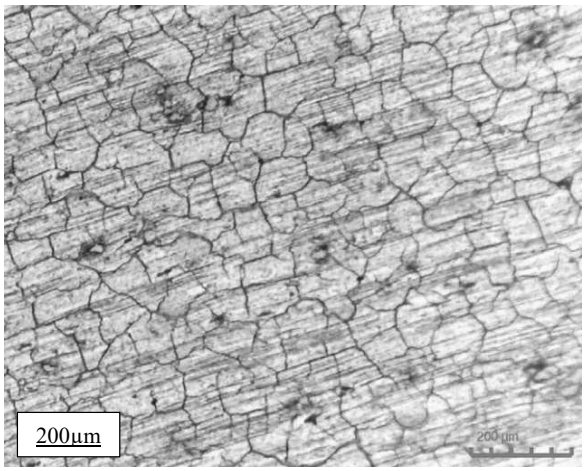


**Figure 4.1.3.1: Optical micrographs 20× 200μm: AA5083-H11 base material.**

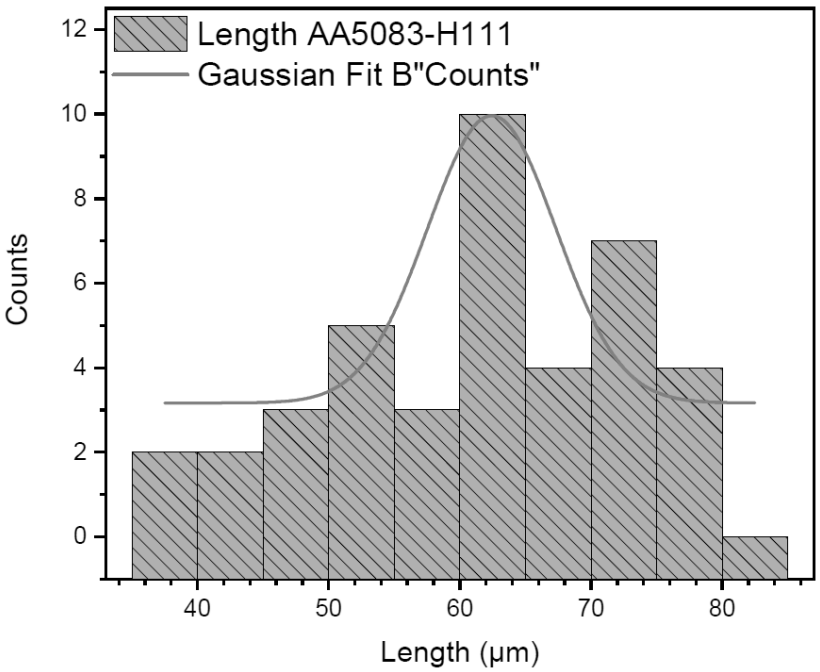


**Figure 4.1.3.2: Grain distribution graphs: AA5083-H111 base material.**

**Table 4.1.3: Grain sizes and standard deviations.**

| Type | Mean grain size µm | Minimum grain size µm | Maximum grain size µm | Standard deviation µm |
|---|---|---|---|---|
| **Base material** | | | | |
| AA5083-H111 | 61.292 | 36.061 | 79.419 | 10.86784 |

4.1.4 Flexural / Bending tests

Bending experiments are crucial to fully understand the mechanical properties of materials under flexural stresses and ensuring that materials function reliably during the intended applications. The post-flexure test specimen and the associated flexural strength and strain for the AA5083-H111 base material are displayed in Figures 4.1.4.1 and 4.1.4.2. The specimen was observed to be fracture-free following a maximum deflection. The AA5083-H111 base material showed a maximum ultimate flexural strength (UFS) of 415.2014 MPa at a flexural strain rate of 26.8235%. The maximum flexural strain (MFS) rate obtained at the fracture point was 29.4118%. Table 4.1.4 shows these flexural properties.

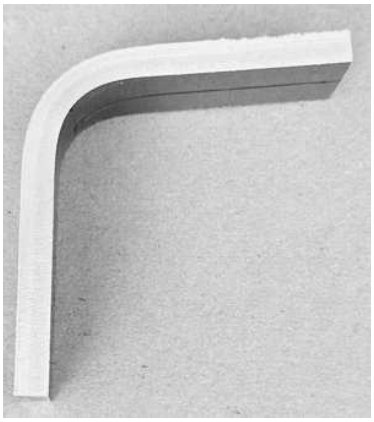

**Figure 4.1.4.1: Post-flexural test specimen: AA5083-H111.**

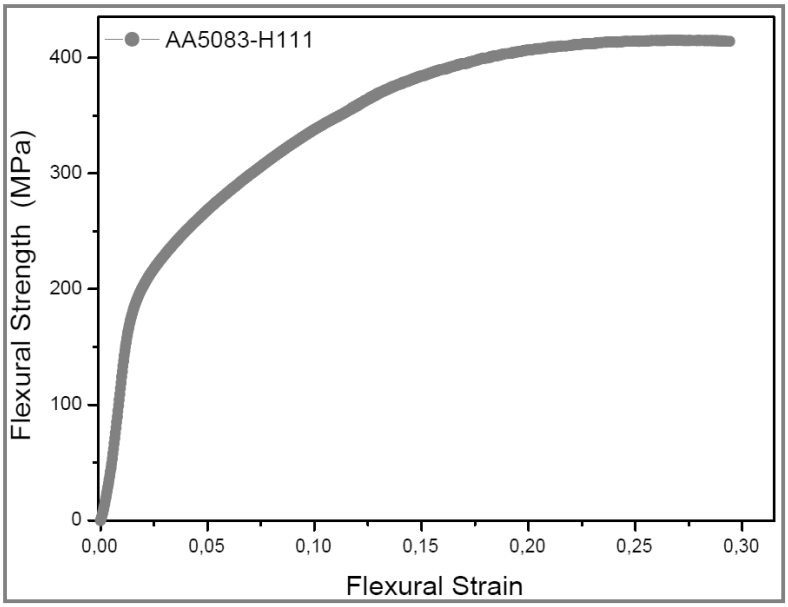


**Figure 4.1.4.2: Flexural strength – strain curve: AA5083-H111.**

**Table 4.1.4: Bending properties of the base material.**

| Type | Ultimate Force (N) | Ultimate Flexural Strength (MPa) | Flexural Strain (%) | Modulus (MPa) |
|---|---|---|---|---|
| **Base material** | | | | |
| AA5083-H111 | 3517 | 415.2014 | 0.268235 | 38600 |

4.1.5 Tensile tests

An essential technique for determining the mechanical properties of materials is tensile testing. Material selection, quality control, research and failure analysis offer full information on a material's strength, ductility and elasticity by applying a controlled tensile force. Users' understanding of these properties ensures that components and materials will function reliably when employed for their intended purposes. Figures 4.1.5.1 and 4.1.5.2 illustrate the post-tensile specimen and tensile stress-strain curve, respectively, of the AA5083 base material. Table 4.1.5 shows the tensile properties. The AA5083 base material had an ultimate tensile strength (UTS) of 311 MPa at a corresponding tensile strain rate of 58.65% and a yield strength of 248.8 MPa. The maximum strain rate at the fracture point was 62.46%.

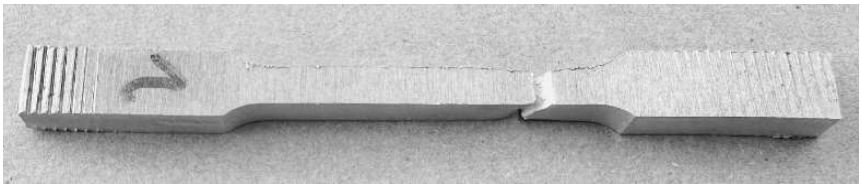

**Figure 4.1.5.1: AA5083-H111 base material: post-tensile specimens.**

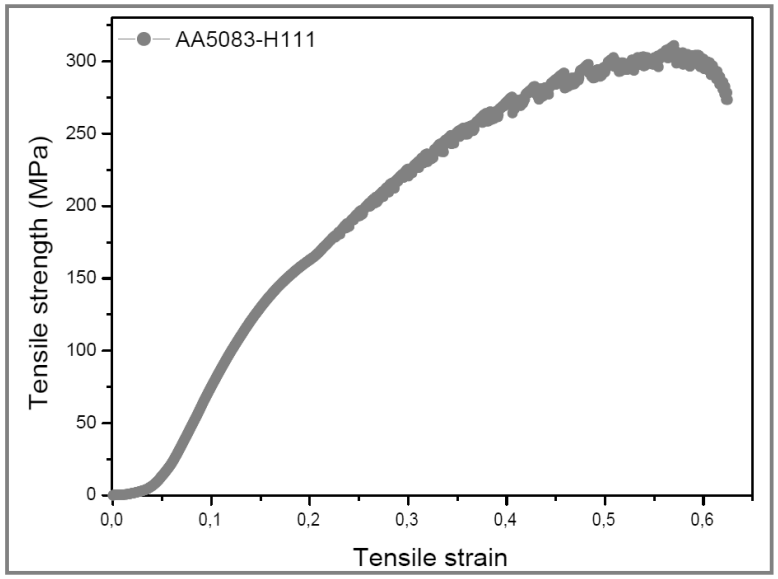


**Figure 4.1.5.2: AA5083-H11 base material: Tensile Stress-Strain curve.**

**Table 4.1.5: Tensile properties of the base material.**

| Type | Ultimate Break Force (N) | Ultimate Tensile Strength (MPa) | Yield strength (MPa) @ 0.2% offset | Strain rate(%) | Fracture location |
|---|---|---|---|---|---|
| **Base material** | | | | | |
| AA5083-H111 | 11200 | 311 | 248.8 | 58.65 | N/A |

4.1.6 Fracture surface analysis

The study of a material's surface that has broken due to tensile testing is known as fracture surface analysis. This investigation contributes to an understanding of the material's properties, overall performance under tensile stresses and failure methods. Information on the ductility, brittleness and nature of the applied stresses of the material may be obtained by examining the fracture surface. Figure 4.1.6 shows the fracture surface morphology of the AA5083-H111 base material. The fractured surfaces displayed a dominant ductile failure mechanism. The ductile fracture was evident from dimples of various sizes (demonstrated with a sample red arrow), microvoids (demonstrated with a sample yellow arrow) and cleavage facets (demonstrated with a sample blue arrow). Similarly, previous studies [260-262] have reported ductile fracture behaviour characterised by dimples, voids and cleavage facets.

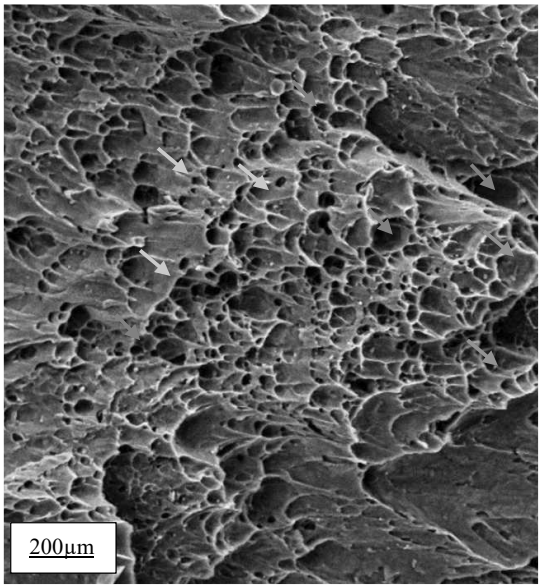


**Figure 4.1.6: Fracture surface morphologies, AA5083 base material.**

4.1.6.1 Energy Dispersive X-ray Spectroscopy (EDS) Analysis

Energy Dispersive X-ray Spectroscopy (EDS) was employed to analyze the elemental composition of the AA5083-H111 base material, particularly focusing on the distribution of elements within the fracture surfaces. Figure 4.1.6.1 shows the EDS spectrum and elemental mapping of the AA5083-H111 fractured surface. The EDS analysis of the fracture surface, as shown in Figure 4.1.6.1, confirms the presence of the primary alloying elements in AA5083-H111, including aluminum (Al) and magnesium (Mg). The relatively uniform distribution of these elements, as indicated by the elemental mapping, suggests a homogeneous microstructure in the base material. Combined with the XRD results in section 4.1.1, the EDS analysis supports the phase identification, where Al-metallic, $Al_6Mn$, AlMnFe, and $Al_3Mg_2$ phases were detected. The ductile fracture surface morphology observed in SEM images (Figure 4.1.6) is consistent with the EDS results, which show no evidence of significant inclusions or secondary phases that would promote brittle fracture.


**Figure 4.1.6.1: Energy Dispersive X-ray Spectroscopy, AA5083 base material.**

4.1.7 Hardness tests

Vickers microhardness is a form of hardness testing used for small samples, thin materials and regions inside a material that require an accurate hardness measurement. The Vickers hardness (HV) test method provides an in-depth examination of microstructural characteristics with a reduced load. This method is useful in determining surface treatments, understanding microstructural properties and guaranteeing the effectiveness and quality of materials in various applications. The Vickers hardness profiles for the AA5083-H111 base material are depicted in Figure 4.1.7. The AA5083-H111 base material exhibited a maximum hardness of 90.57 HV. General fluctuations in hardness measurements were observed within the BM.

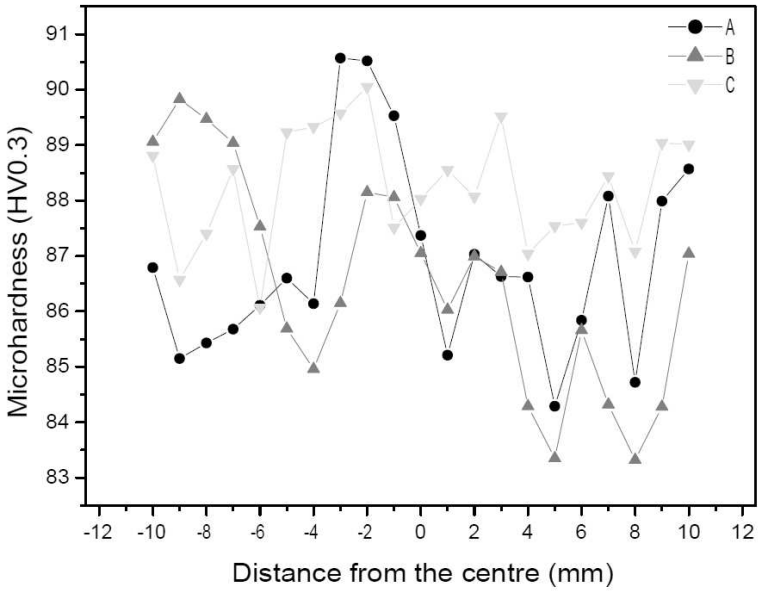


**Figure 4.1.7: Hardness profiles: AA5083 base material.**

It is important to ensure the reliability and accuracy of the hardness measurements. During the Vickers microhardness testing, tests were conducted at various locations across three different samples of the AA5083-H111 base material. These samples are designated as 'A,' 'B,' and 'C' in Figure 4.1.7. This approach provides insight into the consistency of hardness throughout the base material and highlights any potential microstructural inhomogeneities that might influence hardness values.

## 4.2 Comparative study of the AA5083/SiC and AA5083/ Coal composites

This section provides detailed results and discussions of the AA5083/SiC composites and AA5083/Coal composites, focusing on the joints' start, middle and end positions.

### 4.2.1 X-ray diffraction analysis and chemical analysis of the joints

The phases formed during the fabrication of the aluminium metal matrix composite were examined in this section using X-ray diffraction analysis. Table 4.2.1 displays the corresponding chemical compositions, while the XRD patterns for the joints of AA5083/SiC composites and AA5083/Coal composites are displayed in Figures 4.2.1.1 and 4.2.1.2. The XRD pattern reveals a complex phase composition in the AA5083/SiC composite. The primary phase noted was aluminium, evidenced by the strong peaks. Several intermetallic compounds, including $Al_3Si$, $Al_2O_3$, $Al_6(MnFe)$ and $Mg_2Si$, are also present. These compounds likely formed due to the alloying elements in AA5083 and processing conditions. While SiC is identified, it is challenging to determine its specific phase (α-SiC or β-SiC) from this pattern alone. The significant background noise may be attributed to amorphous phases or residual stresses. Aluminium oxide ($Al_2O_3$) is formed during processing due to the exposure of the material to air. $Al_2O_3$ is a ceramic material with exceptional properties that can significantly enhance the performance of AA5083 aluminium alloy composites [263-264]. When dispersed within the aluminium matrix, $Al_2O_3$ particles act as reinforcements that increase hardness and wear resistance. Its excellent thermal conductivity also improves heat dissipation, while its protective oxide layer enhances corrosion resistance [263].

The $Al_3Si$ and $Mg_2Si$ phases are referred to as the intermetallic compounds or phases. The $Al_3Si$ compound is present probably due to the addition of silicon carbide during processing. The presence of $Al_3Si$ can both strengthen the material by hindering dislocation movement and refine the grain structure, but excessive amounts of this compound can lead to embrittlement and hot shortness [265]. The overall impact of $Al_3Si$ on the composite's properties depends on factors such as volume fraction, particle size, distribution and processing conditions. $Mg_2Si$ is an intermetallic compound that plays a crucial role in the microstructure and mechanical properties of AA5083 alloys. It acts as a grain refiner, promoting finer grain formation during solidification and improving strength and toughness [265-266]. Additionally, $Mg_2Si$ can dissolve into the aluminium matrix, forming a solid solution that enhances strength and hardness. It can precipitate from the solid solution during heat treatment, further increasing strength through precipitation hardening.

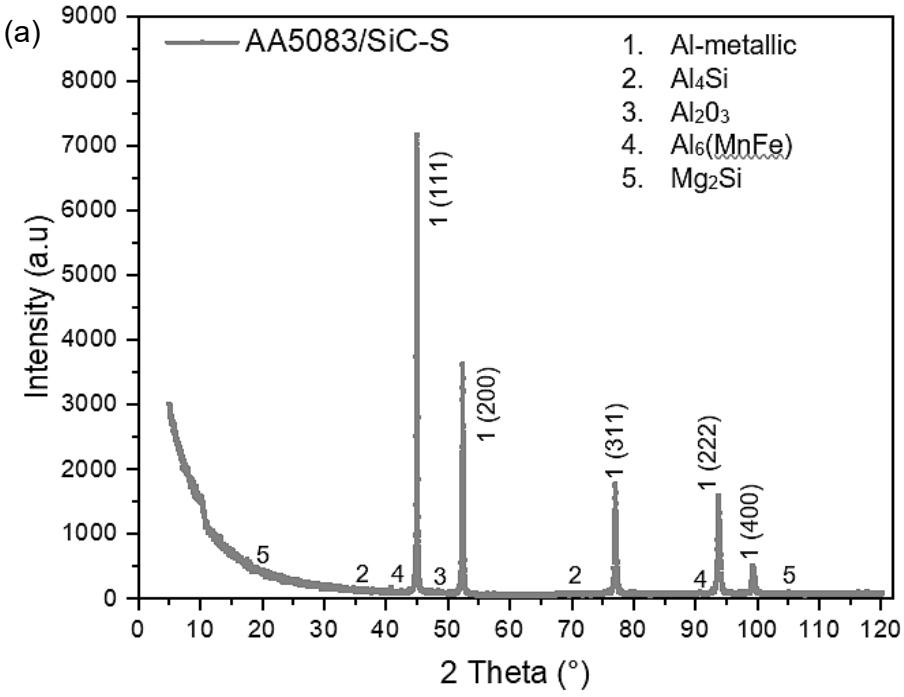
(a)
AA5083/SiC-S
1. Al-metallic
2. Al4Si
3. Al2O3
4. Al6(MnFe)
5. Mg2Si
Intensity (a.u)
2 Theta (°)
1 (111)
1 (200)
1 (311)
1 (222)
1 (400)

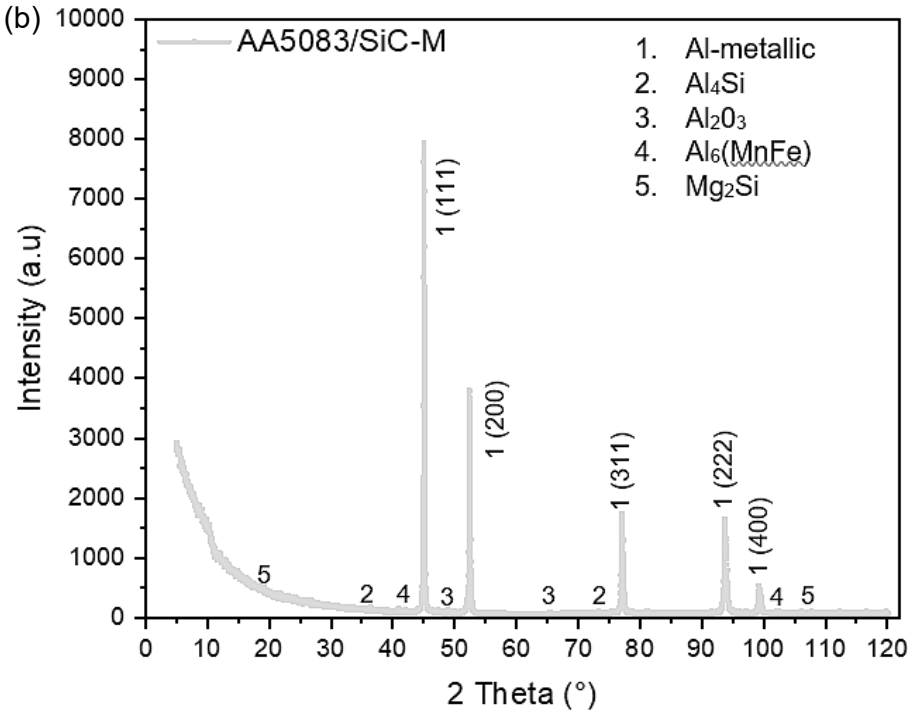
(b)
AA5083/SiC-M
1. Al-metallic
2. Al4Si
3. Al2O3
4. Al6(MnFe)
5. Mg2Si
Intensity (a.u)
2 Theta (°)
1 (111)
1 (200)
1 (311)
1 (222)
1 (400)

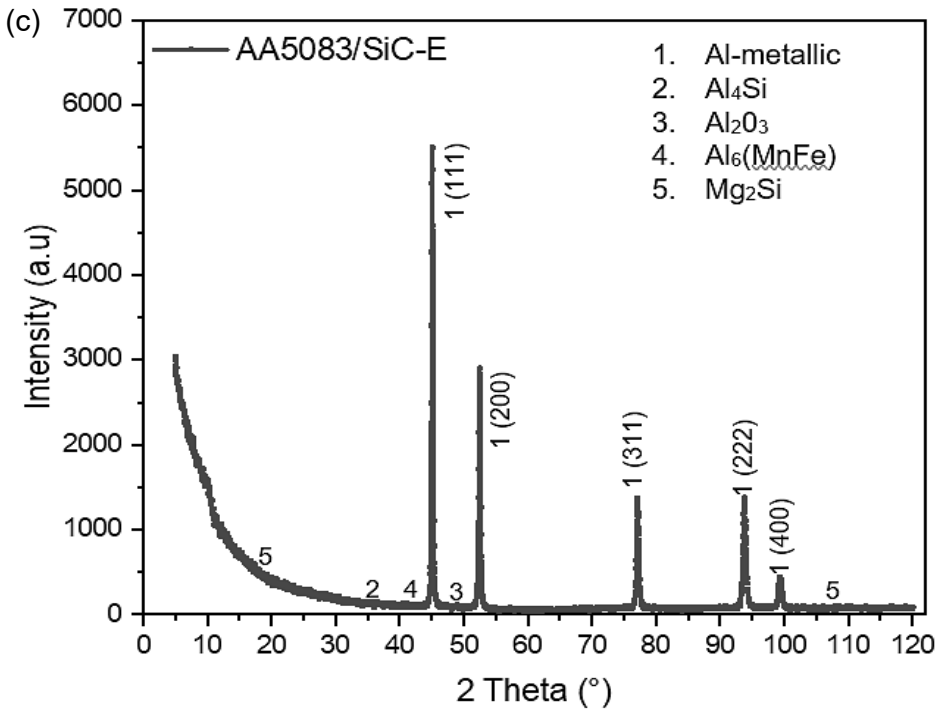


**Figure 4.2.1.1: AA5083/SiC composites joints XRD- Analysis: (a) Start, (b) Middle, (c) End.**

Figure 4.2.1.2 presents the XRD pattern of the AA5083/Coal joints. The prominent peak around 40° 2-theta corresponds to the metallic aluminium phase, i.e., the base material. The presence of aluminium carbide ($Al_4C_3$) is indicated by the peak at 39° 2-theta, suggesting a reaction between aluminium and carbon during the fabrication of the composite. $Al_4C_3$ is a compound known for its hardness and thermal stability. It contributes to improved wear resistance and can be used as an abrasive in cutting tools. Additionally, $Al_4C_3$ reacts with water to produce methane gas, a property that can be utilised in certain applications. Its incorporation into metal matrices as a reinforcement can enhance the mechanical properties of composite materials [267]. A weak peak around 42° 2-theta might indicate the presence of $Al_3Sc$, although its intensity is low. $Al_3Sc$ is an intermetallic compound composed of aluminum (Al) and scandium (Sc) responsible for significantly increasing the strength and thermal stability of aluminum alloys [268]. The broad peak at lower angles (20°-30°) 2-theta) is characteristic of amorphous carbon, highlighting the incorporation of carbon from the coal into the microstructure. Additionally, a peak around 45° 2-theta might correspond to $Mg_2Al_3$, an intermetallic compound present in the AA5083 alloy. $Mg_2Al_3$, or magnesium aluminide, is a complex intermetallic compound with a unique crystal structure.

(a)

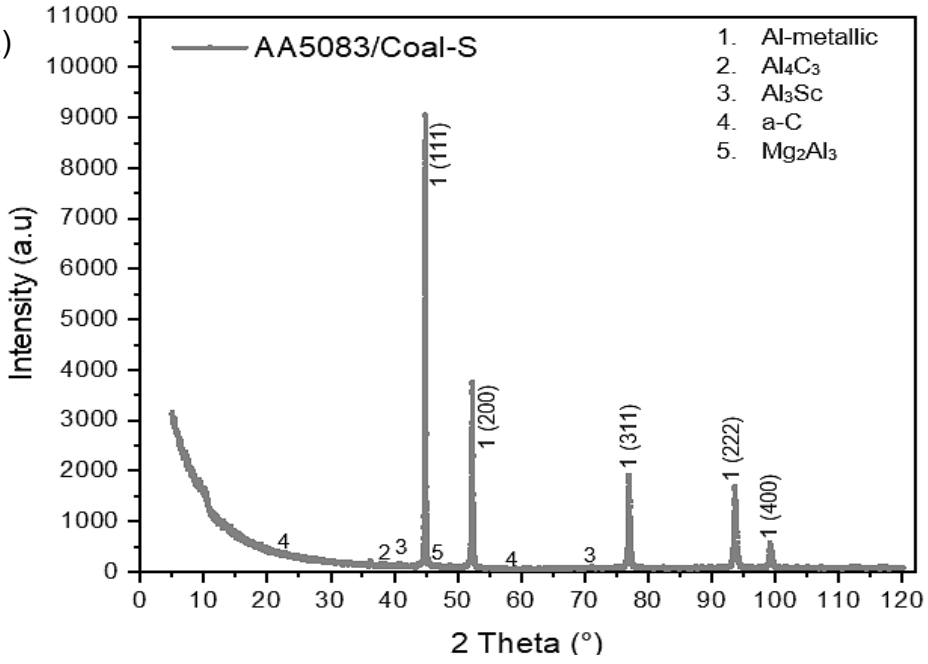
AA5083/Coal-S
1. Al-metallic
2. Al4C3
3. Al3Sc
4. a-C
5. Mg2Al3
Intensity (a.u)
2 Theta (°)
1 (111)
1 (200)
1 (311)
1 (222)
1 (400)

(b)

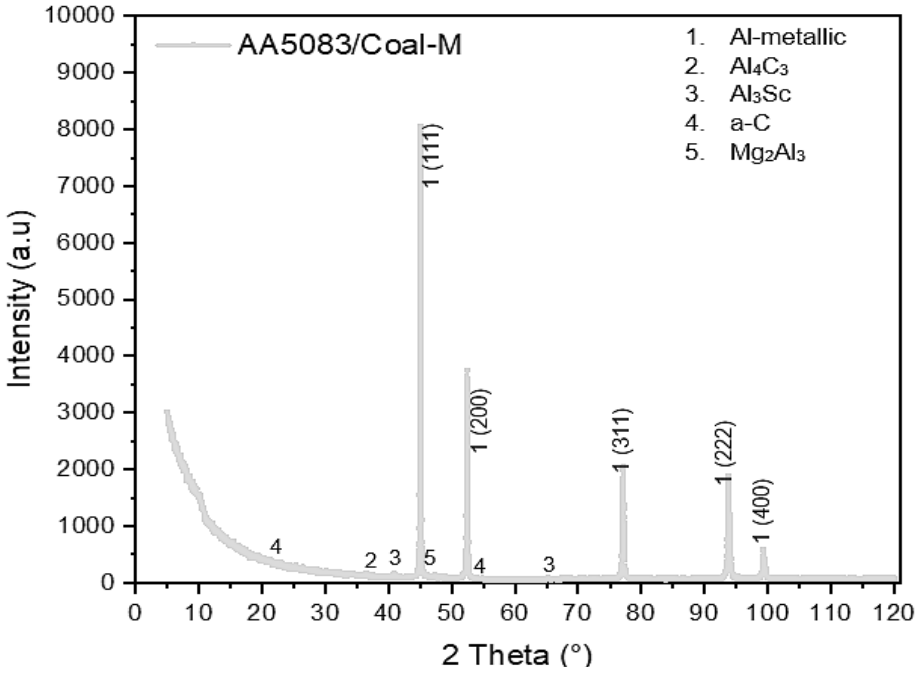
AA5083/Coal-M
1. Al-metallic
2. Al4C3
3. Al3Sc
4. a-C
5. Mg2Al3
Intensity (a.u)
2 Theta (°)
1 (111)
1 (200)
1 (311)
1 (222)
1 (400)

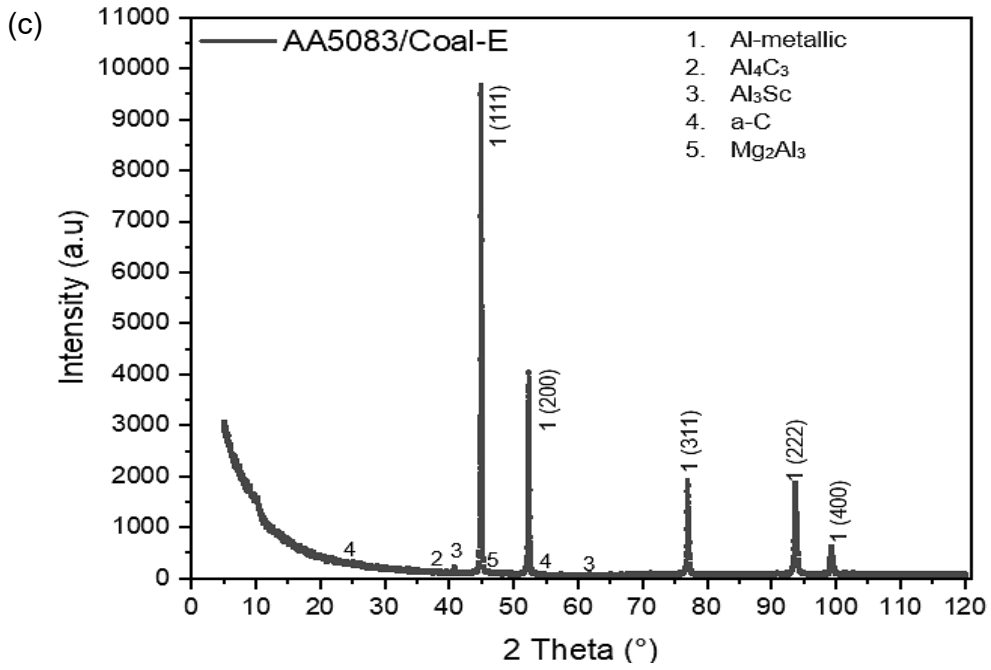


**Figure 4.2.1.2: AA5083/Coal composites joints XRD- Analysis: (a) Start, (b) Middle, (c) End.**

**Table 4.2.1: Chemical composition of joints (wt %).**

| Type | O | Mg | C | Si | Al |
|---|---|---|---|---|---|
| **Base Material** | | | | | |
| AA5083-H111 | 4.0 | 4.3 | 15.8 | 0 | 75.8 |
| **AA5083/SiC composite joint** | | | | | |
| Start | 3.8 | 3.3 | 30.2 | 0 | 62.7 |
| Middle | 0 | 4.5 | 0 | 1.5 | 94.0 |
| End | 7.3 | 0 | 91.2 | 0 | 1.5 |
| **AA5083/Coal composite joint** | | | | | |
| Start | 0 | 0.9 | 12.2 | 0.1 | 15.6 |
| Middle | 2.4 | 5.3 | 10.4 | 0 | 81.9 |
| End | 5.6 | 4.7 | 30.0 | 0 | 59.7 |

4.2.2 Macrostructural analysis

The macrostructural analysis of the AA5083/SiC and AA5083/Coal composite joints revealed the formation of distinct zones—namely the nugget zone (NZ), the thermo-mechanically affected zone (TMAZ), and the heat-affected zone (HAZ)—as illustrated in Figure 4.2.2. Despite the presence of these characteristic zones, several specimens exhibited macro defects, indicating irregularities in internal material flow during the friction stir processing (FSP). Among these, volumetric flow defects were identified in specimens a, c, d, e, and f, as highlighted by red circles in Figure 4.2.2. These defects point to insufficient heat input, which leads to inadequate plasticization of the material and poor mixing during processing [269]. Tunnel defects were observed in specimens a and d, likely caused by similar issues of low

heat input and incomplete material flow [270, 271]. Additionally, the tool traverse speed before sufficient material deposition could have contributed to the void formation, leading to tunnel defects. These defects can significantly degrade the mechanical properties of the composite [272]. Additionally, light cracks were noted in specimens c, e, and f, attributed to a combination of insufficient heat generation, thermal stresses, improper cooling rates, and the inherent brittleness of the material, particularly in the coal-reinforced samples [269].

The occurrence of these defects was closely linked to specific FSP parameters: low rotation speeds and high traverse speeds often resulted in insufficient heat generation, preventing adequate material plasticization and flow. The presence of reinforcement particles, especially hard SiC particles, further increased resistance to material flow and may have contributed to the formation of defects. In contrast, specimen b displayed no macrostructural defects, suggesting that the processing parameters were well-optimized in this case to ensure sufficient heat input and effective material mixing [273-274].

These observations are significant, as macrostructural defects, particularly cracks and tunnel voids, can serve as stress concentration sites that drastically reduce the mechanical performance of the composite joints, affecting properties such as tensile strength and fatigue resistance.

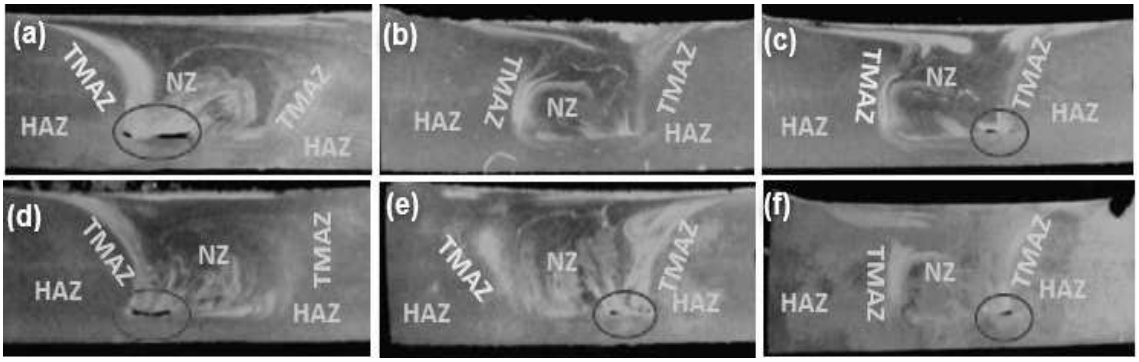


**Figure 4.2.2: Macrographs: AA5083/SiC composites joints; (a) Start, (b) Middle, (c) End; AA5083/Coal composites joints; (d) Start, (e) Middle, (f) End.**

4.2.3 Microstructural analysis

One of the primary challenges in metal matrix composite production is achieving a uniform dispersion of reinforcement particles within the alloy matrix, because this distribution significantly influences the material's strength and overall performance [275]. An understanding of the orientation and distribution of reinforcing fibers or particles within the matrix is crucial for comprehending the composite's overall properties. The microstructural analysis provides valuable insights into these aspects. Figure 4.2.3.1: (a-i) presents micrographs of AA5083/SiC composite joints at 5x magnification, revealing the three distinct microstructural zones: the HAZ, TMAZ and NZ. Microstructural analysis revealed a non-uniform distribution of SiC particles (dark regions) within the AA5083/SiC composite, with clusters or agglomerations evident as shown in Fig. 4.2.3.1. This non-uniform distribution can be attributed to insufficient material flow during the FSP process. Similar observations have been reported in previous studies, in which non-uniform particle distribution has been linked to negative impacts on the mechanical properties of metal-matrix composites [275]. While the FSP process successfully induced dynamic recrystallisation and refined the grain structure, the presence of these agglomerations can hinder the full realisation of the composite's potential mechanical properties [275].

The FSP process effectively refined the microstructure in the NZ of all samples. Similar observations have been reported in previous studies, in which a significant grain size refinement was observed in the stir zone compared to the base material grain size [175, 276-277]. Dynamic recrystallisation mechanisms, including dynamic recovery (DRV), geometric dynamic recrystallisation (GDRX), and discontinuous dynamic recrystallisation (DDRX), have been cited to contribute to this grain refinement [278-280]. The severe plastic deformation and elevated temperatures during FSP facilitated the nucleation and growth of new grains, resulting in a fine-grained microstructure [67,280-281]. The onion-ring pattern observed in the NZ (Fig. 4.2.3.1) is indicative of the complex material flow and heat transfer during the FSP process [282].

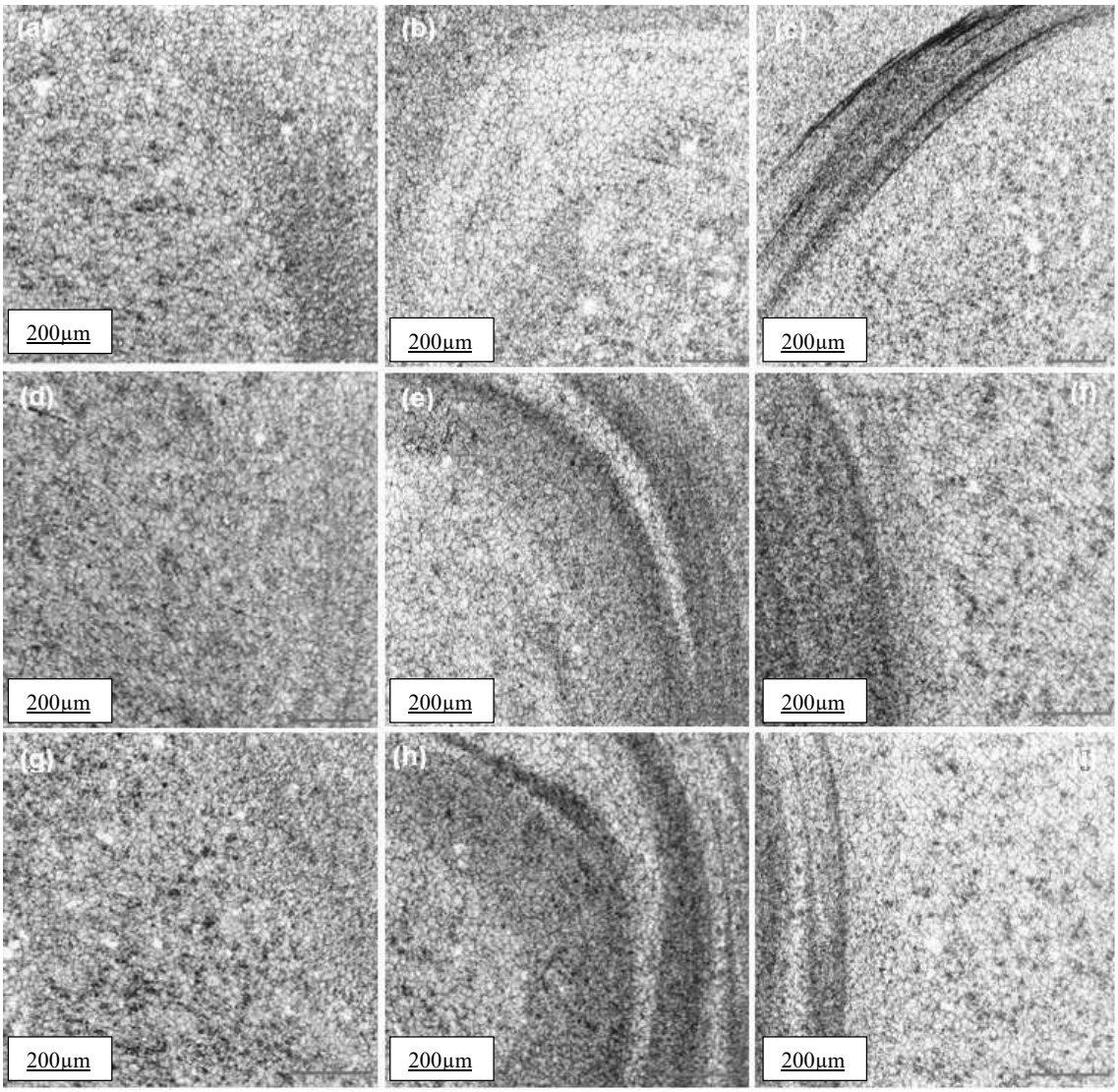


**Figure 4.2.3.1: AA5083/SiC composites joint optical micrographs at objective 5× 1 mm; Start: (a) Advancing side, (b) NZ, (c) Retreating side; Middle (d) Advancing side, (e) NZ (f), Retreating side; End (g) Advancing side, (h) NZ, (i) Retreating side.**

Figure 4.2.3.2: (a-i) presents micrographs of AA5083/Coal composite joints at 5x magnification, also revealing all three distinct microstructural zones: the HAZ, TMAZ and NZ. Microstructural analysis revealed a non-uniform distribution of coal particles (dark regions) within the AA5083/Coal composite, with agglomerations present. This non-uniformity and the

presence of agglomerations can negatively impact the mechanical properties of the composite, this preventing it from reaching its full potential [275]. Despite this problem, the FSP process effectively refined the grain structure in the NZ, due to dynamic recrystallisation [143,175,183,276-277,283–287]. The onion-ring pattern observed in the NZ microstructures (Fig. 4.2.3.2) is indicative of the complex material flow and heat transfer mechanisms during the FSP process [288]. The formation of repetitive ring structures in the microstructure is attributed to periodic changes in the distribution of coal reinforcement. This phenomenon, as explained by Mishra [289], is linked to the tool's rotational and linear movement. The non-uniform distribution of temperatures within the FSP zone, as described by Hamilton et al. [290-291], leads to the creation of material layers with varying precipitate densities. This process is particularly evident in single-pass FSP composites, which exhibit significant heterogeneity in the distribution of the reinforcing phase.

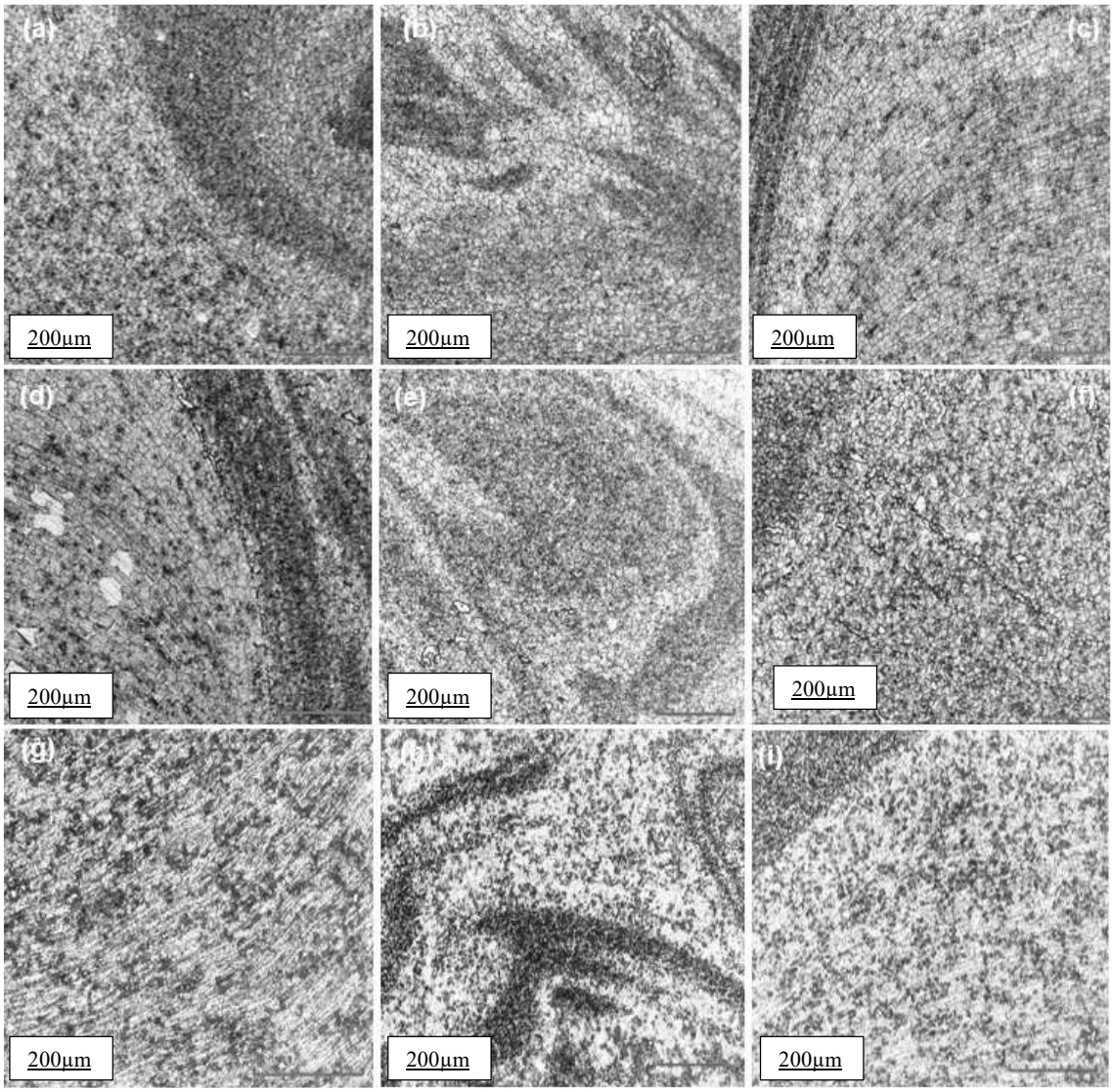


**Figure 4.2.3.2: AA5083/Coal composites joint optical micrographs at objective 5× 1 mm; Start: (a) Advancing side, (b) NZ, (c) Retreating side; Middle (d) Advancing side, (e) NZ (f), Retreating side; End (g) Advancing side, (h) NZ, (i) Retreating side**.

Figure 4.2.3.3 presents the NZ's optical micrographs for AA5083/SiC and AA5083/Coal composite joints at a magnification of 20x, where the refined grain structure is evident. The

FSP techniques effectively refined the grain structure of the composite's joints, as evidenced by the reduced mean grain size (compared to Figure 4.1.3.1) and clearly visible grain boundaries. The stirring action and plastic deformation during FSP contribute to recrystallisation, producing a finer grain structure. This grain refinement is consistent with findings from previous studies [143,175,183,288]. Furthermore, the reduced standard deviation in grain size indicates a more uniform microstructure in the composite's joints.

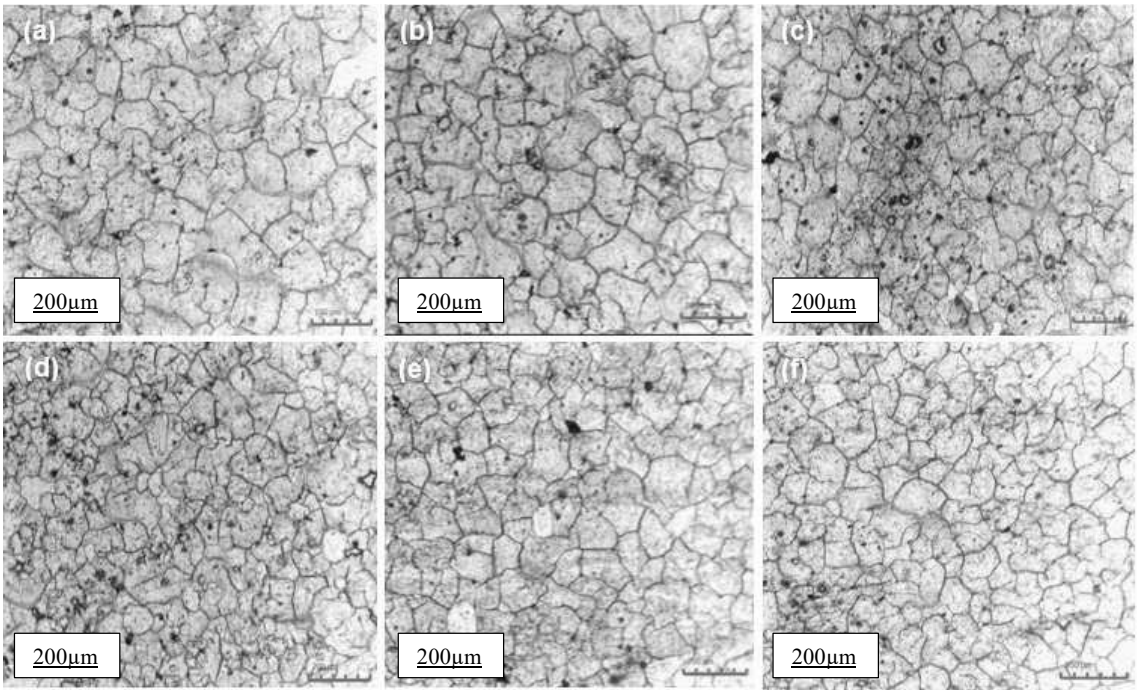


**Figure 4.2.3.3: Optical micrographs at objective 20× 200µm: AA5083/SiC composites joints; (a) Start, (b) Middle, (c) End; AA5083/Coal composites joints; (d) Start, (e) Middle, (f) End.**

Figure 4.2.3.3's measured grain sizes and standard deviations for AA5083/SiC composite and AA5083/Coal composite are tabulated in Table 4.2.3. The AA5083/SiC composite joint's mean grain size ranged from 28.852 µm to 33.218 µm, while the standard deviation ranged from 4.9652 µm to 5.2669 µm. The range of the minimum grain size was 17.446 µm to 23.437 µm, while the range of the maximum grain size was 34.892 µm to 44.742 µm. The standard deviation ranged from 4.8828 µm to 5.9413 µm, while the mean grain size ranged from 27.515 µm to 33.802 µm in the AA5083/Coal composites joints. The range of the minimum grain size was 17.169 µm to 25.049 µm, while the range of the maximum grain size was 37.056 µm to 45.931 µm.

**Table 4.2.3: Grain sizes and standard deviations for the NZ.**

| Type | Mean grain size µm | Minimum grain size µm | Maximum grain size µm | Standard deviation µm |
|---|---|---|---|---|
| **Base material** | | | | |
| AA5083-H111 | 61.292 | 36.061 | 79.419 | 10.868 |
| | | | | |
| **AA5083/SiC composites joints** | | | | |
| Start | 33.218 | 23.437 | 44.742 | 5.2669 |
| Middle | 31.375 | 20.532 | 39.495 | 5.0461 |
| End | 28.852 | 17.446 | 34.892 | 4.9652 |

| | | | | |
|---|---|---|---|---|
| **AA5083/Coal composites joints** | | | | |
| Start | 27.515 | 17.169 | 37.056 | 5.0464 |
| Middle | 32.203 | 20.957 | 38.580 | 4.8828 |
| End | 33.802 | 25.049 | 45.931 | 5.9413 |

Grain distribution graphs and average grain size for AA5083/SiC composite and AA5083/Coal composite are shown in Figures 4.2.3.4 and 4.2.3.5, respectively. When comparing the average grain sizes, both the AA5083/SiC and AA5083/Coal composites exhibited a significant reduction in grain size compared to the base AA5083-H111 material. The AA5083/SiC composite showed a 50.819% reduction, while the AA5083/Coal composite showed a 50.8598% reduction. This enhanced grain refinement is attributed to dynamic recrystallisation, that is promoted by the high levels of plastic deformation and thermal softening within the NZ [143,183,277,288].

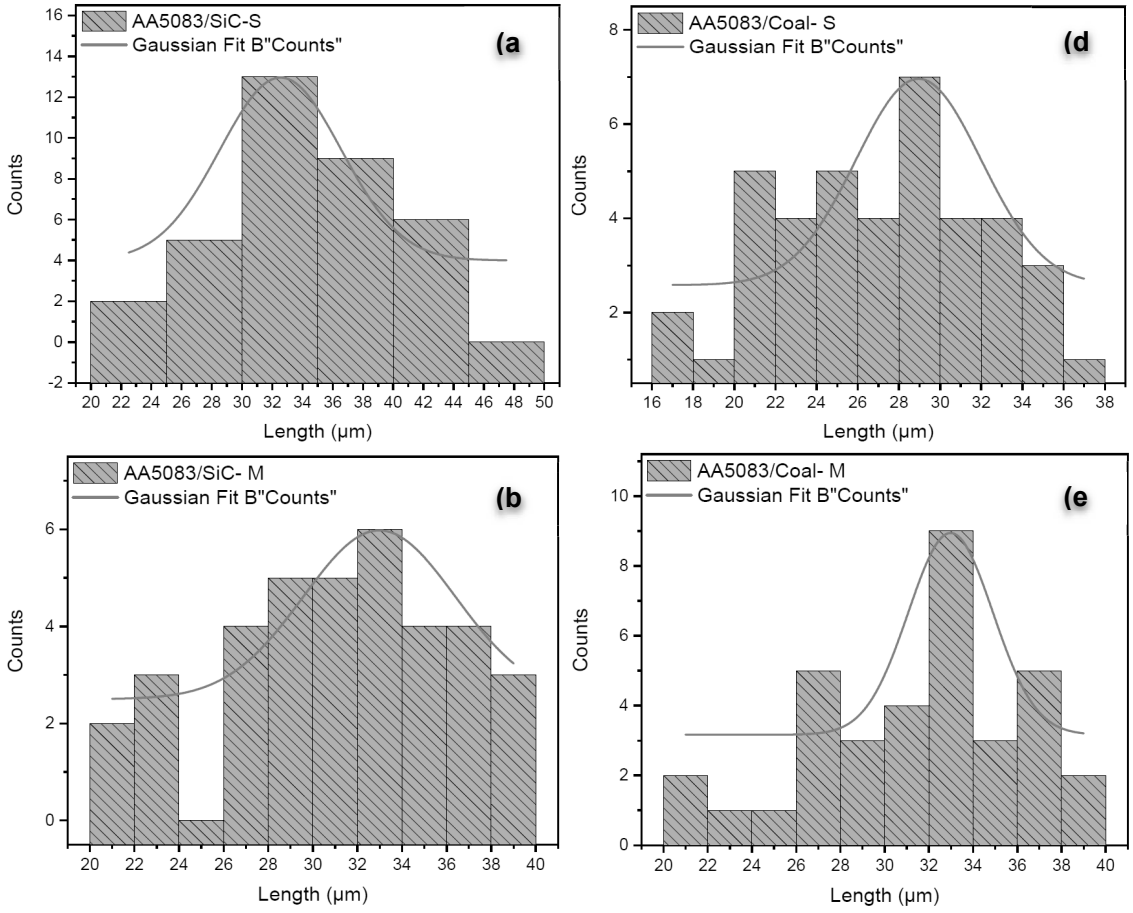

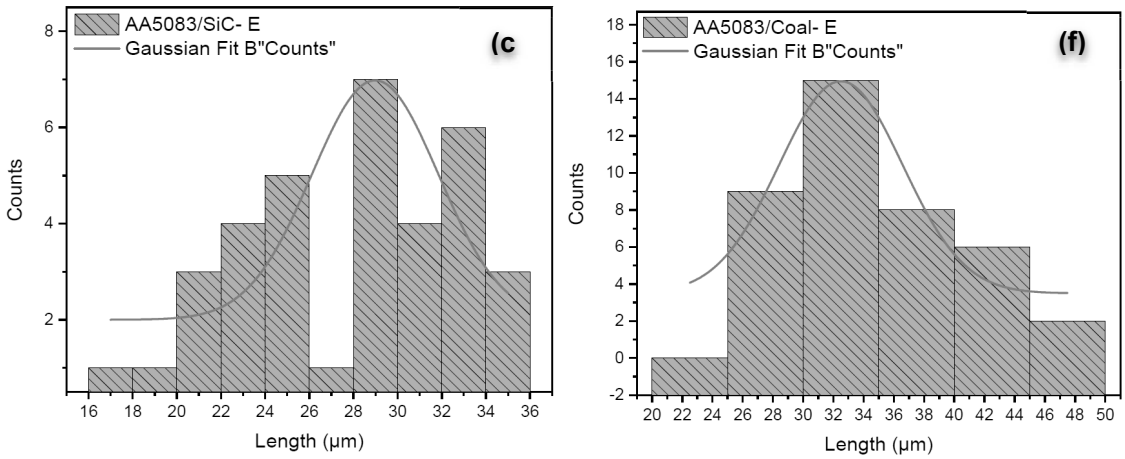


**Figure 4.2.3.4: Grain distribution graphs: AA5083/SiC composites joints: (a) Start (b) Middle (c) End; AA5083/Coal composites joints: (d) Start (e) Middle (f) End.**

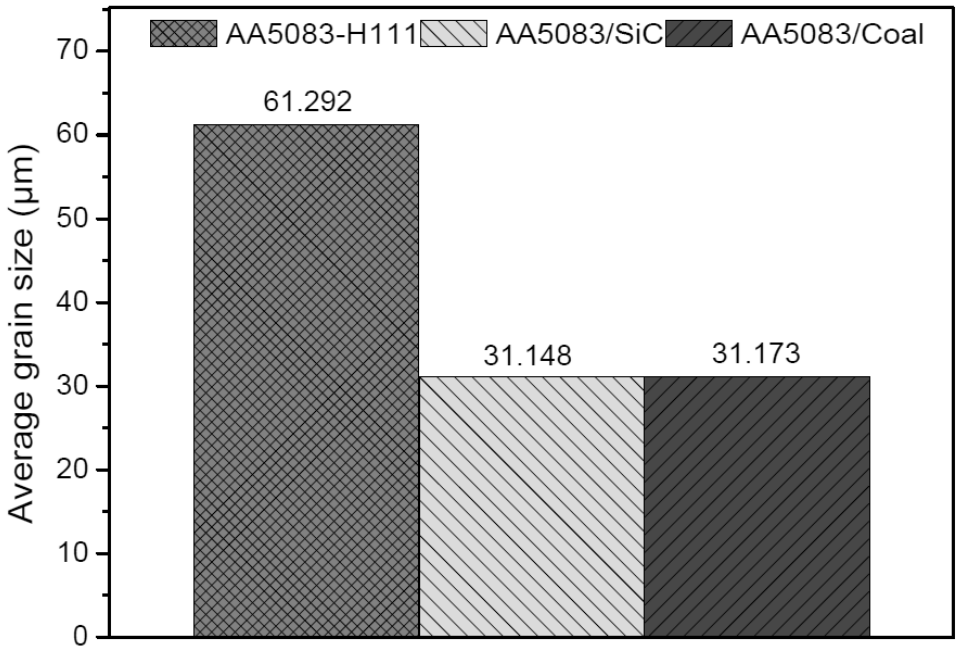


**Figure 4.2.3.5: Average grain sizes of AA5083-H111, AA5083/SiC composite, and AA5083/Coal composite.**

4.2.4 Flexural / Bending tests

The post-flexure test specimens for the AA5083/SiC composite joints and the AA5083/Coal composite joints are displayed in Figure 4.2.4.1. The flexural testing was conducted on the face and root specimens. The results for both these specimens of the AA5083/SiC and AA5083/Coal composite joints revealed that all specimens broke in the middle of the NZ. The cracks observed in the NZ, as seen in Figure 4.2.4.1, are probably due to defects as previously identified in the macrostructural analysis and agglomeration of reinforcement particles. Agglomeration can create stress concentrations, hindering load transfer between the matrix and reinforcement phases and leading to premature failure [191-192,275,277, 292-293]. Additionally, weak interfacial bonding between the reinforcements and the matrix can further degrade the mechanical properties of the composite [191-192,294].

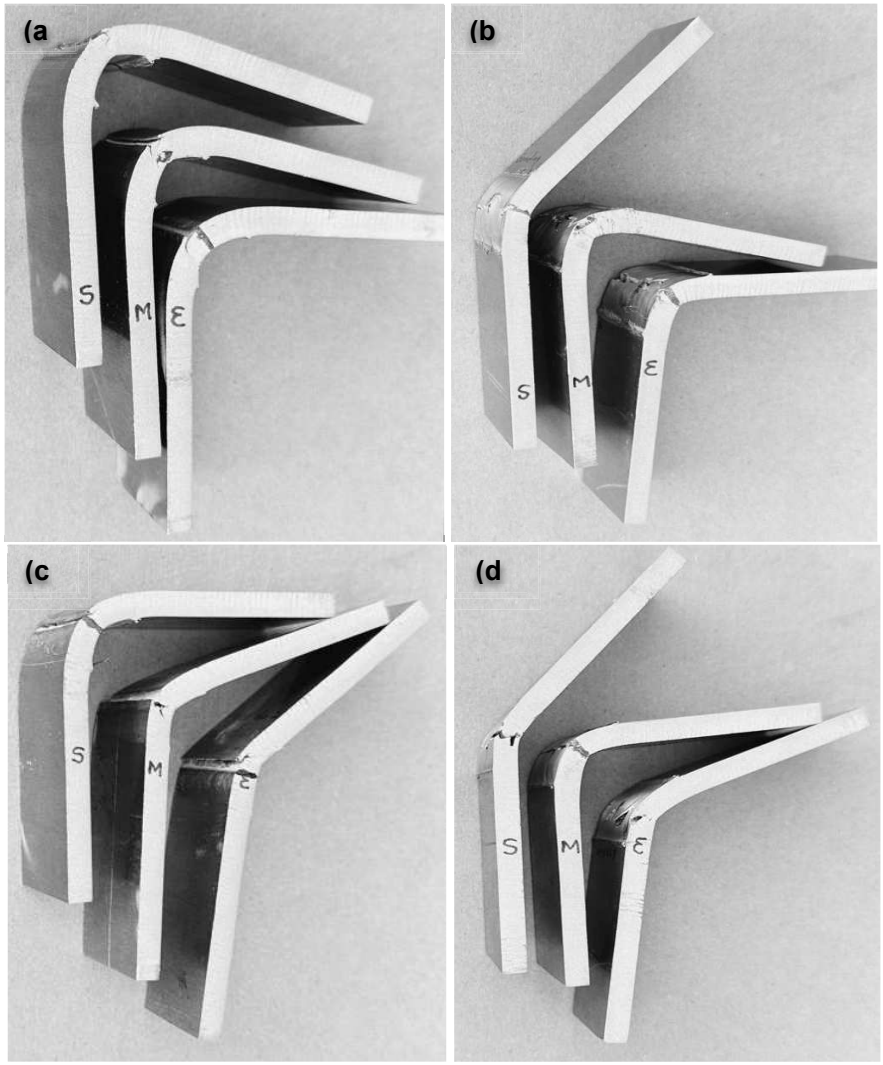


**Figure 4.2.4.1: Post-flexural test specimens: AA5083/SiC composite joints: (a) Face, (b) Root; AA5083/Coal composite joints: (c) Face, (d) Root.**

The flexural strength and strain curves for the AA5083/SiC and AA5083/Coal composite joints are displayed in Figure 4.2.4.2 (a–d). As can be shown in Figure 4.2.4.2 [a], the ultimate flexural strength (UFS) range for the AA5083/SiC composite joints (root) was 476 MPa to 632.7778 MPa for flexural strain (MFS) rates of 11.6353% and 25.1765%, respectively. The minimum and maximum flexural strain rates at fracture points were 17.8824% and 36.7059%, respectively. According to Figure 4.2.4.2 [b], the UFS range for the AA5083/SiC composite (face) was 740.4444 MPa to 765 MPa for flexural strain rates of 23.2941% and 21. 6471%, respectively. The minimum and maximum flexural strain rates at fracture points were 29.6471% and 34.8235%, respectively. The face specimens of the AA5083/SiC composite joint were found to have the largest UFS. Similar results, as reported by Takhakh [295] and Sorger et al. [296], have indicated the superior performance of face specimens compared to root specimens in FSP joints. The results of the AA5083/SiC composite joints also demonstrated that the face results were more accurate than the root results and that there was no obvious trend in the root results. This behaviour was seen for both the flexural strength and the flexural strain.

As shown in Figure 4.2.4.2: [c], the UFS range for the root was 410.5972 MPa to 631.9514 MPa at strain rates of 8.70588% and 22.2353%, respectively. According to Figure 4.2.4.2: [d] the UFS range for the AA5083/Coal composite joints (face) was 404.6944 MPa to 729.85 MPa at strain rates of 5.4471% and 22.9412%, respectively. At the fracture point (root), the minimum and maximum flexural strain rates at the face were 16.23529% and 29.4118%, respectively, whereas minimum and maximum flexural strain rates at the face were found to be 14.9412% and 28%, respectively. The face specimens of the AA5083/Coal composite joint were found to have the largest UFS, a fact that was also noted in AA5083/SiC composite joint results. Similar results, as reported by Takhakh [295] and Sorger et al. [296], have indicated the superior performance of face specimens compared to root specimens in FSP joints. The face results performed better than the root outcomes in the AA5083/Coal composite joints, and there was no obvious trend in the root results, a fact that was also observed in the AA5083/SiC composite joints results. This behaviour was seen for both the flexural strength and the flexural strain. The bending properties for Figure 4.2.4.2 are displayed in Table 4.2.4.

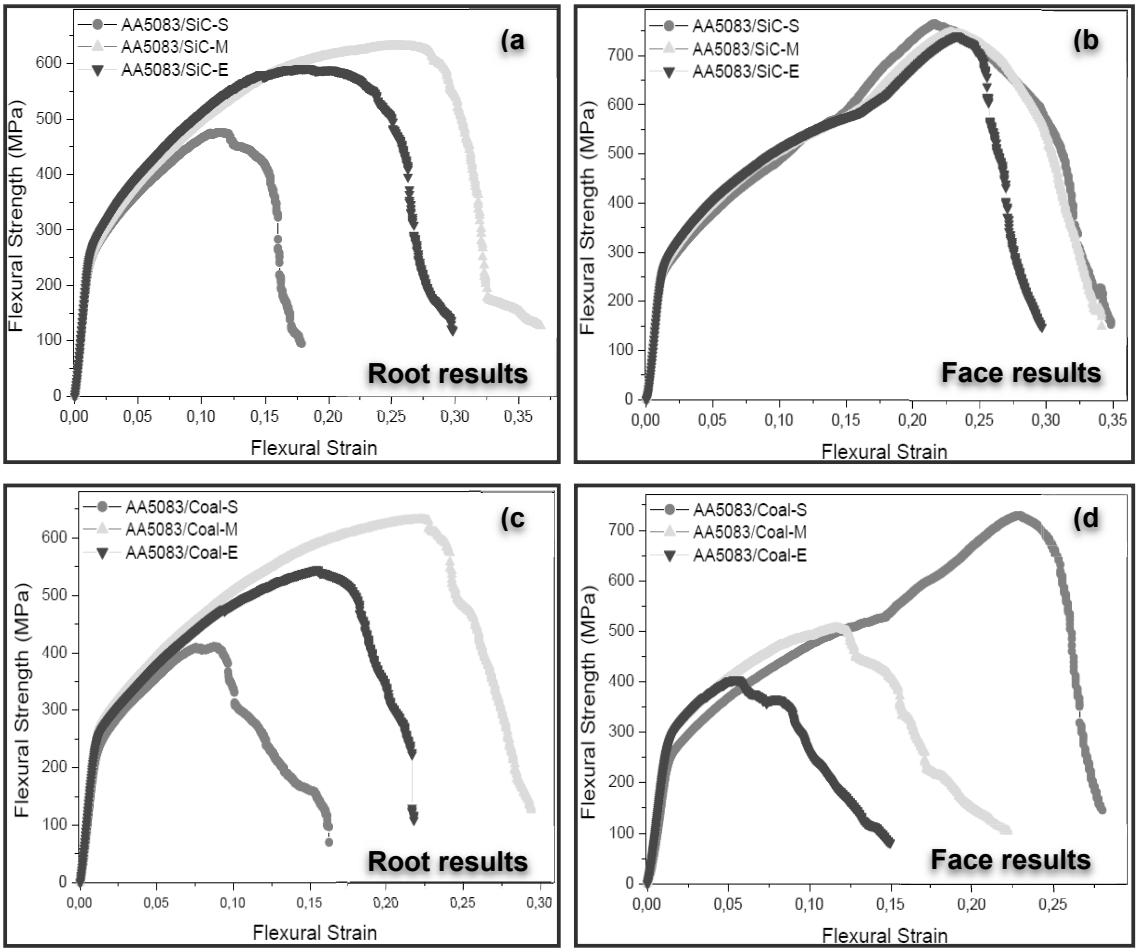


**Figure 4.2.4.2: Flexural strength – strain curves: AA5083/SiC composite joints: (a) Face, (b) Root; AA5083/Coal composite joints: (c) Face, (d) Root.**

**Table 4.2.4: Bending properties of the joints.**

| Type | Ultimate Force (N) | Ultimate Flexural Strength (MPa) | Flexural Strain (%) | Modulus (MPa) |
|---|---|---|---|---|
| **Base material** | | | | |
| AA5083-H111 | 3517 | 415.2014 | 0.268235 | 38600 |
| | | | | |
| **Root specimens** | | | | |
| AA5083/SiC composite joints | | | | |
| S | 4032 | 476.0000 | 0.113882 | 48800 |
| M | 5360 | 632.7778 | 0.251765 | 64100 |
| E | 5016 | 592.1667 | 0.177647 | 52800 |
| | | | | |
| AA5083/Coal composite joints | | | | |
| | | | | |
| S | 3478 | 410.5972 | 0.087058 | 46500 |
| M | 5353 | 631.9514 | 0.222353 | 64100 |
| E | 4615 | 544.8264 | 0.155294 | 64400 |
| | | | | |
| **Face specimens** | | | | |
| AA5083/SiC composite joints | | | | |
| S | 6480 | 765.0000 | 0.216471 | 63900 |
| M | 6332 | 747.5278 | 0.228235 | 65500 |
| E | 6272 | 740.4444 | 0.232941 | 63600 |
| | | | | |
| AA5083/Coal composite joints | | | | |
| S | 6180 | 729.5833 | 0.229412 | 43800 |
| M | 6332 | 747.5278 | 0.228235 | 63100 |
| E | 3428 | 404.6944 | 0.054471 | 47800 |

Figure 4.2.4.3 depicts the ultimate flexural strength (UFS) and maximum flexural strain (MFS) obtained on each joint configuration as discussed. The AA5083/SiC composite joint exhibited the highest UFS for both face and root specimens. The AA5083/SiC composite joint exhibited superior performance, with the face specimens achieving a maximum UFS of 765 MPa, that was significantly higher than the 632.78 MPa of the root specimens. This 132.22 MPa difference highlights the variation in mechanical properties along the joint length. The AA5083/Coal composite joint exhibited a significant difference in UFS between the face and root specimens. The face specimens achieved a maximum UFS of 747.53 MPa, while the root specimens reached a maximum UFS of 631.95 MPa, resulting in a difference of 115.58 MPa. The base material, AA5083-H111, exhibited a higher strain rate compared to both composites. Additionally, the AA5083/SiC composite demonstrated a higher strain rate than the AA5083/Coal composite. These findings suggest an inverse relationship between UFS and strain rate, in which the higher UFS is often associated with lower strain rates. Similar behaviour has been reported in the reviewed literature [297].

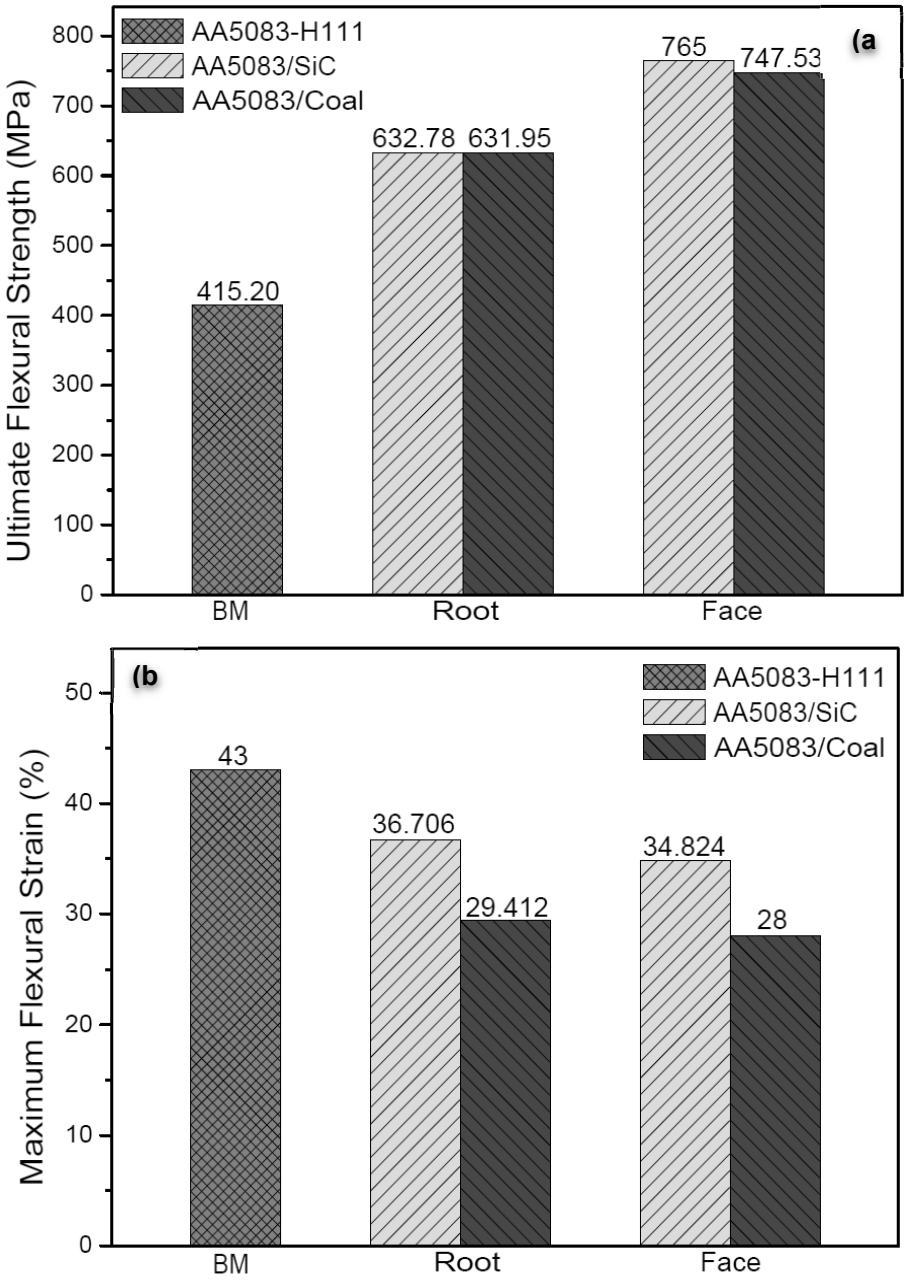


**Figure 4.2.4.3: Bar charts: (a) ultimate flexural strength (MPa); (b) maximum flexural strain (%)**.

4.2.5 Tensile tests

The post-tensile specimens for the AA5083/Coal and AA5083/SiC composite joints, shown in Figure 4.2.5.1, reveal that all fractures occurred within the nugget zone (NZ). This consistent failure location underscores the critical influence of localized defects within the NZ on the tensile behavior of the composites. A key contributing factor to the reduced strength is the agglomeration of reinforcement particles in the NZ, primarily caused by insufficient inter-particle spacing [298–300]. These agglomerated clusters act as stress concentrators, promoting crack initiation and leading to premature failure [301–302]. In addition, the non-uniform distribution of reinforcement particles observed in some specimens compromised the

matrix–reinforcement interface, further reducing the overall mechanical strength of the composite joints [303]. Insufficient tool penetration during FSP can intensify this problem by causing incomplete bonding between the materials, thereby further degrading the structural integrity and overall performance of the joints [275, 277, 292].

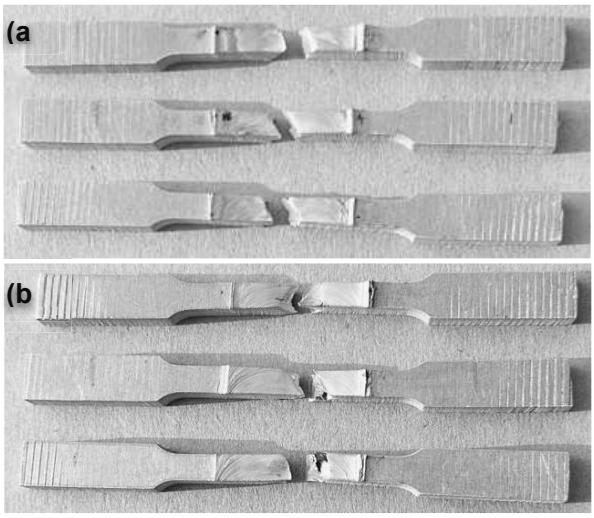


**Figure 4.2.5.1: Post-tensile specimens: (a) AA5083/SiC composite joints; (b) AA5083/Coal composite joints.**

Figure 4.2.5.2 presents the tensile stress-strain curves of the AA5083/SiC composite joints and AA5083/Coal composite joints. The tensile properties for Figure 4.2.5.2 are displayed in Table 4.2.5. The AA5083/SiC composite joint had a maximum UTS of 281 MPa at a corresponding tensile strain rate of 31.49% with a maximum yield strength of 224.8 MPa at the end of the joint (see Figure 4.2.5.2: (a)). The minimum UTS was 265 MPa at a corresponding tensile strain rate of 22.13% and yield strength of 212.0 MPa at the start of the joint. The maximum and minimum tensile strain rates at the fracture point of the AA5083/SiC composite joints were 23.04% and 32.57%, respectively. The AA5083/Coal composite joint had a maximum UTS of 280 MPa at a corresponding tensile strain rate of 33.48% with a maximum yield strength of 225.6 MPa at the start of the joint (see Figure 4.2.5.2: (b)). The minimum UTS was 180 MPa at a corresponding tensile strain rate of 15.17% and yield strength of 144.0 MPa at the end of the joint. The maximum and minimum tensile strain rates at the fracture point of the AA5083/Coal composite joints were 34.11% and 15.82%, respectively.

There was no consistent trend observed in the tensile strength and strain rate for the AA5083/Coal composite joints. The AA5083/SiC composite outperformed the AA5083/Coal composite in terms of tensile strength and strain. Interestingly, the tensile strength and strain rate of the AA5083/SiC composite gradually increased along the joint length, correlating with the observed microstructural grain size trends. Additionally, no consistent strain rate was observed for either the AA5083/SiC or AA5083/Coal composite joints.

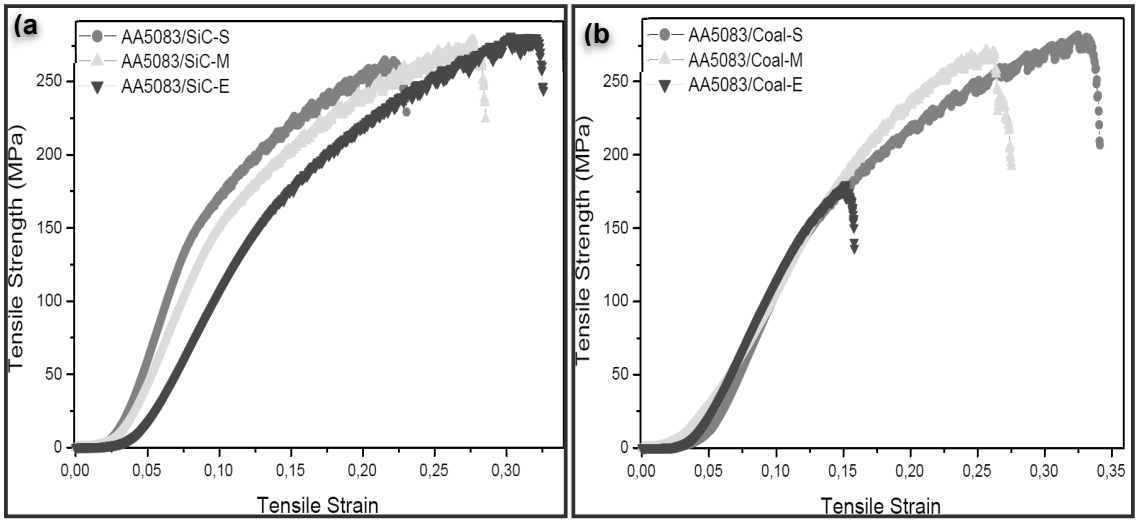


**Figure 4.2.5.2: Tensile Stress-Strain curve: (a) AA5083/SiC composite joints; (b) AA5083/Coal composite joints.**

**Table 4.2.5: Tensile properties of the joints.**

| Type | Ultimate Break Force (N) | Ultimate Tensile Strength (MPa) | Yield strength (MPa) @ 0.2% Offset | Strain rate(%) | Fracture location |
|---|---|---|---|---|---|
| **Base material** | | | | | |
| AA5083-H111 | 11200 | 311 | 248.8 | 58.65 | N/A |
| **AA5083/SiC composite joints** | | | | | |
| S | 9530 | 265 | 212.0 | 22.13 | NZ |
| M | 10000 | 279 | 223.2 | 27.71 | NZ |
| E | 10100 | 281 | 224.8 | 31.49 | NZ |
| **AA5083/Coal composite joints** | | | | | |
| S | 10100 | 282 | 225.6 | 33.48 | NZ |
| M | 9780 | 272 | 217.6 | 25.64 | NZ |
| E | 6470 | 180 | 144.0 | 15.17 | NZ |

The average tensile properties of the AA5083/Coal and AA5083/SiC composite joints are shown in Figure 4.2.5.3. As seen in Figure 4.2.5.3, the addition of reinforcements did not significantly enhance the tensile strength and strain rate of the base material. Both composites exhibited respectable ultimate tensile strength (UTS) values, although slightly lower than the base material. The AA5083/SiC composite showed an 11.576% reduction, while the AA5083/Coal composite showed a 21.318% reduction. The reduced tensile strength can be attributed to inadequate penetration during the FSP process, as reported in previous studies [293]. Similar trends of lower tensile strength in composites compared to the base material have been observed in the reviewed literature [182,277,304].

The specimen at the end of the AA5083/Coal composite exhibited the lowest tensile properties due to agglomerated reinforcement particles. It has been noted in the reviewed literature that higher levels of agglomeration in reinforcement particles can lead to lower ultimate tensile strength (UTS) values [277]. Additionally, poor bonding between the reinforcement particles and the base material can significantly impact the mechanical properties of the composite

[275]. Similar findings have been reported in previous studies [275,301,302], in which agglomeration and inadequate interfacial bonding have been identified as contributing to reduced tensile strength.

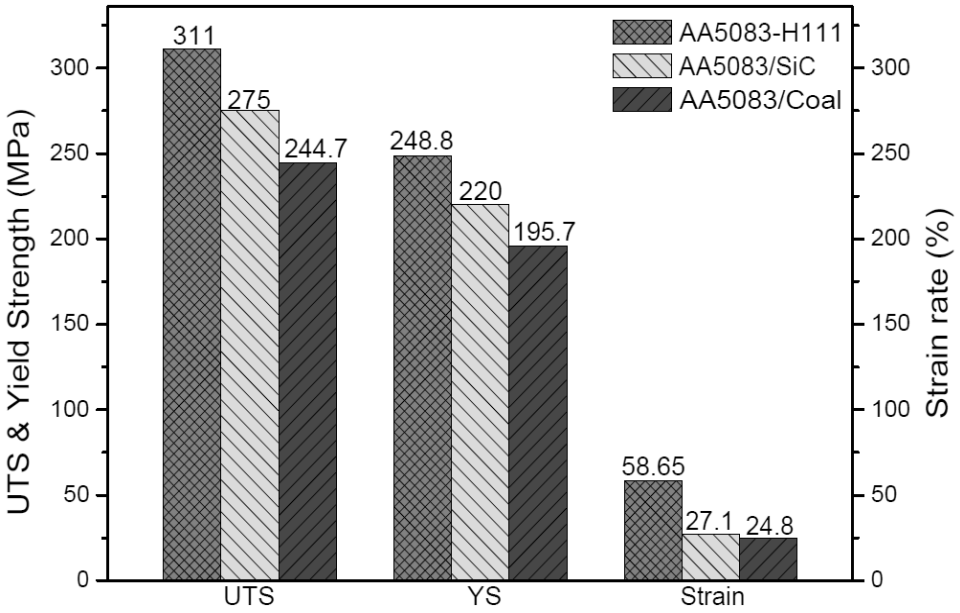


**Figure 4.2.5.3: Average tensile properties.**

These findings align with the macrostructural observations reported in Figure 4.2.2, which revealed the presence of flow-related defects such as tunnel voids and volumetric discontinuities. These defects, acting as additional stress raisers, undermine the structural integrity of the NZ and facilitate crack propagation under tensile loading. The clear correlation between the presence of these macro defects and the lower ultimate tensile strength (UTS) values recorded for both AA5083/Coal and AA5083/SiC composites highlights the importance of achieving uniform particle dispersion and defect-free processing. Thus, both reinforcement agglomeration and flow defects should be recognized as key contributors to the observed reductions in mechanical performance and the altered failure mechanisms of the composite joints. Their combined influence must be explicitly addressed in the interpretation and discussion of the tensile behavior of these materials.

### 4.2.6 Fracture surface analysis

With regard to fracture surface analysis of composites, ductile fracture is initiated by stress concentration near the reinforcement particles, leading to crack nucleation at the particle-matrix interface. Subsequent crack growth and coalescence of microvoids within the matrix contribute to the overall failure mechanism. Brittle fracture, on the other hand, is characterised by particle pull-out, decohesion at matrix-particle interfaces and rapid crack propagation [277].

Figure 4.2.6.1 illustrates the fracture surface morphology of the AA5083/SiC composite joints. The fractured surfaces exhibited a combination of ductile and brittle failure mechanisms, characterised by the presence of microvoids, rough surfaces, dimples and particle clusters. The extent of ductile or brittle failure is influenced by factors such as the number of FSP passes, microstructure arrangement and the degree of reinforcement particle agglomeration [305]. The ductile fracture was evident from the presence of dimples of various sizes (demonstrated with a sample red arrow) and microvoids (demonstrated with a sample yellow arrow). In contrast, the brittle fracture was characterised by small planes and rough patches

(demonstrated with a sample yellow circle). These findings align with previous reviewed studies, that reported similar ductile-brittle fracture behaviour in FSP-processed composites [306,277,287,288,304,307,308]. SiC particle clusters were observed as indicated by the pink circles. This finding also aligns with those of previous studies [191]. The presence of SiC particles on the fracture surface suggests that fracture initiation and propagation occurred at the interface between the matrix and the reinforcement particles [309].

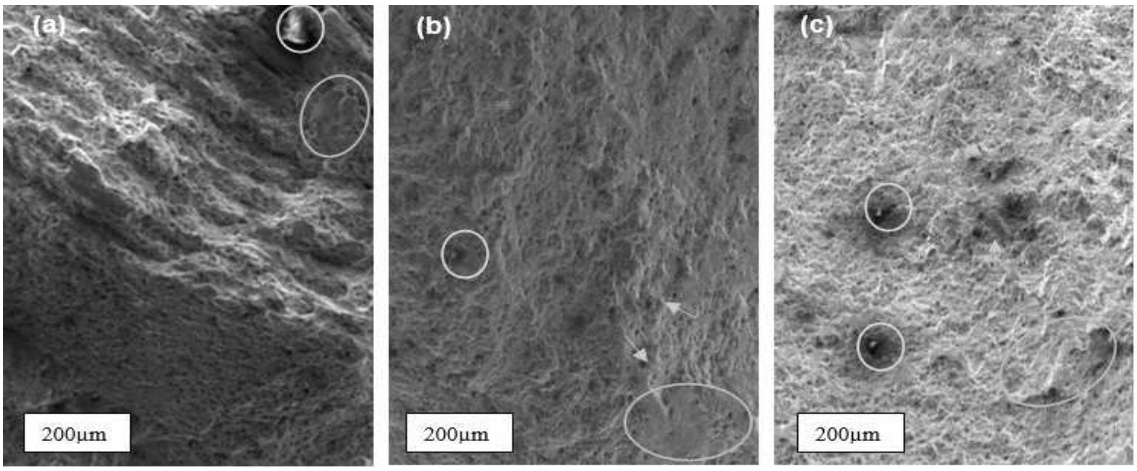


**Figure 4.2.6.1: Fracture surface morphologies of AA5083/SiC composite joints: (a) start, (b) middle, (c) end.**

Figure 4.2.6.2 illustrates the fracture surface morphology of the AA5083/Coal composite joints. The fractured surfaces exhibited a combination of ductile and brittle failure mechanisms, characterised by the presence of microvoids, rough surfaces, dimples and particle clusters. The extent of ductile or brittle failure is influenced by factors such as the number of FSP passes, microstructure arrangement, and the degree of reinforcement particle agglomeration [306]. The ductile fracture was evident from the presence of dimples of various sizes shown with a sample red arrow and microvoids demonstrated with a sample yellow arrow. In contrast, the brittle fracture was characterised by small planes and rough patches demonstrated with a sample yellow circle (see Figure 4.2.6.2: (a) and (b). These findings align with previous studies that reported similar ductile-brittle fracture behaviour in FSP-processed composites [306,277, 287,288,304,307, 308].

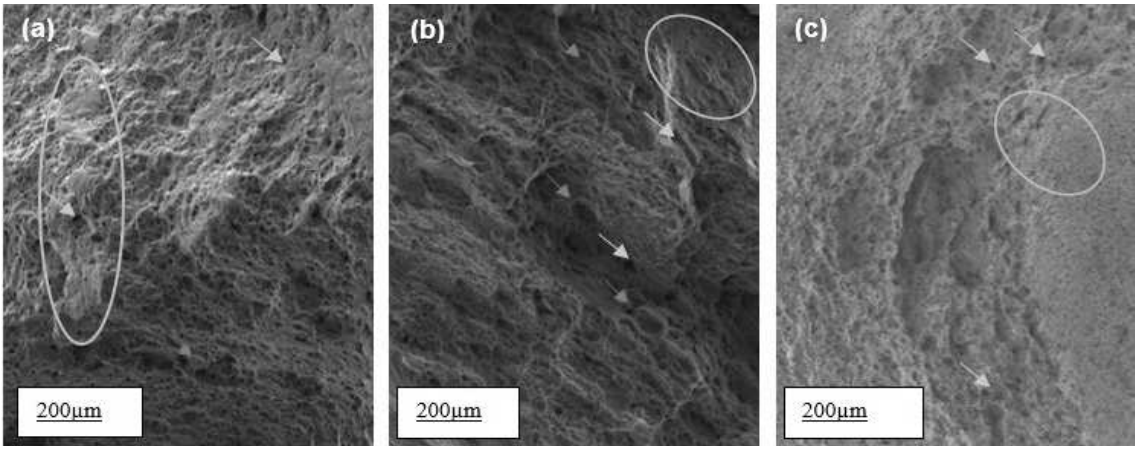


**Figure 4.2.6.2: Fracture surface morphologies of AA5083/Coal composite joints: (a) start, (b) middle, (c) end.**

4.2.6.1 Energy Dispersive X-ray Spectroscopy Analysis

The EDS analysis (Figures 4.2.6.1.1 and 4.2.6.1.2) revealed the elemental composition and distribution across the AA5083/SiC and AA5083/Coal composite joints at different positions (start, middle, end). For the AA5083/SiC joints, silicon was observed to be distributed in the middle region, indicating effective mixing during peak tool engagement, while some particle clustering was evident at the start and end zones. Aluminum remained the predominant element across all regions, as expected. In the AA5083/Coal joints, carbon signals were present throughout, with relatively consistent dispersion in the middle but some segregation near the tool retreat zone, potentially due to material flow dynamics. No significant elemental contamination was noted, suggesting minimal tool degradation. These results confirm the successful incorporation of reinforcements and highlight the influence of process parameters on distribution uniformity.

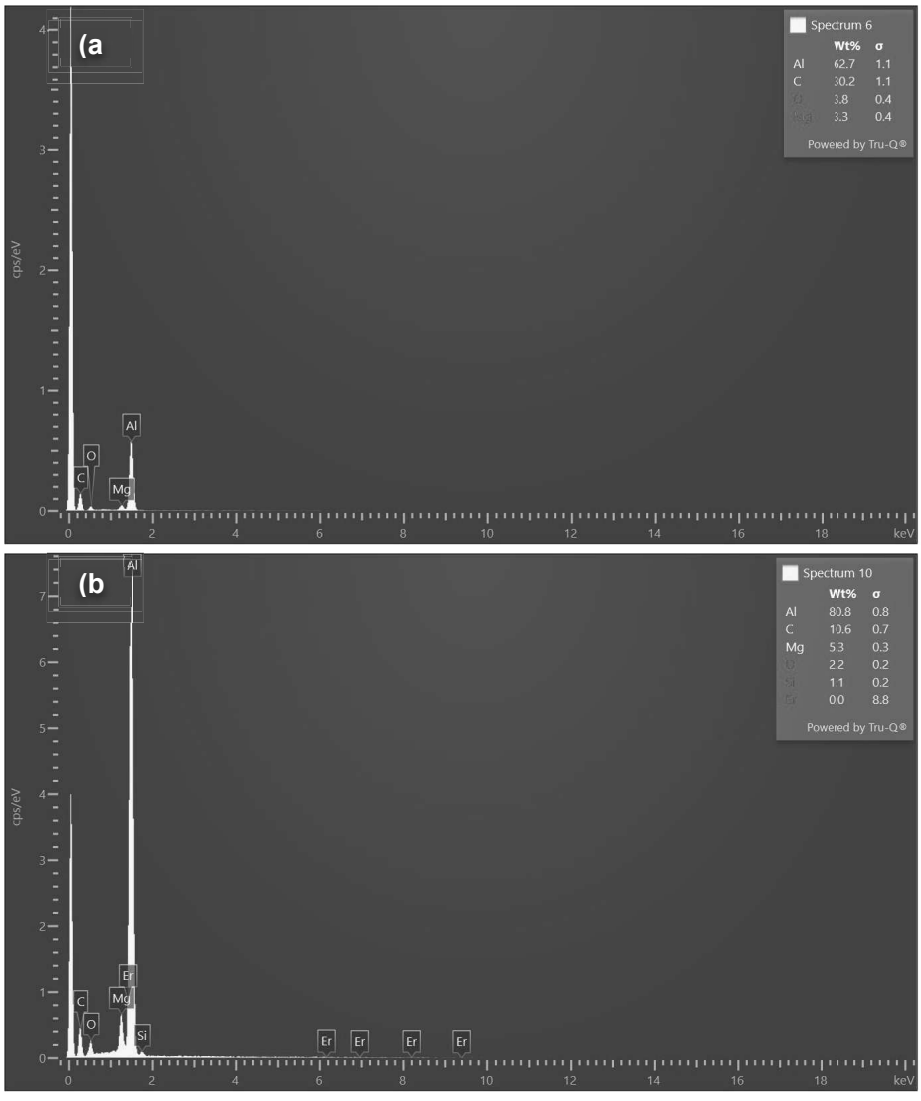


**Figure 4.1.6.1.1: Energy Dispersive X-ray Spectroscopy, AA5083/SiC composites joints; (a) Start, (b) Middle, (c) End.**



**Figure 4.1.6.1.2: Energy Dispersive X-ray Spectroscopy, AA5083/Coal composites joints; (a) Start, (b) Middle, (c) End.**

4.2.7 Hardness tests

Figure 4.2.7.1 shows the Vickers hardness curves for the AA5083/SiC and AA5083/Coal composite joints. The AA5083/SiC composite significantly improved hardness, ranging from 88.9 HV to 93.15 HV, with an average hardness of 92.47 HV. In contrast, the AA5083/Coal composite exhibited a hardness range of 89.24 HV to 91.6 HV, with an average of 91.42 HV. The highest hardness value was obtained in the NZ for both composites, followed by the TMAZ and HAZ. The TMAZ region displayed varying hardness levels due to the competing effects of reinforcement particles and heat. The NZ, characterised by a refined microstructure resulting from dynamic recrystallisation [143,284,304] and intermetallic particle fragmentation/redistribution, exhibited the highest hardness value [309-311]. This improvement is attributed to the combined effect of grain refinement, dislocation pinning by reinforcement particles and the well-established Hall-Petch relationship [283,309,312]. Additionally, interfacial bonding between the matrix and reinforcement particles enhances the overall hardness [277, 309].

While the AA5083/SiC and AA5083/Coal composite joints generally exhibited higher hardness values at the NZ, a decrease in hardness was observed towards the lower regions. This reduction is likely due to the decreasing intensity of the FSP process and the less homogeneous distribution of reinforcement particles. Similar studies [175,304,313] have reported comparable microhardness results. The microstructural analysis confirmed the dense distribution of reinforcement particles in the NZ, aligning with the observed higher hardness values [175,183,275,277,284,287,304,308]. The combined effect of grain refinement, dislocation density and particle distribution contributes to the enhanced mechanical properties of the composite.

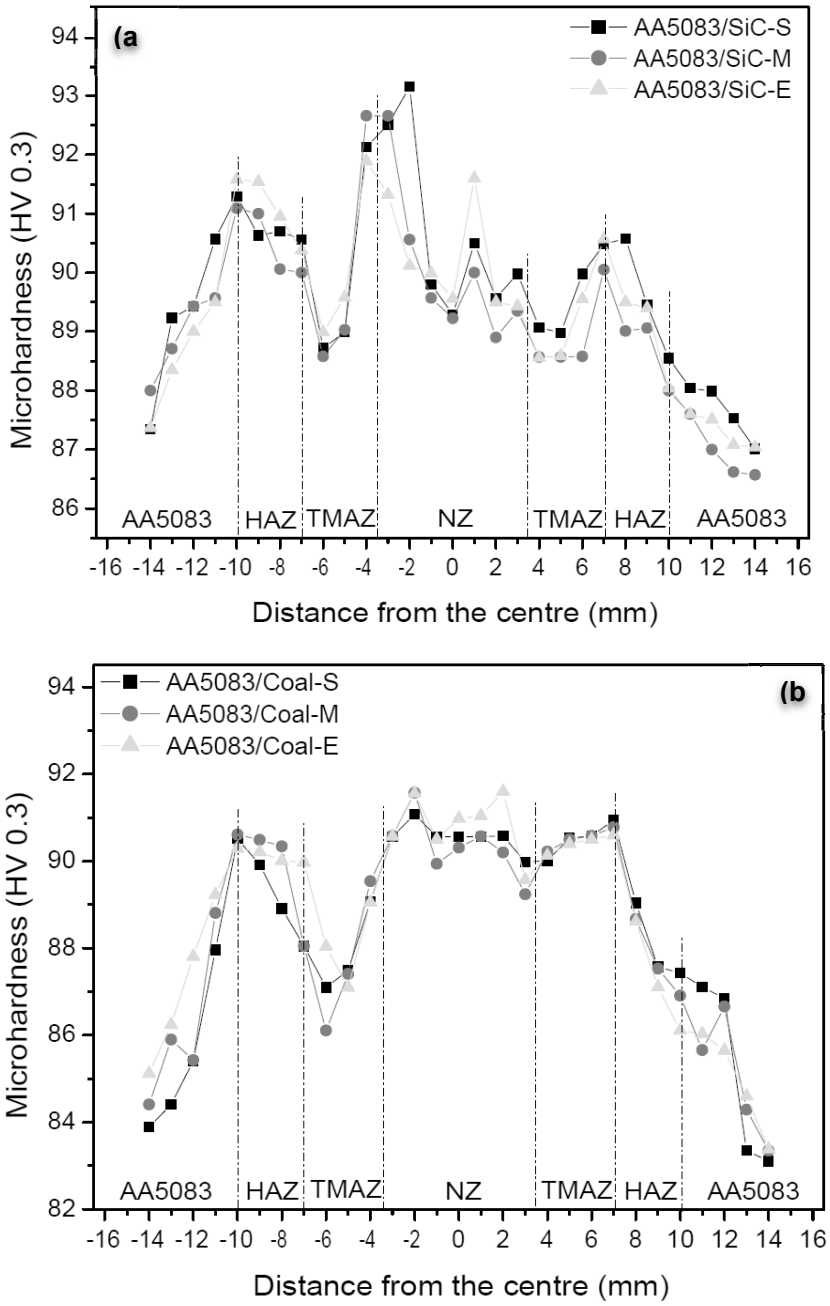


**Figure 4.2.7.1: Hardness profiles: (a) AA5083/SiC composite joints; (b) AA5083/Coal composite joints.**

Figures 4.2.7.2 and 4.2.7.3 present the corresponding NZ summary and average hardness bar charts. As shown in Figure 4.2.7.2, the addition of reinforcements significantly increased the hardness of the AA5083/SiC and AA5083/Coal composites compared to the base material. This enhancement in hardness can be attributed to the Orowan mechanism [277] and the Hall-Petch relationship [283,309,312], that correlates hardness with grain size. The NZ hardness was approximately 1.0221 times higher than the base material hardness for AA5083/SiC composites and 1.0092 times higher for AA5083/Coal composites. The highest hardness value was observed at the start of the AA5083/SiC joint and the end of the AA5083/Coal joint.

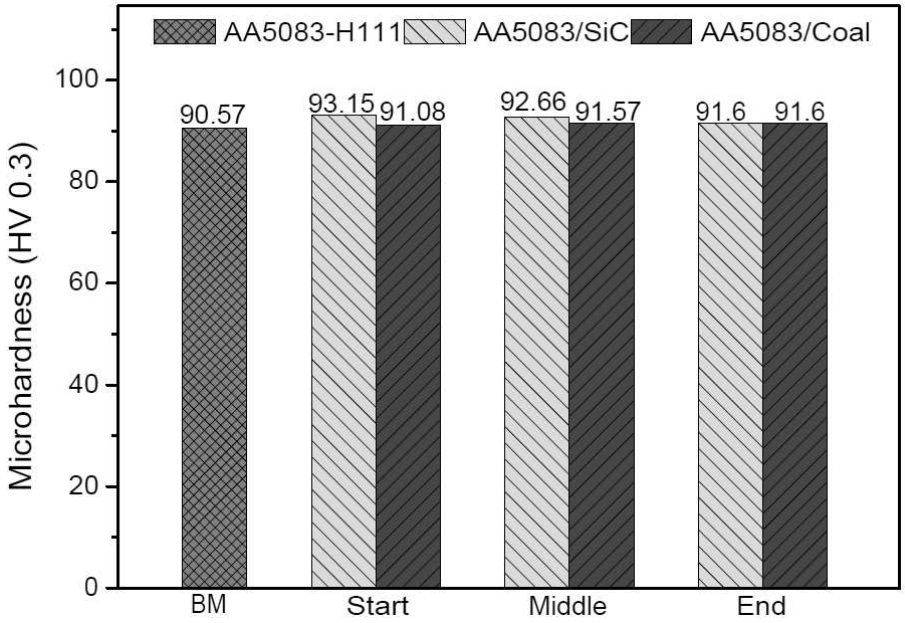


**Figure 4.2.7.2: Hardness summary bar charts.**

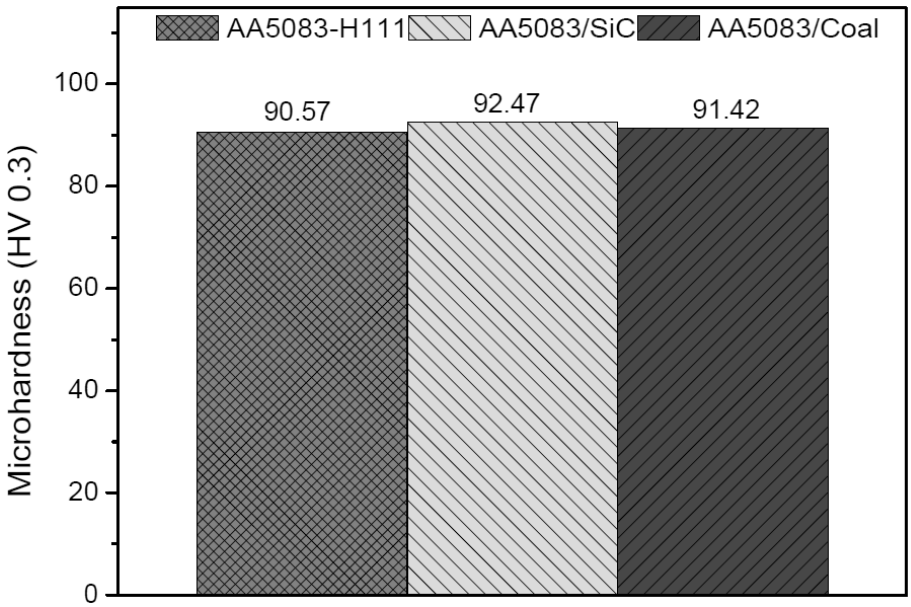


**Figure 4.2.7.3: Average hardness bar charts.**

# CHAPTER FIVE

# CONCLUSIONS AND RECOMMENDATIONS

This chapter offers a summary of the main points of this research study. It also identifies areas that need improvement when one wishes to advance the study.

## 5.1 Conclusions

The study aimed to develop an aluminium metal matrix composite that can be used in the marine industry (ship decks and hulls) using the FSP technique. Predetermined objectives were used to accomplish this aim. These objectives included optimising process parameters using the Taguchi method to find the best conditions for fabricating the required aluminium metal matrix composites (AMMCs). Once the best process parameters were determined, these parameters were then used to fabricate an aluminium metal matrix composite using AA5083 as the parental/base material and SiC as well as Coal as reinforcement. After the fabrication of AMMCs, a comparative analysis was conducted between the data from the AA5083/SiC composite joints and the data from the AA5083/Coal composite joints. The comparison was performed through the analysis of metallographic and mechanical tests. The test comprised X-ray diffraction (XRD) analysis, macro- and microstructural analyses, bending and tensile tests, fracture surface morphology and Vickers hardness tests. The base material findings were provided to make these evaluations clearer and easier to understand. Based on the research results, the following conclusions were made:

The XRD analysis of the AA5083 base alloy and its composites revealed the presence of various phases, including Al-metallic, $Al_6Mn$, AlMnFe, Al3Mg2, $Al_3Si$, Al2O3, Mg2Si, Al4C3 and amorphous carbon. These phases significantly influence the mechanical properties, thermal conductivity and corrosion resistance of the materials. The base alloy's intermetallic phases play a crucial role in its strength and corrosion resistance. In the composites, the formation of $Al_2O_3$, $Al_3Si$ and $Mg_2Si$ enhances hardness, wear resistance and grain refinement. The presence of $Al_4C_3$ in the coal composite improves wear resistance and thermal stability. The amorphous carbon contributes to the overall properties of the composite. Further research is needed to fully understand the interplay of these phases and optimise the performance of these materials for specific applications.

The non-uniform distribution of reinforcement particles, including agglomeration, negatively impacted the mechanical properties of the composites. Despite this adverse effect, FSP successfully induced dynamic recrystallisation, leading to a refined grain structure in the stir zone. The addition of SiC and Coal particles resulted in significant grain refinement compared to that experienced on the base material and the AA5083/Coal composite. The average mean grain size of AA5083-H111 was 61.292 µm. The average mean grain size of the AA5083/SiC composite joints was significantly refined to 31.148 µm. The average mean grain size of the AA5083/Coal composite joints was significantly refined to 31.173 µm. The AA5083/SiC composite showed a 50.819% reduction, while the AA5083/Coal composite showed a 50.8598% reduction.

The maximum tensile properties achieved for the AA5083-H111 were UTS of 311 MPa, yield strength of 248.8 MPa and strain rate of 58.65 %. The maximum tensile properties of the AA5083/SiC composite joint were a UTS of 281 MPa, yield strength of 224.8 MPa and a strain rate of 31.49 %, while for the AA5083/Coal composite joints were 282 MPa UTS, 225.6 MPa yield strength and 33.48 % strain. The tensile results that were obtained correlate with the grain sizes of the different joints. When comparing the AA5083/SiC composite and AA5083/Coal composite average findings, the AA5083/SiC composite joints had the highest tensile 275 MPa, yield strengths of 220 MPA and strain of 27.1%. The addition of reinforcements did not enhance the tensile strength and strain of the base material. Both composites exhibited respectable ultimate tensile strength values, although slightly lower than

the base material. The AA5083/SiC composite showed an 11.576% reduction, while the AA5083/Coal composite showed a 21.318% reduction. This reduction in tensile strength may be attributed to the presence of agglomerated reinforcement particles in the NZ that can act as stress concentrators and lead to premature failure. The fracture surfaces of the AA5083/SiC and AA5083/Coal composites exhibited microvoids, rough surfaces, dimples and particle clusters. These features indicate a mixed-mode fracture mechanism that involves both ductile and brittle failure.

The average hardness size of AA5083-H111 was 90.57 HV. The AA5083/SiC composite joints averaged 92.57 HV, while the AA5083/Coal composite joints averaged 91.42 HV. When compared to AA5083-H111, both the AA5083/SiC composite and AA5083/Coal composite joints increased the hardness of the NZ, with the AA5083SIC composite exhibiting a greater increase. Although the results for AA5083/Coal composite joints were not as excellent as those for AA5083/SiC composite joints, the outcomes were better when compared to those for AA5083-H111. The addition of different reinforcements had a significant influence on the hardness of the composite joints. The SZ hardness was approximately 1.0221 times higher than the base material hardness for AA5083/SiC composites and 1.0092 times higher for AA5083/Coal composites. The enhanced hardness can be attributed to microstructural refinement through dynamic recrystallisation and intermetallic particle fragmentation/ redistribution and dislocation pinning by reinforcement particles. According to the Orowam mechanism and Hall-Petch relationship, the hardness results correlated with grain sizes.

The behaviour of joints when subjected to bending also was investigated. After the bending test, the deflection was detected in various locations of the joints, with some joints exhibiting fractures and others being crack-free. During the analysis, there was no noticeable pattern in flexural strength. The results of the flexural testing for the AA5083-H111 revealed a maximum UFS of 415.20 MPa with an MFS of 26.82% for specimens. The AA5083/SiC composite joint exhibited the highest ultimate flexural strength (UFS) for both face and root specimens. The AA5083/SiC composite joint exhibited superior performance, with the face specimens achieving a maximum UFS of 765 MPa, significantly higher than the 632.78 MPa of the root specimens. This 132.22 MPa difference highlights the variation in mechanical properties along the joint length. The AA5083/Coal composite joint exhibited a significant difference in UFS between the face and root specimens. The face specimens achieved a maximum UFS of 747.53 MPa, while the root specimens reached a maximum UFS of 631.95 MPa, resulting in a difference of 115.58 MPa. The base material, AA5083-H111, exhibited a higher strain rate than both composites. The AA5083/SiC composite also demonstrated a higher strain rate than the AA5083/Coal composite. Compared to the AA5083/SiC composite, the UFS's findings on the AA5083/Coal composite were the most improved.

The study successfully fabricated AA5083-based AMMCs using FSP with SiC and coal reinforcements. It can be concluded that incorporating reinforcement on the FSWed joint, utilising FSP as its fabrication process, influences the mechanical parameters of the joint. This was demonstrated by comparing the base material results to those of the fabricated aluminium metal matrix composite (AA5083/SiC and AA5083/Coal). Both AA5083/SiC and AA5083/Coal composites refined the grain size and enhanced the hardness values compared to the unreinforced base material AA5083-H111 because of the addition of the reinforcements. The AA5083/SiC and AA5083/Coal composites exhibited comparable mechanical properties to the base material, AA5083-H111, in terms of ultimate tensile strength. While slightly lower than those of the base material, both composites maintained respectable UTS values. The fracture surface analysis revealed a mixed-mode fracture mechanism for both AA5083/SiC and AA5083/Coal composites. The presence of microvoids, rough surfaces, dimples and particle clusters indicated a combination of ductile and brittle failure. Both AMMCs demonstrated improved flexural strength compared to the base material. The AA5083/SiC exhibited better results than those of AA5083/Coal.

## 5.2 Recommendations

The following recommendations are proposed based on the research findings:

**To further optimise the fabrication of aluminium metal matrix composites, it is recommended to:**

1. Investigate the impact of tool geometry (slot or drill) on joint quality:

    - Different tool geometries can significantly influence the material flow, heat generation and microstructure. Optimising tool geometry can lead to improved mechanical properties and reduced defect formation.

2. Conduct a comparative study of submerged and normal FSP:

    - By comparing the mechanical properties and microstructural characteristics of composites produced using these two techniques, it is possible to identify the most effective process for achieving optimal performance.

**To improve the mechanical properties of the fabricated aluminium metal matrix composites, it is recommended to:**

1. Evaluate the influence of multiple FSP passes:

    - Multiple passes can enhance the uniformity of particle distribution and refine the microstructure, thereby improving the mechanical properties of the composite.

2. Explore advanced FSP methods:

    - It is recommended that future research explore advanced friction stir processing (FSP) techniques such as Laser-Assisted FSP (LA-FSP), Ultrasonic-Assisted FSP (UA-FSP), and Friction Stir Extrusion (FSE), along with emerging assisted methods like Multi-pass FSP and Vibration-Assisted FSP. These approaches have the potential to enhance particle dispersion, refine grain structures, and improve the overall mechanical performance of the composites. Future studies should focus on evaluating the effects of these techniques on the microstructure, mechanical properties, and wear behavior of the materials. In addition, process parameter optimization for each method, comparative performance analysis with conventional FSP, and the development of predictive models linking processing parameters to material behavior should form the core objectives of subsequent investigations.

By systematically exploring these recommendations, the potential for significant improvements in AMMCs properties can be realised.

# REFERENCES


1. Hambali, A., Sapuan, S.M., Ismail, N. and Nukman, Y., **2010**. Material selection of polymeric composite automotive bumper beam using analytical hierarchy process. *Journal of the Central South University of Technology*, *17*(2), pp.244-256.

2. Kundurti, S.C., Sharma, A., Tambe, P. and Kumar, A., **2022**. Fabrication of surface metal matrix composites for structural applications using friction stir processing–a review. *Materials Today: Proceedings*, *56*, pp.1468-1477.

3. Sharma, A.K., Bhandari, R., Aherwar, A. and Rimašauskienė, R., **2020**. Matrix materials used in composites: A comprehensive study. *Materials Today: Proceedings*, *21*, pp.1559-1562.

4. Pandey, P.C., **2004**. Composite materials, web-based course. *Dept. of Civil Engineering IISc Bangalore: India*.

5.Surappa, M.K., **2003**. Aluminium matrix composites: Challenges and opportunities. *Sadhana*, *28*(1), pp.319-334.

6. Dwivedi, S.P., Sahu, R. and Srivastava, A.K., **2018**. Microstructure and Thermal Expansion Behaviour of Hybrid Composite Material. *International Journal of Engineering & Technology*, *7*(4.39), pp.420-422.

7. Benal, M.M. and Shivanand, H.K., **2006**. Influence of heat treatment on the coefficient of thermal expansion of Al (6061) based hybrid composites. *Materials Science and Engineering: A*, *435*, pp.745-749.

8. Mishra, A.K. and Srivastava, R.K., **2017**. Wear behaviour of Al-6061/SiC metal matrix composites. *Journal of The Institution of Engineers (India): Series C*, *98*(2), pp.97-103.

9. Ramanathan, A., Krishnan, P.K. and Muraliraja, R., **2019**. A review on the production of metal matrix composites through stir casting–Furnace design, properties, challenges, and research opportunities. *Journal of Manufacturing processes*, *42*, pp.213-245.

10. Ramnath, B.V., Elanchezhian, C., Annamalai, R.M., Aravind, S., Atreya, T.S.A., Vignesh, V., and Subramanian, C., **2014**. Aluminium metal matrix composites–a review. *Rev. Adv. Mater. Sci*, *38*(5), pp.55-60.

11. Hashim, J., Looney, L. and Hashmi, M.S.J., **1999**. Metal matrix composites: production by the stir casting method. *Journal of materials processing technology*, *92*, pp.1-7.

12. Davim, J.P. and Gupta, K. eds., **2021**. *Advanced welding and deforming* (pp. 67-104). Amsterdam, The Netherlands: Elsevier.

13. Pooja, K., Tarannum, N. and Chaudhary, P., **2025**. Metal matrix composites: revolutionary materials for shaping the future. *Discover Materials*, *5*(1), p.35.

14. Sayuti, M., Sulaiman, S., Baharudin, B.T.H.T. and Arifin, M.K.A., **2016**. Metal matrix composite products by vibration casting method.

15. Kaur, K. and Pandey, O.P., **2010**. Microstructural characteristics of spray formed zircon sand reinforced LM13 composite. *Journal of alloys and compounds*, *503*(2), pp.410-415.

16. Sree Manu, K.M., Ajay Raag, L., Rajan, T.P.D., Gupta, M. and Pai, B.C., **2016**. Liquid metal infiltration processing of metallic composites: a critical review. *Metallurgical and Materials Transactions B*, *47*, pp.2799-2819.

17. Ejiofo, J.U., Okorie, B.A. and Reddy, R.G., **1997**. Powder processing and properties of zircon-reinforced Al-13.5 Si-2.5 Mg alloy composites. *Journal of materials engineering and performance*, *6*, pp.326-334.

18. Abdizadeh, H., Ashuri, M., Moghadam, P.T., Nouribahadory, A. and Baharvandi, H.R., **2011**. Improvement in physical and mechanical properties of aluminum/zircon composites fabricated by powder metallurgy method. *Materials & Design*, *32*(8-9), pp.4417-4423.

19. Suryanarayana, C., **2019**. Mechanical alloying: a novel technique to synthesize advanced materials. *Research*.

20. Kumar, A., Vichare, O., Debnath, K. and Paswan, M., **2021**. Fabrication methods of metal matrix composites (MMCs). *Materials Today: Proceedings*, *46*, pp.6840-6846.

21. Fauchais, P. and Vardelle, M., **1994**. Plasma spraying: present and future. *Pure and Applied Chemistry*, *66*(6), pp.1247-1258.

22. Pawlowski, L., **2008**. *The science and engineering of thermal spray coatings*. John Wiley & Sons.

23. Reddy, B.S.B., Das, K. and Das, S., **2007**. A review on the synthesis of in situ aluminum based composites by thermal, mechanical and mechanical–thermal activation of chemical reactions. *Journal of Materials Science*, *42*, pp.9366-9378.

24. Doherty, R.D., Hughes, D.A., Humphreys, F.J., Jonas, J.J., Jensen, D.J., Kassner, M.E., King, W.E., McNelley, T.R., McQueen, H.J and Rollett, A.D., **1997**. Current issues in recrystallization: A review. *Materials Science and Engineering: A*, *238*, pp. 219–274.

25. Sanusi, K.O. and Akinlabi, E.T., **2017**. Friction-stir processing of a composite aluminium alloy (AA 1050) reinforced with titanium carbide powder. *Materiali in tehnologije*, *51*(3), pp.427-435.

26. Fatchurrohman, N., Farhana, N. and Marini, C.D., **2018**, March. Investigation of the effect of friction stir processing parameters on microstructure and micro-hardness of rice husk ash reinforced Al6061 metal matrix composites. In *IOP Conference Series: Materials Science and Engineering* (Vol. 319, No. 1, p. 012032). IOP Publishing.

27. Dinaharan, I., **2016**. Influence of ceramic particulate type on microstructure and tensile strength of aluminium matrix composites produced using friction stir processing. *Journal of Asian Ceramic Societies*, *4*(2), pp.209-218.

28. Mabuwa, S. and Msomi, V., **2019**. Effect of Friction Stir Processing on Gas Tungsten Arc-Welded and Friction Stir-Welded 5083-H111 Aluminium Alloy Joints. *Advances in Materials Science and Engineering*, *2019*(1), p.3510236.

29. Mabuwa, S. and Msomi, V., **2020**. The effect of friction stir processing on the friction stir welded AA1050-H14 and AA6082-T6 joints. *Materials Today: Proceedings*, *26*, pp.193-199.

30. Msomi, V., Mbana, N. and Mabuwa, S., **2020**. Microstructural analysis of the friction stir welded 1050-H14 and 5083-H111 aluminium alloys. *Materials Today: Proceedings*, *26*, pp.189-192.

31. Sahraeinejad, S., Izadi, H., Haghshenas, M. and Gerlich, A.P., **2015**. Fabrication of metal matrix composites by friction stir processing with different particles and processing parameters. *Materials Science and Engineering: A*, *626*, pp.505-513.

32. Moharrami, A., Razaghian, A., Paidar, M., Šlapáková, M., Ojo, O.O. and Taghiabadi, R., **2020**. Enhancing the mechanical and tribological properties of $Mg_2Si$-rich aluminium alloys by multi-pass friction stir processing. *Materials Chemistry and Physics*, *250*, p.123066.

33. Palani, K., Elanchezhian, C., Ramnath, B.V., Bhaskar, G.B. and Naveen, E., **2018**. Effect of pin profile and rotational speed on microstructure and tensile strength of dissimilar AA8011, AA01-T6 friction stir welded aluminium alloys. *Materials Today: Proceedings*, *5*(11), pp.24515-24524.

34. Eskandari, H., Taheri, R. and Khodabakhshi, F., **2016**. Friction-stir processing of an AA8026-$TiB_2$-$Al_2O_3$ hybrid nanocomposite: Microstructural developments and mechanical properties. *Materials Science and Engineering: A*, *660*, pp.84-96.

35. Shunmugasundaram, M., Kumar, A.P., Amudhavalli, N.K. and Sivasankar, S., **2020**. Parametric optimization on tensile strength of friction stir butt joints of dissimilar AA6061 and AA5052 aluminium alloys by Taguchi technique. *Materials Today: Proceedings*, *27*, pp.1258-1262.

36. Yang, K., Li, W., Huang, C., Yang, X. and Xu, Y., **2018**. Optimization of cold-sprayed AA2024/$Al_2O_3$ metal matrix composites via friction stir processing: Effect of rotation speeds. *Journal of materials science & technology*, *34*(11), pp.2167-2177.

37. Thankachan, T., Prakash, K.S. and Kavimani, V., **2019**. Investigating the effects of hybrid reinforcement particles on the microstructural, mechanical, and tribological properties of friction stir processed copper surface composites. *Composites Part B: Engineering*, *174*, p.107057.

38. Zhou, M.Y., Ren, L.B., Fan, L.L., Zhang, Y.W.X., Lu, T.H., Quan, G.F. and Gupta, M., **2020**. Progress in research on hybrid metal matrix composites. *Journal of Alloys and Compounds*, *838*, p.155274.

39. Zhang, H., Zhang, B., Gao, Q., Song, J., and Han, G., **2021**. A review of microstructures and properties of graphene-reinforced aluminium matrix composites fabricated by friction stir processing. *Journal of Manufacturing Processes*, *68*, pp.126-135.

40. Sharma, S., Singh, J., Gupta, M.K., Mia, M., Dwivedi, S.P., Saxena, A., Chattopadhyaya, S., Singh, R., Pimenov, D.Y. and Korkmaz, M.E., **2021**. Investigation of mechanical, tribological, and microstructural properties of Al-Mg-Si–T6/SiC/muscovite-hybrid metal-matrix composites for high-strength applications. *Journal of Materials Research and Technology*, *12*, pp.1564-1581.

41. Li, X., Zhang, Z., Peng, Y., Yan, D., Tan, Z., Zhou, Q. and Wang, K., **2021**. In situ synthesized nano-$Al_4C_3$ reinforced aluminium matrix composites via friction stir processing. *Journal of Materials Research and Technology*, *14*, pp.2658-2664.

42. Ikumapayi, O.M., Akinlabi, E.T., Pal, S.K. and Majumdar, J.D., **2019**. A survey on reinforcements used in friction stir processing of aluminium metal matrix and hybrid composites. *Procedia Manufacturing*, *35*, pp.935-940.

43. Venkataiah, M., Anup Kumar, T., Venkata Rao, K., Anand Kumar, S., Siva, I. and Ratna Sunil, B., **2019**. Effect of grain refinement on corrosion rate, mechanical and machining behavior of friction stir processed ZE41 Mg alloy. *Transactions of the Indian Institute of Metals*, *72*(1), pp.123-132.

44. Roy, P., Singh, S. and Pal, K., **2019**. Enhancement of mechanical and tribological properties of SiC-and CB-reinforced aluminium 7075 hybrid composites through friction stir processing. *Advanced Composite Materials*, *28*(sup1), pp.1-18.

45. Mishra, R.S. and Ma Z.Y., **2005**. Friction stir welding and processing. *Materials Science and Engineering R*, *50*, pp.1-78.

46. Kondaiah, V.V., Pavanteja, P., Manvit, M.M., Kumar, R.R., Kumar, R.G. and Sunil, B.R., **2019**. Surface engineering of ZE 41 Mg alloy by friction stir processing: Effect of process parameters on microstructure and hardness evolution. *Materials Today: Proceedings*, *18*, pp.125-131.

47. Rathee, S., Maheshwari, S. and Siddiquee, A.N., **2018**. Issues and strategies in composite fabrication via friction stir processing: A review. *Materials and Manufacturing Processes*, *33*(3), pp.239-261.

48. Baisane, V.P., Sable, Y.S., Dhobe, M.M. and Sonawane, P.M., **2015**. Recent development and challenges in the processing of ceramics reinforced Al matrix composite through stir casting process: A Review. *International Journal of Engineering and Applied Sciences*, *2*(10), p.257814.

49. Reddy, K.S.T., Manohar, H.S., Manjunath, G. and Babu, K.A., **2021**. Synthesis and characterization of silicon nitride and graphite-reinforced aluminium hybrid metal matrix composites. *Materials Today: Proceedings*, *45*, pp.304-306.

50. Callister, W.D. and Rethwisch, D.G., **1999**. *Materials science and engineering: an introduction* (pp. 123-133). New York: Wiley.

51. Clyne, T.W. and Hull, D., **2019**. *An introduction to composite materials*. Cambridge university press.

52. Miracle, D.B., **2005**. Metal matrix composites–from science to technological significance. *Composites science and technology*, *65*(15-16), pp.2526-2540.

53. Chawla, K.K., **2012**. *Composite materials: science and engineering*. Springer Science & Business Media.

54. Sharma, N., Saxena, T., Alam, S.N., Ray, B.C., Biswas, K. and Jha, S.K., **2022**. Ceramic-based nanocomposites: A perspective from carbonaceous nanofillers. *Materials Today Communications*, *31*, p.103764.

55. Ruys, A.J., **2018**. *Alumina ceramics: biomedical and clinical applications*. Woodhead Publishing.

56. Guo, J.F., Liu, J., Sun, C.N., Maleksaeedi, S., Bi, G., Tan, M.J. and Wei, J., **2014**. Effects of nano-$Al_2O_3$ particle addition on grain structure evolution and mechanical behaviour of friction-stir-processed Al. *Materials Science and Engineering: A*, *602*, pp.143-149.

57. Mazaheri, Y., Karimzadeh, F. and Enayati, M.H., **2011**. A novel technique for the development of A356/$Al_2O_3$ surface nanocomposite by friction stir processing. *Journal of materials processing technology*, *211*(10), pp.1614-1619.

58. Shafiei-Zarghani, A., Kashani-Bozorg, S.F. and Zarei-Hanzaki, A., **2009**. Microstructures and mechanical properties of Al/$Al_2O_3$ surface nano-composite layer produced by friction stir processing. *Materials Science and Engineering: A*, *500*(1-2), pp.84-91.

59. Eom, J.H., Kim, Y.W. and Raju, S., **2013**. Processing and properties of macroporous silicon carbide ceramics: A review. *Journal of Asian Ceramic Societies*, *1*(3), pp.220-242.

60. Sharma, A., Narsimhachary, D., Sharma, V.M., Sahoo, B. and Paul, J., **2019**. Surface modification of Al6061-SiC surface composite through impregnation of graphene, graphite & carbon nanotubes via FSP: a tribological study. *Surface and Coatings Technology*, *368*, pp.175-191.

61. Ghanbari, D., Asgarani, M.K., Amini, K. and Gharavi, F., **2017**. Influence of heat treatment on mechanical properties and microstructure of the Al2024/SiC composite produced by multi–pass friction stir processing. *Measurement*, *104*, pp.151-158.

62. Rathee, S., Maheshwari, S., Siddiquee, A.N. and Srivastava, M., **2017**. Investigating effects of groove dimensions on microstructure and mechanical properties of AA6063/SiC surface composites produced by friction stir processing. *Transactions of the Indian Institute of Metals*, *70*, pp.809-816.

63. Wang, W., Shi, Q.Y., Liu, P., Li, H.K. and Li, T., **2009**. A novel way to produce bulk SiCp reinforced aluminium metal matrix composites by friction stir processing. *Journal of materials processing technology*, *209*(4), pp.2099-2103.

64. Della Bona, A., Pecho, O.E. and Alessandretti, R., **2015**. Zirconia as a dental biomaterial. *Materials*, *8*(8), pp.4978-4991.

65. Mirjavadi, S.S., Alipour, M., Hamouda, A.M.S., Matin, A., Kord, S., Afshari, B.M. and Koppad, P.G., **2017**. Effect of multi-pass friction stir processing on the microstructure, mechanical, and wear properties of AA5083/$ZrO_2$ nanocomposites. *Journal of Alloys and Compounds*, *726*, pp.1262-1273.

66. Yadav, D. and Bauri, R., **2015**. Development of Cu particles and Cu core-shell particles reinforced Al composite. *Materials Science and Technology*, *31*(4), pp.494-500.

67. Yadav, D. and Bauri, R., **2011**. Processing, microstructure, and mechanical properties of nickel particles embedded aluminium matrix composite. *Materials Science and Engineering: A*, *528*(3), pp.1326-1333.

68. Dixit, M., Newkirk, J.W. and Mishra, R.S., **2007**. Properties of friction stir-processed Al 1100–NiTi composite. *Scripta Materialia*, *56*(6), pp.541-544.

69. Ni, D.R., Wang, J.J., Zhou, Z.N. and Ma, Z.Y., **2014**. Fabrication and mechanical properties of bulk NiTip/Al composites prepared by friction stir processing. *Journal of Alloys and Compounds*, *586*, pp.368-374.

70. Selvakumar, S., Dinaharan, I., Palanivel, R. and Babu, B.G., **2017**. Development of stainless steel particulate reinforced AA6082 aluminium matrix composites with enhanced ductility using friction stir processing. *Materials Science and Engineering: A*, *685*, pp.317-326.

71. Du, Z., Tan, M.J., Guo, J.F., Bi, G. and Wei, J., **2016**. Fabrication of a new Al-$Al_2O_3$-CNTs composite using friction stir processing (FSP). *Materials Science and Engineering: A*, *667*, pp.125-131.

72. Lim, D.K., Shibayanagi, T. and Gerlich, A.P., **2009**. Synthesis of multi-walled CNT reinforced aluminium alloy composite via friction stir processing. *Materials Science and Engineering: A*, *507*(1-2), pp.194-199.

73. Hosseini, S.A., Ranjbar, K., Dehmolaei, R. and Amirani, A.R., **2015**. Fabrication of Al5083 surface composites reinforced by CNTs and cerium oxide nano particles via friction stir processing. *Journal of Alloys and Compounds*, *622*, pp.725-733.

74. Jeon, C.H., Jeong, Y.H., Seo, J.J., Tien, H.N., Hong, S.T., Yum, Y.J., Hur, S.H. and Lee, K.J., **2014**. Material properties of graphene/aluminium metal matrix composites fabricated by friction stir processing. *International journal of precision engineering and manufacturing*, *15*, pp.1235-1239.

75. Sharma, A., Sharma, V.M., Sahoo, B., Pal, S.K. and Paul, J., **2019**. Effect of multiple micro channel reinforcement filling strategy on Al6061-graphene nanocomposite fabricated through friction stir processing. *Journal of Manufacturing Processes*, *37*, pp.53-70.

76. Mostafapour Asl, A. and Khandani, S.T., **2013**. Role of hybrid ratio in microstructural, mechanical, and sliding wear properties of the Al5083/Graphite/$Al_2O_3$p a surface hybrid nanocomposite fabricated via friction stir processing method. *Materials Science and Engineering. A, Structural Materials: Properties, Microstructure and Processing*, *559*.

77. Dinaharan, I., Kalaiselvan, K., Akinlabi, E.T. and Davim, J.P., **2017**. Microstructure and wear characterization of rice husk ash reinforced copper matrix composites prepared using friction stir processing. *Journal of Alloys and Compounds*, *718*, pp.150-160.

78. Dinaharan, I., Nelson, R., Vijay, S.J. and Akinlabi, E.T., **2016**. Microstructure and wear characterization of aluminium matrix composites reinforced with industrial waste fly ash particulates synthesized by friction stir processing. *Materials Characterization*, *118*, pp.149-158.

79. Wu, T. and Zhang, K., **2023**. Corrosion and protection of magnesium alloys: recent advances and future perspectives. *Coatings*, *13*(9), p.1533.

80. Xi, R. and Li, Y., **2025**. Recent Advances in the Performance and Mechanisms of High-Entropy Alloys Under Low-and High-Temperature Conditions. *Coatings*, *15*(1), p.92.

81. Kurbanbekov, S., Kozhakhmetov, Y., Skakov, M., Seitov, B., Aidarova, M. and Tabiyeva, Y., **2024**. Properties, Advantages, and Prospects of Using Cobalt-Free Composites Based on Tungsten Carbide in Industry. *Materials*, *18*(1), p.129.

82. Clyne, T.W. and Withers, P.J., **1993**. *An introduction to metal matrix composites*. Cambridge university press.

83. Alloys, H.S.A.P.M., **1990**. Properties and selection: Nonferrous alloys and special-purpose materials.

84. Sharma, A.K., Bhandari, R. and Pinca-Bretotean, C., **2021**, February. Impact of silicon carbide reinforcement on characteristics of aluminium metal matrix composite. In *Journal of Physics: Conference Series* (Vol. 1781, No. 1, p. 012031). IOP Publishing.

85. Selvamani, S.T., **2021**. Microstructure and stress corrosion behaviour of CMT welded AA6061 T-6 aluminium alloy joints. *Journal of Materials Research and Technology*, *15*, pp.315-326.

86. Zukor, L.J., **1960**. Nature and properties of engineering materials. ZD Jastrzebski. Wiiey, New York-London, 1959, xvii+ 571 pp. $11.00.

87. Bindu, A.H., Chaitanya, B.S.K., Ajay, K. and Sudhakar, I., **2020**. Investigation on feasibility of dissimilar welding of AA2124 and AA7075 aluminium alloy using tungsten inert gas welding. *Materials Today: Proceedings*, *26*, pp.2283-2288.

88. Aluminum Association, **1984**. *Aluminum: properties and physical metallurgy*. ASM international.

89. Davis, J.R., **1993**. *Aluminum and aluminum alloys*. ASM international.

90. Muribwathoho, O., Msomi, V. and Mabuwa, S., **2024**. Optimization and Regression Analysis of Friction Stir Processing Parameters of AA5083/Coal Composites for Marine Applications. *Crystals*, *15*(1), p.34.

91. Reddy, M.N., Reddy, M.N., Kumar, K.V. and Garre, P., **2014**. Experimental investigation of tensile strength on Al 6351 to the aerospace structural applications. *International Journal of Mechanical Engineering and Technology (IJMET)*, *5*(2), pp.110-114.

92. Rodrıguez-Castro, R., Wetherhold, R.C. and Kelestemur, M.H., **2002**. Microstructure and mechanical behavior of functionally graded Al A359/SiCp composite. *Materials Science and Engineering: A*, *323*(1-2), pp.445-456.

93. Alza, V.A., **2021**. Aging of Cast Aluminum Alloy A356: Effects on Mechanical Properties and Microstructure. *J. Mech. Eng. Sci.*, *18*, pp.54-65.

94. Taya, M. and Arsenault, R.J., **2016**. Metal matrix composites: thermomechanical behavior. Elsevier.

95. Rajan, T.P.D., Pillai, R.M. and Pai, B.C., **1998**. Reinforcement coatings and interfaces in aluminium metal matrix composites. *Journal of materials science*, *33*, pp.3491-3503.

96. Baradeswaran, A. and Perumal, A.E., **2014**. Study on mechanical and wear properties of Al 7075/$Al_2O_3$/graphite hybrid composites. *Composites Part B: Engineering*, *56*, pp.464-471.

97. Rao, R.N., Das, S. and Krishna, P.V., **2008**. Experimental investigation on the influence of SiC particulate reinforcement in aluminium alloy composites. *Proceedings of the Institution of Mechanical Engineers, Part J: Journal of Engineering Tribology*, *222*(1), pp.1-6.

98. Senthilkumar, M., Saravanan, S.D. and Shankar, S., **2015**. Dry sliding wear and friction behavior of aluminium–rice husk ash composite using Taguchi's technique. *Journal of composite materials*, *49*(18), pp.2241-2250.

99. Reeb, A., Walter, V., Schulze, V. and Weidenmann, K.A., **2016**. Characterization of a hybrid $Al_2O_3$–aluminium matrix composite manufactured via composite extrusion. *Journal of Composite Materials*, *50*(8), pp.1099-1108.

100. Mistry, J.M. and Gohil, P.P., **2017**. An overview of diversified reinforcement on aluminium metal matrix composites: Tribological aspects. *Proceedings of the Institution of Mechanical Engineers, Part J: Journal of Engineering Tribology*, *231*(3), pp.399-421.

101. Das, D.K., Mishra, P.C., Singh, S. and Pattanaik, S., **2014**. Fabrication and heat treatment of ceramic-reinforced aluminium matrix composites-a review. *International Journal of Mechanical and Materials Engineering*, *9*, pp.1-15.

102. Hu, Q., Zhao, H. and Li, F., **2016**. Effects of manufacturing processes on microstructure and properties of Al/A356–B4C composites. *Materials and manufacturing processes*, *31*(10), pp.1292-1300.

103. Sahu, M.K. and Sahu, R.K., **2018**. Fabrication of aluminum matrix composites by stir casting technique and stirring process parameters optimization. *Advanced casting technologies*, pp.111-123.

104. Srivatsan, T.S. and Lavernia, E.J., **1992**. Use of spray techniques to synthesize particulate-reinforced metal-matrix composites. *Journal of materials science*, *27*, pp.5965-5981.

105. Grant, P.S., **2007**. Solidification in spray forming. *Metallurgical and Materials transactions A*, *38*, pp.1520-1529.

106. Etemadi, R., Wang, B., Pillai, K.M., Niroumand, B., Omrani, E. and Rohatgi, P., **2018**. Pressure infiltration processes to synthesize metal matrix composites–A review of metal matrix composites, the technology and process simulation. *Materials and Manufacturing Processes*, *33*(12), pp.1261-1290.

107. Klier, E.M., Mortensen, A., Cornie, J.A. and Flemings, M.C., **1991**. Fabrication of cast particle-reinforced metals via pressure infiltration. *Journal of materials science*, *26*, pp.2519-2526.

108. Sadeghi, B. and Cavaliere, P., **2023**. Making ultra-high strengthening and toughening efficiency in hybrid reinforcing of aluminum laminated composites via dispersion engineering. *Advanced Powder Technology*, *34*(12), p.104263.

109. Zhang, J., Zhang, X., Qian, M., Jia, Z., Imran, M. and Geng, L., **2024**. Recent progress in particulate reinforced aluminum composites fabricated via spark plasma sintering: Microstructure and properties. *Critical Reviews in Solid State and Materials Sciences*, *49*(3), pp.408-463.

110. Zhang, X., Shi, C., Liu, E., Zhao, N. and He, C., **2018**. Effect of interface structure on the mechanical properties of graphene nanosheets reinforced copper matrix composites. *ACS applied materials & interfaces*, *10*(43), pp.37586-37601.

111. Varol, T.E.M.E.L. and Canakci, A.Y.K.U.T., **2013**. Effect of weight percentage and particle size of B 4 C reinforcement on physical and mechanical properties of powder metallurgy Al2024-B 4 C composites. *Metals and Materials International*, *19*, pp.1227-1234.

112. Aghajani, S., Pouyafar, V., Meshkabadi, R., Volinsky, A.A. and Bolouri, A., **2023**. Mechanical characterization of high volume fraction Al7075-Al2O3 composite fabricated by semisolid powder processing. *The International Journal of Advanced Manufacturing Technology*, *125*(5), pp.2569-2580.

113. Zhang, L., Shi, J., Shen, C., Zhou, X., Peng, S. and Long, X., **2017**. B4C-Al composites fabricated by the powder metallurgy process. *Applied Sciences*, *7*(10), p.1009.

114. Canakci, A.Y.K.U.T., Erdemir, F.A.T.İ.H., Varol, T.E.M.E.L., Dalmış, R. and Ozkaya, S., **2014**. Effects of a new pre-milling coating process on the formation and properties of a Fe–Al intermetallic coating. *Powder Technology*, *268*, pp.110-117.

115. Canakci, A., Erdemir, F., Varol, T. and Ozkaya, S., **2013**. Formation of Fe–Al intermetallic coating on low-carbon steel by a novel mechanical alloying technique. *Powder Technology*, *247*, pp.24-29.

116. Canakci, A.Y.K.U.T., Erdemir, F.A.T.İ.H., Varol, T.E.M.E.L. and Ozkaya, S., **2014**. Effect of process parameters on the formation of Fe-Al intermetallic coating fabricated by mechanical alloying.

117. Canakci, A.Y.K.U.T., Varol, T.E.M.E.L., Erdemir, F.A.T.İ.H., Ozkaya, S. and Mindivan, H., **2014**. Microstructure and properties of Fe–Al intermetallic coatings on the low carbon steel synthesized by mechanical alloying. *The International Journal of Advanced Manufacturing Technology*, *73*, pp.849-858.

118. Kini, U.A., Sharma, S.S., Jagannath, K., Prabhu, P.R. and Shankar, G., **2015**. Characterization study of aluminium 6061 hybrid composite. *International Journal of Materials and Metallurgical Engineering*, *9*(6), pp.684-688.

119. Falsafi, J., Rosochowska, M., Jadhav, P. and Tricker, D., **2017**. Lower cost automotive piston from 2124/SiC/25p metal-matrix composite. *SAE International Journal of Engines*, *10*(4), pp.1984-1992.

120. Avci, U. and Temiz, S., **2017**. A new approach to the production of partially graded and laminated composite material composed of sic-reinforced 7039 al alloy plates at different rates. Compos B Eng 131:76–81

121. Lee, H., Choi, J.H., Jo, M.C., Jo, I., Lee, S.K. and Lee, S., **2018**. Effects of strain rate on compressive properties in bimodal 7075 Al–SiCp composite. *Metals and Materials International*, *24*(4), pp.894-903.

122. Rodrıguez-Castro, R., Wetherhold, R.C. and Kelestemur, M.H., **2002**. Microstructure and mechanical behavior of functionally graded Al A359/SiCp composite. *Materials Science and Engineering: A*, *323*(1-2), pp.445-456.

123. Surappa, M.K., **2008**. Dry sliding wear of fly ash particle reinforced A356 Al composites. *Wear*, *265*(3-4), pp.349-360.

124. Chakraborty, S., Kar, S., Ghosh, S.K. and Dey, V., **2017**. Parametric optimization of electric discharge coating on Aluminium-6351 alloy with green compact silicon carbide and copper tool: a Taguchi coupled utility concept approach. *Surfaces and Interfaces*, *7*, pp.47-57.

125. Nakamura, T., Obikawa, T., Nishizaki, I., Enomoto, M. and Fang, Z., **2018**. Friction stir welding of non-heat-treatable high-strength alloy 5083-O. *Metals*, *8*(4), p.208.

126. Nicholls, C.J., Boswell, B., Davies, I.J. and Islam, M.N., **2017**. Review of machining metal matrix composites. *The International Journal of Advanced Manufacturing Technology*, *90*(9), pp.2429-2441.

127. Rana, H. and Badheka, V., **2018**. Influence of friction stir processing conditions on the manufacturing of Al-Mg-Zn-Cu alloy/boron carbide surface composite. *Journal of Materials Processing Technology*, *255*, pp.795-807.

128. Zhao, Y., Huang, X., Li, Q., Huang, J. and Yan, K., **2015**. Effect of friction stir processing with $B_4C$ particles on the microstructure and mechanical properties of 6061 aluminium alloy. *The international journal of advanced manufacturing technology*, *78*, pp.1437-1443.

129. Daneshifar, M.H., Papi, A. and Alishahi, M., **2021**. Fabrication of Al-Si/$Mg_2Si$ in-situ composite by friction stir processing. *Materials Letters*, *282*, p.128832.

130. Huang, G. and Shen, Y., **2017**. The effects of processing environments on the microstructure and mechanical properties of the Ti/5083Al composites produced by friction stir processing. *Journal of Manufacturing Processes*, *30*, pp.361-373.

131. Moustafa, E.B. and Mosleh, A.O., **2020**. Effect of (Ti–B) modifier elements and FSP on 5052 aluminium alloy. *Journal of Alloys and Compounds*, *823*, p.153745.

132. Palanivel, R., Dinaharan, I., Laubscher, R.F. and Davim, J.P., **2016**. Influence of boron nitride nanoparticles on microstructure and wear behavior of AA6082/$TiB_2$ hybrid aluminium composites synthesized by friction stir processing. *Materials & Design*, *106*, pp.195-204.

133. Thangarasu, A., Murugan, N., Dinaharan, I. and Vijay, S.J., **2015**. Synthesis and characterization of titanium carbide particulate reinforced AA6082 aluminium alloy composites via friction stir processing. *Archives of Civil and Mechanical Engineering*, *15*(2), pp.324-334.

134. Huang, G., Hou, W. and Shen, Y., **2018**. Evaluation of the microstructure and mechanical properties of WC particle reinforced aluminium matrix composites fabricated by friction stir processing. *Materials characterization*, *138*, pp.26-37.

135. Sidhu, S.S., Batish, A. and Kumar, S., **2013**. Fabrication and electrical discharge machining of metal–matrix composites: A review. *Journal of Reinforced Plastics and Composites*, *32*(17), pp.1310-1320.

136. Arab, S.M., Karimi, S., Jahromi, S.A.J., Javadpour, S. and Zebarjad, S.M., **2015**. Fabrication of novel fiber reinforced aluminium composites by friction stir processing. *Materials Science and Engineering: A*, *632*, pp.50-57.

137. Adeqoyin, I., Mohamed, F.A. and Lavernia, E.J., **1991**. Particulate reinforced MMCs-A review. *J Mat Sci*, *26*, pp.1137-1156.

138. Xiong, B., Xu, Z., Yan, Q., Lu, B. and Cai, C., **2011**. Effects of SiC volume fraction and aluminium particulate size on interfacial reactions in SiC nanoparticulate reinforced aluminium matrix composites. *Journal of Alloys and Compounds*, *509*(4), pp.1187-1191.

139. Bushlya, V., Lenrick, F., Gutnichenko, O., Petrusha, I., Osipov, O., Kristiansson, S. and Stahl, J.E., **2017**. Performance and wear mechanisms of novel superhard diamond and boron nitride based tools in machining Al-SiCp metal matrix composite. *Wear*, *376*, pp.152-164.

140. Previtali, B., Pocci, D. and Taccardo, C., **2008**. Application of traditional investment casting process to aluminium matrix composites. *Composites Part A: Applied Science and Manufacturing*, *39*(10), pp.1606-1617.

141. Singh, J., Jawalkar, C.S. and Belokar, R.M., **2020**. Analysis of mechanical properties of AMC fabricated by vacuum stir casting process. *Silicon*, *12*, pp.2433-2443.

142. Gonfa, B.K., Sinha, D., Vates, U.K., Badruddin, I.A., Hussien, M., Kamangar, S., Singh, G.K., Ahmed, G.M.S., Kanu, N.J. and Hossain, N., **2022**. Investigation of mechanical and tribological behaviors of aluminum based hybrid metal matrix composite and multi-objective optimization. *Materials*, *15*(16), p.5607.

143. Shahraki, S., Khorasani, S., Abdi Behnagh, R., Fotouhi, Y. and Bisadi, H., **2013**. Producing of AA5083/$ZrO_2$ nanocomposite by friction stir processing (FSP). *Metallurgical and Materials Transactions B*, *44*, pp.1546-1553.

144. Liu, Q., Ke, L., Liu, F., Huang, C. and Xing, L., **2013**. Microstructure and mechanical property of multi-walled carbon nanotubes reinforced aluminium matrix composites fabricated by friction stir processing. *Materials & Design*, *45*, pp.343-348.

145. Morisada, Y., Fujii, H., Nagaoka, T., Nogi, K. and Fukusumi, M., **2007**. Fullerene/A5083 composites fabricated by material flow during friction stir processing. *Composites Part A: Applied Science and Manufacturing*, *38*(10), pp.2097-2101.

146. Özes, Ç. and Neşer, N., **2015**. Experimental study on steel to FRP bonded lap joints in marine applications. *Advances in Materials Science and Engineering*, *2015*(1), p.164208.

147. Cao, X., Wanjara, P., Huang, J., Munro, C. and Nolting, A., **2011**. Hybrid fiber laser–Arc welding of thick section high strength low alloy steel. *Materials & Design*, *32*(6), pp.3399-3413.

148. Starke Jr, E.A. and Rashed, H.M.M.A., **2017**. Alloys: aluminium.

149. Sielski, R.A., **2008**. Research needs in aluminium structure. *Ships and Offshore Structures*, *3*(1), pp.57-65.

150. Lamb, T., Beavers, N., Ingram, T. and Schmieman, A., **2011**. The benefits and cost impact of aluminium naval ship structure. *Journal of Ship Production and Design*, *27*(01), pp.35-49.

151. Altenburg, C.J. and Scott, R.J., **1971**. *Design Considerations for Aluminium Hull Structures-Study of Aluminium Bulk Carrier*. GIBBS AND COX INC NEW YORK.

152. Ertuğ, B. and Kumruoğlu, L.C., **2015**. 5083 type Al-Mg and 6082 type Al-Mg-Si alloys for ship building. *Am. J. Eng. Res*, *4*(3), pp.146-150.

153. Nik, W.W., Sulaiman, O., Fadhli, A. and Rosliza, R., **2010**. Corrosion behaviour of aluminum alloy in seawater. *Proceedings of MARTEC*, pp.175-180.

154. Skillingberg, M., **2004**. Making aluminium alloy selection easier. *Marine Log*.

155. **1998**, selection and application, The aluminium Association, Inc, Washington, D.C.

156. Romhanji, E. and Popovic, M., **2006**. Problems and the prospect of Al-Mg alloys application in marine constructions. *Metalurgija*, *12*(4), pp.297-307.

157. Raynaud, G.M. and Gomiero, P., **1997**. The potential of 5383 alloys in marine applications. *The! Aluminium Association (USA)*, pp.351-364.

158. Allan, R.G., **1997**. Applications for aluminium alloys in the marine industry a current perspective. *Proceedings of Alumitech*, *97*, p.292.

159. Dudzik, K. and Charchalis, A., **2013**. Mechanical properties of 5083, 5059, and 7020 aluminium alloys and their joints welded by FSW. *Journal of KONES*, *20*(2), pp.69-73.

160. Grujicic, M., Arakere, G., Yen, C.F. and Cheeseman, B.A., **2011**. Computational investigation of hardness evolution during friction-stir welding of AA5083 and AA2139 aluminium alloys. *Journal of Materials Engineering and Performance*, *20*(7), pp.1097-1108.

161. Galanis, K., **2007**. *Fracture of aluminium naval structures* (Doctoral dissertation, Massachusetts Institute of Technology).

162. Skillingberg, M., **2007**. Aluminium at sea: Speed, endurance, and affordability. *Marine Log*, *112*(5).

163. **2014**. Aluminium alloys for hull construction and marine structure, IACS Soc. Ships.

164. **2014**, Rules for materials welding part 2, American Bureau of Shipping, USA.

165. Epstein, S.G, Kaufman, J.G and Pollok, P, **1994**. Alluminium and its alloys, Aluminium Association Inc, Washington D.C.

166. Sharma, V., Prakash, U. and Kumar, B.M., **2015**. Microstructural and mechanical characteristics of AA2014/SiC surface composite fabricated by friction stir processing. *Materials Today Proceeding, 2*, pp. 2666–2670.

167. Ramesh, R. and Murugan, N., **2012**. Production and characterization of aluminium 7075–T651 alloy/$B_4C$ surface composite by friction stir processing. *International Journal of Engineering and Advanced Technology (IJEAT)*, *2*, pp.80-90.

168. García-Vázquez, F., Vargas-Arista, B., Muñiz, R., Ortiz, J.C., García, H.H. and Acevedo, J., **2016**. The role of friction stir processing (FSP) parameters on TiC reinforced surface Al7075-T651 aluminium alloy. *soldagem & inspeção*, *21*, pp.508-516.

169. Hamdollahzadeh, A., Bahrami, M., Nikoo, M.F., Yusefi, A., Givi, M.B. and Parvin, N., **2015**. Microstructure evolutions and mechanical properties of nano-SiC-fortified AA7075 friction stir weldment: The role of second pass processing. *Journal of Manufacturing Processes*, *20*, pp.367-373.

170. Bharti, S., Ghetiya, N.D. and Patel, K.M., **2020**. Micro-hardness and wear behavior of AA2014/$Al_2O_3$ surface composite produced by friction stir processing. *SN Applied Sciences*, *2*(11), pp.1-16.

171. Moustafa, E., **2017**. Effect of multi-pass friction stir processing on mechanical properties for AA2024/$Al_2O_3$ nanocomposites. *Materials*, *10*(9), p.1053.

172. Yang, K., Li, W., Xu, Y. and Yang, X., **2019**. Using friction stir processing to augment corrosion resistance of cold sprayed AA2024/$Al_2O_3$ composite coatings. *Journal of Alloys and Compounds*, *774*, pp.1223-1232.

173. Sharifitabar, M., Sarani, A., Khorshahian, S. and Afarani, M.S., **2011**. Fabrication of 5052Al/$Al_2O_3$ nanoceramic particle reinforced composite via friction stir processing route. *Materials & Design*, *32*(8-9), pp.4164-4172.

174. Mathur, V., Patel GC, M. and Shettigar, A.K., **2019**. Reinforcement of titanium dioxide nanoparticles in aluminium alloy AA 5052 through friction stir process. *Advances in Materials and Processing Technologies*, *5*(2), pp.329-337.

175. Dolatkhah, A., Golbabaei, P., Givi, M.B. and Molaiekiya, F., **2012**. Investigating effects of process parameters on microstructural and mechanical properties of Al5052/SiC metal matrix composite fabricated via friction stir processing. *Materials & Design*, *37,* pp.458-464

176. Khodabakhshi, F., Gerlich, A.P. and Švec, P., **2017**. Fabrication of a high-strength ultra-fine-grained Al-Mg-SiC nanocomposite by multi-step friction-stir processing. *Materials Science and Engineering: A*, *698*, pp.313-325.

177. Cao, X., Shi, Q., Liu, D., Feng, Z., Liu, Q. and Chen, G., **2018**. Fabrication of in situ carbon fiber/aluminium composites via friction stir processing: Evaluation of microstructural, mechanical, and tribological behaviors. *Composites Part B: Engineering*, *139*, pp.97-105.

178. Behnagh, R.A., Besharati Givi, M.K. and Akbari, M., **2012**. Mechanical properties, corrosion resistance, and microstructural changes during friction stir processing of 5083 aluminium rolled plates. *Materials and manufacturing processes*, *27*(6), pp.636-640.

179. Naghshehkesh, N., Mousavi, S.E., Karimzadeh, F., Ashrafi, A., Nosko, M., Trembošová, V. and Sadeghi, B., **2019**. Effect of graphene oxide and friction stir processing on microstructure and mechanical properties of Al5083 matrix composite. *Materials Research Express*, *6*(10), p.106566.

180. Mishra, R.S., Ma, Z.Y. and Charit, I., **2003**. Friction stir processing: a novel technique for fabrication of surface composite. *Materials Science and Engineering: A*, *341*(1-2), pp.307-310.

181. Deepak, D., Sidhu, R.S. and Gupta, V.K., **2013**. Preparation of 5083 Al-SiC surface composite by friction stir processing and its mechanical characterization. *International Journal of Mechanical Engineering*, *3*(1), pp.1-11.

182. Yuvaraj, N. and Aravindan, S., **2015**. Fabrication of Al5083/$B_4C$ surface composite by friction stir processing and its tribological characterization. *Journal of materials research and technology*, *4*(4), pp.398-410.

183. Jain, V.K.S., Muhammed, P.M., Muthukumaran, S. and Babu, S.P., **2018**. Microstructure, the mechanical and sliding wear behavior of AA5083–$B_4C$/SiC/TiC surface composites fabricated using friction stir processing. *Transactions of the Indian Institute of Metals*, *71*(6), pp.1519-1529.

184. Owa, T. and Shimizu, Y., **2018**. Fabrication and strength behavior of MWCNT-reinforced 5083 aluminum alloy composite via friction stir processing. *Materials transactions*, *59*(11), pp.1798-1804.

185. Prabhakar, G.V.N.B., Kumar, Y.P., Kumar, P.D., Kumar, B.P., Raju, M.G., Naseema, S., Kumar, N.R., Jagannatham, M. and Sunil, B.R., **2019**. Producing Al5083-CNT composites by friction stir processing: influence of grain refinement and CNT on mechanical and corrosion properties. *Materials Today: Proceedings*, *15*, pp.44-49.

186. Zohoor, M., Givi, M.B. and Salami, P., **2012**. Effect of processing parameters on the fabrication of Al-Mg/Cu composites via friction stir processing. *Materials & Design*, *39*, pp.358-365.

187. Bauri, R., Ram, G.J., Yadav, D. and Kumar, C.S., **2015**. Effect of process parameters and tool geometry on the fabrication of Ni particles reinforced 5083 Al composite by friction stir processing. *Materials Today: Proceedings*, *2*(4-5), pp.3203-3211.

188. Kumar, C.S., Yadav, D., Bauri, R. and Ram, G.J., **2015**. Effects of ball milling and particle size on microstructure and properties 5083 Al–Ni composites fabricated by friction stir processing. *Materials Science and Engineering: A*, *645*, pp.205-212.

189. Kumar, C.S., Bauri, R. and Yadav, D., **2016**. Wear properties of 5083 Al–W surface composite fabricated by friction stir processing. *Tribology International*, *101*, pp.284-290.

190. Papantoniou, I.G., Markopoulos, A.P. and Manolakos, D.E., **2020**. A new approach in surface modification and surface hardening of aluminium alloys using friction stir process: Cu-reinforced AA5083. *Materials*, *13*(6), p.1278.

191. Khan, M., Rehman, A., Aziz, T., Naveed, K., Ahmad, I. and Subhani, T., **2017**. Cold formability of friction stir processed aluminium composites containing carbon nanotubes and boron carbide particles. *Materials Science and Engineering: A*, *701*, pp.382-388.

192. Khan, M., Rehman, A., Aziz, T., Shahzad, M., Naveed, K. and Subhani, T., **2018**. Effect of inter-cavity spacing in friction stir processed Al 5083 composites containing carbon

nanotubes and boron carbide particles. *Journal of Materials Processing Technology*, *253*, pp.72-85.

193. Jain, V.K.S., Yazar, K.U. and Muthukumaran, S., **2019**. Development and characterization of Al5083-CNTs/SiC composites via friction stir processing. *Journal of Alloys and Compounds*, *798*, pp.82-92.

194. Rathee, S., Maheshwari, S., Siddiquee, A.N. and Srivastava, M., **2017**. Effect of tool plunge depth on reinforcement particle distribution in surface composite fabrication via friction stir processing. *Defence technology*, *13*(2), pp.86-91.

195. Maurya, R., Kumar, B., Ariharan, S., Ramkumar, J. and Balani, K., **2016**. Effect of carbonaceous reinforcements on the mechanical and tribological properties of friction stir processed Al6061 alloy. *Materials & Design*, *98*, pp.155-166.

196. Dinaharan, I., Kalaiselvan, K. and Murugan, N., **2017**. Influence of rice husk ash particles on microstructure and tensile behavior of AA6061 aluminium matrix composites produced using friction stir processing. *Composites Communications*, *3*, pp.42-46.

197. Sharma, A., Fujii, H. and Paul, J., **2020**. Influence of reinforcement incorporation approach on mechanical and tribological properties of AA6061-CNT nanocomposite fabricated via FSP. *Journal of Manufacturing Processes*, *59*, pp.604-620.

198. Marini, C.D., Fatchurrohman, N. and Zulkfli, Z., **2021**. Investigation of wear performance of friction stir processed aluminium metal matrix composites. *Materials Today: Proceedings*, *46*, pp.1740-1744.

199. Reddy, K.V., Naik, R.B., Rao, G.R., Reddy, G.M. and Kumar, R.A., **2020**. Microstructure and damping capacity of AA6061/graphite surface composites produced through friction stir processing. *Composites Communications*, *20*, p.100352.

200. Sharma, A., Sharma, V.M., Mewar, S., Pal, S.K. and Paul, J., **2018**. Friction stir processing of Al6061-SiC-graphite hybrid surface composites. *Materials and Manufacturing Processes*, *33*(7), pp.795-804.

201. Devaraju, A., Kumar, A. and Kotiveerachari, B., **2013**. Influence of addition of Grp/$Al_2O_3$p with SiCp on wear properties of aluminium alloy 6061-T6 hybrid composites via friction stir processing. *Transactions of Nonferrous Metals Society of China*, *23*(5), pp.1275-1280.

202. Sharma, A., Sharma, V.M. and Jinu, P.A.U.L., **2019**. A comparative study on microstructural evolution and surface properties of graphene/CNT reinforced Al6061− SiC hybrid surface composite fabricated via friction stir processing. *Transactions of Nonferrous Metals Society of China*, *29*(10), pp.2005-2026.

203. Moustafa, E.B., AbuShanab, W.S., Ghandourah, E. and Taha, M.A., **2020**. Microstructural, mechanical and thermal properties evaluation of AA6061/$Al_2O_3$-BN hybrid and mono nanocomposite surface. *Journal of Materials Research and Technology*, *9*(6), pp.15486-15495.

204. Chen, Z., Li, J., Borbely, A., Ji, G., Zhong, S.Y., Wu, Y., Wang, M.L. and Wang, H.W., **2015**. The effects of nanosized particles on microstructural evolution of an in-situ $TiB_2$/6063Al composite produced by friction stir processing. *Materials & Design*, *88*, pp.999-1007.

205. Ma, S.M., Zhang, P., Ji, G., Chen, Z., Sun, G.A., Zhong, S.Y., Ji, V. and Wang, H.W., **2014**. Microstructure and mechanical properties of friction stir processed Al–Mg–Si alloys

dispersion-strengthened by nanosized $TiB_2$ particles. *Journal of alloys and compounds*, *616*, pp.128-136.

206. Joyson Abraham, S., Chandra Rao Madane, S., Dinaharan, I.A. and John Baruch, L., **2016**. Development of quartz particulate reinforced AA6063 aluminium matrix composites via friction stir processing. *Journal of Asian Ceramic Societies*, *4*(4), pp.381-389.

207. Rathee, S., Maheshwari, S., Siddiquee, A.N. and Srivastava, M., **2017**. Analysis of microstructural changes in enhancement of surface properties in sheet forming of Al alloys via friction stir processing. *Materials Today: Proceedings*, *4*(2), pp.452-458.

208. Gangil, N., Maheshwari, S. and Siddiquee, A.N., **2018**. Influence of tool pin and shoulder geometries on the microstructure of friction stir processed AA6063/SiC composites. *Mechanics & Industry*, *19*(2), p.211.

209. Gangil, N., Maheshwari, S. and Siddiquee, A.N., **2018**. Multipass FSP on AA6063-T6 Al: Strategy to fabricate surface composites. *Materials and Manufacturing Processes*, *33*(7), pp.805-811.

210. Dhayalan, R., Kalaiselvan, K. and Sathiskumar, R., **2014**. Characterization of AA6063/SiC-Gr surface composites produced by FSP technique. *Procedia Engineering*, *97*, pp.625-631.

211. Narimani, M., Lotfi, B. and Sadeghian, Z., **2016**. Evaluation of the microstructure and wear behaviour of AA6063-$B_4C$/$TiB_2$ mono and hybrid composite layers produced by friction stir processing. *Surface and Coatings Technology*, *285*, pp.1-10.

212. Thangarasu, A., Murugan, N. and Dinaharan, I., **2014**. Production and wear characterization of AA6082-TiC surface composites by friction stir processing. *Procedia Engineering*, *97*, pp.590-597.

213. Muribwathoho, O., Msomi, V. and Mabuwa, S., **2024**. An Analysis Comparing the Taguchi Method for Optimizing the Process Parameters of AA5083/Silicon Carbide and AA5083/Coal Composites That Are Fabricated via Friction Stir Processing. *Applied Sciences*, *14*(20), p.9616.

214. Muribwathoho, O., Msomi, V. and Mabuwa, S., **2025**. Optimization of FSP parameters in fabricating AA5083/Coal composites using Taguchi method. *Engineering Research Express*.

215. Muribwathoho, O., Msomi, V. and Mabuwa, S., **2025**. Optimizing FSP Parameters for AA5083/SiC Composites: A Comparative Analysis of Taguchi and Regression. *Metals*, *15*(3), p.280.

216. Mukherjee, I. and Ray, P.K., **2006**. A review of optimization techniques in metal cutting processes. *Computers & Industrial Engineering*, *50*(1-2), pp.15-34.

217. Markos, S., Viharos, Z.J. and Monostori, L., **1998**, September. Quality-oriented, comprehensive modelling of machining processes. In *Sixth ISMQC IMEKO symposium on metrology for quality control in production* (pp. 67-74).

218. Montgomery, D.C., **2017**. Design and analysis of experiments. *John wiley & sons.*

219. Ross, P.J., **1988**. Taguchi techniques for quality engineering: loss function, orthogonal experiments, parameter and tolerance design. *McGraw-Hill book Company*

220. Kowalczyk, M., **2014**. Application of Taguchi and Anova methods in selection of process parameters for surface roughness in precision turning of titanium. *Advances in Manufacturing Science and Technology*, *38*(2), pp.21-35.

221. Ahilan, C., Kumanan, S. and Sivakumaran, N., **2010**. Application of grey based Taguchi method in multi-response optimization of turning process. *Advances in production Engineering & management*, *5*(3), pp.171-180.

222. Taguchi, G., Chowdhury, S. and Wu, Y., **2005**. Taguchi's Quality Engineering Handbook, John Willey & Sons. *Inc., Hoboken, New Jersey, USA*, *134*.

223. Ross, P.J., **1995**. Taguchi techniques for quality engineering. *McGraw-Hill book Company*

224. Bauri, R., Yadav, D., Kumar, C.S. and Ram, G.J., **2015**. Optimized process parameters for fabricating metal particles reinforced 5083 Al composite by friction stir processing. *Data in brief*, *5*, pp.309-313.

225. Ahmadkhaniha, D., Sohi, M.H., Zarei-Hanzaki, A., Bayazid, S.M. and Saba, M., **2015**. Taguchi optimization of process parameters in friction stir processing of pure Mg. *Journal of Magnesium and Alloys*, *3*(2), pp.168-172.

226. Mitra, A., **2011**. The taguchi method. *Wiley Interdisciplinary Reviews: Computational Statistics*, *3*(5), pp.472-480.

227. Roy, R.K., **2010**. A primer on the Taguchi method. *Society of manufacturing engineers*.

228. Anil Kumar, K.S., Karur, A.S., Chipli, S. and Singh, A., **2015**. Optimization of FSW parameters to improve the mechanical properties of AA2024-T351 similar joints using Taguchi method. *Journal of Mechanical Engineering and Automation*, *5*(3B), pp.27-32.

229. Pasebani, S., Charit, I. and Mishra, R.S., **2015**. Effect of tool rotation rate on constituent particles in a friction stir processed 2024Al alloy. *Materials Letters*, *160*, pp.64-67.

230. Patel, V.V., Badheka, V. and Kumar, A., **2016**. Influence of friction stir processed parameters on superplasticity of Al-Zn-Mg-Cu alloy. *Materials and Manufacturing Processes*, *31*(12), pp.1573-1582.

231. Li, J., Cao, F. and Shen, Y., **2020**. Effect of welding parameters on friction stir welded Ti–6Al–4V joints: temperature, microstructure and mechanical properties. *Metals*, *10*(7), p.940.

232. Nascimento, F., Santos, T., Vilaça, P., Miranda, R.M. and Quintino, L., **2009**. Microstructural modification and ductility enhancement of surfaces modified by FSP in aluminium alloys. *Materials Science and Engineering: A*, *506*(1-2), pp.16-22.

233. Molla Ramezani, N., Davoodi, B., Aberoumand, M. and Rezaee Hajideh, M., **2019**. Assessment of tool wear and mechanical properties of Al 7075 nanocomposite in friction stir processing (FSP). *Journal of the Brazilian Society of Mechanical Sciences and Engineering*, *41*, pp.1-14.

234. Vigneshkumar, M., Padmanaban, G. and Balasubramanian, V., **2019**. Influence of tool tilt angle on the formation of friction stir processing zone in cast magnesium alloy ZK60/SiCp surface composites. *Metallography, Microstructure, and Analysis*, *8*, pp.58-66.

235. Abbasi, M., Bagheri, B. and Keivani, R., **2015**. Thermal analysis of friction stir welding process and investigation into affective parameters using simulation. *Journal of Mechanical Science and Technology*, *29*, pp.861-866.

236. Sidhu, M.S. and Chatha, S.S., **2012**. Friction stir welding–process and its variables: A review. *International Journal of Emerging Technology and Advanced Engineering*, *2*(12), pp.275-279.

237. Patel, V.V., Badheka, V.J. and Kumar, A., **2017**. Influence of pin profile on the tool plunge stage in friction stir processing of Al–Zn–Mg–Cu alloy. *Transactions of the Indian Institute of Metals*, *70*, pp.1151-1158.

238. Malik, V. and Kailas, S.V., **2021**. Understanding the effect of tool geometrical aspects on intensity of mixing and void formation in friction stir process. *Proceedings of the Institution of Mechanical Engineers, Part C: Journal of Mechanical Engineering Science*, *235*(4), pp.744-757.

239. Ghiasvand, A., Suksatan, W., Tomków, J., Rogalski, G. and Derazkola, H.A., **2022**. Investigation of the effects of tool positioning factors on peak temperature in dissimilar friction stir welding of AA6061-T6 and AA7075-T6 aluminum alloys. *Materials*, *15*(3), p.702.

240. John Baruch, L., Raju, R., Balasubramanian, V., Rao, A.G. and Dinaharan, I., **2016**. Influence of multi-pass friction stir processing on microstructure and mechanical properties of die cast Al–7Si–3Cu aluminum alloy. *Acta Metallurgica Sinica (English Letters)*, *29*, pp.431-440.

241. Bharti, S., Ghetiya, N. and Patel, K., **2022**. Fabrication of AA6061/Al2O3 surface composite by double pass friction stir processing and investigation on mechanical and wear properties. *Advances in Materials and Processing Technologies*, *8*(sup3), pp.1785-1799.

242. Singh, D. and Sarvaiya, J., **2023**. Development of AA5052/TiO2/SiC hybrid surface composites using upward material flow through multipass friction stir processing. *Journal of Adhesion Science and Technology*, *37*(23), pp.3335-3357.

243. Singhal, T.S., Jain, J.K., Kumar, M., Sunil, B.D.Y., Bhojak, V., Saxena, K.K. and Prakash, C., **2024**. Microstructure and mechanical properties of GMAW cladded AA 6063 using friction stir processing as a post-processing technique. *Advances in Materials and Processing Technologies*, *10*(4), pp.3265-3279.

244. Sharma, A., Sharma, V.M., Mewar, S., Pal, S.K. and Paul, J., **2018**. Friction stir processing of Al6061-SiC-graphite hybrid surface composites. *Materials and Manufacturing Processes*, *33*(7), pp.795-804.

245. Salehi, M., Saadatmand, M. and Mohandesi, J.A., **2012**. Optimization of process parameters for producing AA6061/SiC nanocomposites by friction stir processing. *Transactions of Nonferrous Metals Society of China*, *22*(5), pp.1055-1063.

246. Rathee, S., Maheshwari, S., Siddiquee, A.N., Srivastava, M. and Sharma, S.K., **2016**. Process parameters optimization for enhanced microhardness of AA 6061/SiC surface composites fabricated via Friction Stir Processing (FSP). *Materials Today: Proceedings*, *3*(10), pp.4151-4156.

247. Jian, W.A.N.G., Bo, L.I., Cheng, C.H.E.N. and Xiao-feng, L.U., **2021**. Interface repairing for AA5083/T2 copper explosive composite plate by friction stir processing. *Transactions of Nonferrous Metals Society of China*, *31*(9), pp.2585-2596.

248. Msomi, V. and Mabuwa, S., **2021**, July. Optimization of Normal and Submerged FSP Parameters for dissimilar aluminium joints using Taguchi technique. In *Materials Science Forum* (Vol. 1034, pp. 207-218). Trans Tech Publications Ltd.

249. Kosaraju, S., Aziz, M.A., Yadav, V.P.K., Shiva, B., Kolli, M. and Cheepu, M., **2025**. Taguchi optimization of friction stir process parameters for enhancing joint strength of AA8011

reinforced with SiC nano particles. *International Journal on Interactive Design and Manufacturing (IJIDeM)*, *19*(1), pp.533-544.

250. Zass, K., Mabuwa, S. and Msomi, V., **2023**. Introduction of Coal Reinforcing Particles on the Dissimilar FSW AA608/AA5083 Joint via Friction Stir Processing. *Metals*, *13*(12), p.1981.

251. Akbari, M., Ezzati, M. and Asadi, P., **2022**. Investigation of the effect of tool probe profile on reinforced particles distribution using experimental and CEL approaches. *International Journal of Lightweight Materials and Manufacture*, *5*(2), pp.213-223

252. Zass, K.J., Msomi, V. and Mabuwa, S., **2024**. Feasibility of using coal as reinforcement in dissimilar welded joints: Comparative analysis. In *E3S Web of Conferences* (Vol. 552, p. 01014). EDP Sciences.

253. Jalilvand, M.M., Mazaheri, Y., Heidarpour, A. and Roknian, M., **2019**. Development of A356/Al2O3+ SiO2 surface hybrid nanocomposite by friction stir processing. *Surface and Coatings Technology*, *360*, pp.121-132.

254. Sagar, P. and Handa, A., **2021**. Selection of tool transverse speed considering trial run experimentations for AZ61/Tic composite developed via friction stir processing using triangular tool. *Materials Today: Proceedings*, *38*, pp.198-203.

255. Moustafa, E.B., Melaibari, A., Alsoruji, G., Khalil, A.M. and Mosleh, A.O., **2022**. Tribological and mechanical characteristics of AA5083 alloy reinforced by hybridising heavy ceramic particles Ta2C & VC with light GNP and Al2O3 nanoparticles. *Ceramics International*, *48*(4), pp.4710-4721.

256. Papantoniou, I.G. Kyriakopoulou, H.P. Pantelis, D.I. Athanasiou-Ioannou, A. and Manolakos, D.E. **2018**. Manufacturing process of AA5083/nano-cAl2O3 localized composite metal foam fabricated by friction stir processing route (FSP) and microstructural characterization. *Journal of Materials Science*, 53, pp. 3817–3835.

257. Choi, D.H., Ahn, B.W., Quesnel, D.J. and Jung, S.B. **2013**. Behavior of β phase (Al3Mg2) in AA 5083 during friction stir welding. *Intermetallics*, 35, pp. 120-127.

258. Wang, Y., Li, Y., Zhang, H. and Wang, F. **2022**. Effect of intermetallic phases on the corrosion behavior of AA5083 aluminum alloy. *Corrosion Science*, 196, 110183.

259. Yasakau, K.A., Zheludkevich, M.L., Lamaka, S.V. and Ferreira, M.G.S. **2007**. Role of intermetallic phases in localized corrosion of AA5083. *Electrochimica Acta,* 52(27), pp. 7651-7659.

260. Pandey, C., Saini, N., Mahapatra, M.M. and Kumar, P., **2017**. Study of the fracture surface morphology of impact and tensile tested cast and forged (C&F) Grade 91 steel at room temperature for different heat treatment regimes. *Engineering Failure Analysis*, *71*, pp.131-147.

261. Saini, N., Pandey, C., Thapliyal, S. and Dwivedi, D.K., **2018**. Mechanical properties and wear behavior of Zn and MoS 2 reinforced surface composite Al-Si alloys using friction stir processing. *Silicon*, *10*, pp.1979-1990.

262. Pandey, C., Mahapatra, M.M., Kumar, P., Kumar, P., Saini, N., Thakare, J.G. and Kumar, S., **2019**. Study on the effect of double austenitization treatment on fracture morphology tensile tested nuclear grade P92 steel. *Engineering Failure Analysis*, *96*, pp.158-167.

263. Singh, R. and Rai, R.N., **2018**, April. Characterization of B4C-composite-reinforced aluminum alloy composites. In *AIP Conference Proceedings* (Vol. 1943, No. 1). AIP Publishing.

264. Zhao, Z., Pan, Q., Yan, J., Ye, J. and Liu, Y. **2018**. Direct current micro-arc oxidation coatings on Al-Zn-Mg-Mn-Zr extruded alloy with tunable structures and properties templated by discharge stages. *Vacuum,* 15, pp.155-165.

265. Suresh, S., Natarajan, E., Franz, G. and Rajesh, S. **2022.** Differentiation in the SiC filler size effect in the mechanical and tribological properties of friction-spot-welded AA5083-H116 alloy. *Fibers,* 10(109), pp. 1-15.

266. Li, Z., Jiang, H., Zhang, J., Zhang, Y. and Li, L. **2014**. Effect of $Mg_2Si$ on the microstructure and mechanical properties of AA5083 aluminum alloy. *Materials Science and Engineering: A,* 600, pp. 147-153.

267. Trivedi, M.K., Tallapragada, R.M., Branton, A., Trivedi, D., Nayak,G., Latiyal, O. and Jana, S. **2015**. Characterization of physical and structural properties of aluminium carbide powder: impact of biofield treatment*, Aeronautics & Aerospace Engineering,* 4(142), pp. 1-4.

268. Røyset, J. and Ryum, N. **2005.** Scandium in aluminium alloys. *International Materials Reviews*, 50(1), pp. 19-44.

269. Bharathikanna, R. and Elatharasan, G., **2017**. An investigation on microstructures and mechanical properties of AA1050 in friction stir processing technique. *Advances in Natural and Applied Sciences*, *11*(8), pp.316-322.

270. Huang, G., Wu, J., Hou, W. and Shen, Y., **2018**. Microstructure, mechanical properties and strengthening mechanism of titanium particle reinforced aluminum matrix composites produced by submerged friction stir processing. *Materials Science and Engineering: A*, *734*, pp.353-363.

271. Agha Amini Fashami, H., Bani Mostafa Arab, N., Hoseinpour Gollo, M. and Nami, B., **2021**. Numerical and experimental investigation of defects formation during friction stir processing on AZ91. *SN Applied Sciences*, *3*, pp.1-13.

272. Khan, N.Z., Siddiquee, A.N., Khan, Z.A. and Shihab, S.K., **2015**. Investigations on tunneling and kissing bond defects in FSW joints for dissimilar aluminum alloys. *Journal of alloys and Compounds*, *648*, pp.360-367.

273. Habibnia, M., Shakeri, M., Nourouzi, S. and Givi, M.B., **2015**. Microstructural and mechanical properties of friction stir welded 5050 Al alloy and 304 stainless steel plates. *The International Journal of Advanced Manufacturing Technology*, *76*, pp.819-829.

274. Zandsalimi, S., Heidarzadeh, A. and Saeid, T., **2019**. Dissimilar friction-stir welding of 430 stainless steel and 6061 aluminum alloy: Microstructure and mechanical properties of the joints. *Proceedings of the Institution of Mechanical Engineers, Part L: Journal of Materials: Design and Applications*, *233*(9), pp.1791-1801.

275. Akbari, M., Ezzati, M. and Asadi, P., **2022**. Investigation of the effect of tool probe profile on reinforced particles distribution using experimental and CEL approaches. *International Journal of Lightweight Materials and Manufacture*, *5*(2), pp.213-223.

276. Zahmatkesh, B. and Enayati, M.H., **2010**. A novel approach for development of surface nanocomposite by friction stir processing. *Materials Science and Engineering: A*, *527*(24-25), pp.6734-6740.

277. Jain, V.K., Yadav, M.K., Saxena, A., Siddiquee, A.N. and Khan, Z.A., **2021**. Effect of tool rotational speed on microstructure and mechanical properties of friction stir processed AA5083/Fe-Al in-situ composite. *Materials Today: Proceedings*, *46*, pp.6496-6500.

278. McNelley, T.R., Swaminathan, S. and Su, J.Q., **2008**. Recrystallization mechanisms during friction stir welding/processing of aluminum alloys. *Scripta materialia*, *58*(5), pp.349-354.

279. Humphreys, F.J. and Hatherly, M., **2012**. *Recrystallization and related annealing phenomena*. elsevier.

280. Feng, A.H. and Ma, Z.Y., **2009**. Microstructural evolution of cast Mg–Al–Zn during friction stir processing and subsequent aging. *Acta Materialia*, *57*(14), pp.4248-4260.

281. Humphreys, F.J., Prangnell, P.B. and Priestner, R., **2001**. Fine-grained alloys by thermomechanical processing. *Current Opinion in Solid State and Materials Science*, *5*(1), pp.15-21.

282. Colligan, K., **1999**. Material flow behavior during friction welding of aluminum. *Weld J*, *75*(7), pp.229s-237s.

283. Ma, Z.Y., **2008**. Friction stir processing technology: a review. *Metallurgical and materials Transactions A*, *39*, pp.642-658.

284. Shukla, S., Komarasamy, M. and Mishra, R.S., **2018**. Grain size dependence of fatigue properties of friction stir processed ultrafine-grained Al-5024 alloy. *International Journal of Fatigue*, *109*, pp.1-9.

285. Węglowski, M.S., **2018**. Friction stir processing–State of the art. *Archives of civil and Mechanical Engineering*, *18*(1), pp.114-129.

286. Heidarzadeh, A., Mironov, S., Kaibyshev, R., Çam, G., Simar, A., Gerlich, A., Khodabakhshi, F., Mostafaei, A., Field, D.P., Robson, J.D. and Deschamps, A., **2021**. Friction stir welding/processing of metals and alloys: A comprehensive review on microstructural evolution. *Progress in Materials Science*, *117*, p.100752.

287. Patel, M., Jain, S. and Murugesan, J., **2024**. Investigation of Mechanical Properties, Fretting Wear, and Corrosion Behaviour of AA6063/Si3N4 Nanocomposites Fabricated via Friction Stir Processing. *Arabian Journal for Science and Engineering*, pp.1-11.

288. Karmiris-Obratański, P., Papantoniou, I.G. and Leszczyńska-Madej, B., **2024**. Microstructure, mechanical and tribological properties of AA5083-TiO2 nanocomposite by multi-pass friction stir processing. *Archives of Civil and Mechanical Engineering*, *24*(4), p.209.

289. Mishra, R.S., De, P.S., Kumar, N., Mishra, R.S., De, P.S. and Kumar, N., **2014**. Friction stir processing. *Friction stir welding and processing: science and engineering*, pp.259-296.

290. Hamilton, C., Kopyściański, M., Senkov, O. and Dymek, S., **2013**. A coupled thermal/material flow model of friction stir welding applied to Sc-modified aluminum alloys. *Metallurgical and Materials Transactions A*, *44*, pp.1730-1740.

291. Hamilton, C., Węglowski, M.S. and Dymek, S., **2015**. A simulation of friction-stir processing for temperature and material flow. *Metallurgical and Materials Transactions B*, *46*, pp.1409-1418.

292. Azizieh, M., Kokabi, A.H. and Abachi, P., **2011**. Effect of rotational speed and probe profile on microstructure and hardness of AZ31/Al2O3 nanocomposites fabricated by friction stir processing. *Materials & Design*, *32*(4), pp.2034-2041.

293. Xiong, Y., Kong, D., Wen, Z., Wu, G. and Liu, Q., **2022**. Analysis of coal face stability of lower coal seam under repeated mining in close coal seams group. *Scientific Reports*, *12*(1), p.509.

294. Kurt, A., Uygur, I. and Cete, E., **2011**. Surface modification of aluminium by friction stir processing. *Journal of materials processing technology*, *211*(3), pp.313-317.

295. Takhakh, A.M., **2016**. Formability of Friction Stir Welded and Processed AA 2024–O Aluminum Alloy Sheets. *Advances in Natural and Applied Sciences*, *11*, p.10.

296. Sorger, G., Sarikka, T., Vilaça, P. and Santos, T.G., **2018**. Effect of processing temperatures on the properties of a high-strength steel welded by FSW. *Welding in the World*, *62*, pp.1173-1185.

297. Youcef, Y.S. and Chemrouk, M., **2012**. Curvature ductility factor of rectangular sections reinforced concrete beams. *International Journal of Civil and Environmental Engineering*, *6*(11), pp.971-976.

298. Gupta, M., Lai, M.O. and Soo, C.Y., **1996**. Effect of type of processing on the microstructural features and mechanical properties of Al-Cu/SiC metal matrix composites. *Materials Science and Engineering: A*, *210*(1-2), pp.114-122.

299. Flores, O.V., Kennedy, C., Murr, L.E., Brown, D., Pappu, S., Nowak, B.M. and McClure, J.C., **1998**. Microstructural issues in a friction-stir-welded aluminum alloy. *Scripta Materialia*, *38*(5), pp.703-708.

300. Devaraju, A., Kumar, A. and Kotiveerachari, B., **2013**. Influence of rotational speed and reinforcements on wear and mechanical properties of aluminum hybrid composites via friction stir processing. *Materials & Design*, *45*, pp.576-585.

301. Srivastava, M., Rathee, S., Siddiquee, A.N. and Maheshwari, S., **2019**. Investigation on the effects of silicon carbide and cooling medium during multi-pass FSP of Al-Mg/SiC surface composites. *Silicon*, *11*, pp.2149-2157.

302. Srivastava, M., Rathee, S., Maheshwari, S. and Siddiquee, A.N., **2018**. Influence of multiple-passes on microstructure and mechanical properties of Al-Mg/SiC surface composites fabricated via underwater friction stir processing. *Materials Research Express*, *5*(6), p.066511.

303. Ashraf, M.A., Peng, W., Zare, Y. and Rhee, K.Y., **2018**. Effects of size and aggregation/agglomeration of nanoparticles on the interfacial/interphase properties and tensile strength of polymer nanocomposites. *Nanoscale research letters*, *13*, pp.1-7.

304. Kaya, N., Çetinkaya, C., Karakoç, H. and Ada, H., **2024**. Effect of process parameters of Al5083/SiC surface composites fabricated by FSP on microstructure, mechanical properties and wear behaviors. *Materials Chemistry and Physics*, *315*, p.128991.

305. Zangabad, P.S., Khodabakhshi, F., Simchi, A. and Kokabi, A.H., **2016**. Fatigue fracture of friction-stir processed Al–Al3Ti–MgO hybrid nanocomposites. *International journal of fatigue*, *87*, pp.266-278.

306. Bauri, R., Yadav, D., Kumar, C.S. and Balaji, B., **2015**. Tungsten particle reinforced Al 5083 composite with high strength and ductility. *Materials Science and Engineering: A*, *620*, pp.67-75.

307. Khodabakhshi, F., Simchi, A., Kokabi, A., Nosko, M. and Švec, P., **2014**. Strain rate sensitivity, work hardening, and fracture behavior of an Al-Mg TiO 2 nanocomposite prepared by friction stir processing. *Metallurgical and Materials Transactions A*, *45*, pp.4073-4088.

308. Karabacak, A.H., Çanakçı, A., Özkaya, S., Tunç, S.A., Güler, O. and Çelebi, M., **2024**. Effect of AlCrCuFeNi high entropy alloy reinforcements with and without B4C on powder characteristic, mechanical and wear properties of AA5083 metal-metal composites. *Journal of Alloys and Compounds*, *1008*, p.176627.

309. Jha, K.K., Kesharwani, R. and Imam, M., **2023**. Microstructure, texture, and mechanical properties correlation of AA5083/AA6061/SiC composite fabricated by FSAM process. *Materials Chemistry and Physics*, *296*, p.127210.

310. Amra, M., Ranjbar, K. and Hosseini, S.A., **2018**. Microstructure and wear performance of Al5083/CeO2/SiC mono and hybrid surface composites fabricated by friction stir processing. *Transactions of Nonferrous Metals Society of China*, *28*(5), pp.866-878.

311. Li, Q., Huang, G., Cao, Y., Zhang, C., He, J., Jiang, H., Lin, L. and Liu, Q., **2022**. Microstructure refinement, strengthening and ductilization mechanisms in Al–Mg–Mn–Er–Zr alloy with high Mn content by friction stir processing. *Materials Characterization*, *189*, p.111939.

312. Bagheri, B., Abdollahzadeh, A., Sharifi, F. and Abbasi, M., **2022**. The role of vibration and pass number on microstructure and mechanical properties of AZ91/SiC composite layer during friction stir processing. *Proceedings of the Institution of Mechanical Engineers, Part C: Journal of Mechanical Engineering Science*, *236*(5), pp.2312-2326.

313. Faraji, G., Dastani, O. and Mousavi, S.A.A.A., **2011**. Effect of process parameters on microstructure and micro-hardness of AZ91/Al2O3 surface composite produced by FSP. *Journal of Materials Engineering and Performance*, *20*, pp.1583-1590.

# APPENDICES

## APPENDIX A

Plate 1 for optimization

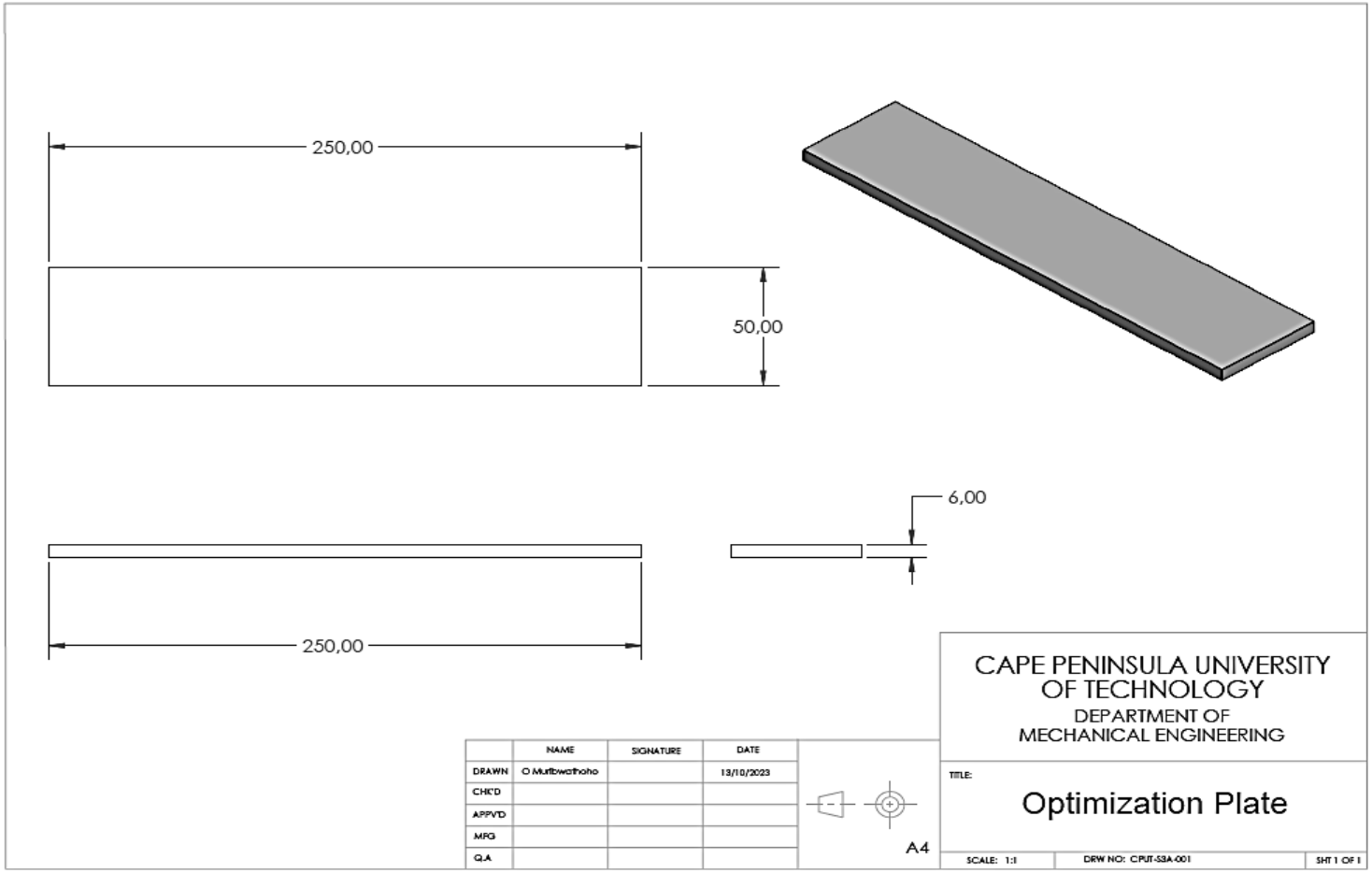


**Figure A1: Plate used for optimization.**

**APPENDIX B**

Plate 2 for fabricating the AMMCs

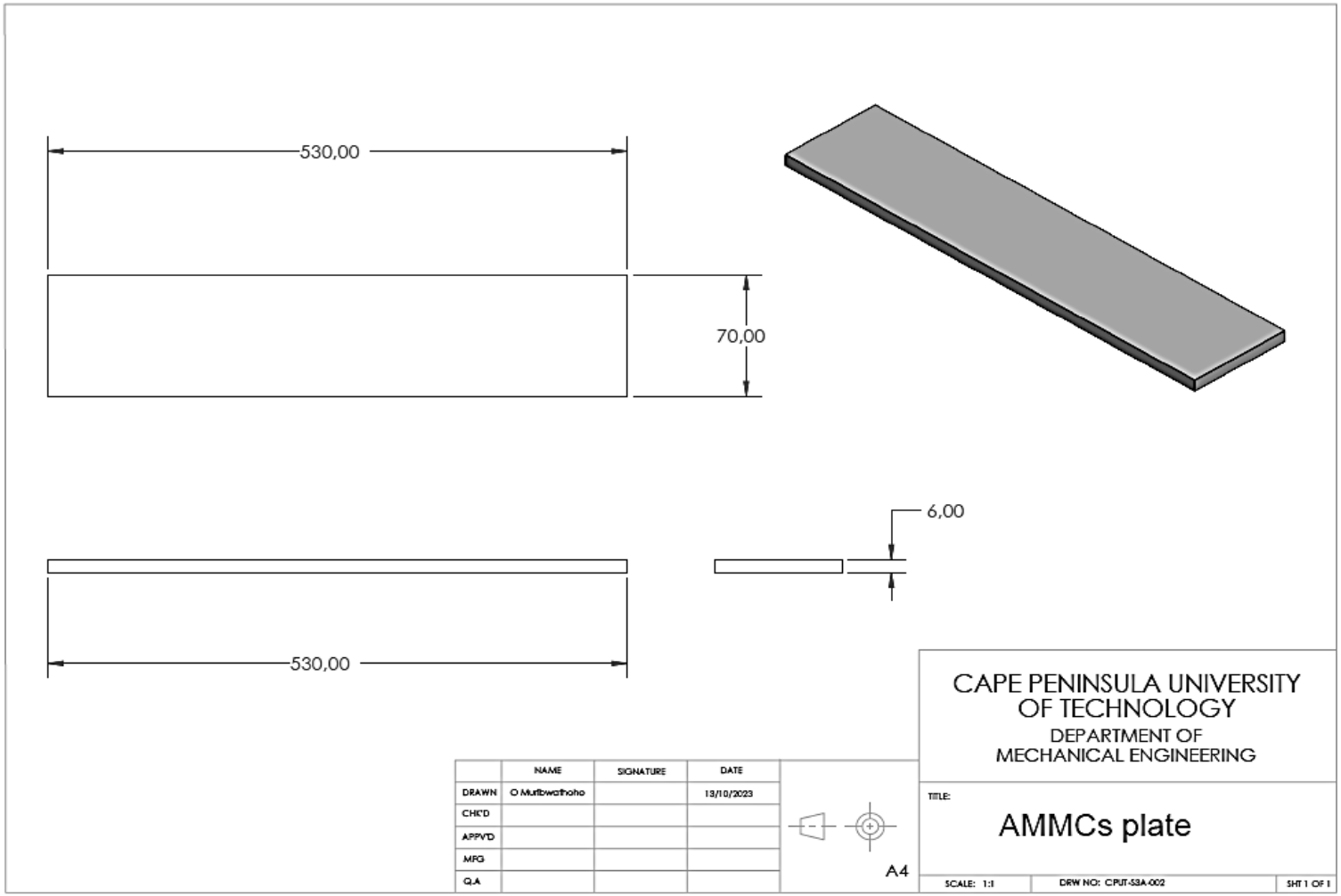


**Figure B1: Plate used for fabricating the AMMCs.**

**APPENDIX C**

FSW/ FSP tool pin profile

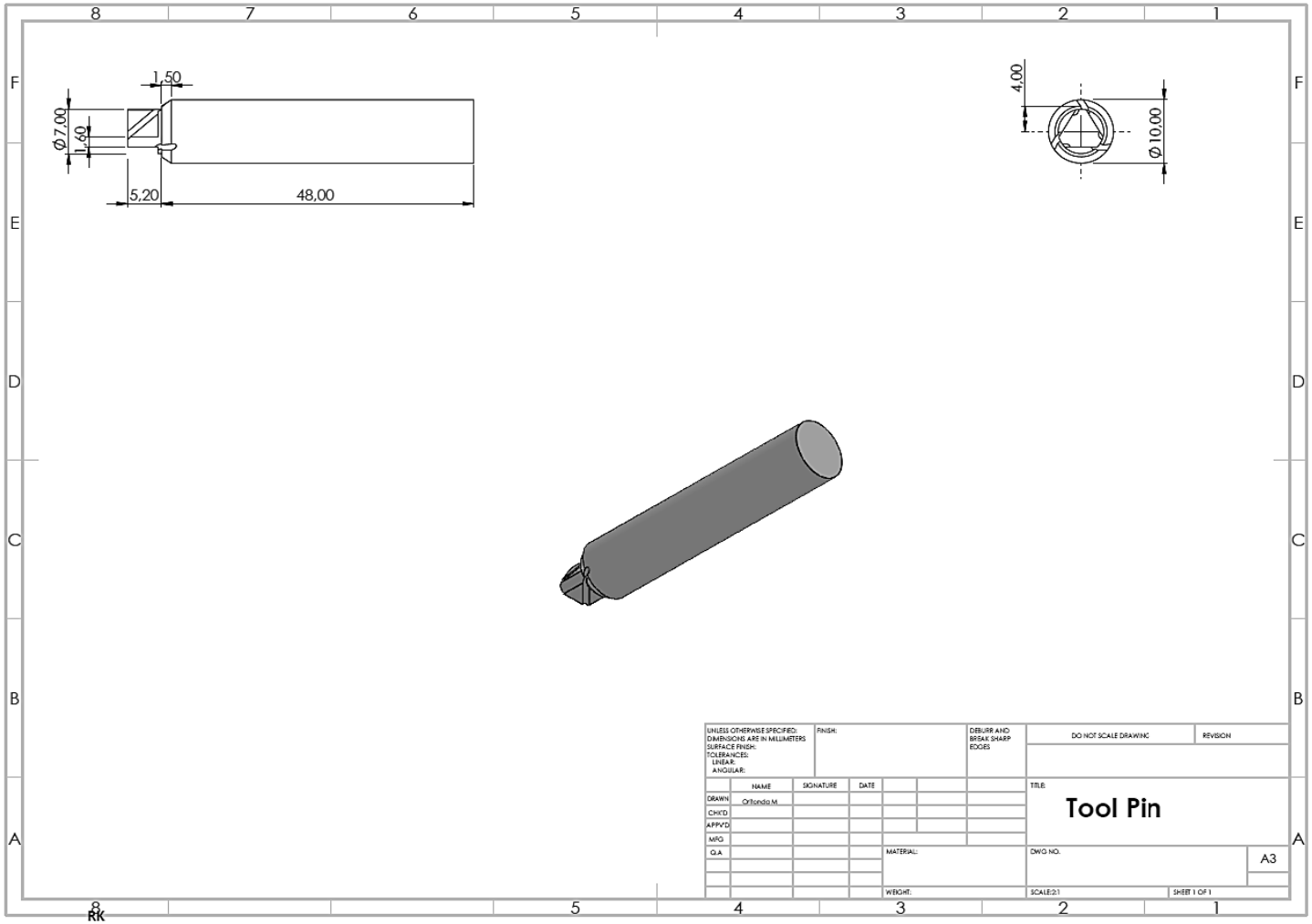


**Figure C1: Pin profile drawing.**

**APPENDIX D**

FSW/ FSP tool shoulder

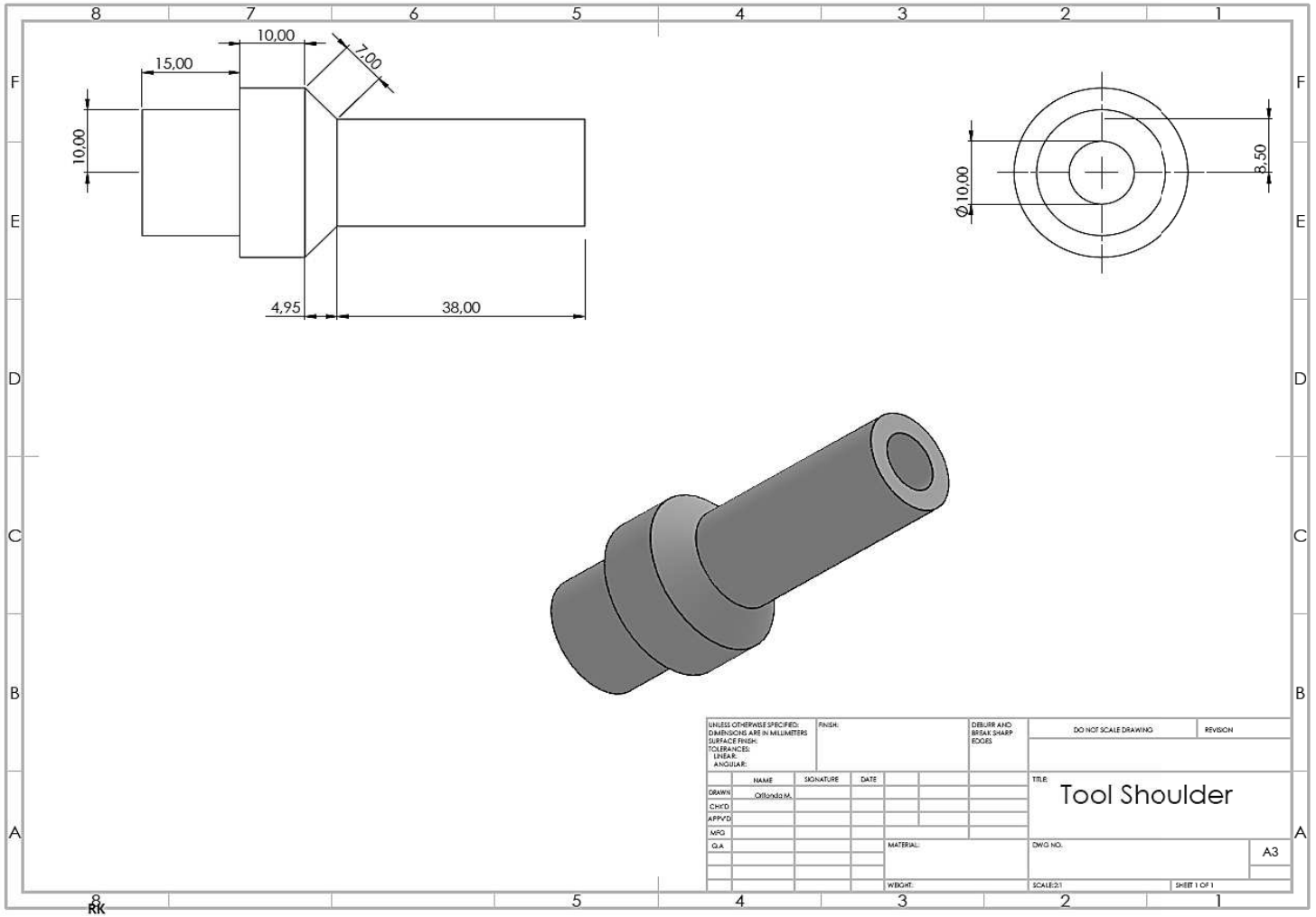


**Figure D1: Shoulder drawing.**

**APPENDIX E**

FSW/FSP tool with pin

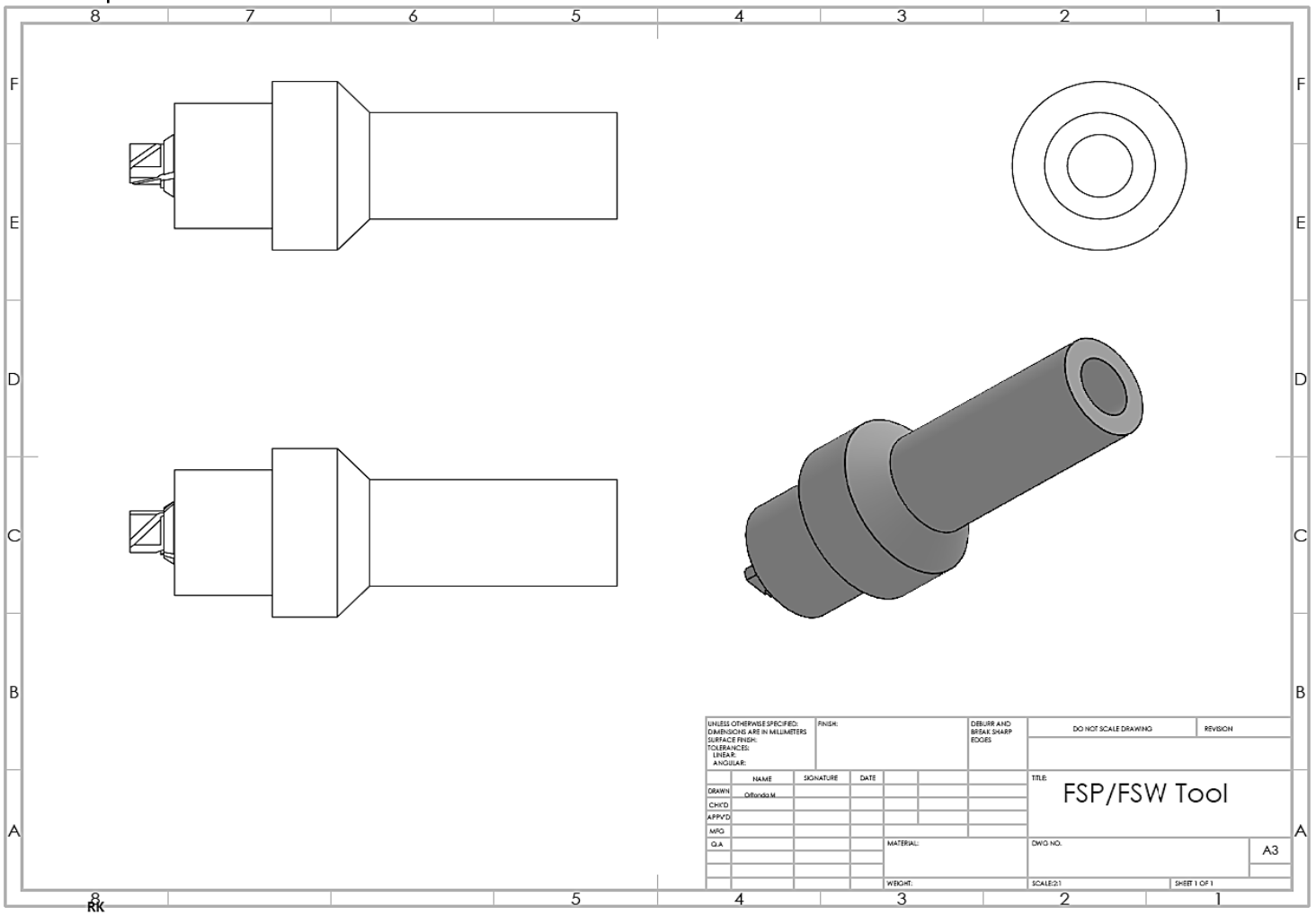


**Figure E1: Tool with pin.**

**APPENDIX F**

Pinless tool

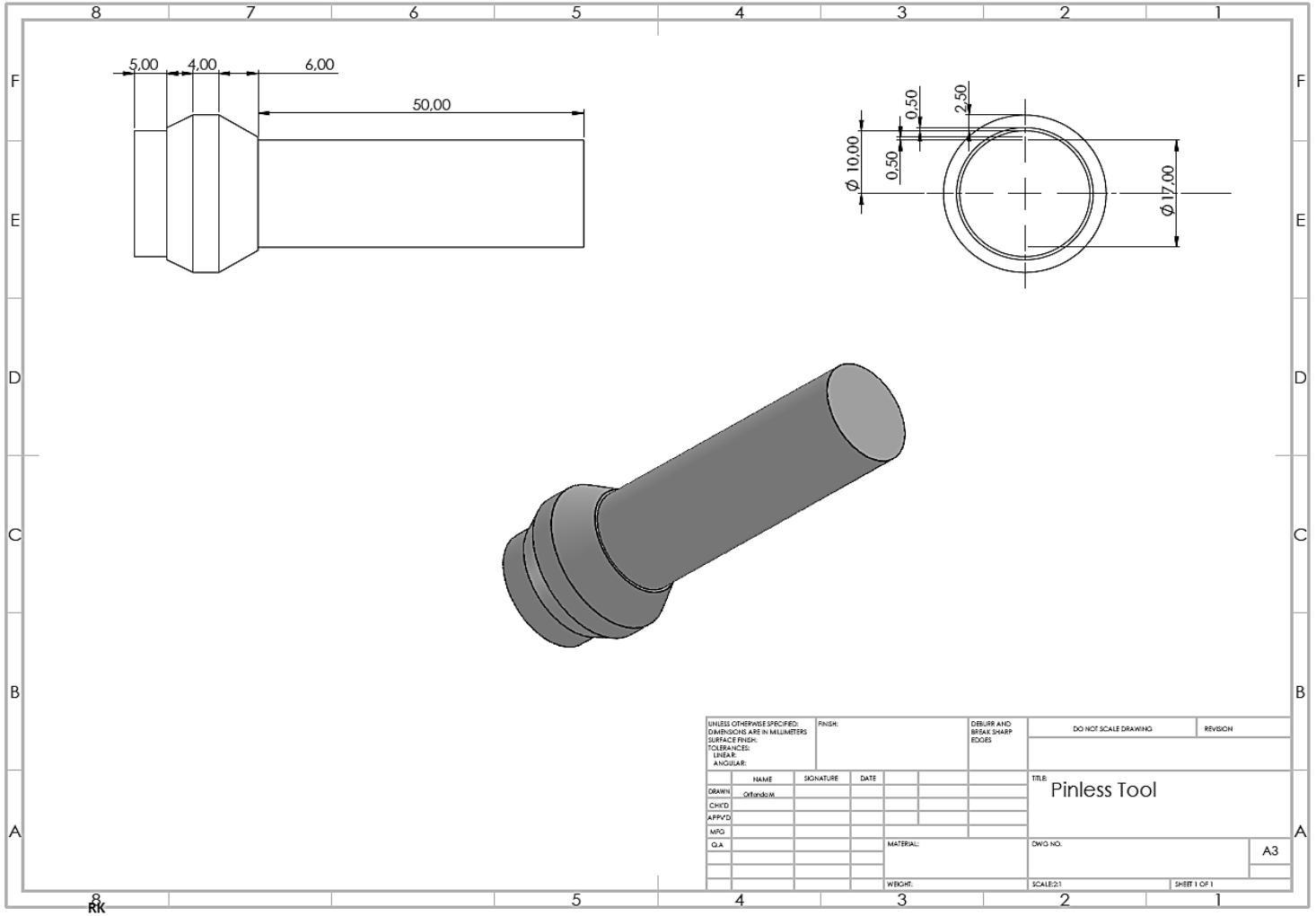


**Figure F1: Pinless tool.**

**APPENDIX G**

Calculations Sample

**Tensile test calculations**

(a) F =0N, A =36mm$^2$

$$\sigma = \frac{F}{A} = \frac{0}{0.000036}$$

= 0 MPa

$$\varepsilon = \frac{\Delta L}{L_o} = \frac{0}{35}$$

= 0

$$\%\, Elongation = \frac{\Delta L}{L_o} \times 100 = \frac{0}{35} \times 100$$

= 0 %

(b) F=20N, A=36mm$^2$

$$\sigma = \frac{F}{A} = \frac{20}{0.000036}$$

= 0.556 MPa

$$\varepsilon = \frac{\Delta L}{L_o} = \frac{0.1637}{35}$$

= 0.0047

$$\%\, Elongation = \frac{\Delta L}{L_o} \times 100 = \frac{0.1637}{35} \times 100$$

= 0.47 %

(c) F=3710N, A=36mm$^2$

$$\sigma = \frac{F}{A} = \frac{3710}{0.000036}$$

= 103.1 MPa

$$\varepsilon = \frac{\Delta L}{L_o} = \frac{3.456}{35}$$

= 0.0987

$$\%\, Elongation = \frac{\Delta L}{L_o} \times 100 = \frac{3.456}{35} \times 100$$

= 9.87 %

**Bending test calculations**

(a) F =0N, L=85mm, b=30mm, d=6mm

$$\sigma_F = \frac{3FL}{2bd^2} = \frac{3\times0\times0.085}{2\times0.03\times0.006^2}$$

= 0 MPa

$$\varepsilon_F = \frac{\Delta L}{L_o} = \frac{0}{85}$$

= 0

(b) F =580N, L=85mm, b=30mm, d=6mm

$$\sigma_F = \frac{3FL}{2bd^2} = \frac{3\times580\times0.085}{2\times0.03\times0.006^2}$$

= 68.4722 MPa

$$\varepsilon_F = \frac{\Delta L}{L_o} = \frac{0.4}{85}$$

= 0.005

(c) F =4562N, L=85mm, b=30mm, d=6mm

$$\sigma_F = \frac{3FL}{2bd^2} = \frac{3\times4562\times0.085}{2\times0.03\times0.006^2}$$

= 538.569 MPa

$$\varepsilon_F = \frac{\Delta L}{L_o} = \frac{22}{85}$$

= 0.259

(d) F =5382N, L=85mm, b=30mm, d=6mm

$$\sigma_F = \frac{3FL}{2bd^2} = \frac{3\times5382\times0.085}{2\times0.03\times0.006^2}$$

= 635.375 MPa

$$\varepsilon_F = \frac{\Delta L}{L_o} = \frac{23.9}{85}$$

= 0.281

## APPENDIX H

An Analysis Comparing the Taguchi Method for Optimizing Process Parameters of AA5083/Silicon Carbide and AA5083/Coal Composites That Are Fabricated via Friction Stir Processing

*applied sciences*

MDPI

*Article*

# An Analysis Comparing the Taguchi Method for Optimizing the Process Parameters of AA5083/Silicon Carbide and AA5083/Coal Composites That Are Fabricated via Friction Stir Processing

**Oritonda Muribwathoho [1,*], Velaphi Msomi [2] and Sipokazi Mabuwa [3]**

[1] Department of Mechanical and Mechatronics Engineering, Cape Peninsula University of Technology, Cape Town 7535, South Africa

[2] Department of Mechanical Engineering, College of Science, University of South Africa, Roodepoort 1709, South Africa; msomiv@unisa.ac.za

[3] Mechanical Engineering Department, Durban University of Technology, P.O. Box 1334, Durban 4000, South Africa; sipokazim@dut.ac.za

* Correspondence: oritondamuribwathoho@gmail.com

**Abstract:** Aluminium metal matrix composites are widely used in automotive, aerospace, marine, and structural engineering due to their high strength-to-weight ratio and superior mechanical properties. Optimizing friction stir process parameters is critical to enhancing the performance of these materials. This study investigates the effects of FSP parameters such as rotational speed, tilt angle, and traverse speed, on the mechanical properties of AA5083/Silicon carbide and AA5083/Coal composites. Using a Taguchi L9 design of experiments, signal-to-noise ratio, and analysis of variance, this study identifies the optimal process settings for maximizing ultimate tensile strength, microhardness, and elongation. From the results, the study revealed that for AA5083/Silicon carbide composites, rotational speed was the most significant factor affecting tensile strength, while for AA5083/Coal composites, tilt angle played a more critical role. Rotational speed consistently influenced microhardness and elongation for both materials. The signal-to-noise ratio analysis indicates that optimal FSP parameters vary depending on the reinforcement material used. This study highlights the importance of tailoring FSP settings to specific reinforcements to achieve optimal mechanical properties. These findings contribute to the advancement of friction stir processing techniques for fabricating high-performance aluminium metal matrix composites, particularly for applications in industries requiring strong, lightweight, and corrosion-resistant materials.

**Keywords:** aluminium alloy; composite; metal matrix composite; mechanical properties; friction stir welding; friction stir processing; Taguchi; S/N Ratio; ANOVA



**Citation:** Muribwathoho, O.; Msomi, V.; Mabuwa, S. An Analysis Comparing the Taguchi Method for Optimizing the Process Parameters of AA5083/Silicon Carbide and AA5083/Coal Composites That Are Fabricated via Friction Stir Processing. *Appl. Sci.* **2024**, *14*, 9616. https://doi.org/10.3390/app14209616

Academic Editors: Guian Qian and Manoj Gupta

Received: 15 September 2024
Revised: 11 October 2024
Accepted: 17 October 2024
Published: 21 October 2024



## 1. Introduction

One of the most important areas of interest in materials science and engineering has been the development of new generation materials with unique and tailored properties. Metal matrix composites (MMCs) represent the most innovative avenue of research in the field of materials engineering, with the potential to significantly improve aluminium alloy mechanical properties by the incorporation of high-modulus, high-strength ceramic particles into aluminium matrices [1,2]. When compared to traditional structural materials, aluminium-based MMCs have higher specific strength and stiffness, which makes them perfect for several uses in the automotive, aerospace, marine, and recreational sectors [3,4]. Exceptional properties that set them apart from traditional materials include high elastic modulus, outstanding resistance to corrosion, increased fatigue strength, better low coefficient of thermal expansion, and resistance to wear [5,6]. AA5083-based composites are ideal for applications demanding lightweight, high-strength materials with excellent formability and corrosion resistance. These properties make them suitable for a diverse range of industries, including construction, marine, automotive, and aerospace [7,8]

To fabricate composites and enhance mechanical properties, friction stir processing (FSP), a novel solid-state method, uses the principles of friction stir welding (FSW) by utilizing a rotating tool to modify surface properties and enhance mechanical performance without melting the base material [9,10]. FSP causes microstructural change, densification, and homogeneity all at the same time by subjecting the material in the stir zone/nugget zone to plastic deformation, mixing, and heat exposure [11]. FSP also encourages shearing and even dispersion of particles inside the matrix [12]. Thus far, metal matrix composites have been successfully fabricated using FSP.

Specific parameter combinations are used in FSP techniques, and each one affects how the processed surface behaves. Depending on the materials used, the desired composite properties, and the equipment available, different process parameters, such as tool geometry, tool rotation speed, traverse speed, preheating temperature, and applied pressure, will apply. Out of all the process parameters that impact FSP, it has been noted that the tool rotation speed and traverse speed [13] have an impact on the even distribution of the reinforcing particles, grain refinery, and heat production during the composites' fabrication, while the tool tilt angle has a major impact on the dispersion of reinforcing particles.

In the stir zone, parameters such tool travel speed, plunge depth, tool rotation rate, and tool angle determine temperatures and microstructure properties [14]. Material flow and temperature distribution behaviour are greatly influenced by tool geometry and welding parameters, which can alter microstructure [15]. Grain size can be refined with lower heat input, but plasticization or softening of the material requires higher heat input. High traverse speeds and low rotating speeds can result in smaller grain sizes, but vice versa because defects may increase [16]. Therefore, it is essential to maximize both traverse and rotational speeds in order to produce a stir zone with fewer defects and smaller grain size. A summary of some of the most important processing parameters is given below.

Rotation speed (rpm): Another significant element that controls the flow and dispersion of the workpiece material is the rotational speed. As the rotation speed of the tool increases, a higher dissolution of soluble particles is likely to occur while the insoluble particles are likely to fragment further [17]. Increasing the speed at which the tool rotates can improve the size of the grain and increase the stir zone's temperature considerably. It is important to note that the microstructural evolution of the material can be affected by the direction in which the tool rotates [18].

Traverse speed (mm/min): Traverse speed is responsible for moving the material from the front end of the workpiece to the end. The grain size in the FSPed zone of the material being processed may increase when the tool traverse speed is decreased. As a result, it barely affects how much the tool wears. Research also indicates that increasing the traversal speed can enhance the surface composite microhardness of the FSPed zone by increasing the dispersion of the reinforcement particles [19].

Tilt angle (deg): The tilt angle of the FSP tool ensures that the substance that has been stirred stays in the tool shoulder and is propelled to the back of the tool shoulder. The processing temperature may rise when the tool tilt angle is increased [20]. Higher tilt angles can result in larger grain and particle sizes, while lower tilt angles may cause defects in the processed zone [21].

Optimizing AMMCs' microstructure and properties to meet the demanding needs of many sectors is crucial to achieving all their full potential. Approaches to optimization issues range from traditional to unconventional [22]. Conventional optimization techniques can be widely divided into two categories: mathematical search techniques (e.g., linear proprogramming, nonlinear programming, dynamic programming) and experimental techniques such as statistical design of experiments (e.g., response surface design approach, or Taguchi method). Non-conventional metaheuristic search methods, like genetic algorithms, tabu search, and simulated annealing, have become more and more popular among scholars in recent years. While alternative optimization methods like mathematical search techniques, RSM, and metaheuristic methods offer their own advantages, they also have limitations that can hinder their practical application in optimizing processes like FSP. The Taguchi

method's efficiency, robustness, and simplicity make it a particularly attractive choice in such scenarios.

The Taguchi method is a robust engineering approach, pioneered by Genichi Taguchi, which aims to enhance product and process quality through structured experimentation. By employing experimental design called orthogonal array design, signal-to-noise ratio, and analysis of variance, this method optimizes factor settings and minimizes variability, resulting in improved product performance and manufacturing efficiency [23,24]. Researchers have used the different design of experiments and FSP in order to determine optimum process parameters for aluminium metal matrix composites utilizing different grades and reinforcements [25–35].

The novelty of this research lies in its comprehensive comparison of AA5083/Silicon carbide and AA5083/Coal composites using identical FSP parameters. Previous studies have often focused on individual reinforcements, but this research addresses a gap by examining multiple reinforcements under identical conditions. Employing a Taguchi L9 design to optimize process parameters for both composites, the study focuses on ultimate tensile strength, microhardness, and percentage elongation. The results will contribute to a deeper understanding of how different reinforcements respond to FSP, guiding the development of more cost-effective and high-performance aluminium metal matrix composites. By acknowledging and addressing the limitations of prior studies, this research offers a more comprehensive and rigorous analysis, making it a valuable contribution to the field of FSP and composite materials fabrication.

## **2.** Material and Methods

### *2.1. Material and Composite Fabrication*

Reinforcement and a base material are needed to create AMMCs. A 6 mm thick AA5083 aluminium alloy plate was chosen for its excellent mechanical properties and corrosion resistance. The dimensions of the AA5083 plates were 250 mm long and 55 mm wide. Table 1 presents the mechanical properties of the alloy. The alloy's composition is primarily magnesium (4.03%), zinc (0.01%), titanium (0.02%), chromium (0.05%), silicon (0.15%), manganese (0.69%), iron (0.16%), and copper (0.02%), as presented in Table 2. The composite materials were fabricated using silicon carbide (SiC) and coal as reinforcements, with 5% volume percentages. AMMCs composites were made using silicon carbide and coal as reinforcements, separately.

**Table 1.** Mechanical Properties.

| **Mechanical Properties** | |
|---|---|
| Ultimate tensile strength | 311 MPa |
| Percentage elongation | 58.6% |
| Microhardness | 93.1 HV |

**Table 2.** Chemical Composition of AA5083 (in % wt) [36].

| **Base Material Composition** | |
|---|---|
| Magnesium | 4.03 |
| Manganese | 0.69 |
| Iron | 0.16 |
| Silicon | 0.15 |
| Chromium | 0.05 |
| Copper | 0.02 |
| Titanium | 0.02 |
| Zinc | 0.01 |
| **Al** | **Bal** |

*2.2. Experimental Design Using Taguchi Method*

The software utilized for constructing the design matrix and analyzing the results was MINITAB 18. The three parameters (rotational speed, traverse speed, and tilt angle) taken into account for this study are included in Table 3 together with the relevant levels for each. The selected parameters were chosen based on their established influence on the microstructure and mechanical properties of composites during FSP [13]. Among FSP parameters, tool rotation speed and traverse speed significantly impact the even distribution of reinforcing particles, grain refinement, and heat generation during composite fabrication. Conversely, tool tilt angle primarily influences the dispersion of reinforcing particles. The parameter levels were determined by considering existing literature and conducting preliminary experiments to establish ranges that effectively balance processing time and mechanical performance [37–40].

**Table 3.** Processing parameters with their levels.

| Processing Parameters | Levels of Parameters | | |
|---|---|---|---|
| | 1 | 2 | 3 |
| Tool traverse speed (TS) in mm/min | 30 | 45 | 60 |
| Tool rotational speed (RS) in rpm | 600 | 900 | 1200 |
| Tool tilt angle (TA) in ° | 1 | 1.75 | 2 |

From the software, a Taguchi L9 factorial design was employed to reduce the number of experimental runs. Using a complete factorial experiment design would have needed 27 experiments; however, the Taguchi approach avoided 18 FSP runs. As a result, expenses and time were greatly reduced. The design matrix, shown in Table 4, includes three processing parameters at three distinct levels, resulting in a total of nine experiments for each composite type.

**Table 4.** Taguchi L9 design matrix.

| No of Tests | Traverse Speed [mm/min] | Rotational Speed [rpm] | Tilt Angle [°] |
|---|---|---|---|
| 1. | 30 | 600 | 1 |
| 2. | 45 | 600 | 1.75 |
| 3. | 60 | 600 | 2 |
| 4. | 30 | 900 | 1.75 |
| 5. | 45 | 900 | 2 |
| 6. | 60 | 900 | 1 |
| 7. | 30 | 1200 | 2 |
| 8. | 45 | 1200 | 1 |
| 9. | 60 | 1200 | 1.75 |

*2.3. Composite Fabrication Process*

In the composite fabrication process, two AA5083 plates were initially joined using Friction Stir Welding (FSW), as illustrated in Figure 1a. Following this, the weld joint was drilled repeatedly to create small holes measuring 2.5 mm in diameter and 4 mm deep, with a spacing of 15 mm between the holes, as shown in Figure 1b; reinforcing particles were then introduced into these holes. To prevent the scattering of particles during subsequent Friction Stir Processing (FSP), the holes were sealed using a pin-less FSP tool, with this step depicted in Figure 1c. The final pass of FSP was carried out at room temperature, and the process is illustrated in Figure 1d. Figure 2 shows the tools, both with pin and pin-less configurations, utilized in the fabrication of the composite materials. A high-speed steel tool (AISI 4140) with a shoulder diameter of 20 mm, a triangular pin measuring 5.8 mm, and a probe diameter of 7 mm was employed for both the FSW and FSP procedures.

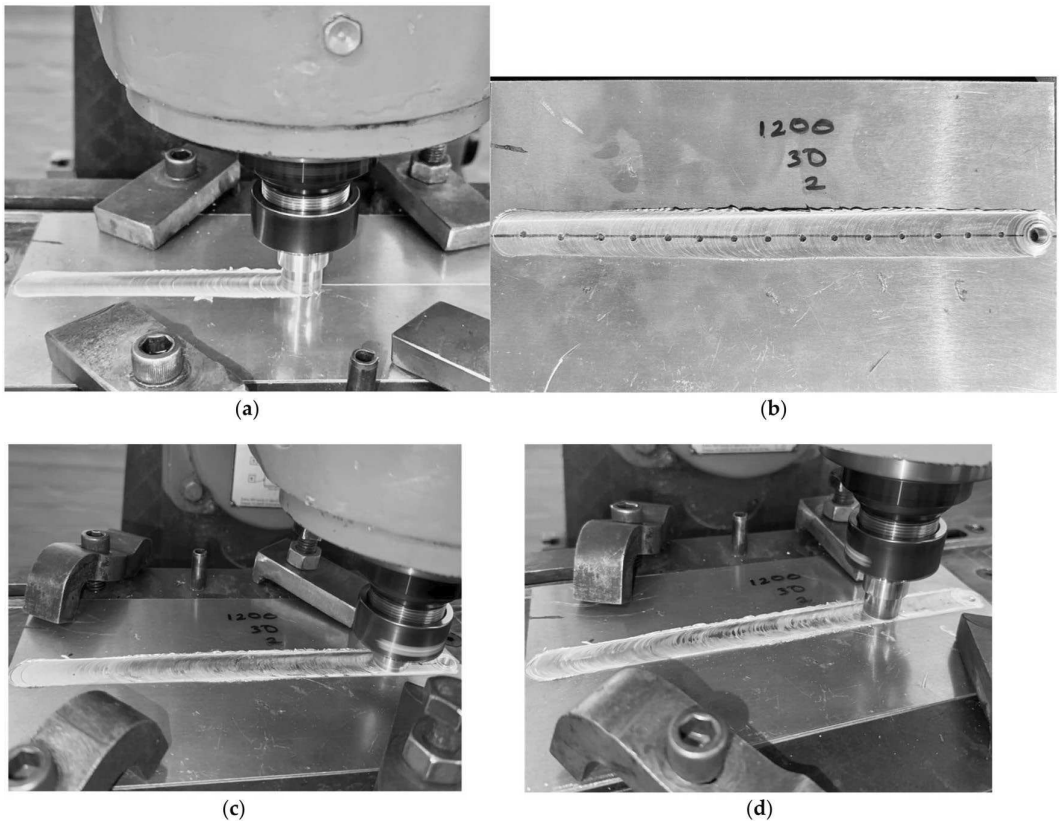


**Figure 1.** (**a**) FSW process; (**b**) Hole drilling and filling with reinforcement particles; (**c**) Closing of hole with pin less tool; (**d**) FSP single pass process.

**Figure 2.** Pin less tool and Pin with tool utilised during the fabrication process.

*2.4. Output Results Preparation*

Waterjet technology was used to cut the produced AMMCs joints (AA5083/Coal and AA5083/Silicon carbide) perpendicular to the processing direction in order to get specimens for the hardness and tensile testing. Tensile specimens were cut for tensile strength testing and generated in compliance with ASTM E8M-04 standards [41], while hardness specimens were cut for Vickers microhardness testing in line with ASTM E384 standards [42]. Figures 3 and 4 show the cut tensile and hardness specimens.

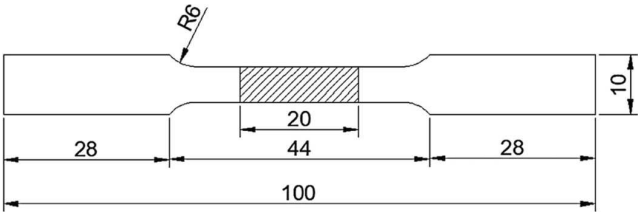


**Figure 3.** Tensile specimen.

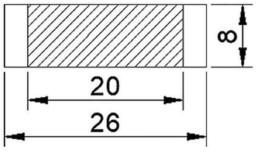


**Figure 4.** Hardness specimen.

### 3. Results and Discussions

Table 5 shows a summary of mechanical properties for different parameters for the AA5083/Silicon carbide and AA5083/Coal composites, respectively. From the results, the AA5083/Silicon Carbide and AA5083/Coal composites generally exhibit comparable mechanical properties to the base AA5083 material in terms of ultimate tensile strength and hardness. In terms of the UTS, while slightly lower than the base material, both composites maintain respectable UTS values. In terms of ductility, reinforcement particles hinder plastic deformation, leading to a significant decrease in ductility compared to the base material. And finally, for the hardness the addition of reinforcements increases the hardness of both composite types.

**Table 5.** Summary of mechanical properties for different composites and parameters.

| TS (mm/min) | RS (rpm) | TA (°) | AA5083/Si icon Carbide Composite | | | AA5083/Coal Composite | | |
|---|---|---|---|---|---|---|---|---|
| | | | MH (Hv) | UTS (MPa) | PE (%) | MH (Hv) | UTS (MPa) | PE (%) |
| 30 | 600 | 1 | 94.8 | 71.5 | 9.88 | 93.6 | 167 | 11.9 |
| 45 | 600 | 1.75 | 89.6 | 114 | 11.8 | 88.3 | 109 | 7.00 |
| 60 | 600 | 2 | 89.6 | 88 | 11.2 | 92.7 | 224 | 22.4 |
| 30 | 900 | 1.75 | 89.4 | 210 | 29.0 | 96.3 | 134 | 12.2 |
| 45 | 900 | 2 | 94.8 | 145 | 18.5 | 90.7 | 242 | 20.7 |
| 60 | 900 | 1 | 92.9 | 141 | 19.9 | 92.4 | 161 | 21.2 |
| 30 | 1200 | 2 | 90.6 | 243 | 29.5 | 95.3 | 101 | 7.60 |
| 45 | 1200 | 1 | 93.7 | 132 | 18.7 | 93.1 | 181 | 12.8 |
| 60 | 1200 | 1.75 | 89.6 | 121 | 12.1 | 95.9 | 141 | 9.38 |

List of symbols: **TS**: Traverse Speed (mm/min), **RS**: Rotational Speed (rpm), **TA**: Tilt Angle (degrees), **MH**: Microhardness (Hv), **UTS**: Ultimate Tensile Strength (MPa), **PE**: Percentage Elongation (%).

The highest hardness of both composite types is generally higher than the base material. This is due to the presence of hard reinforcement particles, which strengthen the matrix and increase its resistance to indentation. It is important to note that specific mechanical properties will depend on various factors, such as the volume fraction of reinforcements, the size and distribution of reinforcement particles, and the processing parameters used.

It should be noted that, since two different reinforcements (silicon carbide and coal) were used to optimize the AMMC fabrication parameters, the data analysis for the fabricated AA5083/Silicon carbide composite will be provided first, and then the analysis for the created AA5083/Coal composite will be shown in the next section.

*3.1. Signal-to-Noise Ratio Analysis*

The ultimate tensile strength, percentage elongation, and microhardness of the fabricated AA5083/Silicon carbide and AA5083/Coal composite joints were assessed using the Taguchi methods to find their optimal parameters. Taguchi's approach, a single-response optimization strategy, uses the signal-to-noise ratio to evaluate each parameter's effect on response factors. To optimize the response, the S/N ratio in this investigation was determined using the 'larger-the-better' criteria. The impact of each control factor on the response, the means, and S/N ratios were computed. The following formula can be used to compute the "larger-the-better" criteria [43]:

$$\frac{S}{N} = -10 \log\left(\frac{1}{n}\sum_{i-1}^{3}\frac{1}{y^2}\right) \quad (1)$$

where $n$ is the number of experimental repeats and $y$ is the response factor. The desirable output value is represented by 'Signal (S)', while the undesired value is represented by 'Noise (N)'.

The S/N ratio for parameter combinations of the AA5083/Silicon carbide composite is shown in Table 6, while the S/N ratio for parameter combinations of the AA5083/Coal composite is shown in Table 7.

**Table 6.** AA5083/Silicon carbide composite experimental results with relevant S/N ratio.

| TS (mm/min) | RS (rpm) | TA (°) | MH (Hv) | UTS (MPa) | PE (%) | S/N Ratio for HV | S/N Ratio for UTS | S/N Ratio for PE |
|---|---|---|---|---|---|---|---|---|
| 30 | 600 | 1 | 94.8 | 71.5 | 9.88 | 38.89 | 37.09 | 19.89 |
| 45 | 600 | 1.75 | 89.6 | 114 | 11.8 | 39.04 | 41.14 | 21.40 |
| 60 | 600 | 2 | 89.6 | 88 | 11.2 | 39.04 | 38.89 | 21.01 |
| 30 | 900 | 1.75 | 89.4 | 210 | 29.0 | 39.03 | 46.44 | 29.25 |
| 45 | 900 | 2 | 94.8 | 145 | 18.5 | 39.37 | 43.23 | 25.32 |
| 60 | 900 | 1 | 92.9 | 141 | 19.9 | 39.37 | 42.98 | 25.98 |
| 30 | 1200 | 2 | 90.6 | 243 | 29.5 | 39.14 | 47.71 | 29.39 |
| 45 | 1200 | 1 | 93.7 | 132 | 18.7 | 39.22 | 42.41 | 25.44 |
| 60 | 1200 | 1.75 | 89.6 | 121 | 12.1 | 39.04 | 41.66 | 21.64 |

List of symbols: **TS**: Traverse Speed (mm/min), **RS**: Rotational Speed (rpm), **TA**: Tilt Angle (degrees), **MH**: Microhardness (Hv), **UTS**: Ultimate Tensile Strength (MPa), **PE**: Percentage Elongation (%), **S/N Ratio**: Signal to noise ratio.

**Table 7.** AA5083/Coal composite experimental results with relevant S/N ratio.

| TS (mm/min) | RS (rpm) | TA (°) | MH (Hv) | UTS (MPa) | PE (%) | S/N Ratio for HV | S/N Ratio for UTS | S/N Ratio for PE |
|---|---|---|---|---|---|---|---|---|
| 30 | 600 | 1 | 93.6 | 167 | 11.9 | 38.66 | 44.45 | 21.55 |
| 45 | 600 | 1.75 | 88.3 | 109 | 7.00 | 38.92 | 40.75 | 16.90 |
| 60 | 600 | 2 | 92.7 | 224 | 22.4 | 39.34 | 47.01 | 27.02 |
| 30 | 900 | 1.75 | 96.3 | 134 | 12.2 | 39.67 | 42.54 | 21.71 |
| 45 | 900 | 2 | 90.7 | 242 | 20.7 | 39.15 | 47.68 | 26.33 |
| 60 | 900 | 1 | 92.4 | 161 | 21.2 | 39.32 | 44.14 | 26.52 |
| 30 | 1200 | 2 | 95.3 | 101 | 7.60 | 39.42 | 40.09 | 17.62 |
| 45 | 1200 | 1 | 93.1 | 181 | 12.8 | 39.38 | 45.15 | 22.11 |
| 60 | 1200 | 1.75 | 95.9 | 141 | 9.38 | 39.28 | 42.98 | 19.44 |

List of symbols: **TS**: Traverse Speed (mm/min), **RS**: Rotational Speed (rpm), **TA**: Tilt Angle (degrees), **MH**: Microhardness (Hv), **UTS**: Ultimate Tensile Strength (MPa), **PE**: Percentage Elongation (%), **S/N ratio**: Signal to noise ratio.

*3.2. Analysis of Variance*

3.2.1. Analysis of Variance Experimental Data for AA5083/Silicon Carbide Composite

1. Ranking of Contributing Factors

Analysing the factors that influence each response factor of the fabricated compos- ite joints is essential. Utilizing the delta ranking approach, MINITAB software Ver- sion 18 displays the most significant factors influencing the response factor of the fab- ricated AA5083/Silicon carbide composite joint. Tables 8–10 show that the fabricated AA5083/Silicon carbide composite joint's ultimate tensile strength, percentage elongation, and microhardness are significantly impacted by rotational speed (rank 1), traverse speed (rank 2), and tilt angle (rank 3). Based on the results, it can be observed that parameters for maximizing ultimate tensile strength and percentage elongation in AA5083/Silicon carbide composite joints are traversal speed at level 1, rotational speed at level 2, and tilt angle at level 3, as seen in Tables 8 and 9. The best parameters for optimum microhardness are traversal speed at level 2, and rotational speed at level 2, and tilt angle at level 3 (See Table 10).

**Table 8.** Table of Responses for the S/N ratio of ultimate tensile strength parameters.

| Level | Traverse Speed (mm/min) | Rotational Speed (rpm) | Tilt Angle (°) |
|---|---|---|---|
| 1 | **43.75** | 39.04 | 40.83 |
| 2 | 42.26 | **44.22** | 43.08 |
| 3 | 41.18 | 43.93 | **43.28** |
| Delta | 2.57 | 5.18 | 2.45 |
| Rank | 2 | 1 | 3 |

**Table 9.** Table of Responses for the S/N ratio of percentage elongation parameters.

| Level | Traverse Speed (mm/min) | Rotational Speed (rpm) | Tilt Angle (°) |
|---|---|---|---|
| 1 | **26.18** | 20.77 | 23.77 |
| 2 | 24.05 | **26.85** | 24.10 |
| 3 | 22.88 | 25.49 | **25.24** |
| Delta | 3.30 | 6.08 | 1.47 |
| Rank | 2 | 1 | 3 |

**Table 10.** Table of Responses for the S/N ratio of microhardness parameters.

| Level | Traverse Speed (mm/min) | Rotational Speed (rpm) | Tilt Angle (°) |
|---|---|---|---|
| 1 | 39.02 | 38.99 | 39.16 |
| 2 | **39.21** | **39.25** | 39.04 |
| 3 | 39.15 | 39.14 | **39.18** |
| Delta | 0.19 | 0.26 | 0.15 |
| Rank | 2 | 1 | 3 |

2. Percentage of Contribution Factors

Analysing the percentage contributions and F-values of the factors is crucial to gaining a clearer understanding of individual parameters on the output responses. The percentage contributions by S/N ratio analysis of variance for microhardness, elongation percentage, and ultimate tensile strength are displayed in Tables 11–13. Based on the results, the most significant factor influencing ultimate tensile strength was determined to be rotational speed, which accounted for 57.55% of the output response. Though less significant, tilt angle nonetheless made 12.58% of the total contribution (see Table 11). Discrepancies were seen between the percentage contribution in Table 11 and rankings in Table 8. A more comprehensive statistical analysis, including confidence intervals and replicate ex- periments, could enhance the reliability and interpretability of the findings. Therefore,

carefully considering research objectives and data characteristics is crucial when selecting between these methods to ensure accurate and reliable results. It was discovered that rotational speed and traverse speed, with percentage contributions of 60.36% and 16.62%, respectively, were significant parameters for percentage elongation (see Table 12). These results are consistent with the ranks that were shown in Table 9. Research by Salehi et al. [13], Chanakyan et al. [26], Syed et al. [35], and Puviyarasan et al. [44] also showed a similar pattern, identifying tool rotational speed as the main factor influencing ultimate tensile strength. Furthermore, it was shown that rotational speed and traverse speed were important factors in microhardness with percentage contributions of 48.17% and 27.40%, respectively (see Table 13). These results are consistent with the ranks that were shown in Table 10. Research by Chanakyan et al. [26], Syed et al. [35], and Butola et al. [45] also showed a similar pattern, identifying tool rotational speed as the main factor influencing microhardness. For percentage elongation and microhardness, the percentage contributions and F-values match the ranks as well.

**Table 11.** Contribution of individual factor to the variation of ultimate tensile strength.

| Source | Degree of Freedom (DF) | Seq SS | F-Value | *p*-Value | Percentage Contribution |
|---|---|---|---|---|---|
| TS (mm/min) | 2 | 9.9970 | 0.61 | 0.621 | 11.32 |
| RS (rpm) | 2 | 50.823 | 3.10 | 0.244 | **57.55** |
| TA (°) | 2 | 11.110 | 0.68 | 0.596 | 12.58 |
| Error | 2 | 16.379 | | | 18.55 |
| Total | 8 | 88.308 | | | |

**Table 12.** Contribution of individual factor to the variation of percentage elongation.

| Source | Degree of Freedom (DF) | Seq SS | F-Value | *p*-Value | Percentage Contribution |
|---|---|---|---|---|---|
| TS (mm/min) | 2 | 16.831 | 0.85 | 0.540 | 16.62 |
| RS (rpm) | 2 | 61.127 | 3.10 | 0.244 | **60.36** |
| TA (°) | 2 | 3.5830 | 0.18 | 0.846 | 3.538 |
| Error | 2 | 19.734 | | | 19.49 |
| Total | 8 | 101.275 | | | |

**Table 13.** Contribution of individual factor to the variation of microhardness.

| Source | Degree of Freedom (DF) | Seq SS | F-Value | *p*-Value | Percentage Contribution |
|---|---|---|---|---|---|
| TS (mm/min) | 2 | 0.05777 | 4.25 | 0.191 | 27.40 |
| RS (rpm) | 2 | 0.10103 | 7.39 | 0.119 | **48.17** |
| TA (°) | 2 | 0.03729 | 2.73 | 0.268 | 17.78 |
| Error | 2 | 0.01367 | | | 6.452 |
| Total | 8 | 0.20975 | | | |

3.2.2. Analysis of Variance Experimental Data for AA5083/Coal Composite

1. Ranking of Contributing Factors

An analysis of the factors affecting each response element of the fabricated AA5083/Coal composite joint was also carried out. The results shows that the resulting tensile strength of the fabricated AA5083/Coal composite joint is influenced by the tilt angle (rank 1), traverse speed (rank 2), and rotation speed (rank 3), as seen in Table 14. The percentage elongation and microhardness of the fabricated AA5083/Coal composite joint are influenced by the rotation speed (rank 1), tilt angle (rank 2), and traverse speed (rank 3), as indicated by Tables 15 and 16. Based on the results, it can be observed that parameters for maximizing ultimate tensile strength, percentage elongation, and tilt angle in AA5083/Coal composite joints are traversal speed at level 3, rotational speed at level 2, and tilt angle at level 3 as seen in Tables 14–16.

**Table 14.** Table of Responses for the S/N ratio of ultimate tensile strength parameters.

| Level | Traverse Speed (mm/min) | Rotational Speed (rpm) | Tilt Angle (°) |
|---|---|---|---|
| 1 | 42.36 | 44.07 | 44.58 |
| 2 | 44.53 | **44.78** | 42.09 |
| 3 | **44.71** | 42.74 | **44.92** |
| Delta | 2.35 | 2.04 | 2.83 |
| Rank | 2 | 3 | 1 |

**Table 15.** Table of Responses for the S/N ratio of percentage elongation parameters.

| Level | Traverse Speed (mm/min) | Rotational Speed (rpm) | Tilt Angle (°) |
|---|---|---|---|
| 1 | 20.29 | 21.82 | 23.39 |
| 2 | 21.78 | **24.85** | 19.35 |
| 3 | **24.33** | 19.72 | **23.65** |
| Delta | 4.03 | 5.13 | 4.30 |
| Rank | 3 | 1 | 2 |

**Table 16.** Table of Responses for the S/N ratio of microhardness parameters.

| Level | Traverse Speed (mm/min) | Rotational Speed (rpm) | Tilt Angle (°) |
|---|---|---|---|
| 1 | 39.25 | 38.97 | 39.12 |
| 2 | 39.15 | **39.38** | 39.29 |
| 3 | **39.31** | 39.36 | **39.30** |
| Delta | 0.16 | 0.40 | 0.18 |
| Rank | 3 | 1 | 2 |

2. Percentage of Contribution Factors

The percentage contributions by S/N ratio analysis of variance for microhardness, elongation percentage, and ultimate tensile strength are displayed in Tables 17–19. Based on the results, the most significant factors influencing ultimate tensile strength are tilt angle and traverse speed, which accounted for 27.0% and 19.3% respectively, of the output response (see Table 17). These results are consistent with the ranks that were shown in Table 14. It was discovered that rotational speed and tilt angle, with percentage contributions of 34.4% and 30.0%, respectively, were significant parameters for percentage elongation (see Table 18). These results are consistent with the ranks that were shown in Table 15. The most significant factor influencing microhardness was determined to be rotational speed, which accounted for 44.89% of the output response. Though less significant, tilt angle nonetheless made 9.131% of the total (see Table 19). These results are consistent with the ranks that were shown in Table 16. Research by Chanakyan et al. [26], Syed et al. [35], and Butola et al. [45] also showed a similar pattern, identifying tool rotational speed as the main factor influencing microhardness. The percentage contributions for ultimate tensile strength, percentage elongation, and microhardness match the rankings and the F-values.

**Table 17.** Contribution of individual factor to the variation of ultimate tensile strength.

| Source | Degree of Freedom (DF) | Seq SS | F-Value | *p*-Value | Percentage Contribution |
|---|---|---|---|---|---|
| TS (mm/min) | 2 | 10.233 | 0.47 | 0.682 | 19.3 |
| RS (rpm) | 2 | 6.4510 | 0.29 | 0.773 | 12.8 |
| TA (°) | 2 | 14.329 | 0.65 | 0.605 | **27.0** |
| Error | 2 | 21.969 | | | 41.5 |
| Total | 8 | 52.982 | | | |

**Table 18.** Contribution of individual factor to the variation of percentage elongation.

| Source | Degree of Freedom (DF) | Seq SS | F-Value | *p*-Value | Percentage Contribution |
|---|---|---|---|---|---|
| TS (mm/min) | 2 | 24.97 | 1.52 | 0.397 | 21.5 |
| RS (rpm) | 2 | 39.93 | 2.43 | 0.292 | **34.4** |
| TA (°) | 2 | 34.89 | 2.12 | 0.320 | 30.0 |
| Error | 2 | 16.44 | | | 14.1 |
| Total | 8 | 116.23 | | | |

**Table 19.** Contribution of individual factor to the variation of microhardness.

| Source | Degree of Freedom (DF) | Seq SS | F-Value | *p*-Value | Percentage Contribution |
|---|---|---|---|---|---|
| TS (mm/min) | 2 | 0.04040 | 0.14 | 0.874 | 5.792 |
| RS (rpm) | 2 | 0.31316 | 1.12 | 0.472 | **44.89** |
| TA (°) | 2 | 0.06369 | 0.23 | 0.815 | 9.131 |
| Error | 2 | 0.28026 | | | 40.18 |
| Total | 8 | 0.69751 | | | |

The optimized parameter micrographs for the AA5083/SiC and AA5083/Coal composite joints, captured at 50× and 100× magnifications, are presented in Figures 5a and 5b, respectively. Figure 5($a_1$,$b_1$) correspond to the optimal parameters of 900 rpm, 30 mm/min, and a 2° tilt angle for AA5083/SiC. Figure 5($a_2$,$b_2$) depicts 900 rpm, 45 mm/min, and a 2° tilt angle for AA5083/SiC. Figure 5($a_3$,$b_3$) shows 900 rpm, 60 mm/min, and a 2° tilt angle for AA5083/Coal. The microstructural images reveal the distribution of the reinforcement particles (SiC or Coal) within the AA5083 matrix, showing how different FSP parameters influence particle dispersion and bonding in the composites. These details explain the variations in mechanical properties based on the reinforcement material and processing conditions. The microstructural results show incomplete bonding between the reinforcement particles and the matrix, which can impact mechanical properties such as hardness, tensile strength, and ductility. As a result, it can be concluded that when it comes to the microstructure, proper bonding and uniform particle dispersion result in better mechanical performance, while incomplete bonding or uneven distribution can lead to reduced strength and ductility.

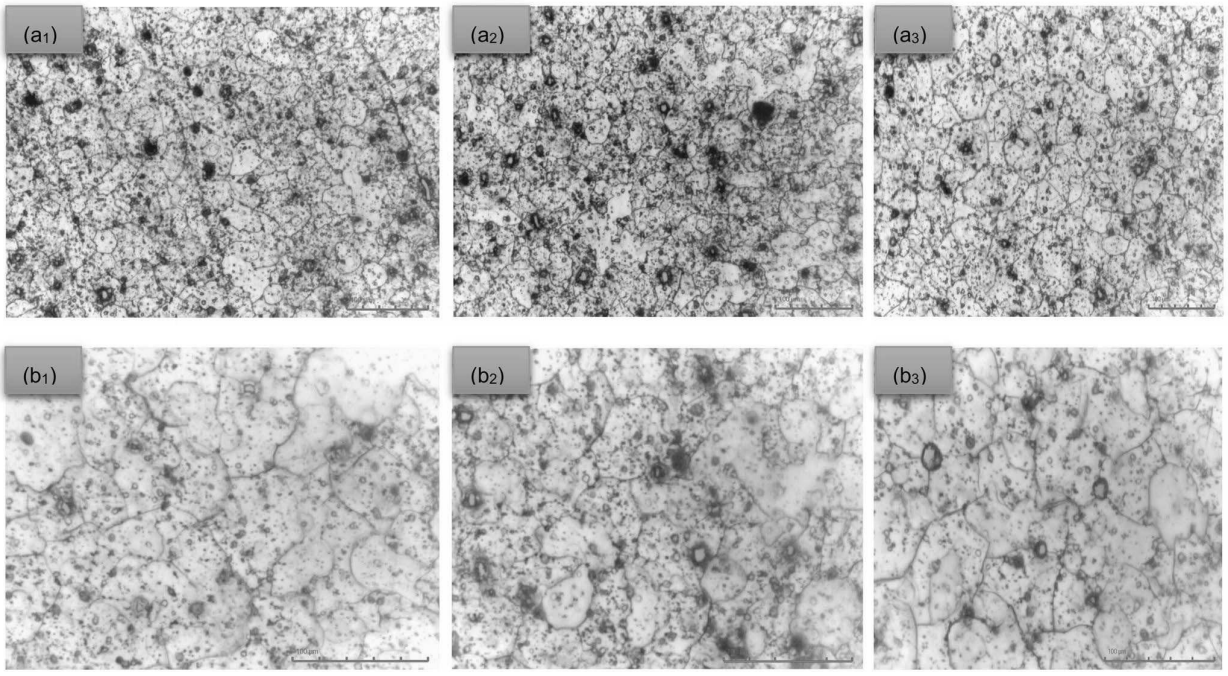


**Figure 5.** (**a**). Microstructure micrographs 50×: AA5083/SiC; (**a1**,**a2**) & AA5083/Coal (**a3**); (**b**). Microstructure micrographs 100×: AA5083/SiC; (**b1**,**b2**) & AA5083/Coal (**b3**).

## 4. Conclusions

To improve FSP parameters for AMMC joint fabrication, a Taguchi L9 factorial design was employed. The process of optimizing the parameters involved fabricating AMMCs with two distinct reinforcements, namely silicon and coal. The fabricated composites were AA5083/Silicon carbide composite and AA5083/Coal composite. Mechanical prop- erties such as hardness, tensile strength, and percent elongation were evaluated after the composites were fabricated.

The Taguchi approach based on the S/N ratio demonstrated that:

- The highest UTS and the percentage elongation for the AA5083/Silicon carbide composites fabrication process can be achieved if the rotation speed has been set to level 2 on the control panel, the traverse speed at level 1, and the tilt angle was at level 3. The best parameters for optimum microhardness are tilt angle at level 3, traversal speed at level 2, and rotational speed at level 2.
- At the second level of rotational speed, the third level of traversal speed, and the third level of tilt angle, for the the AA5083/Coal composite joints had the best FSP parameters to enhance the ultimate tensile strength, percentage elongation, and micro hardness.

The Taguchi approach based on the ANOVA demonstrated that:

- According to an ANOVA study, rotating speed has a larger impact on percentage elongation and microhardness for AA5083/Silicon carbide and AA5083/Coal composite joints. The ultimate tensile strength of AA5083/Silicon carbide is more affected by rotating speed, whereas the ultimate tensile strength of AA5083/Coal is more affected by tilt angle. The results indicate that the two different reinforcements have varying effects on the process parameters, suggesting that customized optimization strategies may be required based on the type of reinforcement used. These differences in ranking order are significant because they highlight the distinct material behaviors of the reinforcements during FSP. Harder reinforcements like SiC rely more on heat generation and plastic deformation for effective distribution and bonding, which is

why rotational speed is dominant. In contrast, softer reinforcements like coal benefit more from controlled material flow and uniform particle dispersion, making tilt angle a critical factor.

Based on the results the conclusion was drawn that:

- The best processing parameters for fabricating AA5083/Coal composite were a tilt angle of 2 degrees, a traverse speed of 60 mm/min, and a rotation speed of 900 rpm.
- The best processing parameters used when fabricating AA5083/Silicon carbide composite that yielded maximum microhardness were at a rotational speed of 900 rpm, traversal speed of 45 mm/min, and tilt angle of 2 degrees; the best combination of parameters to attain the maximum ultimate tensile strength and percentage elongation of the composite was achieved at a rotational speed of 900 rpm, traverse speed of 30 mm/min, and tilt angle of 2 degrees.

## 5. Limitation of Current Study

While this study offers valuable insights into FSP parameter optimization for AA5083-based composites, it has certain limitations. The focus on only two composite combinations may not fully capture the diverse range of materials that can be processed using FSP. The choice between S/N ratio and ANOVA can significantly influence the ranking order of factors, particularly in the presence of non-linear relationships and interaction effects. A more comprehensive statistical analysis, including confidence intervals and replicate experiments, could enhance the reliability and interpretability of the findings. Therefore, carefully considering the research objectives and data characteristics is crucial when selecting between these methods to ensure accurate and reliable results. These limitations highlight the need for further research to explore the broader applicability of the findings and address the challenges associated with FSP parameter optimization for AMCs.

## 6. Future Study

This study highlights the need for further research to delve deeper into the complexities of FSP in aluminium-based composites. Expanding the experimental design beyond the Taguchi L9 design and investigating additional factors such as tool geometry, process atmosphere, and thermal cycling could provide a more comprehensive understanding of the process. Moreover, conducting confirmation tests to validate the effectiveness of identified optimal parameter levels is essential. These research avenues hold the potential to significantly enhance the knowledge and application of FSP in this field.

**Author Contributions:** Conceptualization, V.M.; methodology, S.M.; software, O.M.; validation, O.M., V.M. and S.M.; formal analysis, S.M.; investigation, O.M.; resources, V.M.; data curation, S.M. and O.M.; writing—original draft, O.M.; writing—review and editing, S.M. and V.M.; visualization, O.M.; supervision, V.M. and S.M.; project administration, V.M. All authors have read and agreed to the published version of the manuscript.

**Funding:** This research received no external funding.

**Institutional Review Board Statement:** Not applicable.

**Informed Consent Statement:** Not applicable.

**Data Availability Statement:** The original contributions presented in the study are included in the article, further inquiries can be directed to the corresponding author.

**Acknowledgments:** The authors would also like to acknowledge the financial support provided by the CPUT through the Vice Chancellor's Prestigious Bursary award.

**Conflicts of Interest:** The authors declare no conflict of interest.

## Nomenclature

| | |
|---|---|
| AA | Aluminium Alloy |
| Al | Aluminium |
| AISI | American Iron and Steel Institute. |
| AMMCs | Aluminium Metal Matrix Composite |
| ASTM | American Society for Testing and Materials |
| ANOVA | Analysis of Variance |
| FSW | Friction Stir Welding |
| FSP | Friction Stir Processing |
| S/N ratio | Signal to Noise ratio |

## References


1. Clyne, T.W.; Withers, P.J. *An Introduction to Metal Matrix Composites*; Cambridge University Press: Cambridge, UK, 1993.
2. Rohatgi, P.K.; Asthana, R.; Das, S. Solidification, structures, and properties of cast metal-ceramic particle composites. *Int. Met. Rev.* **1986**, *31*, 115–139. [CrossRef]
3. Zhang, W.W.; Hu, Y.; Wang, Z.; Yang, C.; Zhang, G.Q.; Prashanth, K.G.; Suryanarayana, C. A novel high-strength Al-based nanocomposite reinforced with Ti-based metallic glass nanoparticles produced by powder metallurgy. *Mater. Sci. Eng. A* **2018**, *734*, 34–41. [CrossRef]
4. Jeyasimman, D.; Sivasankaran, S.; Sivaprasad, K.; Narayanasamy, R.; Kambali, R.S. An investigation of the synthesis, consolidation and mechanical behaviour of Al 6061 nanocomposites reinforced by TiC via mechanical alloying. *Mater. Des.* **2014**, *57*, 394–404. [CrossRef]
5. Scudino, S.; Liu, G.; Prashanth, K.G.; Bartusch, B.; Surreddi, K.B.; Murty, B.S.; Eckert, J. Mechanical properties of Al-based metal matrix composites reinforced with Zr-based glassy particles produced by powder metallurgy. *Acta Mater.* **2009**, *57*, 2029–2039. [CrossRef]
6. Kumar, K.R.; Kiran, K.; Sreebalaji, V.S. Micro structural characteristics and mechanical behaviour of aluminium matrix composites reinforced with titanium carbide. *J. Alloys Compd.* **2017**, *723*, 795–801. [CrossRef]
7. Shanavas, S.; Edwin Raja Dhas, J.; Murugan, N. Weldability of marine grade AA 5052 aluminum alloy by underwater friction stir welding. *Int. J. Adv. Manuf. Technol.* **2018**, *95*, 4535–4546. [CrossRef]
8. Abioye, T.E.; Mustar, N.; Zuhailawati, H.; Suhaina, I. Prediction of the tensile strength of aluminium alloy 5052-H32 fibre laser weldments using regression analysis. *Int. J. Adv. Manuf. Technol.* **2019**, *102*, 1951–1962. [CrossRef]
9. Dolatkhah, A.; Golbabaei, P.; Givi, M.B.; Molaiekiya, F. Investigating effects of process parameters on microstructural and mechanical properties of Al5052/SiC metal matrix composite fabricated via friction stir processing. *Mater. Des.* **2012**, *37*, 458–464. [CrossRef]
10. Saini, N.; Dwivedi, D.K.; Jain, P.K.; Singh, H. Surface modification of cast Al-17% Si alloys using friction stir processing. *Procedia Eng.* **2015**, *100*, 1522–1531. [CrossRef]
11. Zykova, A.P.; Tarasov, S.Y.; Chumaevskiy, A.V.; Kolubaev, E.A. A review of friction stir processing of structural metallic materials: Process, properties, and methods. *Metals* **2020**, *10*, 772. [CrossRef]
12. Gangil, N.; Siddiquee, A.N.; Maheshwari, S. Aluminium based in-situ composite fabrication through friction stir processing: A review. *J. Alloys Compd.* **2017**, *715*, 91–104. [CrossRef]
13. Salehi, M.; Saadatmand, M.; Mohandesi, J.A. Optimization of process parameters for producing AA6061/SiC nanocomposites by friction stir processing. *Trans. Nonferrous Met. Soc. China* **2012**, *22*, 1055–1063. [CrossRef]
14. Pashazadeh, H.; Teimournezhad, J.; Masoumi, A. Numerical investigation on the mechanical, thermal, metallurgical and material flow characteristics in friction stir welding of copper sheets with experimental verification. *Mater. Des.* **2014**, *55*, 619–632. [CrossRef]
15. Sidhu, M.S.; Chatha, S.S. Friction stir welding–process and its variables: A review. *Int. J. Emerg. Technol. Adv. Eng.* **2012**, *2*, 275–279.
16. Carlone, P.; Palazzo, G.S. Influence of process parameters on microstructure and mechanical properties in AA2024-T3 friction stir welding. *Metallogr. Microstruct. Anal.* **2013**, *2*, 213–222. [CrossRef]
17. Pasebani, S.; Charit, I.; Mishra, R.S. Effect of tool rotation rate on constituent particles in a friction stir processed 2024Al alloy. *Mater. Lett.* **2015**, *160*, 64–67. [CrossRef]
18. Nascimento, F.; Santos, T.; Vilaça, P.; Miranda, R.M.; Quintino, L. Microstructural modification and ductility enhancement of surfaces modified by FSP in aluminium alloys. *Mater. Sci. Eng. A* **2009**, *506*, 16–22. [CrossRef]
19. Molla Ramezani, N.; Davoodi, B.; Aberoumand, M.; Rezaee Hajideh, M. Assessment of tool wear and mechanical properties of Al 7075 nanocomposite in friction stir processing (FSP). *J. Braz. Soc. Mech. Sci. Eng.* **2019**, *41*, 182. [CrossRef]
20. Abbasi, M.; Bagheri, B.; Keivani, R. Thermal analysis of friction stir welding process and investigation into affective parameters using simulation. *J. Mech. Sci. Technol.* **2015**, *29*, 861–866. [CrossRef]
21. Vigneshkumar, M.; Padmanaban, G.; Balasubramanian, V. Influence of tool tilt angle on the formation of friction stir processing zone in cast magnesium alloy ZK60/SiCp surface composites. *Metallogr. Microstruct. Anal.* **2019**, *8*, 58–66. [CrossRef]

22. Mukherjee, I.; Ray, P.K. A review of optimization techniques in metal cutting processes. *Comput. Ind. Eng.* **2006**, *50*, 15–34. [CrossRef]
23. Montgomery, D.C. *Design and Analysis of Experiments*; John Wiley & Sons: Hoboken, NJ, USA, 2017.
24. Ross, P.J. *Taguchi Techniques for Quality Engineering: Loss Function, Orthogonal Experiments, Parameter and Tolerance Design*; McGraw-Hill: New York, NY, USA, 1988.
25. Saravanakumar, S.; Prakash, K.B.; Dinesh, D.; Kumar, P.M.; Fouad, Y.; Soudagar, M.E.M.; Ali, M.M.; Bashir, M.N. Optimizing friction stir processing parameters for aluminium alloy 2024 reinforced with SiC particles: A taguchi approach of investigation. *J. Mater. Res. Technol.* **2024**, *30*, 4847–4855. [CrossRef]
26. Chanakyan, C.; Sivasankar, S.; Meignanamoorthy, M.; Ravichandran, M.; Mohanavel, V.; Alfarraj, S.; Almoallim, H.S.; Manikandan, V.; Isaac JoshuaRamesh Lalvani, J. Optimization of FSP process parameters on AA5052 employing the S/N ratio and ANOVA method. *Adv. Mater. Sci. Eng.* **2021**, *2021*, 6450251. [CrossRef]
27. Bauri, R.; Yadav, D.; Kumar, C.S.; Ram, G.J. Optimized process parameters for fabricating metal particles reinforced 5083 Al composite by friction stir processing. *Data Brief* **2015**, *5*, 309–313. [CrossRef]
28. Rahman, M.Z.; Khan, Z.A.; Siddiquee, A.N.; Abidi, M.H.; Aboudaif, M.K.; Al-Ahmari, A. Mechanical and microstructural characterization of Ti-SiC reinforced AA5083 surface composites fabricated via friction stir process. *Mater. Res. Express* **2021**, *8*, 126523. [CrossRef]
29. Rahman, Z.; Siddiquee, A.N.; Khan, Z.A. Effect of Ti/SiC reinforcement on AA5083 surface composites prepared by friction stir processing. In *IOP Conference Series: Materials Science and Engineering*; IOP Publishing: Bristol, UK, 2021; Volume 1149, p. 012001.
30. Jain, V.K.; Yadav, M.K.; Siddiquee, A.N.; Khan, Z.A. Optimization of friction stir processing parameters for enhanced microhardness of AA5083/Al-Fe in-situ composites via Taguchi technique. *Mater. Sci. Eng. Appl.* **2021**, *1*, 55–61. [CrossRef]
31. D Ghetiya, N.; Bharti, S.; Patel, K.M.; Kumar, S.; Rahimian Koloor, S.S. An insight on optimization of FSP process parameters for the preparation of AA5083/(SiC-Gr) hybrid surface composites using the response surface methodology. *Compos. Adv. Mater.* **2023**, *32*, 26349833231186162. [CrossRef]
32. Bharti, S.; Ghetiya, N.D.; Patel, K.M. Parametric optimization of process parameters during friction stir processing of AA5083/(SiC-Gr) hybrid surface composite. *Mater. Today Proc.* **2023**, *78*, 420–425. [CrossRef]
33. Kaya, N.; Çetinkaya, C.; Karakoç, H.; Ada, H. Effect of process parameters of Al5083/SiC surface composites fabricated by FSP on microstructure, mechanical properties and wear behaviors. *Mater. Chem. Phys.* **2024**, *315*, 128991. [CrossRef]
34. Saxena, P.; Bongale, A.; Kumar, S.; Suresh, R. Tribological and hardness analyses of friction-stir-processed composites using the Taguchi approach. *Materials* **2023**, *16*, 420. [CrossRef]
35. Syed, K.; Ali, M.A.; Reddy, K.P.K.; Rao, B.N. Analyzing the Influence of Tool Profile on Friction Stir Process with Taguchi Optimization and Tungsten Nano Powder. *Int. J. Veh. Struct. Syst.* **2023**, *15*, 802–807.
36. Zass, K.; Mabuwa, S.; Msomi, V. Introduction of Coal Reinforcing Particles on the Dissimilar FSW AA608/AA5083 Joint via Friction Stir Processing. *Metals* **2023**, *13*, 1981. [CrossRef]
37. Rathee, S.; Maheshwari, S.; Siddiquee, A.N.; Srivastava, M.; Sharma, S.K. Process parameters optimization for enhanced microhardness of AA 6061/SiC surface composites fabricated via Friction Stir Processing (FSP). *Mater. Today Proc.* **2016**, *3*, 4151–4156. [CrossRef]
38. Jian, W.A.N.G.; Wang, X.W.; Bo, L.I.; Cheng, C.H.E.N.; Lu, X.F. Interface repairing for AA5083/T2 copper explosive composite plate by friction stir processing. *Trans. Nonferrous Met. Soc. China* **2021**, *31*, 2585–2596.
39. Msomi, V.; Mabuwa, S. Optimization of Normal and Submerged FSP Parameters for Dissimilar Aluminium Joints Using Taguchi Technique. *Mater. Sci. Forum* **2021**, *1034*, 207–218. [CrossRef]
40. Kosaraju, S.; Aziz, M.A.; Yadav, V.P.K.; Shiva, B.; Kolli, M.; Cheepu, M. Taguchi optimization of friction stir process parameters for enhancing joint strength of AA8011 reinforced with SiC nano particles. *Int. J. Interact. Des. Manuf. (IJIDeM)* **2024**, 1–12. [CrossRef]
41. *ASTM E8M-04*; Test Methods for Tension Testing of Metallic Materials. ASTM: West Conshohocken, PA, USA, 1995.
42. *ASTM E384*; Standard Test Method for Microindentation Hardness of Materials. ASTM: West Conshohocken, PA, USA, 2017.
43. Ahmadkhaniha, D.; Sohi, M.H.; Zarei-Hanzaki, A.; Bayazid, S.M.; Saba, M. Taguchi optimization of process parameters in friction stir processing of pure Mg. *J. Magnes. Alloys* **2015**, *3*, 168–172. [CrossRef]
44. Puviyarasan, M.; Kumar, V.S. Optimization of friction stir process parameters in fabricating AA6061/SiCp composites. *Procedia Eng.* **2012**, *38*, 1094–1103. [CrossRef]
45. Butola, R.; Ranganath, M.S.; Murtaza, Q. Fabrication and optimization of AA7075 matrix surface composites using Taguchi technique via friction stir processing (FSP). *Eng. Res. Express* **2019**, *1*, 025015. [CrossRef]

**APPENDIX I**

Optimization of FSP parameters in fabricating AA5083/Coal composites using Taguchi method

Engineering Research
Express



**PAPER** • **OPEN ACCESS**

# Optimization of FSP parameters in fabricating AA5083/Coal composites using Taguchi method

To cite this article: Oritonda Muribwathoho *et al* 2025 *Eng. Res. Express* **7** 015536

Engineering Research Express

PAPER

# Optimization of FSP parameters in fabricating AA5083/Coal composites using Taguchi method

Oritonda Muribwathoho[1], Velaphi Msomi[2] and Sipokazi Mabuwa[3]

[1] Cape Peninsula University of Technology, Mechanical and Mechatronics Engineering Department, 7535, South Africa
[2] University of South Africa, Department of Mechanical Engineering, College of Science, South Africa
[3] Durban University of Technology, Mechanical Engineering Department, PO Box 1334, Durban, 4000, South Africa

E-mail: oritondamuribwathoho@gmail.com, msomiv@gmail.com and sipokazimabuwa@gmail.com

Keywords: aluminium alloy, composite, metal matrix composite, mechanical properties, friction stir welding, friction stir processing, Taguchi

OPEN ACCESS

RECEIVED
20 August 2024

REVISED
23 December 2024

ACCEPTED FOR PUBLICATION
30 December 2024

PUBLISHED
31 January 2025



## Abstract

This study investigates the optimization of Friction Stir Processing parameters to fabricate AA5083/Coal composites using the Taguchi method. The influence of key process parameters—tool tilt angle, tool rotation speed, and traverse speed—on the mechanical properties of the composites was evaluated, specifically focusing on ultimate tensile strength, microhardness, and elongation. Taguchi's $L_9$ orthogonal array was employed to minimize the number of experiments and maximize the efficiency of parameter selection. A Hounsfield tensile test machine was used to evaluate ultimate tensile strength, and Innova Test Falcon 500 hardness testing machine was used to determine microhardness. The highest ultimate tensile strength, microhardness and percentage elongation achieved with the orthogonal arrays were 242 MPa, 96.27 HV, and 22.43%, respectively. The optimal parameters were identified as a tool tilt angle of 2°, a tool rotation speed of 900 rpm, and a traverse speed of 60 mm $min^{-1}$ based on signal-to-noise ratio. Furthermore, an analysis of variance was conducted to evaluate the parameter contributions. Analysis of Variance revealed that rotational speed had the most significant impact on microhardness and percentage elongation, while tilt angle most strongly influenced ultimate tensile strength. This study demonstrates the viability of coal particles as a cost-effective reinforcement material for AA5083 composites and provides a robust framework for optimizing friction stir processing parameters using statistical methods.

## 1. Introduction

Material selection is fundamental for the success of engineering products in diverse fields like marine, automotive, construction, and aerospace. Aluminium alloys have become the go-to choose because of their impressive properties: high strength-to-weight ratio (strong yet lightweight), excellent corrosion (durable) and wear resistance, and superior thermal and electrical conductivity (valuable for heat transfer or electrical applications) [1, 2]. Additionally, aluminium offers advantages over other metal matrix composites in terms of availability, cost-effectiveness, and lightweight nature, making it a practical and sustainable selection for a wide range of engineering applications.

Despite their excellent properties, aluminium alloys lack sufficient stiffness and strength. To address this, a focus has emerged on enhancing surface properties through various methods. The properties of aluminium alloys can be enhanced through heat treatments adding alloying elements and incorporating reinforcing particles to boost their performance in applications requiring strength wear resistance and structural applications [3]. Aluminium metal matrix composites (AMMCs) have become a popular solution, created by incorporating reinforcement particles into the alloy. AMMCs offer not only improved mechanical properties but also better electrical and thermal conductivity, making them suitable for demanding applications [4].

Friction Stir Processing (FSP) is now acknowledged as a cost eco promising method, for creating composites.

FSP is primarily a surface modification technique that refines the grain structure at the material's surface derived from Friction Stir Welding (FSW) [5] and has since been widely adopted as a novel technique for producing MMCs [6]. Unlike traditional methods such as powder metallurgy, squeeze casting, and stir casting for producing Metal Matrix Composites that can suffer from drawbacks, FSP offers a unique solution. It refines the grain structure at the surface and eliminates issues like porosity, defects, and weak bonding between particles. This localized modification process even allows for the creation of desirable micro or nanostructures within the material [6]. As a result, FSP significantly enhances AMMCs properties like tensile strength, hardness, wear resistance, and even resistance to harsh environments [7].

During the process of Friction Stir Processing (FSP), a localized section of a metal sheet is altered using a rotating tool equipped with both a pin and shoulder. The FSP tool is inserted into the designated area, as the pin plunges and rotates the material heat generated from friction softens the metal. The selected area and the tool move in relation, to each other allowing for the processing of the designated region. As a result, material is transferred from the leading edge towards the trailing face of the pin. Subsequently, the movement of the tool refines the microstructure and eliminates imperfections resulting in a quality layer [8]. This method significantly enhances the properties of Metal Matrix Composites (MMCs) such as resistance to corrosion, wear resistance, microhardness, fatigue endurance, and resistance to deformation over time.

Friction stir welding (FSP) relies on several critical parameters to achieve optimal results. These include tool geometry, traverse speed, tilt angle, tool rotation speed, and others [9]. Among these, traverse speed, tool geometry, and rotation speed have the biggest impact on heat generation, which significantly affects the quality of the welded joint. Many welding businesses traditionally employ a one-factor-at-a-time experimental approach, in which a single parameter is adjusted while others are kept constant. This trial-and-error method is time-consuming and inefficient [10, 11], especially for complex processes like Friction Stir Processing, which involves multiple interacting parameters. Researchers have explored alternative optimization methods to address these challenges, such as mathematical iterative search techniques, design of experiments (e.g., Response Surface Methodology, Taguchi), problem-specific heuristic approaches, and metaheuristic approaches (e.g., Genetic Algorithms, Tabu Search) [12].

While these advanced methods offer certain advantages, each comes with limitations that can hinder their practical application in FSP optimization. Mathematical iterative search techniques often concentrate on specific aspects of machining, such as cutting force, temperature, or tool wear. However, due to the numerous interdependent variables and their stochastic nature, these techniques may struggle to fully capture the complexities of the overall cutting process [13]. RSM techniques, relying on a series of experiments, may not be practical or cost-effective for many manufacturing scenarios [14]. Additionally, RSM requires a continuously differentiable objective function to determine optimal cutting conditions, which might not be the case in complex physical processes [12]. Metaheuristic methods offer a robust approach to optimization problems, bypassing the need for derivative information or explicit functional relationships. Genetic Algorithms (GAs),a popular metaheuristic technique, have demonstrated effectiveness in various applications. However, GAs are not without their limitations. Uncertain convergence, sensitivity to parameter settings, computational cost, and inconsistent results can hinder their performance. While GAs have proven valuable, it's essential to acknowledge these shortcomings and explore alternative metaheuristic techniques or hybridization strategies to address these limitations [12].

Given these limitations, the Taguchi method, with its orthogonal arrays, provides a robust alternative that optimizes FSP parameters with fewer experimental runs, offering a more practical and efficient approach for industrial applications. Taguchi's method employs Analysis of Variance (ANOVA) to identify the input parameters that significantly influence the quality or characteristics of the output. This is accomplished by looking for variations in the tested collections of items' average performance [15]. While extensive research exists on improving AA5083's surface properties with FSP, limited studies have explored how process parameters specifically impact surface quality during FSP of AA5083 [16–23].

Bauri *et al* [16] optimized FSP parameters for incorporating Nickel (Ni) particles into a metal-reinforced 5083 aluminium composite. Their focus was on identifying the ideal combination of traverse speeds, and tool rotation to achieve a defect-free nugget zone with uniform particle distribution. Experiments explored many parameters (tool rotation speeds: 1000–1800 rpm, traverse speeds: 6–24 mm $min^{-1}$) to optimize these goals. Using the optimized parameters, both coarse particles and finer particles from a ball mill were added to the Al matrix. The study revealed that a higher heat input [17], achieved through a lower traverse speed (15–12 mm $min^{-1}$), was necessary for effective dispersion of the coarser Ni particles (70 μm). However, this approach was unsuccessful, and even increasing the rotation speed did not improve the distribution of these coarse particles.

Taguchi's $L_8$ orthogonal array was utilized by Rahman *et al* [18] to assess the effects of FSP parameters on the surface characteristics and microstructure of AA5083 composites reinforced with Ti and SiC. Two levels were investigated for each of the following parameters: traverse speed, shoulder diameter, and tool rotation speed. The study revealed significant improvements in surface hardness after FSP, with a maximum recorded value of

90.4 HV. Interestingly, a strong correlation was observed between surface hardness and the processed zone (PZ) geometry. Specimens with a lower width-to-depth ratio exhibited superior hardness. The chosen parameters significantly impacted the PZ geometry, ranging from deep bowl shapes (smaller shoulder diameters) to shallow cups (larger diameters). Notably, specific parameter combinations—355 rpm, 63 mm $min^{-1}$ traverse speed, 17 mm shoulder diameter, and 355 rpm, 80 mm $min^{-1}$ traverse speed, 20 mm shoulder diameter—yielded exceptional tensile strengths of 292 and 294 MPa, respectively, which demonstrated remarkable stability even at elevated temperatures of 540 °C.

Rahman *et al* [19] investigated the use of FSP to create AA5083 surface composites reinforced with Ti and SiC. The main focus was identifying the optimal FSP parameters for achieving maximum surface hardness. Three parameters were studied: traverse speed, shoulder diameter, and tool rotation speed, using a Taguchi $L_4$ orthogonal array. The study found that the largest hardness (measured 2 mm below the processed surface) was achieved with a combination of 355 rpm tool rotational speed, 63 mm $min^{-1}$ tool traverse speed, and 17 mm shoulder diameter. Interestingly, this parameter combination also resulted in the lowest width-to-depth ratio in the processed zone. The microstructure analysis revealed significant grain size variations within the processed region. The stir zone (SZ) exhibited the highest hardness resulting from dynamic grain refinement and a more homogeneous distribution of reinforcement particles.

Jain *et al* [20] investigated the use of Taguchi's method to optimize FSP parameters for enhancing the microhardness of AA5083/Al-Fe *in situ* composites. The focus was on three key parameters: shoulder diameter, traverse speed, and rotation speed, each with three different settings. Using Taguchi's design and Minitab software for analysis, the study identified the optimal parameter combination for maximizing microhardness with minimal experimentation. The experimental setup utilized a tool with a 21 mm shoulder diameter rotating at 900 rpm and traversing at a speed of 63 mm $min^{-1}$. With these parameters, the processed zone's microhardness significantly increased (to about 123.30 HV), which is an improvement of 50.6% over the base material.

Ghediya *et al* [21] introduced a novel method for creating AA5083 surface composites reinforced with both SiC and Gr particles using FSP. The research centered on enhancing the parameters of the FSP process to achieve the desired composite properties. To create a mathematical model that could forecast the performance of the hybrid composites, Response Surface Methodology was used. The model was created using a Box-Behnken design with four key factors having three different settings each. Statistical analysis (ANOVA) revealed that the number of FSP passes and the ratio of SiC to Gr reinforcement particles were the most significant factors influencing the composite's properties ($p$-value $< 0.05$). This research demonstrates the effectiveness of RSM for optimizing the FSP process to create new hybrid metal matrix composites.

Similar to Ghetiya *et al* [21], Bharti *et al* [22] investigated optimizing the FSP process for AA5083 surface composites reinforced with a hybrid mixture of SiC and Gr particles. The focus was on maximizing the hardness of the resulting composite. Using RSM, a mathematical model to predict the composite's hardness based on various FSP parameters was developed. The study optimized factors such as the number of FSP passes, traverse speed, the SiC to Gr reinforcement ratio, and tool rotation speed. The analysis revealed that the optimal parameter combination for achieving the highest hardness (32.6 HRB) was 1000 rpm tool speed, traversing at a speed of 80 mm $min^{-1}$, 3 FSP passes, and a 75:25 ratio of SiC to Gr reinforcement.

Kaya [23] studied how the properties of FSP affect the surface, strength, and wear resistance of aluminium alloy (AA5083) surface composites that are strengthened with silicon carbide particles. The study used a single-pass FSP process on pre-treated AA5083-H111 alloy and investigated the influence of two key parameters: tool rotation speed and axial load. Different combinations of axial load (6000N, 8000n, and 10000 N) and rotation speed (560 rpm, 710 rpm, and 900 rpm) were tested. The optimal results were achieved with a combination of 900 rpm rotation speed and 8000 N axial load (sample N8). This sample exhibited significant improvements in both hardness (38% increase) and wear resistance (42% increase under 15 N load) compared to the parental material. Furthermore, sample N8 displayed tensile strength performance that remained close to the base metal, reaching 97% of its original strength.

Extensive research shows that Metal Matrix Composites (MMCs) are often reinforced with materials like nickel [16, 17], silicon carbide [18, 19, 21–23], titanium [18, 19], iron [20], or graphene [21, 22] which improve strength and wear resistance but can be costly. As far as AA5083 composites reinforced with coal particles developed via Friction Stir Processing (FSP) are concerned, no published research has investigated the impact of process parameters on their mechanical properties. This study explores coal as an alternative reinforcement material, given its abundant availability, low cost, and carbon-rich structure, which contribute to hardness and wear resistance. Although unconventional, coal has the potential to offer similar benefits to traditional reinforcements, making it a sustainable choice for MMCs. By optimizing FSP parameters—such as tool rotational speed, traverse speed, and tilt angle—using Taguchi's method and ANOVA, this study aims to maximize the mechanical performance of AA5083/coal composites. Unlike previous studies focused on traditional reinforcements, this work fills a gap in the literature by examining the effect of coal particles

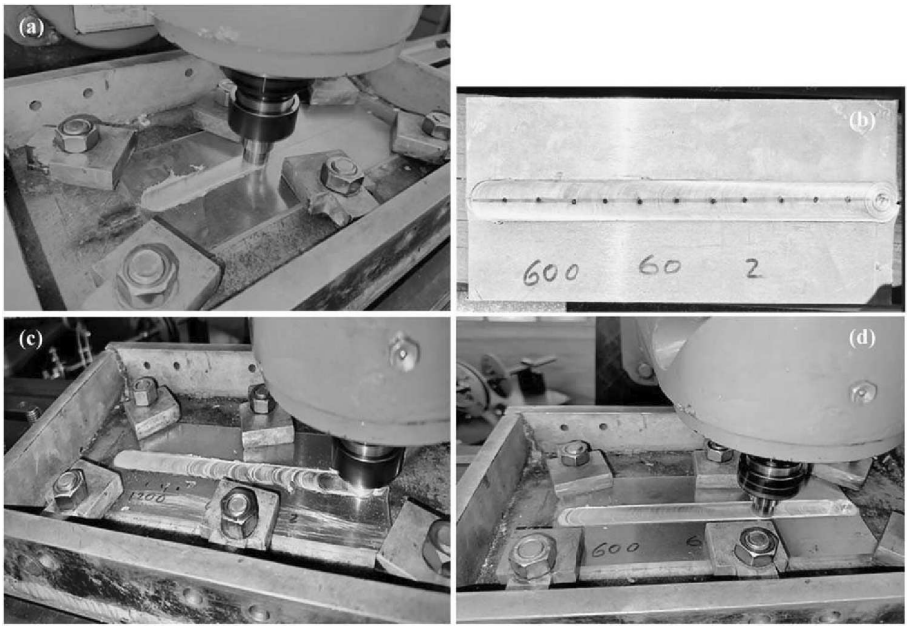


Table 1. Mechanical properties of AA5083 alloy.

| Mechanical properties | |
|---|---|
| Ultimate tensile strength | 311 MPa |
| Microhardness | 93.07 HV |

combined with optimized FSP parameters on AA5083, contributing novel insights into sustainable, cost-effective reinforcement options for MMCs.

## 2. Experimental procedure

In this study, a 6 mm thick AA5083 alloy plate served as the base material for producing aluminium metal matrix composites (AMMCs). Coal particles were incorporated as reinforcement material, constituting 5% of the composite's volume. The AA5083 alloy, widely used in marine and automotive applications, was chosen for its high strength-to-weight ratio and excellent corrosion resistance [24, 25]. Its composition includes 4.03% magnesium, 0.01% zinc, 0.02% titanium, 0.05% chromium, 0.15% silicon, 0.69% manganese, 0.16% iron, and 0.02% copper [26]. Coal particles were selected as the reinforcement material based on their low cost, abundant availability, and properties conducive to enhancing hardness and tensile strength. These characteristics make coal a promising, sustainable alternative to more traditional reinforcement materials like silicon carbide (SiC) or titanium (Ti), contributing to the composite's improved mechanical properties while reducing production costs. The mechanical properties of the AA5083 alloy are summarized in table 1.

To fabricate the AA5083/coal composite, two AA5083 plates (measuring 55 mm in width and 250 mm in length each) were first friction stir welded (FSWed) to create a joint, as illustrated in figure 1(a). The FSW process employed a high-strength AISI 4140 steel tool with a 20 mm shoulder diameter, a 5.7 mm triangular pin, and a 7 mm probe diameter. The experimental procedure for fabricating the Coal-AA5083 composite was adapted from established methods in Friction Stir Processing (FSP) commonly used for particle-reinforced composites.
Similar techniques were used in particle reinforcement and FSP composite fabrication in earlier research, which supports the experimental design and validates the parameter choices [26–33].

Following the welding, multiple holes with a depth of 4 mm and a diameter of 2.5 mm were drilled into the joint and filled with coal particles to serve as reinforcement, as shown in figure 1(b). The choice of hole dimensions was guided by previous studies [26, 27, 32–36], which emphasized the importance of optimizing

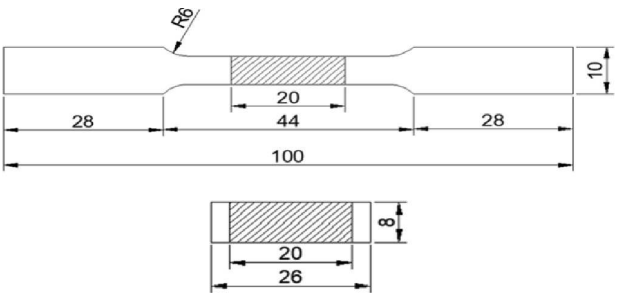


Table 2. Process variables and their corresponding values.

| Parameters | Units | Level | | |
|---|---|---|---|---|
| | | 1 | 2 | 3 |
| Rotational speed (RS) | [rpm] | 600 | 900 | 1200 |
| Tilt angle (TA) | [°] | 1 | 1.75 | 2 |
| Traverse speed (TS) | [mm/min] | 30 | 45 | 60 |

Table 3. Taguchi $L_9$ orthogonal design matrix.

| No of experiments | Rotational speed [rpm] | Traverse speed [mm/min] | Tilt angle [°] |
|---|---|---|---|
| 1. | 600 | 30 | 1 |
| 2. | 600 | 45 | 1.75 |
| 3. | 600 | 60 | 2 |
| 4. | 900 | 30 | 1.75 |
| 5. | 900 | 45 | 2 |
| 6. | 900 | 60 | 1 |
| 7. | 1200 | 30 | 2 |
| 8. | 1200 | 45 | 1 |
| 9. | 1200 | 60 | 1.75 |

these parameters to ensure uniform particle dispersion and adequate reinforcement volume within the stir zone. These dimensions were also selected to accommodate the coal particle size while preserving the structural integrity of the material during processing. To secure the coal particles within the matrix during processing, a pinless FSP tool was used to seal the holes, as depicted in figure 1(c). Finally, the composite underwent a finishing FSP pass at room temperature, as illustrated in figure 1(d).

Nine experiments were designed using Taguchi's $L_9$ orthogonal array, a statistical approach for optimizing parameters with a minimal number of tests. Minitab-18 software was employed to analyze the data obtained from these experiments. The study investigated three critical FSP process parameters—tool tilt angle, tool rotation speed, and traverse speed—each set at three different levels. These parameters were selected based on prior research, which indicates their significant influence on heat input, material flow, and the uniform distribution of reinforcement particles within the matrix [37, 38]. Tables 2 and 3 outline the specific parameter settings, their ranges, and the complete experimental layout.

The experimental procedure for fabricating the Coal-AA5083 composite was adapted from established methods in Friction Stir Processing (FSP) commonly used for particle-reinforced composites. The process involved drilling holes with a diameter of 2.5 mm and a depth of 4 mm into the base material, which were then filled with coal particles to ensure effective reinforcement. The choice of hole dimensions was guided by previous studies that demonstrated the importance of optimizing these parameters for uniform particle dispersion and adequate reinforcement volume within the stir zone. These dimensions were also selected to

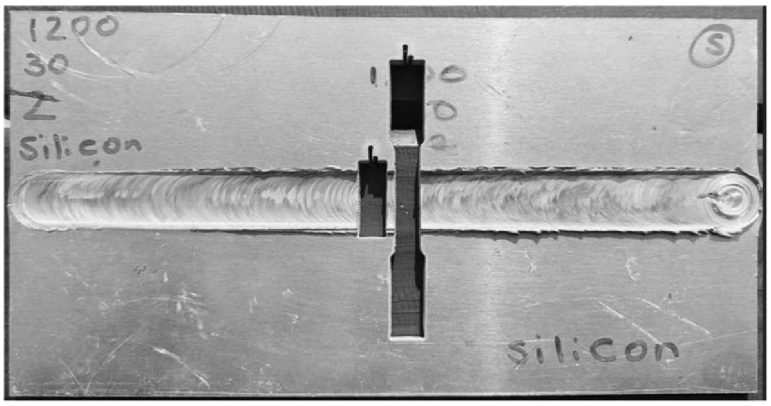


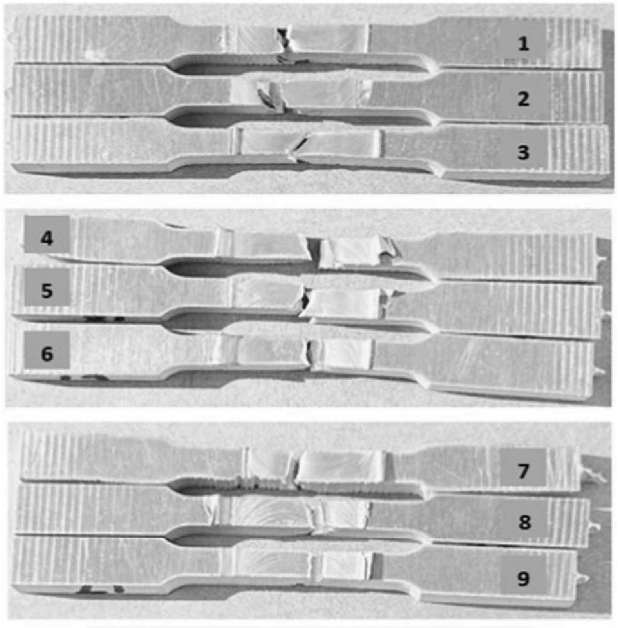


accommodate the particle size of coal while preserving the structural integrity of the base material during processing. References to similar methodologies in FSP composite fabrication and particle reinforcement methods support the experimental design and validate the chosen parameters.

Following the fabrication of AA5083/coal composites, waterjet cutting technology was used to precisely cut specimens perpendicular to the FSP direction for mechanical testing. Tensile specimens were prepared according to ASTM E8M-04 standards to assess the tensile strength of the composite joint, ensuring consistent dimensions across all samples for accurate comparison. Additional specimens were prepared for microhardness evaluation in line with ASTME384 standard, with testing conducted using a load of 300 gf and a dwell time of 10 s. Indentations were made along the cross-section of the stir zone at regular intervals to evaluate the uniformity of hardness distribution. All tensile and microhardness tests were performed at room temperature in a controlled environment to maintain consistent testing conditions, with no preheating or post-processing treatments applied to the specimens.

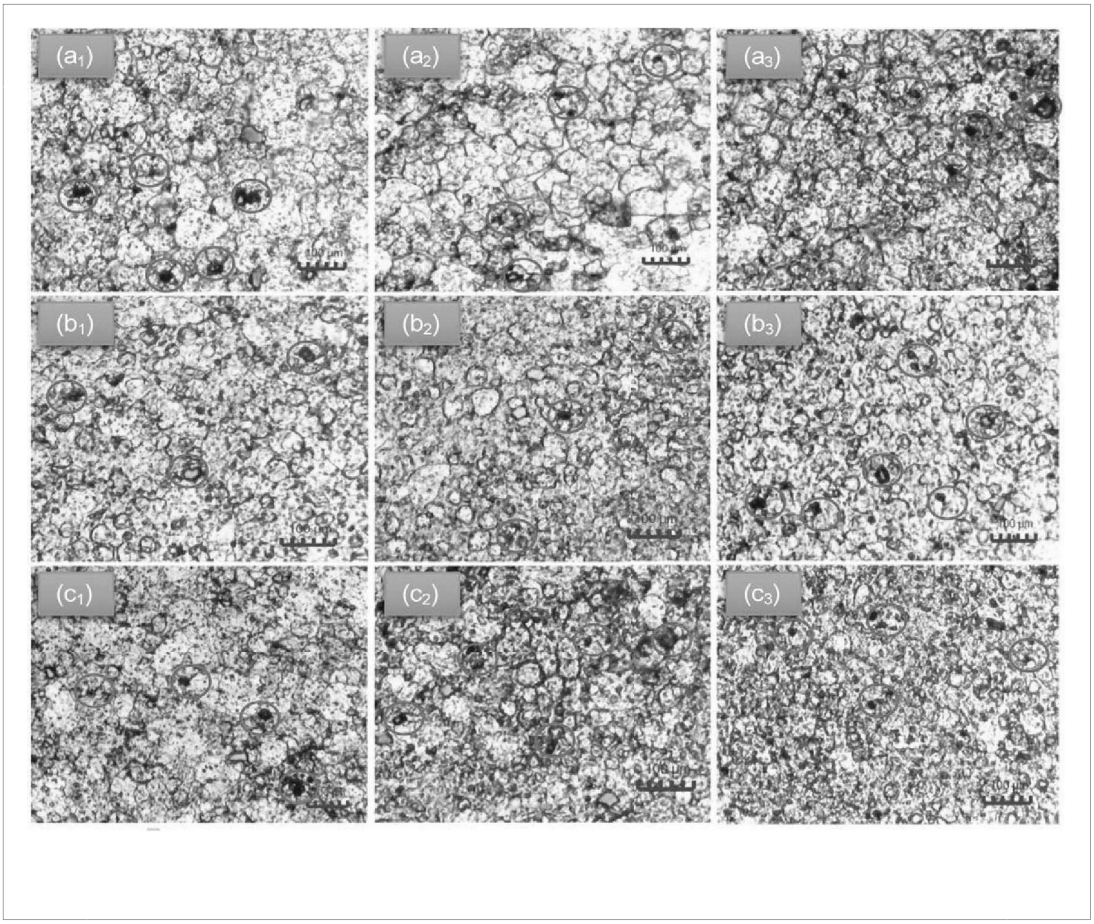


Table 4. Mechanical properties of AA5083/coal composites.

| Experiment no. | UTS (MPa) | PE (%) | MH (HV) |
|---|---|---|---|
| 1. | 167 | 11.95 | 93.62 |
| 2. | 109 | 7.000 | 88.34 |
| 3. | 224 | 22.43 | 92.65 |
| 4. | 134 | 12.18 | 96.27 |
| 5. | 242 | 20.73 | 90.65 |
| 6. | 161 | 21.18 | 92.43 |
| 7. | 101 | 7.600 | 95.33 |
| 8. | 181 | 12.75 | 93.09 |
| 9. | 141 | 9.380 | 95.85 |
| Base Material | 311 | 58.65 | 93.07 |

Figure 2 illustrates the dimensions and configuration of the tensile specimens and microhardness indentation layout. Figure 3 shows the plate with cut tensile and microhardness specimens, while figure 4 displays the sample after tensile testing.

## 3. Results and discussion

### 3.1. Microstructure

Figure 5 illustrates the optical microstructures of each surface composite tested. Figures 4($a_1$), ($a_2$), and ($a_3$) showcase the microstructure for the AA5083/Coal composite at 600 rpm, 30 mm $min^{-1}$, and a 1° tilt; 600 rpm, 45 mm $min^{-1}$, and a 1.75° tilt; and 600 rpm, 60 mm $min^{-1}$, and a 2° tilt, respectively. Similarly, figures 4($b_1$),

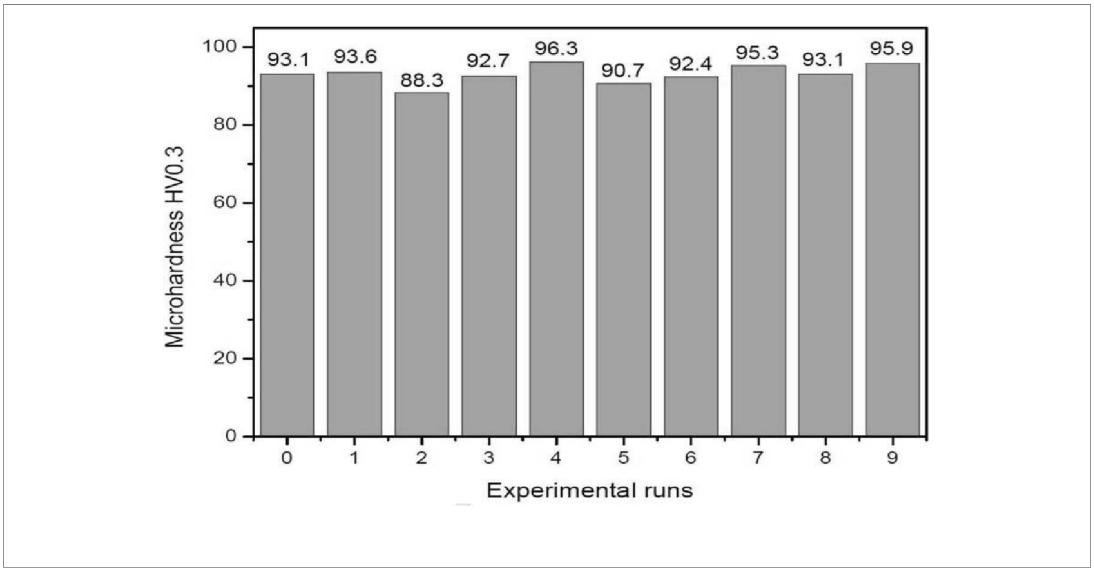


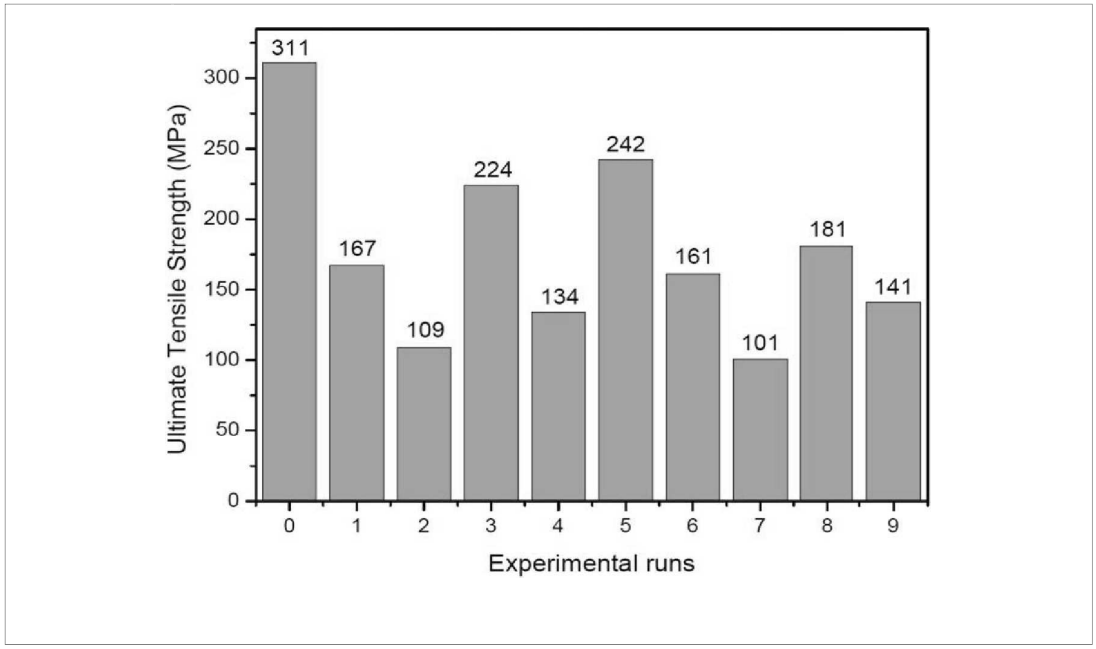


($b_2$), and ($b_3$) present the microstructure for another set of composites at 900 rpm, with tilt angles of 1.75°, 2°, and 1° for traverse speeds of 30 mm $min^{-1}$, 45 mm $min^{-1}$, and 60 mm $min^{-1}$, respectively. Lastly, figures 4($c_1$), ($c_2$), and ($c_3$) detail the microstructure at 1200 rpm, with corresponding tilt angles and traverse speeds as 2° at 30 mm $min^{-1}$, 1° at 45 mm $min^{-1}$, and 1.75° at 60 mm $min^{-1}$.

The microstructural images provide insights into the distribution of coal reinforcement particles within the AA5083 matrix, highlighting how varying FSP parameters affect particle dispersion and bonding within the composites. The microstructure images reveal that the coal particles are dispersed within the stir zone, but there is a low-particle-percentage bond, likely due to limited vertical material mobility. Similar findings were reported by [32], who observed that non-uniform particle dispersion significantly affects the failure properties and plastic deformation behavior of metal-based composites. These observations clarify the differences in mechanical properties, which are influenced by both the reinforcement material and processing conditions. The results suggest that incomplete bonding between the reinforcement particles and the matrix can negatively impact mechanical properties, including hardness, tensile strength, and ductility.

Table 5. AA5083/Coal composite experimental results with relevant S/N ratio.

| RS (rpm) | TS (mm/min) | TA (°) | UTS (MPa) | PE (%) | MH (HV) | S/N ratio For UTS | S/N ratio For PE | S/N ratio For HV |
|---|---|---|---|---|---|---|---|---|
| 600 | 30 | 1 | 167 | 11.95 | 93.62 | 44.4543 | 21.5474 | 38.6606 |
| 600 | 45 | 1.75 | 109 | 7.000 | 88.34 | 40.7485 | 16.9020 | 38.9231 |
| 600 | 60 | 2 | 224 | 22.43 | 92.65 | 47.0050 | 27.0166 | 39.3369 |
| 900 | 30 | 1.75 | 134 | 12.18 | 96.27 | 42.5421 | 21.7129 | 39.6698 |
| 900 | 45 | 2 | 242 | 20.73 | 90.65 | 47.6763 | 26.3320 | 39.1474 |
| 900 | 60 | 1 | 161 | 21.18 | 92.43 | 44.1365 | 26.5185 | 39.3163 |
| 1200 | 30 | 2 | 101 | 7.600 | 95.33 | 40.0864 | 17.6163 | 39.4190 |
| 1200 | 45 | 1 | 181 | 12.75 | 93.09 | 45.1536 | 22.1102 | 39.3781 |
| 1200 | 60 | 1.75 | 141 | 9.380 | 95.85 | 42.9844 | 19.4441 | 39.2833 |

Table 6. Signal to Noise ratio response for ultimate tensile strength.

| Level | Rotational speed(rpm) | Traverse speed (mm/min) | Tilt angle (°) |
|---|---|---|---|
| 1 | 44.07 | 42.36 | 44.58 |
| 2 | 44.78 | 44.53 | 42.09 |
| 3 | 42.74 | 44.71 | 44.92 |
| Delta | 2.04 | 2.35 | 2.83 |
| Rank | 3 | 2 | 1 |

Table 7. Signal to Noise ratio response for percentage elongation.

| Level | Rotational speed(rpm) | Traverse speed (mm/min) | Tilt angle (°) |
|---|---|---|---|
| 1 | 21.82 | 20.29 | 23.39 |
| 2 | 24.85 | 21.78 | 19.35 |
| 3 | 19.72 | 24.33 | 23.65 |
| Delta | 5.13 | 4.03 | 4.30 |
| Rank | 1 | 3 | 2 |

3.2. Mechanical properties Table 4 presents the mechanical properties of the AA5083/coal composites. The study achieved the highest tensile strength of 242 MPa with a tool tilt angle of 2°, a rotational speed of 900 rpm, and a traverse speed of 45 mm $min^{-1}$. Additionally, the highest percentage elongation achieved was 22.43%, obtained with a tool tilt angle of 2°, a tool rotational speed of 600 rpm, and a traverse speed of 60 mm $min^{-1}$. The highest microhardness measured was 96.27 HV, achieved with a tool tilt angle of 1.75°, a tool rotational speed of 900 rpm, and a traverse speed of 30 mm $min^{-1}$. The AA5083/coal composites showed lower ultimate tensile strength values compared to the base material. A similar trend, with reduced tensile strengths observed in single-pass composites compared to the base material, has been reported by Ayvaz *et al* [39], Yuvaraj *et al* [40], and Srivastava *et al* [41, 42]. Srivastava *et al* attributed the lower tensile strength to the agglomeration of reinforcement particles in single-pass specimens.

The addition of reinforcements increased hardness, with the highest values generally surpassing those of the base material, although some regions exhibited lower hardness. This variation can be attributed to dynamic recrystallization, differences in grain size, particle distribution [43], and fragmentation or redistribution of intermetallic particles [44]. The higher hardness is largely due to a more homogeneous distribution of the coal reinforcement on the surface and the ultra-refinement of grains [23]. Similar studies have reported compatible microhardness results, consistent with this study's findings [45]. Figure 6 presents the ultimate tensile strength bar graph, while figure 7 displays the hardness bar graph.

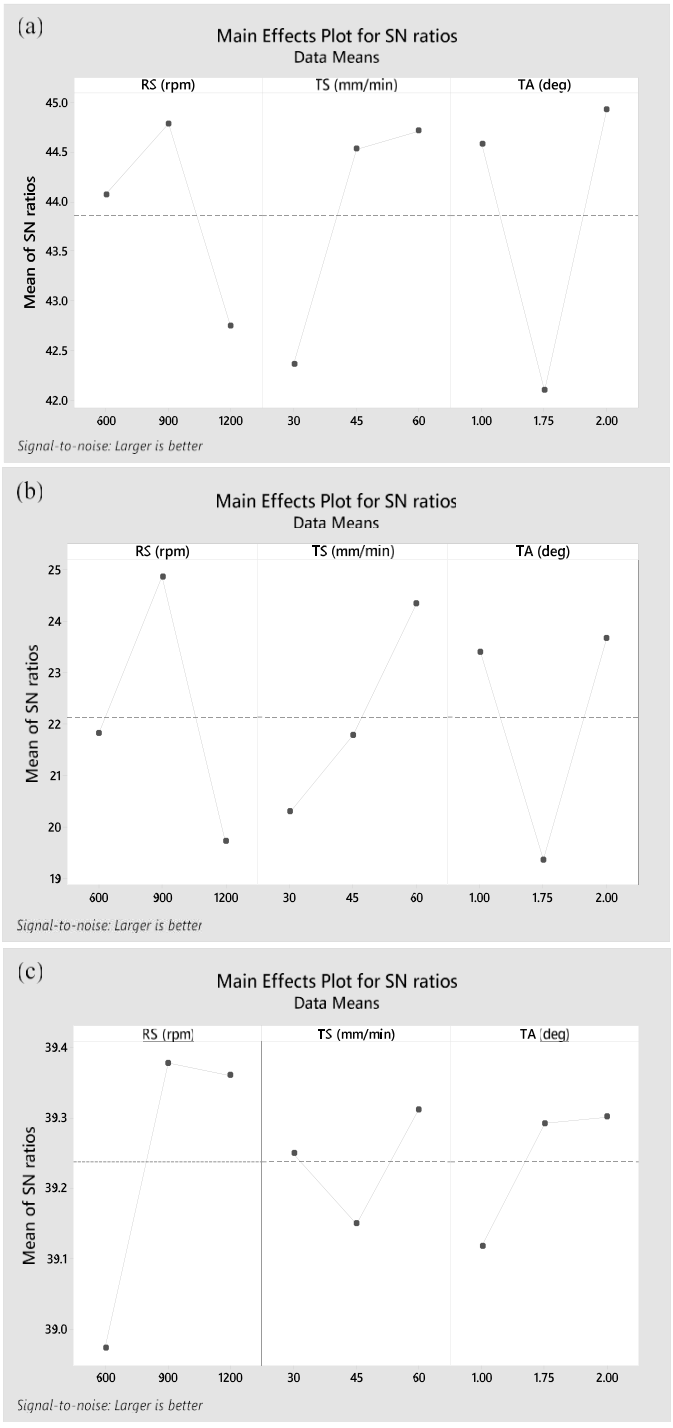


Figure 8. AA5083/Coal composite S/N ratio plot (a) UTS; (b) PE; (c) HV.

3.3. Signal-to-noise ratio analysis

Taguchi's method was utilized to optimize the AMMC parameters based on the fabricated AA5083/Coal composite joints. This approach involved analysing three key response factors: ultimate tensile strength, microhardness, and percent elongation. Taguchi's signal-to-noise ratio was utilized to assess the influence of each process parameter on these response factors using the experimental data. Higher S/N ratios indicate better

Table 8. Signal to noise ratio response for microhardness.

| Level | Rotational speed(rpm) | Traverse speed (mm/min) | Tilt angle (°) |
|---|---|---|---|
| 1 | 38.97 | 39.25 | 39.12 |
| 2 | 39.38 | 39.15 | 39.29 |
| 3 | 39.36 | 39.31 | 39.30 |
| Delta | 0.40 | 0.16 | 0.18 |
| Rank | 1 | 3 | 2 |

Table 9. Factors that impact/contribute to the variation of ultimate tensile strength.

| Source | Degree of freedom (DF) | F-value | P-value | % Contribution |
|---|---|---|---|---|
| RS (rpm) | 2 | 0.29 | 0.773 | 12.18 |
| TS (mm/min) | 2 | 0.47 | 0.682 | 19.31 |
| TA (°) | 2 | 0.65 | 0.605 | 27.05 |
| Error | 2 | | | 41.47 |
| Total | 8 | | | |

Table 10. Factors that impact/contribute to the variation of percentage elongation.

| Source | Degree of freedom (DF) | F-value | P-value | % Contribution |
|---|---|---|---|---|
| RS (rpm) | 2 | 2.43 | 0.292 | 34.35 |
| TS (mm/min) | 2 | 1.52 | 0.397 | 21.48 |
| TA (°) | 2 | 2.12 | 0.320 | 30.02 |
| Error | 2 | | | 14.14 |
| Total | 8 | | | |

Table 11. Factors that impact/contribute to the variation of microhardness.

| Source | Degree of freedom (DF) | F-value | P-value | % Contribution |
|---|---|---|---|---|
| RS (rpm) | 2 | 1.12 | 0.472 | 44.89 |
| TS (mm/min) | 2 | 0.14 | 0.874 | 5.792 |
| TA (°) | 2 | 0.23 | 0.815 | 9.131 |
| Error | 2 | | | 40.18 |
| Total | 8 | | | |

process parameter settings, following the 'larger-the-better' approach. The objective in this case is to determine parameter combinations that maximize the composite joints' microhardness, percentage elongation, and UTS. The following formula can be used to compute the 'larger-the-better' criterion [46, 47]:

$$\frac{S}{N} = -10\log\left(\frac{1}{n}\sum_{i-1}^{3}\frac{1}{y^2}\right) \quad (1)$$

In the formula, n represents the number of recurrences of experiments, and y denotes the response factors, which in this study are UTS, microhardness, and percentage elongation. 'Noise (N)' denotes the unwanted value for the output characteristic, whereas 'Signal (S)' denotes the desired value. Table 5 presents the experimental results alongside their corresponding S/N ratios for every combination of FSP parameters used with the AA5083/Coal composite. These results are further visualized in graphical form in figure 8.

The maximum ultimate tensile strength, percentage elongation, and microhardness for the AA5083/Coal composite joints are achieved when the tilt angle and traverse speed are set to level 3, and the rotational speed is set to level 2 (see figures 8(a)–(c)). Analysis of the signal-to-noise ratio indicated that the optimal process parameters are a tilt angle of 2 degrees, a traverse speed of 60 mm $min^{-1}$, and a rotational speed of 900 rpm. The larger-the-better approach has been successfully utilized to optimize mechanical properties in metal matrix composites, as demonstrated in previous research [20, 48].

### 3.4. Ranking of contributing factors and determining optimum factor

Minitab 18 software was employed to analyses the S/N ratio data and identify the most significant factors influencing each response variable ultimate tensile strength, elongation, microhardness) for the AA5083/Coal

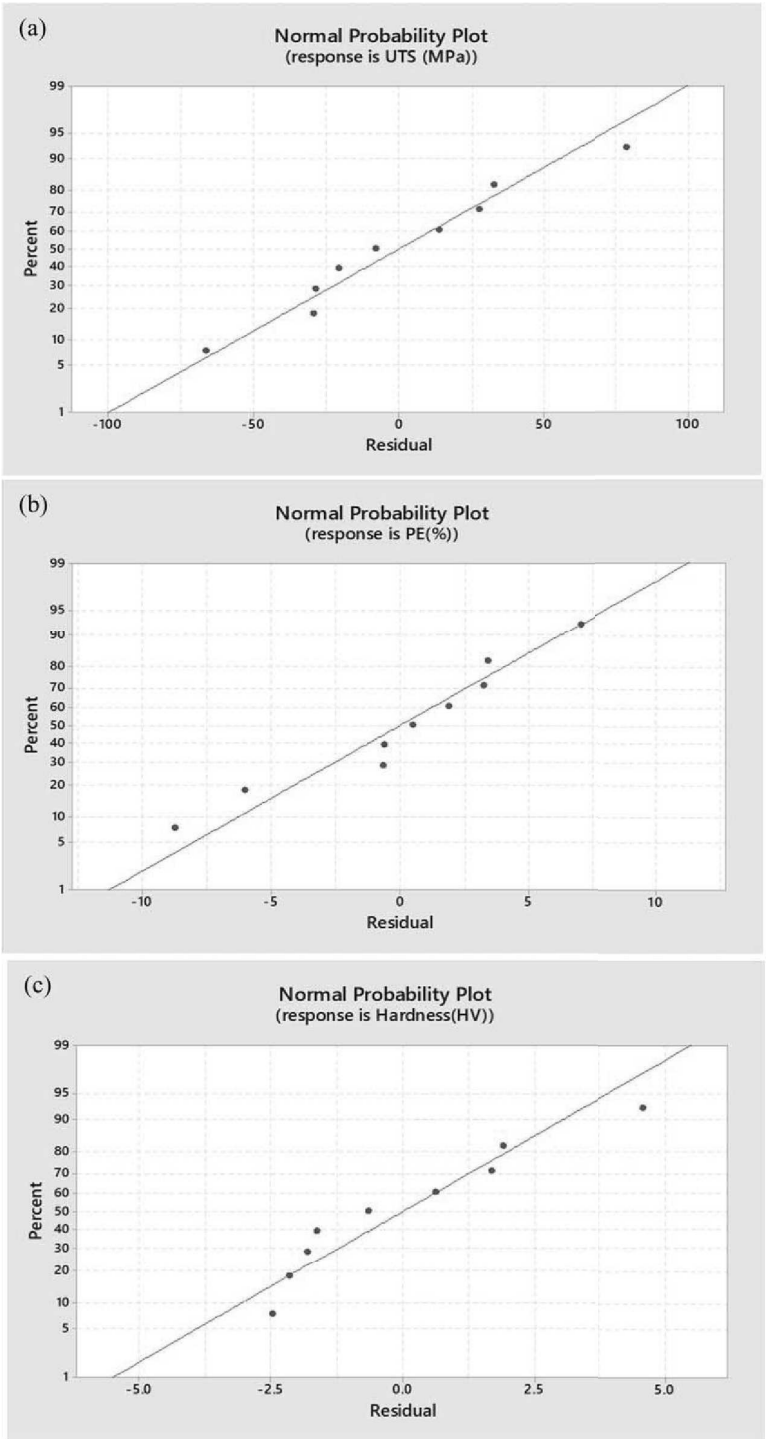


composite joints. This analysis utilized a delta ranking system within Minitab. For all three levels, the mean S/N ratio was computed across the three FSP process parameters (tilt angle, traverse speed, and rotational speed). Tables 6–8 summarize these findings. Table 6 indicates that tilt angle exerts the most significant influence on the ultimate tensile strength of the composite joint at rank 1, followed by traverse speed at rank 2 and rotational speed at rank 3. Tables 7 and 8 revealed that the percentage elongation and microhardness are primarily influenced by the rotational speed (rank 1), the tilt angle at rank 2, and lastly the traverse speed at rank 3. The study reveals that

the optimal traversal speed, rotational speed, and tilt angle for maximizing ultimate tensile strength, percentage elongation, and tilt angle in AA5083/Coal composite joints are at level 3, level 2, and level 3 as see in tables 6–8. The S/N ratio mean response table was used to determine the ideal settings for each response. Optimal values for UTS, PE, and HV were achieved using a tool rotational speed of 900 rpm, a tool traverse speed of 60 mm $min^{-1}$, and a tool tilt angle of 2 degrees.

### 3.5. Analysis of variance

To statistically evaluate the significance of each FSP parameter on the response variables (ultimate tensile strength, elongation, microhardness), a frequency test was employed [49]. This approach helps determine the percent contribution of each factor and its impact on the desired properties. Tables 9–11 summarize the ANOVA results for the S/N ratio of ultimate tensile strength, percentage elongation, and microhardness. Table 9 reveals that tilt angle is the most dominant factor influencing ultimate tensile strength, contributing 27.05% according to the ANOVA analysis. This aligns with the ranking in table 6. The tilt angle's influence on ultimate tensile strength can be explained by its role in controlling material flow and tool penetration into the workpiece. Higher tilt angles can lead to larger grain and particle sizes, potentially affecting the mechanical properties. Conversely, lower tilt angles may result in defects in the processed zone [50].

Similarly, the findings for elongation (table 10) and microhardness (table 11) support the rankings in tables 7 and 8, respectively. Table 10 indicates that rotational speed is the most influential factor affecting percentage elongation (PE), contributing 34.35% to the variation. Similarly, table 11 shows that rotational speed is the primary factor influencing microhardness, contributing 44.89%. The significant effect of rotational speed on microhardness aligns with previous research (e.g., Chanakyan *et al* [51], Syed *et al* [52], and Butola *et al* [53]). The rotational speed is a dominant process variable in FSP, significantly influencing the even distribution of reinforcement particles, grain refinement, and heat input during the process [54–57], all of which contribute to increased hardness.

#### *3.5.1. Residual analysis using normal probability plot*

The normality of residuals was assessed using Normal Probability Plots for the responses—Ultimate Tensile Strength, Percentage Elongation, and Microhardness as shown in figure 9. These plots serve as a graphical method to evaluate whether the residuals follow a normal distribution, which is a key assumption for the validity of ANOVA. The Normal Probability Plot for UTS showed that the residuals aligned closely with the straight line, indicating an approximate normal distribution and validating the ANOVA assumptions for this response. Similarly, the residuals for Microhardness exhibited a strong linear trend, confirming their normality.

For Percentage Elongation, the residuals displayed slight deviations from the straight line, suggesting minor departures from normality. However, these deviations were not severe enough to undermine the reliability of the ANOVA results. These findings align with previous studies [5, 58–61] that advocate for the use of Normal Probability Plots in residual analysis to ensure the validity of statistical models.

Overall, the Normal Probability Plots demonstrate that the residuals for UTS, PE, and MH are approximately normally distributed, ensuring the reliability of the ANOVA results. While the graphical analysis supports the normality assumption, minor deviations in PE suggest that additional quantitative tests, such as the Kolmogorov-Smirnov test, may be conducted in future studies to confirm the findings further.

## 4. Conclusion

The Taguchi L9 factorial method and Analysis of Variance were employed to optimize FSP parameters for fabricating AA5083/Coal composites. The Taguchi L9 orthogonal array efficiently examined three critical FSP parameters: tool rotational speed, tool tilt angle, and traverse speed. Key findings are summarized below:

- The maximum UTS, PE and HV obtained were 242 MPa, 22.43 and 96.27 HV respectively.
- Based on S/N ratio analysis, the optimal processing conditions for achieving the highest tensile strength, elongation, and microhardness in AA5083/Coal composites were identified as a rotational speed of level 2, traverse speed of level 3, and tilt angle of level 3. Using the S/N ratio approach, the study determined statistically validated optimal parameters: a tool tilt angle of 2°, a tool rotation speed of 900 rpm, and a traverse speed of 60 mm $min^{-1}$. By selecting parameters that maximized the S/N ratio for UTS, microhardness, and elongation, the study ensured consistent and reproducible results, enhancing the reliability of the results and their practical application.
- ANOVA results indicate that tilt angle significantly influences ultimate tensile strength, while rotational speed has the most significant impact on percentage elongation and microhardness. The tilt angle's role in controlling material flow and tool penetration, which are crucial for avoiding defects and ensuring good

bonding, explains its influence on ultimate tensile strength. Rotational speed's high contribution to microhardness highlights the importance of heat generation in grain refinement and particle distribution. This methodical approach of using ANOVA provides a clear understanding of parameter influence on mechanical properties and ensures the reproducibility and reliability of the findings.

- The Taguchi method provided a systematic approach to optimizing FSP parameters, ensuring statistical robustness. This guarantees the accuracy of the mechanical improvements observed. The results suggest that coal particles can be a viable, cost-effective, and sustainable reinforcement material for AA5083 composites.

## 5. Future work

The findings suggest that coal particles can be a cost-effective and sustainable reinforcement material. Future research should focus on the long-term durability of coal-reinforced composites and the scalability of the FSP process for industrial applications. Additionally, exploring other statistical methods like Response Surface Methodology (RSM) could further refine the process and assess the long-term performance of these composites under various service conditions.

The ANOVA results revealed high p-values, indicating that none of the individual FSP parameters significantly influenced the response variables within the tested parameter range. This suggests that the mechanical properties may depend more on the interactions between parameters than on their independent effects. Future research should include a broader parameter range and additional experimental repetitions to reduce variability, explore interaction effects, and refine the statistical significance of the factors and their contributions to optimizing mechanical properties.

## Acknowledgments

The authors gratefully acknowledge the CPUT for providing unlimited access to the equipment necessary for this study, and funding this study through the Vice Chancellors Prestigious Bursary Award. The authors also extend deep gratitude to Miss Shaheeda Petersen and Mr Zukile Cobothwana in the Department of Mechanical and Mechatronics Engineering at CPUT, for their support, input, and for assistance with the experimentation.

## Conflict of interest

The paper in question has no possible conflicts of interest, according to the authors.

## Data availability statement

All data that support the findings of this study are included within the article (and any supplementary files).

## ORCID iDs

Oritonda Muribwathoho https://orcid.org/0000-0001-6905-7310
Velaphi Msomi https://orcid.org/0000-0002-5752-8848
Sipokazi Mabuwa https://orcid.org/0000-0002-3775-7731

## References

[1] Shanavas S, Edwin Raja Dhas J and Murugan N 2018 Weldability of marine grade AA 5052 aluminum alloy by underwater friction stir welding *Int. J. Adv. Manuf. Technol.* 95 4535–46

[2] Abioye T E, Mustar N, Zuhailawati H and Suhaina I 2019 Prediction of the tensile strength of aluminium alloy 5052-H32 fibre laser weldments using regression analysis *Int. J. Adv. Manuf. Technol.* 102 1951–62

[3] Mathavan J J and Patnaik A 2016 Analysis of wear properties of aluminium based journal bearing alloys with and without lubrication *IOP Conf. Series: Mater. Sci. Eng.* 149 (IOP Publishing) 012052

[4] Rajan T P D, Pillai R M and Pai B C 1998 Reinforcement coatings and interfaces in aluminium metal matrix composites *J. Mater. Sci.* 33 3491–503

[5] Akinlabi E T, Mahamood R M, Akinlabi S A and Ogunmuyiwa E 2014 Processing parameters influence on wear resistance behaviour of friction stir processed Al-TiC composites *Adv. Mater. Sci. Eng.* 2014 724590

[6] Devaraj A, Kumar A and Kotiveerachari B 2013 Influence of rotational speed and reinforcement on wear and mechanical prorperties of aluminium hybrid composites via friction stir processing *Mater. Des.* 45 576–85

[7] Lee C J, Huang J C and Hsieh P J 2006 Mg based nano-composites fabricated by friction stir processing *Scr. Mater.* 54 1415–20

[8] Gholami S, Emadoddin E, Tajally M and Borhani E 2015 Friction stir processing of 7075 Al alloy and subsequent aging treatment *Transactions of Nonferrous Metals Society of China* 25 2847–55

[9] Anil Kumar K S, Karur A S, Chipli S and Singh A 2015 Optimization of FSW parameters to improve the mechanical properties of AA2024-T351 similar joints using Taguchi method *Journal of Mechanical Engineering and Automation* 5 27–32

[10] Pawar S P and Shete M T 2013 Optimization of friction stir welding process parameter using taguchi method and response surface methodology: a review *Int. J. Res. Eng. Technol* 2 551–4

[11] Lakshminarayanan A K and Balasubramanian V 2008 Process parameters optimization for friction stir welding of RDE-40 aluminium alloy using Taguchi technique *Transactions of Nonferrous Metals Society of China* 18 548–54

[12] Mukherjee I and Ray P K 2006 A review of optimization techniques in metal cutting processes *Comput. Ind. Eng.* 50 15–34

[13] Markos S, Viharos Z J and Monostori L 1998 Quality-oriented, comprehensive modelling of machining processes *Sixth ISMQC IMEKO Symposium on Metrology for Quality Control in Production* 67–74

[14] Montgomery D C 2017 *Design and Analysis of Experiments* (Wiley)

[15] Kowalczyk M 2014 Application of Taguchi and Anova methods in selection of process parameters for surface roughness in precision turning of titanium *Advances in Manufacturing Science and Technology* 38 21–35

[16] Bauri R, Yadav D, Kumar C S and Ram G J 2015 Optimized process parameters for fabricating metal particles reinforced 5083 Al composite by friction stir processing *Data in Brief* 5 309–13

[17] Mishra R S and Ma Z Y 2005 Friction stir welding and processing *Mater. Sci. Eng.* R 50 1–78

[18] Rahman M Z, Khan Z A, Siddiquee A N, Abidi M H, Aboudaif M K and Al-Ahmari A 2021 Mechanical and microstructural characterization of Ti-SiC reinforced AA5083 surface composites fabricated via friction stir process *Mater. Res. Express* 8 126523

[19] Rahman Z, Siddiquee A N and Khan Z A 2021 Effect of Ti/SiC reinforcement on AA5083 surface composites prepared by friction stir processing *IOP Conf. Series: Mater. Sci. Eng.* 1149 (IOP Publishing) 012001

[20] Jain V K, Yadav M K, Siddiquee A N and Khan Z A 2021 Optimization of friction stir processing parameters for enhanced microhardness of AA5083/Al-Fe *in situ* composites via Taguchi technique *Material Science, Engineering and Applications* 1 55–61

[21] D Ghetiya N, Bharti S, Patel K M, Kumar S and Rahimian Koloor S S 2023 An insight on optimization of FSP process parameters for the preparation of AA5083/(SiC-Gr) hybrid surface composites using the response surface methodology *Composites and Advanced Materials* 32 26349833231186162

[22] Bharti S, Ghetiya N D and Patel K M 2023 Parametric optimization of process parameters during friction stir processing of AA5083/(SiC-Gr) hybrid surface composite *Mater. Today Proc.* 78 420–5

[23] Kaya N, Çetinkaya C, Karakoç H and Ada H 2024 Effect of process parameters of Al5083/SiC surface composites fabricated by FSP on microstructure, mechanical properties and wear behaviors *Mater. Chem. Phys.* 315 128991

[24] Nik W W, Sulaiman O, Fadhli A and Rosliza R 2010 Corrosion behaviour of aluminum alloy in seawater *Proceedings of MARTEC The International Conference on Marine Technology* 175–80

[25] Ertuğ B and Kumruoğlu L C 2015 5083 type Al-Mg and 6082 type Al-Mg-Si alloys for ship building *Am. J. Eng. Res* 4 146–50

[26] Zass K, Mabuwa S and Msomi V 2023 Introduction of coal reinforcing particles on the dissimilar FSW AA608/AA5083 joint via friction stir processing *Metals* 13 1981

[27] Yang X, Dong P, Yan Z, Cheng B, Zhai X, Chen H, Zhang H and Wang W 2020 AlCoCrFeNi high-entropy alloy particle reinforced 5083Al matrix composites with fine grain structure fabricated by submerged friction stir processing *J. Alloys Compd.* 836 155411

[28] Singh T, Tiwari S K and Shukla D K 2020 Preparation of aluminium alloy-based nanocomposites via friction stir welding *Mater. Today Proc.* 27 2562–8

[29] Kundurti S C, Sharma A, Tambe P and Kumar A 2022 Fabrication of surface metal matrix composites for structural applications using friction stir processing–a review *Mater. Today Proc.* 56 1468–77

[30] Vasava A S and Singh D 2022 Microhardness and microstructure of AA7075-T651/graphene surface composite through FSP *Mater. Today Proc.* 58 140–5

[31] Patel K, Ghetiya N D and Bharti S 2022 Effect of single and double pass friction stir processing on microhardness and wear properties of AA5083/Al2O3 surface composites *Mater. Today Proc.* 57 38–43

[32] Akbari M, Ezzati M and Asadi P 2022 Investigation of the effect of tool probe profile on reinforced particles distribution using experimental and CEL approaches *International Journal of Lightweight Materials and Manufacture* 5 213–23

[33] Zass K J, Msomi V and Mabuwa S 2024 Feasibility of using coal as reinforcement in dissimilar welded joints: comparative analysis *E3S Web of Conferences* 552 (EDP Sciences) 01014

[34] Jalilvand M M, Mazaheri Y, Heidarpour A and Roknian M 2019 Development of A356/$Al_2O_3$+ $SiO_2$ surface hybrid nanocomposite by friction stir processing *Surf. Coat. Technol.* 360 121–32

[35] Sagar P and Handa A 2021 Selection of tool transverse speed considering trial run experimentations for AZ61/Tic composite developed via friction stir processing using triangular tool *Mater. Today Proc.* 38 198–203

[36] Moustafa E B, Melaibari A, Alsoruji G, Khalil A M and Mosleh A O 2022 Tribological and mechanical characteristics of AA5083 alloy reinforced by hybridising heavy ceramic particles Ta2C & VC with light GNP and $Al_2O_3$ nanoparticles *Ceram. Int.* 48 4710–21

[37] Salehi M, Saadatmand M and Mohandesi J A 2012 Optimization of process parameters for producing AA6061/SiC nanocomposites by friction stir processing *Transactions of Nonferrous Metals Society of China* 22 1055–63

[38] Kosaraju S, Aziz M A, Yadav V P K, Shiva B, Kolli M and Cheepu M 2024 Taguchi optimization of friction stir process parameters for enhancing joint strength of AA8011 reinforced with SiC nano particles *International Journal on Interactive Design and Manufacturing (IJIDeM)* 1–12

[39] Ayvaz S I, Arslan D and Ayvaz M 2022 Investigation of mechanical and tribological behavior of SiC and B4C reinforced Al-Zn-Mg-Si-Cu alloy matrix surface composites fabricated via friction stir processing *Materials Today Communications* 31 103419

[40] Yuvaraj N and Aravindan S 2015 Fabrication of Al5083/B4C surface composite by friction stir processing and its tribological characterization *Journal of Materials Research and Technology* 4 398–410

[41] Srivastava M, Rathee S, Maheshwari S and Siddiquee A N 2018 Influence of multiple-passes on microstructure and mechanical properties of Al-Mg/SiC surface composites fabricated via underwater friction stir processing *Mater. Res. Express* 5 066511

[42] Srivastava M, Rathee S, Siddiquee A N and Maheshwari S 2019 Investigation on the effects of silicon carbide and cooling medium during multi-pass FSP of Al-Mg/SiC surface composites *Silicon* 11 2149–57

[43] Li Q, Huang G, Cao Y, Zhang C, He J, Jiang H, Lin L and Liu Q 2022 Microstructure refinement, strengthening and ductilization mechanisms in Al–Mg–Mn–Er–Zr alloy with high Mn content by friction stir processing *Mater. Charact.* 189 111939

[44] Amra M, Ranjbar K and Hosseini S A 2018 Microstructure and wear performance of Al5083/$CeO_2$/SiC mono and hybrid surface composites fabricated by friction stir processing *Transactions of Nonferrous Metals Society of China* 28 866–78

[45] Faraji G, Dastani O and Mousavi S A A A 2011 Effect of process parameters on microstructure and micro-hardness of AZ91/$Al_2O_3$ surface composite produced by FSP *J. Mater. Eng. Perform.* 20 1583–90
[46] Ahmadkhaniha D, Sohi M H, Zarei-Hanzaki A, Bayazid S M and Saba M 2015 Taguchi optimization of process parameters in friction stir processing of pure Mg *Journal of Magnesium and Alloys* 3 168–72
[47] Roy R K 2010 *A Primer on the Taguchi Method* (Society of Manufacturing Engineers)
[48] Kolli M, Naresh D S, Devaraju A and Satyanarayana K 2023 Investigation of mechanical properties in friction stir processing parameters of Cu-TiB2 composite using Taguchi approach *International Journal on Interactive Design and Manufacturing (IJIDeM)* 1–12
[49] Muthukrishnan N and Davim J P 2009 Optimization of machining parameters of Al/SiC-MMC with ANOVA and ANN analysis *J. Mater. Process. Technol.* 209 225–32
[50] Vigneshkumar M, Padmanaban G and Balasubramanian V 2019 Influence of tool tilt angle on the formation of friction stir processing zone in cast magnesium alloy ZK60/SiCp surface composites *Metallography, Microstructure, and Analysis* 8 58–66
[51] Chanakyan C, Sivasankar S, Meignanamoorthy M, Ravichandran M, Mohanavel V, Alfarraj S, Almoallim H S, Manikandan V and Isaac JoshuaRamesh Lalvani J 2021 Optimization of FSP process parameters on AA5052 employing the S/N ratio and ANOVA method *Adv. Mater. Sci. Eng.* 2021 6450251
[52] Syed K, Ali M A, Reddy K P K and Rao B N 2023 Analyzing the influence of tool profile on friction stir process with Taguchi optimization and tungsten nano powder *International Journal of Vehicle Structures & Systems* 15 802–7
[53] Butola R, Ranganath M S and Murtaza Q 2019 Fabrication and optimization of AA7075 matrix surface composites using Taguchi technique via friction stir processing (FSP) *Eng. Res. Express* 1 025015
[54] Valerio F O 1998 Micro structural issues in a friction stir welded aluminium alloy *Script. Mater* 38 703–8
[55] Gupta M, Lai M O and Soo C Y 1996 Effect of type of processing on the microstructural features and mechanical properties of Al-Cu/SiC metal matrix composites *Mater. Sci. Eng.* A 210 114–22
[56] Devaraju A, Kumar A and Kotiveerachari B 2013 Influence of rotational speed and reinforcements on wear and mechanical properties of aluminum hybrid composites via friction stir processing *Mater. Des.* 45 576–85
[57] Devaraju A, Kumar A, Kumaraswamy A and Kotiveerachari B 2013 Influence of reinforcements (SiC and $Al_2O_3$) and rotational speed on wear and mechanical properties of aluminum alloy 6061-T6 based surface hybrid composites produced via friction stir processing *Mater. Des.* 51 331–41
[58] Swain P K, Mohapatra K D, Das R, Sahoo A K and Panda A 2020 Experimental investigation into characterization and machining of Al+ SiCp nano-composites using coated carbide tool *Mechanics & Industry* 21 307
[59] Gunasekaran J, Sevvel P, Roy J V and Sivaramakrishnan A 2023 Analysis of sensitivity and formulation of empirical relationship between parameters of FSW process and tensile strength of AZ80A Mg alloy joints *Mater. Res. Express* 10 056513
[60] Gunasekaran J, Sevvel P, John Solomon I and Vasanthe Roy J 2024 Multi objective optimization of parameters during FSW of AZ80A-AZ31B Mg alloys using grey relational analysis *J. Mech. Sci. Technol.* 38 4971–82
[61] Adiga K, Herbert M A, Rao S S and Shettigar A K 2024 Optimization of process parameters for friction stir processing (FSP) of AA8090/boron carbide surface composites *Welding in the World* 68 2683–700

**APPENDIX J**

Optimization and Regression Analysis of Friction Stir Processing Parameters of AA5083/Coal Composites for Marine Applications

crystals

MDPI

Article

# Optimization and Regression Analysis of Friction Stir Processing Parameters of AA5083/Coal Composites for Marine Applications

**Oritonda Muribwathoho [1,*], Velaphi Msomi [2] and Sipokazi Mabuwa [3]**

[1] Mechanical and Mechatronics Department, Cape Peninsula University of Technology, Cape Town 7535, South Africa
[2] Department of Mechanical Engineering, College of Science, University of South Africa, Pretoria 0002, South Africa; msomiv@unisa.ac.za
[3] Mechanical Engineering Department, Durban University of Technology, Durban 4000, South Africa; sipokazim@dut.ac.za
* Correspondence: oritondamuribwathoho@gmail.com

**Abstract:** This study aimed to optimize friction stir processing parameters to enhance the mechanical properties of AA 5083/coal composites, a novel material combination with potential applications in marine environments. By systematically varying process parameters such as tilt angle, traverse speed, and rotational speed using a Taguchi experimental design, the FSP process was optimized. Signal-to-noise ratio and analysis of variance techniques were used to determine the most influential parameters on microhardness and ultimate tensile strength. A regression model was developed to predict composite behavior under these optimal conditions. This study found that a combination of 900 rpm, 60 mm/min, and a 2° tilt angle significantly improved mechanical properties. This research contributes to the advancement of FSP for producing high-performance, lightweight, and corrosion-resistant aluminum composites, particularly for marine applications.

**Keywords:** aluminum alloy; friction stir welding/processing; metal matrix composite; mechanical properties; Taguchi; ANOVA; *S*/*N* ratio



Academic Editor: Hongbin Bei

Received: 27 November 2024
Revised: 19 December 2024
Accepted: 29 December 2024
Published: 30 December 2024

**Citation:** Muribwathoho, O.; Msomi, V.; Mabuwa, S. Optimization and Regression Analysis of Friction Stir Processing Parameters of AA5083/Coal Composites for Marine Applications. *Crystals* **2025**, *15*, 34. https://doi.org/10.3390/cryst15010034



## 1. Introduction

Metal matrix composites (MMCs) offer a combination of high specific strength, specific modulus, excellent high-temperature performance, and superior wear and abrasion resistance, making them highly desirable for advanced applications. Among these, aluminum-based MMCs (AMMCs) are particularly favored due to their lightweight nature and enhanced mechanical properties [1]. AA5083, a widely used aluminum alloy, stands out for its remarkable corrosion resistance, weldability, and moderate strength, making it a preferred material for marine-grade applications. However, the challenge in the field remains constantly to enhance the mechanical properties of the alloy, including tensile strength, and hardness without increasing the cost of production and affecting environmental concerns.

Over the years, various fabrication techniques have been developed to produce AMMCs, including stir casting [2–4], compo-casting [5], squeeze casting [6], spray forming [7], liquid metal infiltration [8], powder metallurgy [9], mechanical alloying, and in situ methods [10]. Each method offers unique advantages and limitations, driving ongoing research into optimizing processing techniques to achieve superior performance and efficiency. Friction stir processing (FSP) is a new technique that has been developed for joining materials for which a remelting technique is not suitable. It is an economical and environmentally friendly technique for fabricating AMMCs.

FSP does not involve conventional melting and solidification and has been used widely for improving the surface and mechanical properties of non-ferrous metals, particularly aluminum alloys with numerous types of reinforcements such as ceramics [11,12], carbon nanotubes, and particles from agricultural waste [13]. Heat is produced in FSP by the rubbing action of the tool and workpiece, contact between the pin and base metal, and dynamic recrystallization [14,15]. This heat makes the material soft and suitable for the integration of reinforcements and plastic deformation, among other processes. It was found that the process parameters used in FSP affect the quality of the composites fabricated, their microstructure, and particle distribution. Tool geometry likewise affects the mate- rial flow and heat input as indicated [16]. Second-phase particle incorporation can be achieved by way of intense material flow, but optimizing the FSP parameters is essential for improvement.

Traditional welding businesses often rely on a one-factor-at-a-time experimental approach, which is inefficient for complex processes like friction stir processing [17,18]. While mathematical iterative search techniques, problem-specific heuristics, and metaheuristics offer potential solutions [19], they are limited by their complexity, impracticality, high cost, and the requirement for a continuously differentiable objective function [20]. To address these limitations and achieve more efficient optimization, the Taguchi method provides a robust and practical alternative. By utilizing orthogonal arrays, the Taguchi method significantly reduces the number of required experiments, making it a suitable choice for industrial applications [21,22]. ANOVA determines the key parameters responsible for the variation in the output responses and evaluates the effect of one or multiple input parameters on the response [23,24].

The processing parameters in friction stir processing (FSP) play a critical role in influencing the tensile properties and microstructural characteristics of aluminum metal matrix composites (AMMCs). Understanding the interplay between these parameters and the resulting structure and properties of fabricated composites is essential for optimizing performance. Researchers have widely employed FSP in conjunction with Taguchi methods to determine optimal processing conditions for various aluminum grades and reinforce- ments, enabling the fabrication of high-performance metal matrix and surface composites. A review of studies focusing on the fabrication of marine-grade AMMCs reveals the use of diverse reinforcements such as ceramics (e.g., SiC, $Al_2O_3$), carbon nanotubes, and particles derived from agricultural waste. These materials have demonstrated significant improve- ments in the tribological and mechanical properties of aluminum alloys, highlighting the potential of FSP as a versatile and effective processing technique [25–33].

Singh et al. [25] studied the flow characteristics of AA5052/$TiO_2$/SiC hybrid surface composites employing multi-pass FSP with upward material flow. Unlike conventional downward flow, upward flow, generated by a right-handed threaded pin tool, caused plas- tic deformation and material movement within the stir zone. The multi-pass FSP techniques proved useful as they generated new sub-grains and improved the uniform distribution of reinforcements. The maximum microhardness of the composites achieved was 88.73 Hv after the fourth pass, and the highest tensile strength of 220.8 MPa was observed after four passes with additional improvements in the wear properties of the composites.

Bozorgmehr et al. [26] investigated the impact of traverse speed on the characteristics of microstructure, wear properties, and mechanical properties of the Al5052/$ZrO_2$/$ZrSiO_4$ surface hybrid fabricated by FSP at a fixed rpm 1400. The experiment was performed at test speeds of 20 mm/min, 25 mm/min, 31.5 mm/min, and 40 mm/min. The hardness, microstructure, and wear resistance of an Al5052/$ZrO_2$/$ZrSiO_4$ hybrid surface composite material were analyzed after effecting FSP with different traverse speeds. FSP enhanced the composite's properties because the microstructure was fine-grained and there were

reinforcing particles. In this study, the slowest traverse rate of 20mm/min gave the best results of an increase in hardness of about 27.3%, and the wear resistance of the base material increased by 68.9%. This was attributed to increased heat generation and an improvement in the uniform distribution of particles, thus enhancing minimal adhesive wear.

Kaya et al. [27] examined the influence of the load (6000 N, 8000 N, and 10,000 N) and tool rotational rate (560 rpm, 710 rpm and 900 rpm) on the mechanical properties, microstructure, and wear behavior of an FSP Al5083/SiC surface composite. The study results revealed that the microhardness of the stir zone (SZ) was the highest and it was found to be about 1.4 times higher than the base material hardness.

The maximum applied forces of 8000 N, along with a critical speed of 900 rpm, offered a 38% increase in maximum hardness and an increase in wear resistance of 42%, and the ultimate tensile strength of the base material decreased by 3%.

Singhal et al. [28] fine-tuned FSP parameters for enhancing the microstructures and mechanical properties of in situ AA5083-H111/Al–Fe surficial hybrid composites. The composites under consideration were produced from Fe–40 wt% Al powder, which was subjected to mechanical alloying, and the welded samples were prepared using FSP with a reverse tool path. In a bid to minimize the number of experiments, it was necessary to utilize the Taguchi L9 orthogonal array design to collect the relevant data. The properties of FSP joined plates were investigated and quantified in terms of mechanical properties after each traverse of the FSP tool. It was noted that increasing the number of passes to a second pass led to an improvement in tensile strength from 225.8 MPa to 253.6 MPa. Microhardness also progressively increased and reached 128.3 Hv on the second pass. These improvements were attributed to optimized FSP parameters: shoulder diameters of21 mm, traverse speed of 63 mm/min, rotational speed of 900 rpm, and tilt angle of 1.5◦.Based on the fractographic analysis of the failure, it was found that the AA5083/Al–Fe composite failed in ductile mode, as expected for the system. This ductile failure mode had its contribution to the mechanical performance of the material, which was outstanding.

Venkatesh et al. [29] used the Taguchi optimization technique to study the betterment of FSW process parameters of AA6061-6% SiC composite plates by analyzing the influence of axial load, tool rotational speed, and pin profile on microhardness and UTS. The study showed that an axial load of 6 kN, a tool rotational speed of 750 rpm, and a square pin profile were effective in achieving the highest UTS. For microhardness, peak values of 6 kN, 900 rpm, and a pin profile in the form of a cylinder were identified to be optimal. ANOVA revealed that the tool profile had the most significant impact on Vickers hardness, with a percentage contribution of 53.84%, followed by tool rotational speed, with a percentage contribution of 20.16%, and axial force, with a percentage contribution of 21.32%.

Megahed et al. [30] attempted to enhance the FSP parameters of microstructure and hardness, together with the wear resistance characteristics, of AA6061/WC nanocomposite. The control factors were transverse feed, tool rotational speed, volume fraction, and number of passes of the WC nanoparticles. Detailed characterization analysis revealed that the dispersion of WC particles in the AA6061 matrix of the composite was uniform with no evidence of defect. Owing to the high strain rate and high temperature, the FSP underwent significant plastic deformation and heat, which might pin the break of coarse particles and porous holes and could promote dynamic recrystallization to generate an ultra-fine grain structure. The microhardness of the processed composite was 144 VHN, which is higher than that of the base metal by a percentage of 39.81. In all the samples, there was reduced weight loss. From the analysis of variance obtained, it was observed that the passes significantly affect microhardness by 40.1% and weight loss by 56.94% of WC volume fraction. Among all the cases studied, the maximum microhardness and wear

resistance were achieved using an 1800 r.p.m. feed rate of 120 mm/min containing 6% WC and with three FSP passes.

Teo et al. [31] worked on the study of the friction stir processing parameters of recycled aluminum alloy 6063/TiO2 surface composites for enhanced tribological properties. For sample fabrication, a moderate range of process parameters was employed, and in the other case, the rotational speed was selected as 2442 rpm and the feed rate was 50 mm/min. A microhardness test was carried out for the mechanical properties of the developed material, and its friction and anti-wear properties were evaluated using a pin-on-disk tribo-tester under a starve lubrication mode. At the high setting, the research revealed enhanced surface composite mechanical properties, with a 45% enhancement in microhardness, a reduction in the friction coefficient by 39%, and a 73% reduction in the wear rate of the base materials. The study showed that TiO2 particles were well dispersed within the aluminum matrix and the average grain size was reduced, which enhanced the mechanical and wear characteristics.

Bharathikanna et al. [32] investigated the mechanical properties and corrosion behavior of friction stir processed AA6082 alloy with the addition of $Cr_3C_2$ particles. Tool rotation speed, axial force, and traverse speed were also analyzed in their work using Taguchi's orthogonal array and Gray Relational Analysis. Tests like tensile properties, metallographs, etc., were performed to analyze the effects of these variables. By comparing the results obtained, it was highlighted that axial force and traverse speed can significantly affect the performance of the composites. According to the above findings, it can be concluded the optimum values of parameters should be 1200 rpm, 45 mm/min, and 5 kN, as these values provide better tensile strength and surface hardness. Consequently, the investigation demonstrated that it was possible to use multi-objective optimization techniques to alter the properties of FSP AMCs.

Kumar et al. [33] fabricated Al 6082/SiC composites using FSP. SiC particles were used in different volume fractions (2%, 4%, 6%) and were dispersed in the aluminum matrix. A micrograph study depicted fine grain sizes and good interfacial adhesion of SiC-reinforced particles with the aluminum matrix. Mechanical tests proved that the ultimate tensile strength of the composites was enhanced up to 1.58-fold compared to the base material, with a hardness of 85.75 HB. The FSP process changed the Al 6082 matrix from a coarse-grained structure to a fine recrystallized grain structure with a nearly uniform distribution of SiC particles. This homogenous dispersion contributed to the improved mechanical properties and also proved the efficiency of FSP for preparing SiC-reinforced aluminum composites.

Coal, as an innovative reinforcement material, presents distinct advantages, including cost-effectiveness, abundance, and potential sustainability, setting it apart from traditional ceramic or metallic reinforcements. Despite these benefits, limited research has examined its integration into aluminum alloys, particularly for lightweight applications like those in marine environments. This study addresses this gap by optimizing the friction stir processing (FSP) parameters for AA5083/coal composites, advancing the development of cost-effective and durable materials. This study employs the Taguchi method and regression analysis to refine FSP design parameters and evaluate mechanical properties such as tensile strength and hardness. The findings are expected to demonstrate that coal can serve as a viable and economical reinforcement material, offering excellent durability for marine applications demanding long-term performance and reliability.

## 2. Materials and Methods

*2.1 Material Selection*

The base material used for this study was aluminum AA5083 plates of dimensions of 250 mm × 55 mm × 6 mm to prepare aluminum metal matrix composite materials. Based on mechanical tests, these alloys possessed an ultimate tensile strength of 311 MPa, a percentage of elongation of 58.65%, and 93.07 HV hardness. The content of the components of the AA5083 alloy is described in Table 1. The balance of this composition is important in the assessment of its material properties and the application potential of the alloy, especially concerning the friction stir processing explored in this study. Coal particles, comprising 5% of the composite's volume, were incorporated as a reinforcement material.

**Table 1.** The composition of AA5083-H111 in wt % [34].

| BM | Cu | Cr | Cr | Fe | Mg | Mn | Si | Ti | Zn | Al |
|---|---|---|---|---|---|---|---|---|---|---|
| AA5083 | 0.02 | 0.05 | 0.05 | 0.16 | 4.03 | 0.69 | 0.15 | 0.02 | 0.01 | Bal |

*2.2 Parameter Selection Using Taguchi*

A Taguchi L9 orthogonal array was employed to systematically investigate the effects of three key FSP parameters—tool tilt angle, tool traverse speed, and tool rotational speed—on the desired response variables. MINITAB18 software was used to analyze the experimental data. Each of these parameters was used at three different levels, therefore leading to a total number of nine experimental conditions. These parameters were chosen based on prior research [35]. The experimental matrix is provided in two tables, namely, Tables 2 and 3, illustrating the precise parameter variations that were employed in the tests. This systematic method allows the different conditions of the chosen FSP parameters and their effects on the properties of the developed aluminum matrix composites to be evaluated systematically to identify the best option as informed by the results of the experiments.

**Table 2.** Processing factors and levels.

| Level | Tilt Angle (TA) [°] | Traverse Speed (TS) [mm/min] | Rotational Speed (RS) [rpm] |
|---|---|---|---|
| 1 | 1 | 30 | 600 |
| 2 | 1.75 | 45 | 900 |
| 3 | 2 | 60 | 1200 |

**Table 3.** Taguchi $L_9$ design matrix.

| No of Tests | Tilt Angle [°] | Traverse Speed [mm/min] | Rotational Speed [rpm] |
|---|---|---|---|
| 1. | 1 | 30 | 600 |
| 2. | 1.75 | 45 | 600 |
| 3. | 2 | 60 | 600 |
| 4. | 1.75 | 30 | 900 |
| 5. | 2 | 45 | 900 |
| 6. | 1 | 60 | 900 |
| 7. | 2 | 30 | 1200 |
| 8. | 1 | 45 | 1200 |
| 9. | 1.75 | 60 | 1200 |

*2.3 Fabrication Method*

To create the aluminum metal matrix composite, two AA5083 sheets were first friction stir-welded together. Subsequently, holes of 2.5 mm diameter, 4 mm depth, and 15 mm interval along the weld line were drilled. Coal reinforcement was then inserted into these drilled holes, after which a pinless friction stir processing (FSP) tool was utilized to close them securely. Subsequently, a high-speed steel FSP tool featuring a triangular pin profile was employed to conduct the FSP pass. To detail the FSW/FSP tool, this tool has a shoulder diameter of 20 mm, a probe diameter of 7 mm, and a pin length of 5.7 mm, which enables the processing of the aluminum composite material.

## 3 Results and Discussions

*3.1 Mechanical Properties*

Following FSP, tensile and hardness specimens with orientation perpendicular to the processing direction were cut. Tensile specimens were prepared based on ASTM E-8M-04 standards [36] and tested on the Hounsfield tensile test machine. Microhardness measurements were carried out using a Vickers microhardness tester following ASTM E-384 [37] at room temperature with the help of the Innova Test Falcon 500 hardness testing machine. The tensile and microhardness specimen samples and size configuration are depicted in Figures 1 and 2 below. The tensile strength and hardness of AA5083/coal composites are represented in Table 4, highlighting the effects of different process parameters with confidence intervals (CI).

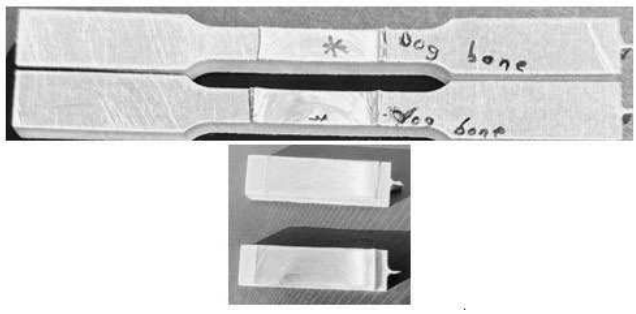


**Figure 1.** Samples of tensile and hardness specimens.

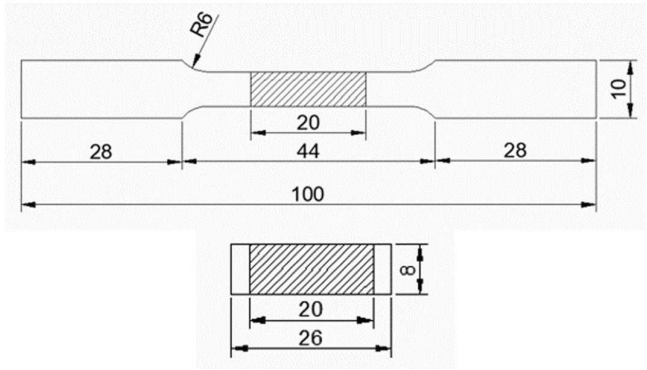


**Figure 2.** Tensile and hardness specimen size and configuration.

**Table 4.** AA5083/coal composite mechanical properties with confidence intervals.

| Experiment No. | UTS (MPa) | CI for UTS (MPa) | PE (%) | CI for PE (%) | MH (HV) | CI for MH (HV) |
|---|---|---|---|---|---|---|
| 1. | 167 | 167 ± 5 | 11.9 | 11.9 ± 0.3 | 93.6 | 93.6 ± 0.5 |
| 2. | 109 | 109 ± 5 | 7.00 | 7.00 ± 0.3 | 88.3 | 88.3 ± 0.5 |
| 3. | 224 | 224 ± 5 | 22.4 | 22.4 ± 0.3 | 92.7 | 92.7 ± 0.5 |
| 4. | 134 | 134 ± 5 | 12.2 | 12.2 ± 0.3 | 96.3 | 96.3 ± 0.5 |
| 5. | 242 | 242 ± 5 | 20.7 | 20.7 ± 0.3 | 90.7 | 90.7 ± 0.5 |
| 6. | 161 | 161 ± 5 | 21.2 | 21.2 ± 0.3 | 92.4 | 92.4 ± 0.5 |
| 7. | 101 | 101 ± 5 | 7.60 | 7.60 ± 0.3 | 95.3 | 95.3 ± 0.5 |
| 8. | 181 | 181 ± 5 | 12.8 | 12.8 ± 0.3 | 93.1 | 93.1 ± 0.5 |
| 9. | 141 | 141± 5 | 9.38 | 9.38 ± 0.3 | 95.9 | 95.9 ± 0.5 |

3.1.1 Tensile Strength

The UTS of the base AA5083/coal composite was very comparable to the base AA5083 material; however, the particle reinforcement decreased the ductility of the material. The results of this study align with the literature [38–41], wherein single-pass composites recorded lower tensile strengths than the base material.

3.1.2 Hardness

Reinforcements enhance hardness, surpassing base material values. Variations due to recrystallization, grain size, particle distribution, and intermetallic particle fragmen- tation contribute to higher hardness [42,43]. This study's findings align with previous research [44].

3.1.3 Comparison Plots of Investigational and Regression-Predicted Values

The regression equation is adjusted with the help of taking the investigational output responses to define the correlation between the input process parameters and required mechanical properties. Equations (1)–(3) represent the regression models developed to predict the maximum tensile strength, percentage elongation, and hardness of the AA5083/coal composites.

The following equations represent the developed regression models:

$$UTS\ (MPa): 135 - 0.0428\ RS\ (rpm) + 1.38\ TS\ (mm/min) + 2.1\ TA\ (deg). \quad (1)$$

The regression equation for tensile strength indicates a negative relationship with rotational speed (*RS*) and positive relationships with traverse speed (*TS*) and tilt angle (*TA*). This aligns with physical expectations, as excessive rotational speed can lead to overheating, causing grain growth and reducing tensile strength. Conversely, higher traverse speeds promote finer grain structures and improved bonding, enhancing tensile strength. The tilt angle's positive effect is consistent with its role in optimizing material flow and ensuring adequate consolidation during *FSP*.

$$PE\ (\%): 9.9 - 0.00647\ RS\ (rpm) + 0.236\ TS\ (mm/min) - 0.53\ TA\ (deg). \quad (2)$$

The equation for percentage elongation reveals a slight reduction in elongation with increasing rotational speed and tilt angle. This is physically justifiable, as higher rotational speeds and tilt angles can introduce excessive thermal gradients and reinforce particle agglomeration, leading to reduced ductility. The positive influence of traverse speed

suggests that moderate deformation rates support better distribution of reinforcements, maintaining ductility to some extent.

$$MH\ (HV): 81.65 + 0.00667\ RS\ (rpm) + 0.0183\ TS\ (mm/min) + 2.00\ TA\ (deg). \quad (3)$$

The equation for microhardness reflects a positive relationship with all parameters, with tilt angle having the most substantial influence. This supports the notion of high heat generation, where rotational and traverse speeds are high to promote the development of a fine-grained microstructure and well-distributed reinforcements that would increase the hardness of the material. Additionally, the significant effect of tilt angle highlights its critical role in achieving optimal surface contact and particle integration during FSP.

Below, we detail the alignment with physical expectations achieved by these equations. The regression equations generally align with established theories of material behavior under FSP. The dominant role of traverse speed and tilt angle in tensile strength and microhardness is consistent with their impact on material flow and thermal dynamics. But such variations regarding physical expectations, for instance, the incremented positive slope of rotational speed on microhardness, may be due to local variation in heat input or particle distribution that the regression model has failed to capture completely.

The findings determined using the regression equations to analyze the mechanical properties of AA5083/coal composites are shown in Table 5. Figure 3 displays the relative UTS, PE, and MH obtained from experiment and regression equations predictions.

**Table 5.** Regression-predicted values with % errors.

| Experiment No. | *UTS* (MPa) | Fits | Error (%) | *PE* (%) | Fits | Error (%) | *MH* (HV) | Fits | Error (%) |
|---|---|---|---|---|---|---|---|---|---|
| 1. | 167 | 153.2 | 8.270 | 11.9 | 12.6 | 6.030 | 93.6 | 88.2 | 5.77 |
| 2. | 109 | 175.4 | 60.92 | 7.00 | 15.7 | 125.2 | 88.3 | 89.9 | 1.89 |
| 3. | 224 | 196.6 | 12.25 | 22.4 | 19.2 | 14.38 | 92.7 | 90.7 | 2.11 |
| 4. | 134 | 141.9 | 5.900 | 12.2 | 10.3 | 15.74 | 96.3 | 91.7 | 4.78 |
| 5. | 242 | 163.8 | 32.60 | 20.7 | 13.7 | 33.85 | 90.7 | 92.5 | 1.95 |
| 6. | 161 | 181.7 | 12.87 | 21.2 | 17.8 | 16.22 | 92.4 | 90.8 | 1.79 |
| 7. | 101 | 129.6 | 28.30 | 7.60 | 8.21 | 7.970 | 95.3 | 942 | 1.16 |
| 8. | 181 | 148.2 | 18.12 | 12.8 | 12.8 | 4.100 | 93.1 | 92.5 | 0.67 |
| 9. | 141 | 170.4 | 20.87 | 9.38 | 15.4 | 64.47 | 95.9 | 94.2 | 1.73 |

Confidence intervals: *CI* for *UTS* (MPa) = ±5 *CI* for *PE* (%) = ±0.3 *CI* for *MH* (HV) = ±0.5.

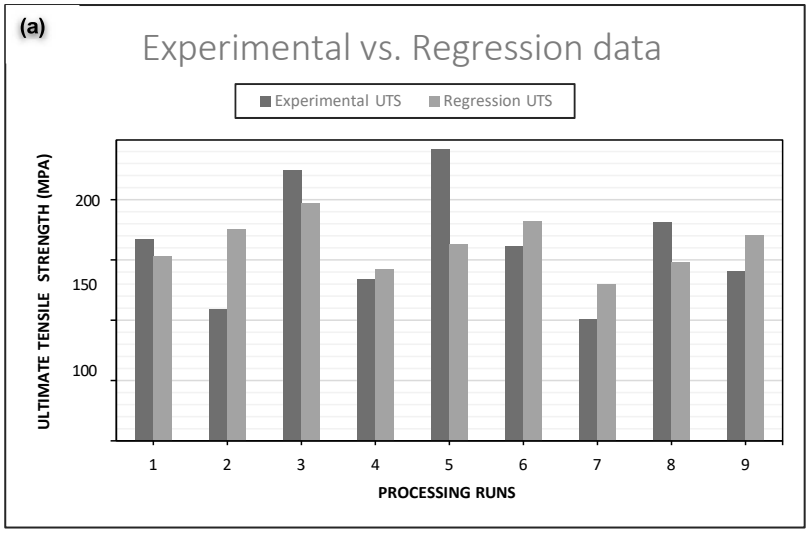


**Figure 3.** *Cont.*

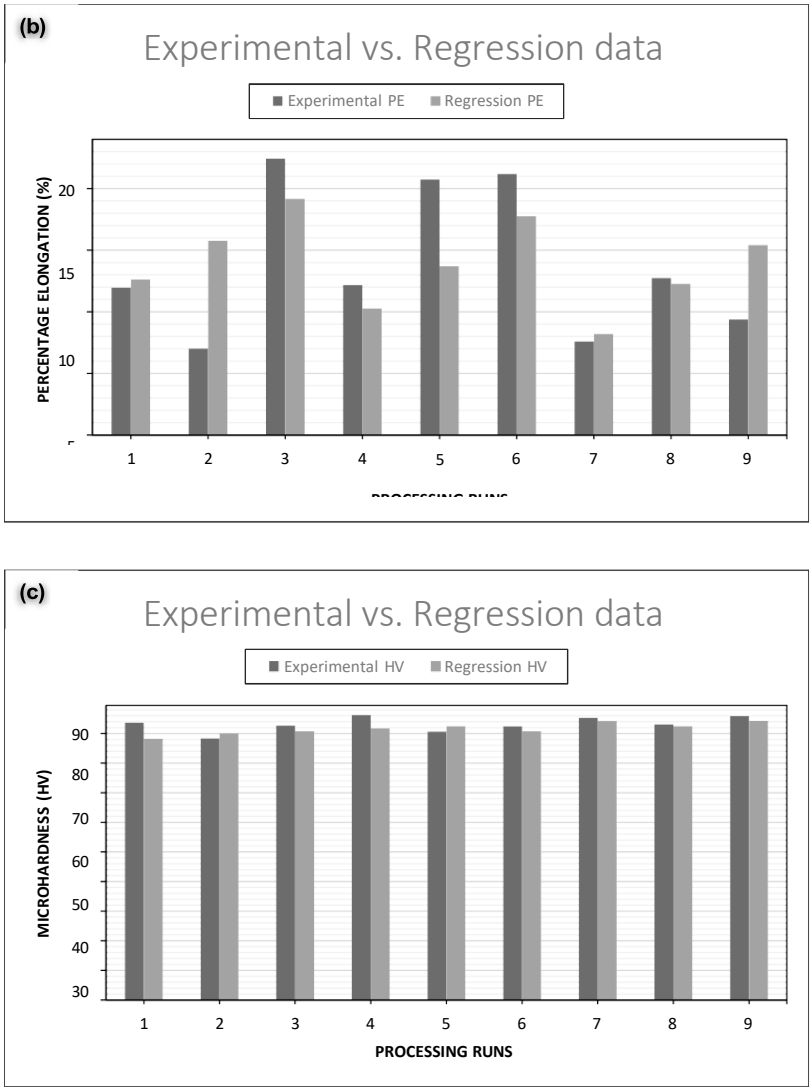


**Figure 3.** Experimental and regression predicted values: (**a**) ultimate tensile strength; (**b**) percentage elongation; and (**c**) microhardness.

### 3.1.4 Microstructural Analysis

Figure 4 displays the optical microstructures of the composites evaluated under varying friction stir processing (FSP) parameters. Figure 4a–c illustrate the microstructure of the AA5083/coal composite at rotational speeds of 600 rpm and traverse speeds of 30 mm/min, 45 mm/min, and 60 mm/min, with corresponding tilt angles of 1°, 1.75°, and 2°, respectively. Similarly, Figure 4d–f present the microstructures at 900 rpm, with tilt angles of 1.75°, 2°, and 1°, paired with traverse speeds of 30 mm/min, 45 mm/min, and 60 mm/min, respectively. Lastly, Figure 4g–i detail the microstructure at 1200 rpm, where the tilt angles and traverse speeds are set at 2° and 30 mm/min, 1° and 45 mm/min, and 1.75° and 60 mm/min, respectively.

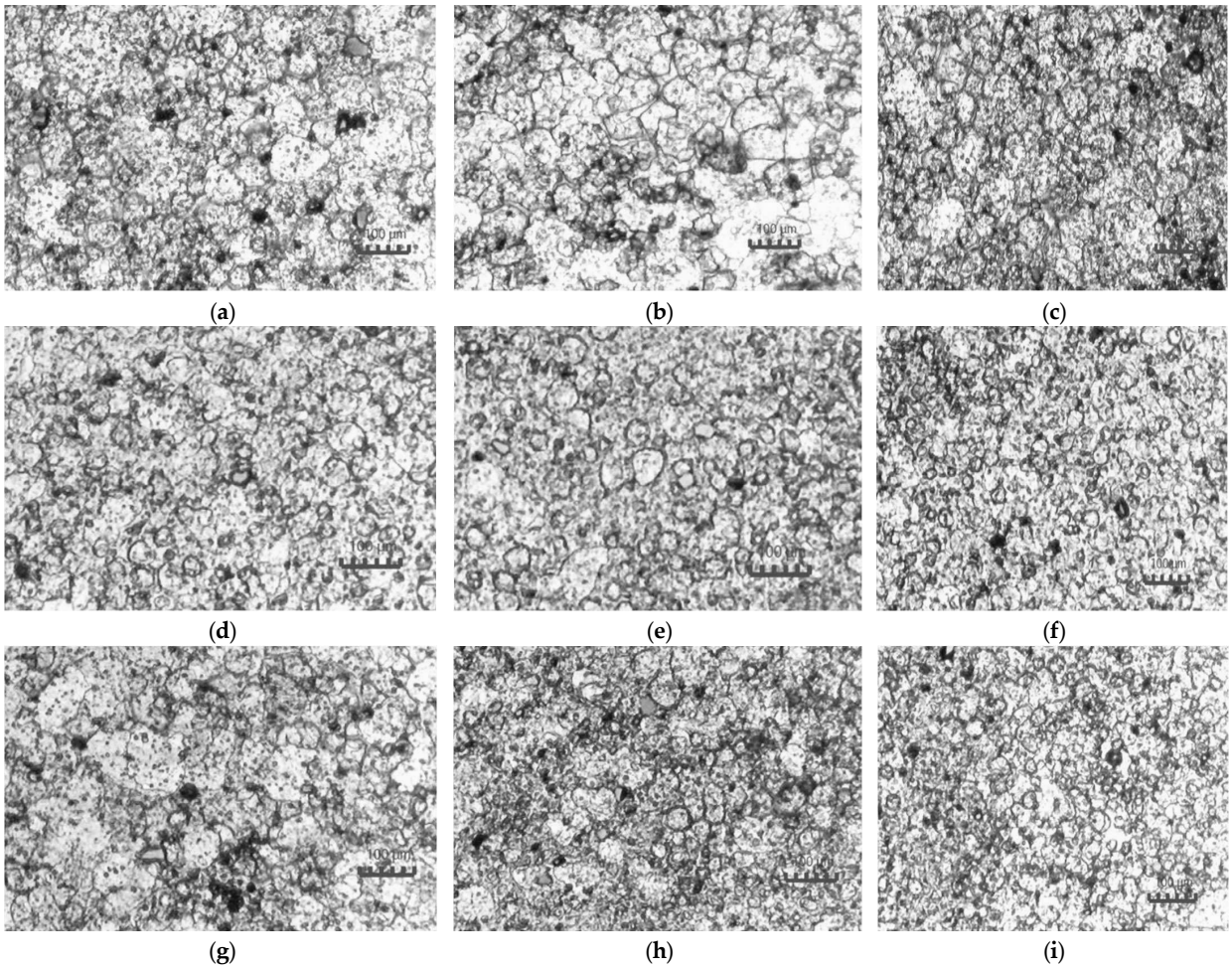


**Figure 4.** Optical microstructures of AA5083/coal composites captured at 20× 100 µm magnification, showing the effects of varying FSP parameters. (**a–c**) Microstructures at 600 rpm with traverse speeds of 30 mm/min, 45 mm/min, and 60 mm/min, and tilt angles of 1°, 1.75°, and 2°, respectively. (**d–f**) Microstructures at 900 rpm with traverse speeds of 30 mm/min, 45 mm/min, and 60 mm/min, and tilt angles of 1.75°, 2°, and 1°, respectively. (**g–i**) Microstructures at 1200 rpm with traverse speeds of 30 mm/min, 45 mm/min, and 60 mm/min, and tilt angles of 2°, 1°, and 1.75°, respectively.

The microstructural analysis provides crucial insights into the dispersion of coal reinforcement particles within the AA5083 matrix, highlighting the influence of varying FSP parameters on particle distribution and bonding. The images indicate that while coal particles are present within the stir zone, the percentage of bonded particles appears low, potentially due to limited material flow during processing [45–49]. These findings align with observations in [50–52], which noted that non-uniform particle dispersion significantly impacts the failure behavior and plastic deformation of metal-based composites.

This uneven distribution and incomplete bonding between the coal reinforcement and the matrix adversely affect mechanical properties, including tensile strength and ductility [50,53]. These results underscore the critical role of processing conditions in optimizing particle dispersion and improving the overall composite performance.

*3.2 Signal-to-Noise Ratio Analysis*

In order to compare the means of the responses obtained for varying levels of speed, feed, and tilt angle and find out the significance of speed, feed, and tilt angle on hardness

and tensile strength, the data were analyzed by using MINITAB18 software. For this, the following steps were taken: The means and signal/noise ratio were calculated. The goal was to maximize hardness and tensile strength, so "the-larger-the-better" criteria were used for signal-to-noise ratio calculations. For optimization, $S/N$ ratios are used instead of mean values to evaluate response characteristics. The choice of $S/N$ ratio depends on the desired outcome. Since higher values of microhardness and ultimate tensile strength are desirable, a "the-higher-the-better" quality characteristic is applicable. This corresponds to a higher $S/N$ ratio, indicating optimal process parameter levels.

"The-larger-the-better" signal-to-noise ratio can be calculated using the following formula [54–57]:

$$\frac{S}{N} = -10 \log\left(\frac{1}{n}\sum_{i-1}^{3}\frac{1}{y^2}\right) \quad (4)$$

where $n$ = the number of experimental repetitions and $y$ = the re-response factor at the i-th level. The $S/N$ ratio for parameter combinations for AA5083/coal composite based on the experimental test result is also presented in Table 6 and Figure 5.

**Table 6.** $S/N$ ratio on ultimate tensile strength, percentage elongation, and hardness.

| Experiment No. | *UTS* (MPa) | *S/N* Ratio For *UTS* | *PE* (%) | *S/N* Ratio For *PE* | *MH* (HV) | *S/N* Ratio For *HV* |
|---|---|---|---|---|---|---|
| 1. | 167 | 44.45 | 11.9 | 21.55 | 93.6 | 38.66 |
| 2. | 109 | 40.745 | 7.00 | 16.90 | 88.3 | 38.92 |
| 3. | 224 | 47.00 | 22.4 | 27.02 | 92.7 | 39.34 |
| 4. | 134 | 42.54 | 12.2 | 21.71 | 96.3 | 39.67 |
| 5. | 242 | 47.68 | 20.7 | 26.33 | 90.7 | 39.15 |
| 6. | 161 | 44.14 | 21.2 | 26.52 | 92.4 | 39.34 |
| 7. | 101 | 40.09 | 7.60 | 17.62 | 95.3 | 39.42 |
| 8. | 181 | 45.15 | 12.8 | 22.11 | 93.1 | 39.38 |
| 9. | 141 | 42.98 | 9.38 | 19.44 | 95.9 | 39.28 |

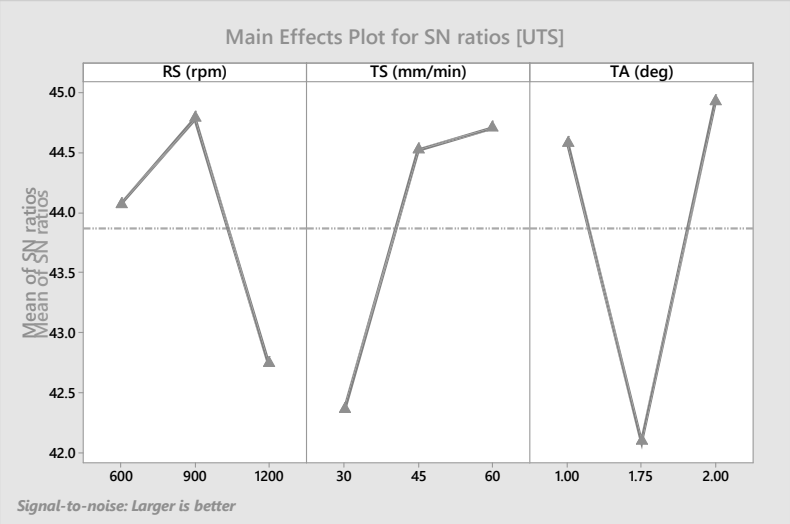


(**a**)

**Figure 5.** *Cont.*

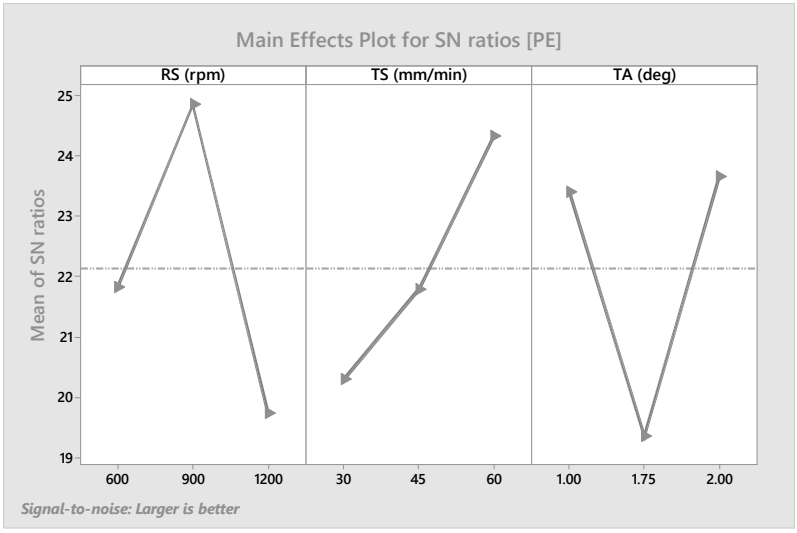


(**b**)

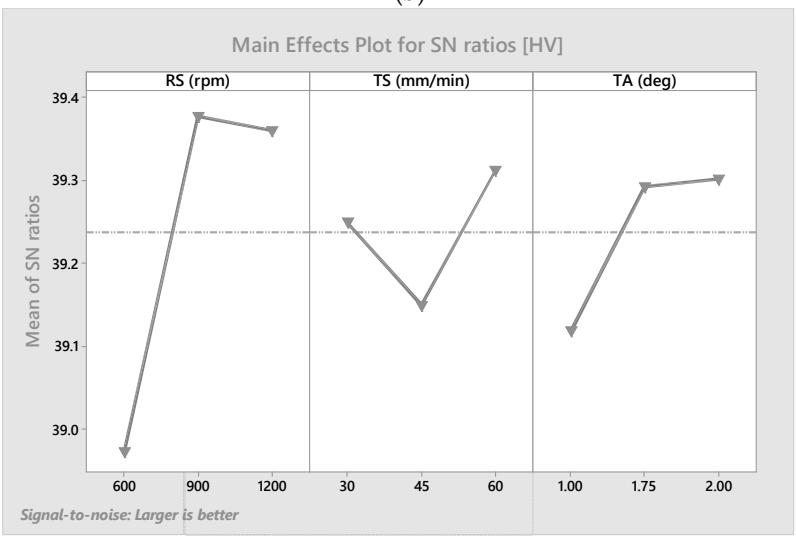


(**c**)

**Figure 5.** AA5083/coal composite *SN* ratio and mean plot: (**a**) *UTS*; (**b**) PE; (**c**) *HV*.

For the AA5083/coal composite, the increases in ultimate tensile strength, percentage elongation, and microhardness by tilt angle at level three, traverse speed at level three, and rotary speed at level two are shown in Figure 5. In the experiment, it was found that the best parameters were achieved at a tilt angle of 2 degrees, a traverse speed of 60 mm/min, and a rotational speed of 900 rpm. Earlier works [56,57] have used a larger-is-better approach to optimize the mechanical characteristics of metal matrix composites.

Ranking of Contributing Factors and Determining Optimum Conditions

The *S*/*N* ratios and mean responses of *UTS*, *PE*, and *HV* are depicted in Tables 7–9. The results in Table 7 also illustrate that tilt angle has the highest impact on UTS at rank 1, followed by traverse speed at rank 2 and rotational speed at rank 3. Rating analysis of the extent of effects provided in Table 8 shows that percentage elongation is most influenced by rotational speed at rank 1, followed by tilt angle at rank 2 and then traverse speed at rank 3. Finally, the values ranking the input parameters with respect to microhardness are presented in Table 9. Among those, rotational speed is most important, tilt angle is the second most important, and traverse speed is the least important parameter. From the main

effects response results, it is clear that the best values for process parameters that yield the highest UTS, PE, and HV are rpm 900, feed rate 60mm/min, and angle 2°, as discussed in Section 3.2.

**Table 7.** Main effect response table for ultimate tensile strength.

| *S/N* Ratio Response Level | Mean Response | | | | | |
|---|---|---|---|---|---|---|
| | Tilt Angle (°) | Traverse Speed (mm/min) | Rotational Speed (rpm) | Tilt Angle (°) | Traverse Speed (mm/min) | Rotational Speed (rpm) |
| 1 | 44.58 | 42.36 | 44.07 | 169.7 | 134.0 | 166.7 |
| 2 | 42.09 | 44.53 | 44.78 | 128.0 | 177.3 | 179.0 |
| 3 | 44.92 | 44.71 | 42.74 | 189.0 | 175.3 | 141.0 |
| Delta | 2.83 | 2.35 | 2.04 | 61.0 | 43.3 | 38.0 |
| Rank | 1 | 2 | 3 | 1 | 2 | 3 |

**Table 8.** Main effect response table for *S*/*N* ratio of parameters on percentage elongation.

| *S/N* ratio Response Level | Mean Response | | | | | |
|---|---|---|---|---|---|---|
| | Tilt Angle (°) | Traverse Speed (mm/min) | Rotational Speed (rpm) | Tilt Angle (°) | Traverse Speed (mm/min) | Rotational Speed (rpm) |
| 1 | 23.39 | 20.29 | 21.82 | 15.29 | 10.58 | 13.79 |
| 2 | 19.35 | 21.78 | 24.85 | 9.520 | 13.49 | 18.03 |
| 3 | 23.65 | 24.33 | 19.72 | 16.92 | 17.66 | 9.910 |
| Delta | 4.30 | 4.03 | 5.13 | 7.400 | 7.087 | 8.120 |
| Rank | 2 | 3 | 1 | 2 | 3 | 1 |

**Table 9.** Main effect response table for *S*/*N* ratio of parameters on microhardness.

| *S/N* Ratio Response Level | Mean Response | | | | | |
|---|---|---|---|---|---|---|
| | Tilt Angle (°) | Traverse Speed (mm/min) | Rotational Speed (rpm) | Tilt Angle (°) | Traverse Speed (mm/min) | Rotational Speed (rpm) |
| 1 | 39.12 | 39.25 | 38.97 | 90.41 | 91.84 | 88.90 |
| 2 | 39.29 | 39.15 | 39.38 | 92.23 | 90.69 | 93.12 |
| 3 | 39.31 | 39.31 | 39.36 | 92.28 | 92.39 | 92.90 |
| Delta | 0.18 | 0.16 | 0.40 | 1.87 | 1.69 | 4.22 |
| Rank | 2 | 3 | 1 | 2 | 3 | 1 |

*3.3 Analysis of Variance*

In the evaluation of process parameters, ANOVA was applied to identify the statistical significance of the findings. A frequency test was used in statistics to analyze the parameter effects that define the quality of properties [58]. From the analysis conducted below, the parameter contribution to the output response in terms of percentile and F-value (probability distribution) was established. Tables 10 and 11 show the results of analysis of variance for the signal-to-noise ratio and mean of ultimate tensile strength, percentage elongation, and hardness. Based on the analysis of variance results, none of the factors (TA, TS, and RS) were found to have a statistically significant impact on any of the response variables (UTS, PE, and HV) at the 0.05 significance level. This indicates that the experimental design may not have been effective in identifying significant factors or that the chosen factors do not have a strong influence on the responses. Further analysis, such as examining interaction effects or refining the experimental design, may be necessary to gain more insights.

**Table 10.** Factor contribution to the variation in $S/N$ ratio.

| Source | Degree of Freedom (DF) | Seq SS | Adj SS | Adj MS | % Contribution | F-Value | *p*-Value |
|---|---|---|---|---|---|---|---|
| For UTS | | | | | | | |
| TA (°) | 2 | 14.33 | 14.33 | 7.165 | 27.05 | 0.65 | 0.605 |
| TS (mm/min) | 2 | 10.23 | 10.23 | 5.116 | 19.31 | 0.47 | 0.682 |
| RS (rpm) | 2 | 6.451 | 6.451 | 3.226 | 12.18 | 0.29 | 0.773 |
| Error | 2 | 21.97 | 21.97 | 10.98 | 41.47 | | |
| Total | 8 | 52.98 | | | | | |
| For PE | | | | | | | |
| TA (°) | 2 | 34.89 | 34.89 | 17.45 | 30.03 | 2.12 | 0.320 |
| TS (mm/min) | 2 | 24.97 | 24.97 | 12.49 | 21.89 | 1.52 | 0.397 |
| RS (rpm) | 2 | 39.93 | 39.93 | 19.96 | 34.36 | 2.43 | 0.292 |
| Error | 2 | 16.44 | 16.44 | 8.221 | 14.15 | | |
| Total | 8 | 116.2 | | | | | |
| For HV | | | | | | | |
| TA (°) | 2 | 0.064 | 0.064 | 0.032 | 9.169 | 0.23 | 0.815 |
| TS (mm/min) | 2 | 0.040 | 0.040 | 0.020 | 5.731 | 0.14 | 0.874 |
| RS (rpm) | 2 | 0.313 | 0.313 | 0.157 | 44.84 | 1.12 | 0.472 |
| Error | 2 | 0.280 | 0.280 | 0.140 | 40.11 | | |
| Total | 8 | 0.698 | | | | | |

**Table 11.** Factor contribution to the variation in means.

| Source | Degree of Freedom (DF) | Seq SS | Adj SS | Adj MS | % Contribution | F-Value | *p*-Value |
|---|---|---|---|---|---|---|---|
| For UTS | | | | | | | |
| TA (°) | 2 | 5831 | 5831 | 2915 | 31.71 | 0.87 | 0.535 |
| TS (mm/min) | 2 | 3590 | 3590 | 1795 | 19.53 | 0.54 | 0.651 |
| RS (rpm) | 2 | 2255 | 2255 | 1127 | 12.27 | 0.34 | 0.748 |
| Error | 2 | 6710 | 6710 | 3355 | 36.49 | | |
| Total | 8 | 18386 | | | | | |
| For PE | | | | | | | |
| TA (°) | 2 | 90.74 | 90.74 | 45.37 | 31.48 | 4.05 | 0.198 |
| TS (mm/min) | 2 | 76.12 | 76.12 | 38.06 | 26.41 | 3.40 | 0.227 |
| RS (rpm) | 2 | 98.96 | 98.96 | 49.48 | 34.33 | 4.42 | 0.185 |
| Error | 2 | 22.40 | 22.40 | 11.20 | 7.772 | | |
| Total | 8 | 288.2 | | | | | |
| For HV | | | | | | | |
| TA (°) | 2 | 6.799 | 6.799 | 3.400 | 8.948 | 0.22 | 0.820 |
| TS (mm/min) | 2 | 4.477 | 4.477 | 2.239 | 5.892 | 0.14 | 0.873 |
| RS (rpm) | 2 | 33.83 | 33.83 | 16.91 | 44.52 | 1.10 | 0.477 |
| Error | 2 | 30.88 | 30.88 | 15.44 | 40.64 | | |
| Total | 8 | 75.98 | | | | | |

Percentage of Contributions

Figure 6 displays the percentage contribution based on ANOVA. The ANOVA of the $S/N$ ratio for UTS, PE, and HV reveals that tilt angle significantly impacts the output response for ultimate tensile strength, with a percentage of 27.05%. Elongation and hardness also show strong dependency on tool rotational speed, at 34.37% and 44.84%, respectively. The frequency value agrees with the contribution percentage and the ranking in the table. The results support the importance of tool rotational speed in the output response. The tilt angle's impact on tensile strength is due to its control over material flow and tool penetration, which are essential for defect prevention and bonding [59]. Rotational speed

significantly influences microhardness, emphasizing the significance of heat generation in grain refinement and particle distribution [60–62].

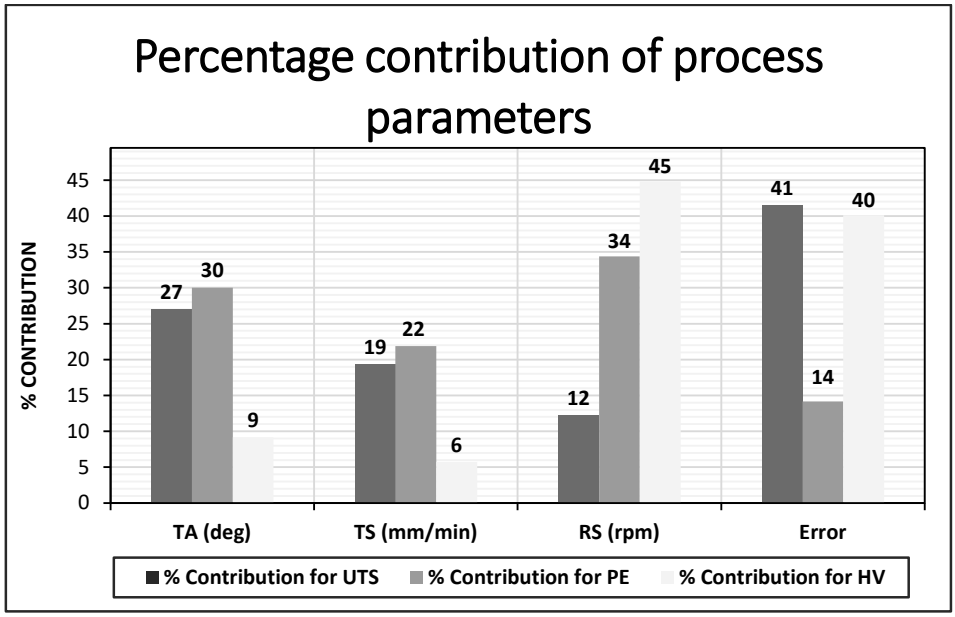


**Figure 6.** Percentage contribution of process parameters for UTS, PE, and HV.

*3.4 Confirmation Test*

Additional experiments were conducted using the identified optimal settings to vali- date the optimized process parameters. The tool rotational speed, traverse speed, and tilt angle were set to 900 rpm, 60 mm/min, and 2 degrees [63]. Three confirmation tests were conducted on AA5083/coal composites. The average UTS was found to be 244.7 MPa. The average hardness was determined to be 91.42. These confirmation tests demonstrated the effectiveness of the optimized parameters in enhancing the mechanical properties of the composites, reinforcing the findings from the initial experimental phase.

## 4. Conclusions

This study successfully optimized the fabrication of AMMCs using friction stir pro- cessing and the Taguchi L9 factorial method. This study effectively developed a surface composite by employing AA5083 as the matrix material and coal as the reinforcement. The Taguchi method was employed to identify the optimal process parameters for maximizing both tensile strength and hardness in the AA5083/coal composite. The Taguchi technique allowed us to draw the following conclusions:

- The experimental tensile strength of the AA5083/coal composite reached a maximum of 242 MPa, which is comparable to the 311 MPa ultimate tensile strength of the base AA5083 material. Although the composite exhibited similar mechanical properties to the base material, its ductility was reduced due to the presence of reinforcing coal particles.
- The experimental microhardness of the AA5083/coal composite reached a maximum of 96.3 HV, which is higher than the 93.1 HV hardness of the base material AA5083. The incorporation of reinforcements enhanced the hardness of the composite, surpassing the base material values. These parameters include recrystallization, grain refinement, particle distribution, and intermetallic particle fracture.

- The extent to which tool rotation, traverse speed, and tool tilt influenced the tensile strength, elongation, and hardness of the AA5083/coal composite joints was found to be highest at 900 rpm, 60 mm/min, and 2 degrees, in that order. Specific values for tilt angle, traverse speed, and rotational speed set at level 3 and level 2 resulted in optimal mechanical properties for these features.
- The ANOVA results revealed that tilt angle was the most influential factor influencing ultimate tensile strength, contributing 27.047% to the overall variance. Traverse speed and rotational speed followed, accounting for 19.307% and 12.176%, respectively. For percentage elongation, rotational speed emerged as the most significant factor, contributing 34.368% to the variance. Tilt angle and traverse speed had contributions of 30.025% and 21.888%, respectively. Finally, rotational speed was again identified as the most influential factor for microhardness, contributing 44.842% to the variance. Tilt angle and traverse speed followed, with contributions of 9.1691% and 5.7306%, respectively.
- Despite this, the regression models used give useful predictive estimates, and their validity is constrained by the design of the experiment and the ranges of the parameters used. Further analysis incorporating interaction terms or advanced regression techniques (e.g., response surface methodology) could offer a more nuanced understanding of the complex interdependencies between FSP parameters and mechanical properties.

## 5. Limitations

Although this study did not directly assess corrosion resistance, AA5083 is well-known for its exceptional corrosion performance in marine environments. Future research will focus on evaluating the effect of coal reinforcement on the alloy's corrosion resistance and its durability under simulated marine conditions.

## 6. Scientific Contributions

The authors' scientific contribution lies in the innovative use of coal particles as a reinforcement material for AA5083 aluminum matrix composites produced through friction stir processing (FSP). This study uniquely integrates the Taguchi method and regression analysis to systematically optimize FSP parameters—rotational speed, traverse speed, and tilt angle—and examine their impact on mechanical properties such as tensile strength, hardness, and ductility.

In contrast to prior research, which primarily focuses on conventional reinforcements like ceramics or carbon-based materials, this study explores the potential of coal as a plentiful, cost-effective, and environmentally sustainable alternative. The findings provide valuable insights into the viability of incorporating coal particles into aluminum alloys, particularly for marine applications, where corrosion resistance and mechanical performance are crucial. Moreover, the inclusion of confirmation tests enhances the reliability of the optimized parameters, establishing a robust framework for future research on unconventional reinforcement materials.

**Author Contributions:** Conceptualization, V.M.; methodology, S.M.; software, O.M.; validation, O.M., V.M., and S.M.; formal analysis, S.M.; investigation, O.M.; resources, V.M.; data curation, S.M. and OM.; writing—original draft, O.M.; writing—review and editing, S.M. and V.M.; visualization, O.M.; supervision, V.M. and S.M.; project administration, V.M. All authors have read and agreed to the published version of the manuscript.

**Funding:** This research received no external funding.

**Data Availability Statement:** Data are contained within this article

**Acknowledgments:** The authors would like to thank the Cape Peninsula University of Technology for granting the authors a chance to use the equipment required in this study as much as possible.

**Conflicts of Interest:** The authors declare that they have no conflicts of interest.

## References

1. Thandalam, S.K.; Ramanathan, S.; Sundarrajan, S. Synthesis, microstructural and mechanical properties of ex-situ zircon particles (ZrSiO4) reinforced Metal Matrix Composites (MMCs): A review. *J. Mater. Res. Technol.* **2015**, *4*, 333–347. [CrossRef]
2. Kumar, T.S.; Subramanian, R.; Shalini, S.; Angelo, P.C. Microstructure, mechanical properties and corrosion behaviour of Al–Si–Mg alloy matrix/zircon and alumina hybrid composite. *Forsch. Im Ingenieurwesen* **2015**, *79*, 123–130. [CrossRef]
3. Kumar, T.S.; Subramanian, R.; Shalini, S.; Anburaj, J.; Angelo, P.C. Synthesis, microstructure and mechanical properties of Al-Si-Mg alloy hybrid (zircon+ alumina) composite. *Indian J. Eng. Mater. Sci.* **2016**, *23*, 20–26.
4. Kumar, T.S.; Subramanian, R.; Shalini, S.; Angelo, P.C. Age hardening behaviour of Al-Si-Mg alloy matrix/zircon and alumina hybrid composite. *J. Sci. Ind. Res.* **2016**, *75*, 89–94.
5. Sharma, S.C.; Girish, B.M.; Somashekar, D.R.; Satish, B.M.; Kamath, R. Sliding wear behaviour of zircon particles reinforced ZA-27 alloy composite materials. *Wear* **1999**, *224*, 89–94. [CrossRef]
6. Ejiofo, J.U.; Okorie, B.A.; Reddy, R.G. Powder processing and properties of zircon-reinforced Al-13.5 Si-2.5 Mg alloy composites. *J. Mater. Eng. Perform.* **1997**, *6*, 326–334. [CrossRef]
7. Abdizadeh, H.; Ashuri, M.; Moghadam, P.T.; Nouribahadory, A.; Baharvandi, H.R. Improvement in physical and mechanical properties of aluminum/zircon composites fabricated by powder metallurgy method. *Mater. Des.* **2011**, *32*, 4417–4423. [CrossRef]
8. Kaur, K.; Pandey, O.P. Microstructural characteristics of spray formed zircon sand reinforced LM13 composite. *J. Alloys Compd.* **2010**, *503*, 410–415. [CrossRef]
9. Weissgaerber, T.; Kieback, B. Dispersion strengthened materials obtained by mechanical alloying-an overview. *Mater. Sci. Forum* **2000**, *34*, 275–283. [CrossRef]
10. Reddy, B.S.; Das, K.; Das, S. A review on the synthesis of in situ aluminum-based composites by thermal, mechanical and mechanical–thermal activation of chemical reactions. *J. Mater. Sci.* **2007**, *42*, 9366–9378. [CrossRef]
11. Salih, O.S.; Ou, H.; Wei, X.; Sun, W. Microstructure and mechanical properties of friction stir welded AA6092/SiC metal matrix composite. *Mater. Sci. Eng. A* **2019**, *742*, 78–88. [CrossRef]
12. Abioye, T.E.; Zuhailawati, H.; Anasyida, A.S.; Yahaya, S.A.; Dhindaw, B.K. Investigation of the microstructure, mechanical and wear properties of AA6061-T6 friction stir weldments with different particulate reinforcements addition. *J. Mater. Res. Technol.* **2019**, *8*, 3917–3928. [CrossRef]
13. Hussain, Z.; Halmy, M.N.; Almanar, I.P.; Dhindaw, B.K. Friction stir processed of 6061-T6 aluminum alloy reinforced with silica from rice husk ash. *Adv. Mater. Res.* **2014**, *1024*, 227–230. [CrossRef]
14. Mr, P.S.; Badheka, V. An experimental investigation of temperature distribution and joint properties of Al 7075 T651 friction stir welded aluminium alloys. *Procedia Technol.* **2016**, *23*, 543–550.
15. Patel, V.V.; Badheka, V.J.; Kumar, A. Influence of pin profile on the tool plunge stage in friction stir processing of Al–Zn–Mg–Cu alloy. *Trans. Indian Inst. Met.* **2017**, *70*, 1151–1158. [CrossRef]
16. Elangovan, K.; Balasubramanian, V. Influences of pin profile and rotational speed of the tool on the formation of friction stir processing zone in AA2219 aluminium alloy. *Mater. Sci. Eng. A* **2007**, *459*, 7–18. [CrossRef]
17. Pawar, S.P.; Shete, M.T. Optimization of friction stir welding process parameter using taguchi method and response surface methodology: A review. *Int. J. Res. Eng. Technol.* **2013**, *2*, 551–554.
18. Lakshminarayanan, A.K.; Balasubramanian, V. Process parameters optimization for friction stir welding of RDE-40 aluminium alloy using Taguchi technique. *Trans. Nonferrous Met. Soc. China* **2008**, *18*, 548–554. [CrossRef]
19. Mukherjee, I.; Ray, P.K. A review of optimization techniques in metal cutting processes. *Comput. Ind. Eng.* **2006**, *50*, 15–34. [CrossRef]
20. Markos, S.; Viharos, Z.J.; Monostori, L. Quality-oriented, comprehensive modeling of machining processes. In Proceedings of the Sixth ISMQC IMEKO Symposium on Metrology for Quality Control in Production, Vienna, Austria, 8–10 September 1998; pp. 67–74.
21. Montgomery, D.C. *Design and Analysis of Experiments*; John Wiley & Sons: Hoboken, NJ, USA, 2017.
22. Kowalczyk, M. Application of Taguchi and ANOVA methods in the selection of process parameters for surface roughness in precision turning of titanium. *Adv. Manuf. Sci. Technol.* **2014**, *2*. [CrossRef]
23. Ross, P.J. Taguchi techniques for quality engineering: Loss function, orthogonal experiments, parameter and tolerance design. *Natl. Acad. Sci. Eng. Med.* **1988**.
24. Santha, D.R.; Ramanaiah, N. Process Parameters Optimization for Producing AA6061/TiB Composites by Friction Stir Processing. *Stroj. Časopis-J. Mech. Eng.* **2017**, *67*, 101–118. [CrossRef]

25. Singh, D.; Sarvaiya, J. Development of AA5052/TiO2/SiC hybrid surface composites using upward material flow through multipass friction stir processing. *J. Adhes. Sci. Technol.* **2023**, *37*, 3335–3357. [CrossRef]
26. Bozorgmehr, M.; Heidari, A.; Amini, K.; Loh Mousavi, M.; Gharavi, F. The effect of traverse speed in friction stir process on the microstructure, mechanical properties and wear behavior Al5052/ZrO2/ZrSiO4 surface hybrid composite. *J. Weld. Sci. Technol. Iran* **2024**, *9*, 1–4.
27. Kaya, N.; Çetinkaya, C.; Karakoç, H.; Ada, H. Effect of process parameters of Al5083/SiC surface composites fabricated by FSP on microstructure, mechanical properties and wear behaviors. *Mater. Chem. Phys.* **2024**, *315*, 128991. [CrossRef]
28. Singhal, V.; Jain, V.K.; Raman, R.S.; Patharia, D.; Mittal, V.; Mishra, S.; Kumar, H. Optimization of friction stir processing parameters for improving structural and mechanical properties in in situ AA5083-H111/Al–Fe composites. *Proc. Inst. Mech. Eng. Part C J. Mech. Eng. Sci.* **2024**, *238*, 4477–4490. [CrossRef]
29. Venkatesh, B.N.; Hebbal, U.; Siddappa, P.N.; Kousik, S.; Nagaraja, T.K. Optimization of FSW parameters of AA6061-6 wt.% SiC composite plates. *Manuf. Rev.* **2022**, *9*, 34.
30. Megahed, A.A.; Mohamed, M.A.; Abdel Hamid, M.; Zoalfakar, S.H. Microstructure, hardness, and wear properties of AA6061/WC nanocomposite fabricated by friction stir processing. *Proc. Inst. Mech. Eng. Part C J. Mech. Eng. Sci.* **2022**, *236*, 9148–9156. [CrossRef]
31. Teo, G.S.; Liew, K.W.; Kok, C.K. A study on friction stir processing parameters of recycled AA 6063/TiO2 surface composites for better tribological performance. *Metals* **2022**, *12*, 973. [CrossRef]
32. Bharathikanna, R.; Elatharasan, G. Microstructure, Mechanical and Corrosion Behavior of Friction Stir Processed AA6082 with Cr 3 C 2 Particles. *Soldag. Inspeção* **2022**, *27*, e2723. [CrossRef]
33. Kumar, N.; Gupta, P.; Singh, R.K. Fabrication of Al 6082/SiC composite using friction stir processing. *J. Inst. Eng. Ser. D* **2023**, *104*, 603–608. [CrossRef]
34. Zass, K.; Mabuwa, S.; Msomi, V. Introduction of Coal Reinforcing Particles on the Dissimilar FSW AA608/AA5083 Joint via Friction Stir Processing. *Metals* **2023**, *13*, 1981. [CrossRef]
35. Kosaraju, S.; Aziz, M.A.; Yadav, V.P.; Shiva, B.; Kolli, M.; Cheepu, M. Taguchi optimization of friction stir process parameters for enhancing joint strength of AA8011 reinforced with SiC nano particles. *Int. J. Interact. Des. Manuf.* **2024**, 1–12. [CrossRef]
36. *ASTM E8M-04*; Standard Test Methods for Tension Testing of Metallic Materials. ASTM International: West Conshohocken, PA, USA, 2004; pp. 1–24.
37. *ASTM E384-11*; Standard Test Method for Microindentation Hardness of Materials. ASTM International: West Conshohocken, PA, USA, 2011; pp. 1–24.
38. Ayvaz, S.I.; Arslan, D.; Ayvaz, M. Investigation of mechanical and tribological behavior of SiC and B4C reinforced Al-Zn-Mg-Si-Cu alloy matrix surface composites fabricated via friction stir processing. *Mater. Today Commun.* **2022**, *31*, 103419. [CrossRef]
39. Yuvaraj, N.; Aravindan, S. Fabrication of Al5083/B4C surface composite by friction stir processing and its tribological characterization. *J. Mater. Res. Technol.* **2015**, *4*, 398–410. [CrossRef]
40. Srivastava, M.; Rathee, S.; Maheshwari, S.; Siddiquee, A.N. Influence of multiple-passes on microstructure and mechanical properties of Al-Mg/SiC surface composites fabricated via underwater friction stir processing. *Mater. Res. Express* **2018**, *5*, 066511. [CrossRef]
41. Srivastava, M.; Rathee, S.; Siddiquee, A.N.; Maheshwari, S. Investigation on the effects of silicon carbide and cooling medium during multi-pass FSP of Al-Mg/SiC surface composites. *Silicon* **2019**, *11*, 2149–2157. [CrossRef]
42. Li, Q.; Huang, G.; Cao, Y.; Zhang, C.; He, J.; Jiang, H.; Lin, L.; Liu, Q. Microstructure refinement, strengthening and ductilization mechanisms in Al–Mg–Mn–Er–Zr alloy with high Mn content by friction stir processing. *Mater. Charact.* **2022**, *189*, 111939. [CrossRef]
43. Amra, M.; Ranjbar, K.; Hosseini, S.A. Microstructure and wear performance of Al5083/CeO2/SiC mono and hybrid surface composites fabricated by friction stir processing. *Trans. Nonferrous Met. Soc. China* **2018**, *28*, 866–878. [CrossRef]
44. Faraji, G.; Dastani, O.; Mousavi, S.A. Effect of process parameters on microstructure and micro-hardness of AZ91/Al 2 O 3 surface composite produced by FSP. *J. Mater. Eng. Perform.* **2011**, *20*, 1583–1590. [CrossRef]
45. Bharathikanna, R.; Elatharasan, G. An investigation on microstructures and mechanical properties of AA1050 in friction stir processing technique. *Adv. Nat. Appl. Sci.* **2017**, *11*, 316–322.
46. Huang, G.; Wu, J.; Hou, W.; Shen, Y. Microstructure, mechanical properties and strengthening mechanism of titanium particle reinforced aluminum matrix composites produced by submerged friction stir processing. *Mater. Sci. Eng. A* **2018**, *734*, 353–363. [CrossRef]
47. Agha Amini Fashami, H.; Bani Mostafa Arab, N.; Hoseinpour Gollo, M.; Nami, B. Numerical and experimental investigation of defects formation during friction stir processing on AZ91. *SN Appl. Sci.* **2021**, *3*, 1–13. [CrossRef]
48. Habibnia, M.; Shakeri, M.; Nourouzi, S.; Givi, M.B. Microstructural and mechanical properties of friction stir welded 5050 Al alloy and 304 stainless steel plates. *Int. J. Adv. Manuf. Technol.* **2015**, *76*, 819–829. [CrossRef]

49. Zandsalimi, S.; Heidarzadeh, A.; Saeid, T. Dissimilar friction-stir welding of 430 stainless steel and 6061 aluminum alloy: Microstructure and mechanical properties of the joints. *Proc. Inst. Mech. Eng. Part L J. Mater. Des. Appl.* **2019**, *233*, 1791–1801. [CrossRef]
50. Akbari, M.; Ezzati, M.; Asadi, P. Investigation of the effect of tool probe profile on reinforced particles distribution using experimental and CEL approaches. *Int. J. Lightweight Mater. Manuf.* **2022**, *5*, 213–223. [CrossRef]
51. Hamilton, C.; Kopyściański, M.; Senkov, O.; Dymek, S. A coupled thermal/material flow model of friction stir welding applied to Sc-modified aluminum alloys. *Metall. Mater. Trans. A* **2013**, *44*, 1730–1740. [CrossRef]
52. Hamilton, C.; We˛glowski, M.S.; Dymek, S. A simulation of friction-stir processing for temperature and material flow. *Metall. Mater. Trans. B* **2015**, *46*, 1409–1418. [CrossRef]
53. Khan, N.Z.; Siddiquee, A.N.; Khan, Z.A.; Shihab, S.K. Investigations on tunneling and kissing bond defects in FSW joints for dissimilar aluminum alloys. *J. Alloys Compd.* **2015**, *648*, 360–367. [CrossRef]
54. Ahmadkhaniha, D.; Sohi, M.H.; Zarei-Hanzaki, A.; Bayazid, S.M.; Saba, M. Taguchi optimization of process parameters in friction stir processing of pure Mg. *J. Magnes. Alloys* **2015**, *3*, 168–172. [CrossRef]
55. Roy, R.K. *A Primer on the Taguchi Method*; Society of manufacturing engineers: Southfield, MI, USA, 2010.
56. Jain, V.K.; Yadav, M.K.; Siddiquee, A.N.; Khan, Z.A. Optimization of friction stir processing parameters for enhanced microhardness of AA5083/Al-Fe in-situ composites via Taguchi technique. *Mater. Sci. Eng. Appl.* **2021**, *1*, 55–61. [CrossRef]
57. Kolli, M.; Naresh, D.S.; Devaraju, A.; Satyanarayana, K. Investigation of mechanical properties in friction stir processing parameters of Cu-TiB2 composite using Taguchi approach. *Int. J. Interact. Des. Manuf.* **2023**, 1–12. [CrossRef]
58. Muthukrishnan, N.; Davim, J.P. Optimization of machining parameters of Al/SiC-MMC with ANOVA and ANN analysis. *J. Mater. Process. Technol.* **2009**, *209*, 225–232. [CrossRef]
59. Vigneshkumar, M.; Padmanaban, G.; Balasubramanian, V. Influence of tool tilt angle on the formation of friction stir processing zone in cast magnesium alloy ZK60/SiCp surface composites. *Metallogr. Microstruct. Anal.* **2019**, *8*, 58–66. [CrossRef]
60. Chanakyan, C.; Sivasankar, S.; Meignanamoorthy, M.; Ravichandran, M.; Mohanavel, V.; Alfarraj, S.; Almoallim, H.S.; Manikandan, V.; Isaac JoshuaRamesh Lalvani, J. Optimization of FSP process parameters on AA5052 employing the S/N ratio and ANOVA method. *Adv. Mater. Sci. Eng.* **2021**, *2021*, 6450251. [CrossRef]
61. Syed, K.; Ali, M.A.; Reddy, K.P.; Rao, B.N. Analyzing the Influence of Tool Profile on Friction Stir Process with Taguchi Optimization and Tungsten Nano Powder. *Int. J. Veh. Struct. Syst.* **2023**, *15*, 802–807.
62. Butola, R.; Ranganath, M.S.; Murtaza, Q. Fabrication and optimization of AA7075 matrix surface composites using Taguchi technique via friction stir processing (FSP). *Eng. Res. Express* **2019**, *1*, 025015. [CrossRef]
63. Muribwathoho, O.; Msomi, V.; Mabuwa, S. An Analysis Comparing the Taguchi Method for Optimizing the Process Parameters of AA5083/Silicon Carbide and AA5083/Coal Composites That Are Fabricated via Friction Stir Processing. *Appl. Sci.* **2024**, *14*, 9616. [CrossRef]

**APPENDIX K**

Optimizing FSP Parameters for AA5083/SiC Composites: A Comparative Analysis of Taguchi and Regression

*metals*

MDPI

*Article*

# Optimizing FSP Parameters for AA5083/SiC Composites: A Comparative Analysis of Taguchi and Regression

**Oritonda Muribwathoho [1,*], Velaphi Msomi [2] and Sipokazi Mabuwa [3]**

[1] Mechanical and Mechatronics Engineering Department, Cape Peninsula University of Technology, Cape Town 7535, South Africa
[2] Mechanical, Bioresources and Biomedical Engineering Department, School of Engineering and Built Environment, College of Science, Engineering and Technology, University of South Africa, Roodepoort 1724, South Africa; msomiv@unisa.ac.za
[3] Mechanical Engineering Department, Durban University of Technology, Durban 4000, South Africa; sipokazim@dut.ac.za
* Correspondence: oritondamuribwathoho@gmail.com

**Abstract:** The fabrication of AA5083/SiC composites by the friction stir processing (FSP) method is the main objective of this study. The study looks at how the mechanical properties of the composites are affected by three important process parameters: traversal speed, rotational speed, and tilt angle. The Taguchi $L_9$ design matrix was used to effectively investigate parameter effects, decreasing experimental trials and cutting expenses. Tensile testing measured tensile strength, whereas microhardness tests evaluated hardness. The findings showed that a maximum tensile strength of 243 MPa and a maximum microhardness of 94.80 HV were attained. The findings also showed that the optimal ultimate tensile strength (UTS) and percentage elongation (PE) were achieved at a tilt angle of 2°, a traverse speed of 30 mm per minute, and a rotating speed of 900 rev/min. On the other hand, a slightly greater traverse speed of 45 mm per minute was required to reach maximal microhardness (MH) with the same rotational speed and tilt angle. Analysis of variance (ANOVA) showed that rotational speed has a substantial impact on all mechanical properties, highlighting how important it is for particle dispersion and grain refining. This work is unique in that it systematically optimizes FSP parameters by using regression analysis and the Taguchi technique in addition to ANOVA. This allows for a better understanding of how these factors affect the mechanical properties of SiC-reinforced composites. The findings contribute to advancing the cost-effective fabrication of high-performance metal matrix composites for industrial applications requiring enhanced strength and durability.

**Keywords:** ANOVA; aluminum alloy; mechanical properties; metal matrix composite; friction stir welding/processing; Taguchi



Academic Editors: Luca Sorrentino and Guido Di Bella

Received: 18 January 2025
Revised: 19 February 2025
Accepted: 3 March 2025
Published: 5 March 2025

**Citation:** Muribwathoho, O.; Msomi, V.; Mabuwa, S. Optimizing FSP Parameters for AA5083/SiC Composites: A Comparative Analysis of Taguchi and Regression. *Metals* **2025**, *15*, 280. https://doi.org/10.3390/met15030280



## 1. Introduction

Aluminum matrix composites (AMMCs) have been recognized as a suitable material in several applications because they possess impressive mechanical, thermal, and tribological properties. Relative to conventional lightweight materials such as aluminum alloys and monolithic material classes, AMMCs possess greater specific stiffness and strength, higher operating temperature tolerance, reduced creep rates, and better wear characteristics [1]. AMMCs are widespread and use of AMMCs may range from bicycles to spacecraft, medical equipment to electronic packaging, and home appliances to space vehicles. Because of their superior surface contact characteristics, high strength-to-mass ratio, and improved

corrosion potential, ceramic-reinforced aluminum matrix composites are gradually taking the place of monolithic alloys in the automotive, marine, and aviation sectors [2–4].

AMMC manufacturing techniques fall into two main categories: liquid phase processing techniques including squeeze casting, stir casting, and compo casting, and solid-state processing techniques like FSP, physical vapor deposition, diffusion bonding, and powder metallurgy. During the liquid stage, unwanted intermetallic compounds are produced that are detrimental to the material's mechanical properties. However, the conventional methods of solid-state processing have excluded the formation of intermetallic besides reducing distortion, defects on the material, and hydrogen porosity that was evident during the fabrication of aluminum alloy through liquid phase processing [5].

FSP offers numerous advantages over other fabrication techniques, including low environmental impact, high energy efficiency, minimal processing steps, and no required heat treatment. Primary FSP applications for microstructure alteration in various metallic materials include homogenization of Al alloys [6] and AMMCs [7,8], superplasticity enhancement [9,10], fatigue life improvement in arc-welded steel [11,12], improvement of as-cast Al alloys [13,14], fabrication of ex situ [15–18] and in situ composites [19–23], and metal foam fabrication [24].

FSP is a cutting-edge technique for surface modification and composite fabrication, controlling material microstructure and mechanical properties. It functions as a surface modification technique without reinforcement and as a composite fabrication technique when reinforcements are included. It alters material properties by inducing high levels of localized plastic deformation [25]. While inspired by friction stir welding (FSW), developed in 1991 at a welding institute [26,27], FSP does not join metals.

When performing FSP, a one-of-a-kind tool that cannot be removed is employed. This tool has a pin with a small diameter and a shoulder with a concentric, larger diameter. The tool pin and shoulder work together to control the depth of material penetration. The process begins with the tool rotating at high speed while exerting a downward force. As the rotating pin engages with the workpiece surface, frictional heat is generated. This localized heating softens the material, allowing the pin to penetrate deeper into the workpiece. Once the pin penetrates the material, the shoulder comes into contact with the workpiece surface, generating further frictional heat. This combination of pin rotation, downward force, and frictional heat leads to localized heating, material softening, and plastic deformation within the workpiece [28].

The impact of plastic deformation processes on the mechanical properties of the composites was examined, and the results showed that there was a substantial link between plastic deformation and mechanical properties. Recent research has emphasized the critical role of these mechanisms in overall performance. Studies on particle-reinforced metal matrix composites (MMCs) [29,30] have highlighted the importance of interface bonding and particle distribution for strength and ductility. Strong interfacial bonding facilitates effective load transfer, whereas uniform particle distribution minimizes stress concentrations. Several studies [31,32] show that FSP can significantly influence these factors by promoting homogeneous particle distribution and improving interfacial bonding through localized plastic deformation and heat input. However, the specific mechanisms vary depending on the processing parameters and the composite system.

Some studies [33] suggested that high rotational speeds can cause excessive heat and detrimental interfacial reactions, whereas others [34] showed that optimized FSP parameters can significantly improve strength and ductility by refining the microstructure and promoting uniform deformation. The role of dislocation activity in the matrix and its interaction with reinforcement particles have also been extensively studied [35,36]. These studies demonstrate that reinforcement particles can impede dislocation motion,

leading to strengthening, but can also introduce stress concentrations that affect fracture behavior. Therefore, understanding the interplay between the FSP parameters, plastic deformation mechanisms, and resulting mechanical properties is crucial for tailoring composite materials.

The process parameters, such as the tool rotating speed, tool profile, traverse speed, preheat temperature, pressure applied, and so on, are subject to significant variation and change depending on the material that is utilized, the composite property that is required, and the availability of equipment that is utilized during the fabrication process utilizing FSP. These parameters require optimization through experimentation and process development to achieve desired AMMC characteristics. Many researchers use Design of Experiments (DOE) to determine the impact of multiple parameters on aluminum matrix composite mechanical properties [26].

The Taguchi approach, mathematical programming, response surface design, simulated annealing, tabu search, and genetic algorithms are further techniques used for this purpose [37]. Among all these, the Taguchi method is one of the most used Design of Experiments techniques for optimizing the control aspects in a real approach in addition to the result analysis of various control factors on performance behavior [38]. Taguchi's technique is applied to investigate the rank of each process parameter of an alloy or composites for the performance features [39,40]. ANOVA, or analysis of variance, is one of the models used to build and evaluate experiment data when the least squares approach is applied.

There has been a limited amount of research conducted on improving the process parameters in order to improve the mechanical properties of AA5083/SiC composites, despite the fact that FSP is used extensively. Specifically, in AA5083/SiC composites, understanding how FSP influences SiC particle distribution, interfacial bonding with the AA5083 matrix, and the resulting plastic deformation is crucial for optimizing properties like ultimate tensile strength (UTS), percentage elongation (PE), and microhardness (MH). This work seeks to close this gap by carefully investigating the impacts of rotational speed, traverse speed, and tilt angle on UTS, PE, and MH. This study is unique in that it uses both the Taguchi technique and regression analysis, as well as ANOVA, to determine the contributions of these factors to the mechanical performance of SiC-reinforced composites. By filling this gap, the study helps to create cost-effective production methods for high-strength composites designed for industrial applications.

## 2. Experimental Procedure

### *2.1. Material Used*

The base alloy used in this study, AA5083, has the following specific composition: 0.05% chromium, 0.02% copper, 0.16% iron, 4.03% magnesium, 0.69% manganese, 0.15% silicon, 0.02% titanium, and 0.01% zinc [41]. The chemical composition of the base material was analyzed using a Belec Compact Spectrometer HLC, manufactured by Belec Spectrometry Opto-Electronics GmbH (Georgsmarienhütte, Germany). Aluminum plates measuring 250 mm × 50 mm × 6 mm were used. Table 1 displays the mechanical properties of AA5083. The reinforcement in this study was silicon carbide particle powder, which makes up 5% of the composite's volume.

**Table 1.** The base material AA5083's mechanical properties.

| **Mechanical Properties** | |
|---|---|
| Ultimate Tensile Strength | 311 MPa |
| Percentage Elongation | 58.65% |
| Microhardness | 93.07 HV |

*2.2. Parameter Selection for Fabrication of AMMCs*

A Taguchi $L_9$ orthogonal array was employed to optimize friction stir processing (FSP) parameters and minimize experimental runs. This design efficiently investigates three factors at three levels with only nine trials, significantly reducing the 27 runs required for a full factorial design. The chosen parameters were traverse speed (30, 45, 60 mm per min), rotational speed (600, 900, 1200 rev/min), and tilt angle (1°, 1.75°, 2°). The $L_9$ matrix systematically assigns parameter levels across the nine trials, ensuring unbiased analysis using the Minitab 18 software. This approach offers substantial time and resource savings, enables statistical analysis via signal-to-noise (S/N) ratios and ANOVA, and facilitates the identification of optimal conditions for improved AA5083/SiC composite mechanical properties. Table 2 details the factors and levels, while Table 3 presents the resulting nine-run design matrix generated using the Minitab 18 program.

**Table 2.** Parameters of Processing and Their Levels.

| Process Parameters | Factor Symbol | Unit | Level of Parameters | | |
|---|---|---|---|---|---|
| | | | 1 | 2 | 3 |
| Traverse speed | (TS) | [mm per min] | 30 | 45 | 60 |
| Rotational speed | (RS) | [rev/min] | 600 | 900 | 1200 |
| Tilt angle | (TA) | [°] | 1 | 1.75 | 2 |

**Table 3.** The design matrix of Taguchi $L_9$.

| No of Experiments | Tilt Angle [°] | Rotational Speed [rev/min] | Traverse Speed [mm per min] |
|---|---|---|---|
| 1. | 1 | 600 | 30 |
| 2. | 1.75 | 600 | 45 |
| 3. | 2 | 600 | 60 |
| 4. | 1.75 | 900 | 30 |
| 5. | 2 | 900 | 45 |
| 6. | 1 | 900 | 60 |
| 7. | 2 | 1200 | 30 |
| 8. | 1 | 1200 | 45 |
| 9. | 1.75 | 1200 | 60 |

*2.3. Fabrication of AMMCs*

The fabrication of AA5083/SiC composites was carried out using friction stir processing (FSP), with the AA5083 aluminum alloy as the base material and silicon carbide (SiC) particles as the reinforcement. Initially, two AA5083 plates (250 mm × 50 mm × 6 mm) were joined using friction stir welding (FSW) to create a stable workpiece as shown in Figure 1a. A series of 2.5 mm diameter holes, spaced 15 mm apart and drilled to a depth of 4 mm, were prepared along the weld line. These holes were filled with SiC particle powder (5% volume fraction) as shown in Figure 1b and sealed using a pinless FSP tool to prevent particle loss before processing as shown in Figure 1c. Finally, the last FSP pass is performed as shown in Figure 1d at room temperature.

The FSW/FSP was performed using a Lagun FU.1-LA universal milling machine manufactured by the Lagun Machine Tools S.L.U. in Gipuzkoa in Spain and a custom-designed tool made of AISI 4140 high-speed steel, with a shoulder diameter of 20 mm, probe diameter of 7 mm, and a triangular pin of 5.8 mm. The pin-equipped tool and pinless tool are displayed in Figure 1e,f, respectively. It should be noted that the processing parameters used were determined through the Taguchi $L_9$ orthogonal array, as described in Section 2.2, ensuring an optimized and systematic approach to parameter selection.

Traverse speed (30, 45, and 60 mm per min), rotational speed (600, 900, and 1200 rev/min), and tilt angle (1°, 1.75°, and 2°) were the final parameters that varied with each run.

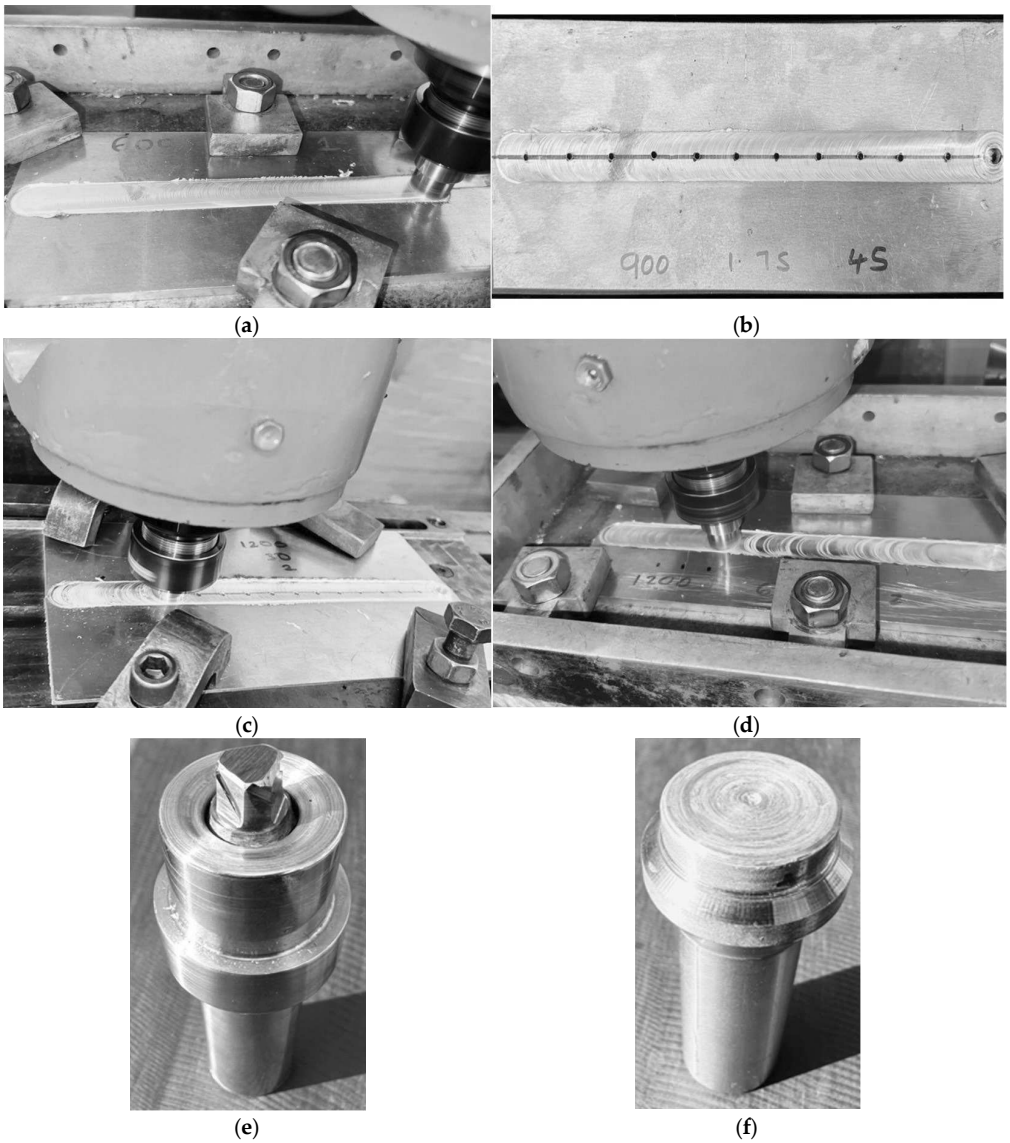


(**a**) (**b**) (**c**) (**d**) (**e**) (**f**)

**Figure 1.** (**a**) FSW procedure; (**b**) Drilling of holes and filling them with SiC particles; (**c**) Using a pinless tool to close the hole; (**d**) FSP single-pass procedure; (**e**) Tool with pin tool; (**f**) Pinless.

In the end, nine AA5083/SiC composite joints were successfully constructed and tested for tensile and hardness. Tensile specimens were extracted perpendicular to the processing direction following ASTM-E8M-04 [42] standards to ensure uniform sampling, and one specimen per condition was used to evaluate the mechanical performance. The Hounsfield tensile test machine was employed for specimen preparation and tensile testing. For hardness evaluation, microhardness specimens were also extracted perpendicular to the processing direction, and measurements were conducted using the Innova Test Falcon 500 (manufactured by the INNOVATEST Europe BV Manufacturing Maastricht in the Netherlands). Hardness testing followed ASTM-E384 standard [43]. It should also be noted that one specimen was used to assess the microhardness in each condition.

The tensile specimen dimensions and microhardness dimensions are shown in Figure 2, while Table 4 presents the measured values of the ultimate tensile strength (UTS),

yield strength (YS), percentage elongation (PE), and microhardness (MH) for each experimental run.

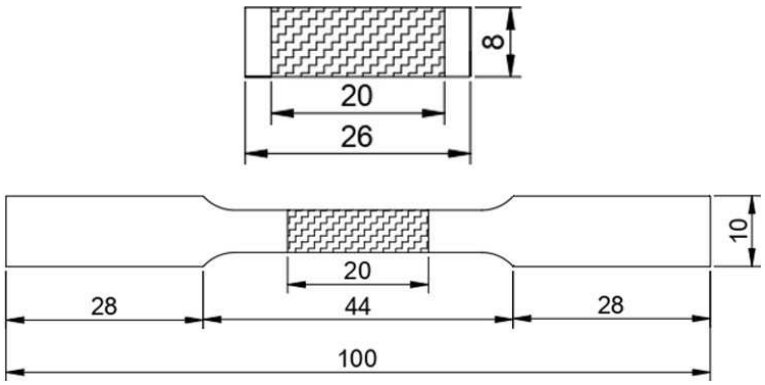


**Figure 2.** Dimensions and arrangement of the hardness and tensile specimens.

**Table 4.** AA5083/SiC Composite Mechanical Properties.

| Trial No. | UTS (MPa) | YS (MPa) | PE (%) | MH (HV) |
|---|---|---|---|---|
| 1. | 71.5 | 57.20 | 9.88 | 94.78 |
| 2. | 114 | 91.20 | 11.75 | 89.57 |
| 3. | 88 | 70.40 | 11.23 | 89.57 |
| 4. | 210 | 168.0 | 29 | 89.39 |
| 5. | 145 | 116.0 | 18.45 | 94.80 |
| 6. | 141 | 112.8 | 19.9 | 92.95 |
| 7. | 243 | 194.4 | 29.5 | 90.56 |
| 8. | 132 | 105.6 | 18.7 | 93.65 |
| 9. | 121 | 96.80 | 12.08 | 89.56 |

## 3. Results and Discussion

### *3.1. Mechanical Properties*

#### 3.1.1. Hardness

The microhardness of the developed AA5083/SiC composites was higher than the base metal AA5083, having an average value of 93.07 HV. The outcome shows that hardness values presented here have marked differences under various FSP parameters from that of the base material. The improved microhardness is due to phenomena like recrystallization, grain refinement, distribution of particles, and intermetallic particle fragmentation [44,45]. These findings align with previous studies [46].

#### 3.1.2. Tensile Strength

The produced AA5083/SiC composites were found to have a UTS that was comparable to the AA5083 base material. However, as compared to the base material, the produced AA5083/SiC composites showed a slight reduction in ultimate tensile strength. The reduced tensile strength is due to SiC particle agglomeration and poor interfacial bonding between the reinforcement and the AA5083 matrix. Agglomeration creates stress concentrations that initiate cracks, weakening the composite. Poor bonding hinders effective load transfer, further reducing strength. This aligns with previous research [47–50] showing lower tensile strength in single-pass FSP composites compared to the base material, attributed to particle aggregation and resulting stress concentrations. This suggests that further optimization of processing parameters, such as multi-pass FSP or improved tool design, may be necessary to enhance particle distribution and bonding, ultimately improving tensile properties.

3.1.3. Comparison Plots of Regression-Predicted Values and Investigational Values

The investigative output answers are used to develop the regression equation, which ensures the equivalence between the observed process parameters for FSP. Equations (1)–(3) display the regression equations that yield the maximum hardness, tensile strength, and percentage elongation.

*Microhardness (HV): 86.60 + 0.00244 RS (rev/min) + 0.0453 TS (mm per min) − 0.24 TA (deg).* (1)

Microhardness shows a positive relationship with both rotational speed (RS) and traverse speed (TS). Higher RS promotes fine grain structures and better dispersion of reinforcements, increasing hardness. Similarly, increased TS results in rapid cooling and refined grains, positively impacting hardness. Conversely, the negative effect of tool tilt angle (TA) suggests that steeper angles may reduce contact pressure or material mixing, slightly compromising hardness. These relationships align with the Hall–Petch effect, where finer grains enhance hardness.

*Percentage Elongation (%): 11.7 + 0.01523 RS (rev/min) − 0.280 TS (mm per min) + 3.19 TA (deg).* (2)

Percentage elongation, a measure of ductility, increases with rotational speed (RS), albeit at a smaller coefficient than tensile strength. This reflects improved material ductility due to better mixing and reduced defects at higher RS. A negative relationship with traverse speed (TS) suggests that faster tool movement compromises material homogeneity, reducing ductility. The positive impact of tool angle (TA) indicates enhanced material flow and grain refinement, contributing to greater elongation. These trends align with the expected relationship between processing parameters and ductility.

*Tensile strength (MPa): 46.9 + 0.1236 RS (rev/min) − 1.94 TS (mm per min) + 44.0 TA (deg).* (3)

The model indicates that rotational speed (RS) positively contributes to tensile strength, aligning with the expectation that higher rotational speeds promote better mixing of materials and defect reduction, enhancing strength. Traverse speed (TS) negatively affects tensile strength, likely due to reduced heat input and mixing time at higher speeds, leading to weaker bonding. The tool angle (TA) significantly increases tensile strength, as a higher tool angle improves material flow and consolidation. These effects align with the physical principles governing friction stir processing.

Alignment with Physical Expectations

The developed models effectively represent the known effects of friction stir processing (FSP) parameters on the mechanical characteristics of the material. This consistency with established physical assumptions enhances the credibility and reliability of the models. Higher rotational speeds (RSs) improve material properties by increasing heat input and enhancing mixing, leading to better bonding and defect reduction. Lower traverse speeds (TSs) contribute to improved material homogeneity and bonding but may reduce hardness due to slower cooling rates. Tool tilt angle (TA) plays a critical role in optimizing material flow and grain refinement, significantly enhancing tensile strength and elongation, although it may slightly compromise hardness in certain cases. By accurately capturing these relationships, the models demonstrate their reliability and consistency with established principles in mechanical and materials science, making them effective tools for predicting the properties of SiC composites.

Table 5 displays the results obtained from the regression equations established to examine the mechanical properties of composites made of AA5083 and SiC. This study is further demonstrated in Figure 3, which compares the regression equation predictions with the experimental results for microhardness, % elongation, and tensile strength.

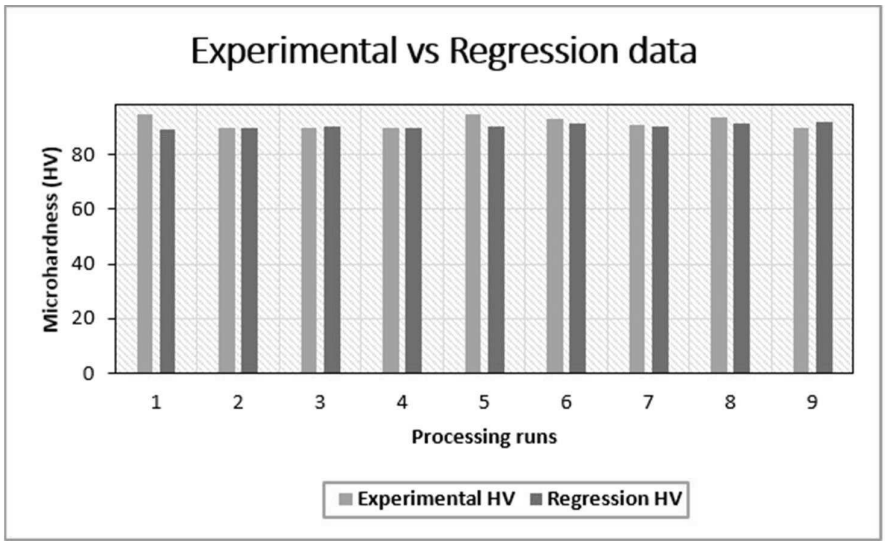


(**a**)

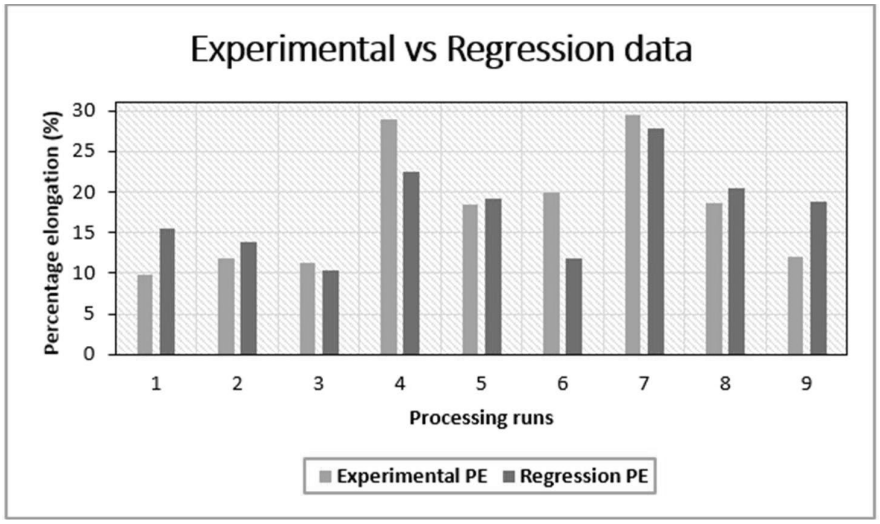


(**b**)

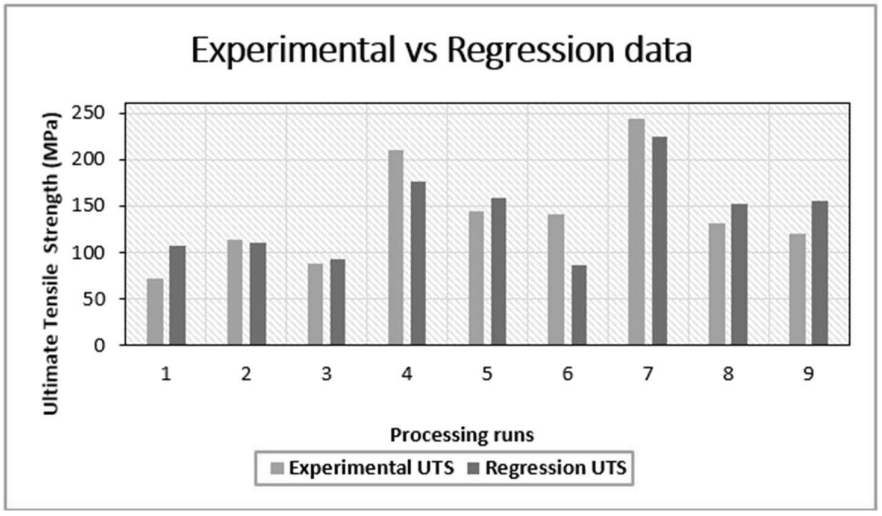


(**c**)

**Figure 3.** Results from experiments and regressions for (**a**) Microhardness (MH), (**b**) Percentage elongation (PE), and (**c**) Ultimate tensile strength (UTS).

**Table 5.** Experimental values vs. regression.

| TA (°) | TS (mm per min) | RS (rev/min) | UTS (MPa) | Fits UTS | % Error | PE (%) | Fits PE | % Error | MH (HV) | Fits HV | % Error |
|---|---|---|---|---|---|---|---|---|---|---|---|
| 1 | 30 | 600 | 71.5 | 106.929 | 49.6 | 9.88 | 15.5965 | 57.9 | 94.78 | 89.1813 | 5.90 |
| 1.75 | 45 | 600 | 114 | 110.865 | 2.75 | 11.75 | 13.7938 | 17.4 | 89.57 | 89.6832 | 0.13 |
| 2 | 60 | 600 | 88 | 92.788 | 5.44 | 11.23 | 10.3963 | 7.43 | 89.57 | 90.3038 | 0.82 |
| 1.75 | 30 | 900 | 210 | 177.032 | 15.7 | 29 | 22.5588 | 22.2 | 89.39 | 89.7349 | 0.39 |
| 2 | 45 | 900 | 145 | 158.955 | 9.59 | 18.45 | 19.1613 | 3.85 | 94.80 | 90.3555 | 4.69 |
| 1 | 60 | 900 | 141 | 85.846 | 39.1 | 19.9 | 11.7765 | 40.8 | 92.95 | 91.2729 | 1.81 |
| 2 | 30 | 1200 | 243 | 225.122 | 7.37 | 29.5 | 27.9263 | 5.33 | 90.56 | 90.4072 | 0.17 |
| 1 | 45 | 1200 | 132 | 152.013 | 15.1 | 18.7 | 20.5415 | 9.87 | 93.65 | 91.3246 | 2.48 |
| 1.75 | 60 | 1200 | 121 | 155.949 | 28.8 | 12.08 | 18.7388 | 55.2 | 89.56 | 91.8265 | 2.53 |

*3.2 Microstructural Analysis*

The microstructures of the AA5083/SiC composites are illustrated in Figure 4, highlighting the effects of different processing parameters. Figure 4($a_1$–$a_3$) display the microstructures of composites processed at a rotational speed of 600 rev/min, with traverse speeds of 30, 45, and 60 mm per min and tilt angles of 1°, 1.75°, and 2°, respectively. Similarly, Figure 4($b_1$–$b_3$) show the microstructures at a higher rotational speed of 900 rev/min, using the same traverse speeds of 30, 45, and 60 mm per min but with tilt angles of 1.75°, 2°, and 1°. Lastly, Figure 4($c_1$–$c_3$) present the microstructures obtained at 1200 rev/min, where the traverse speeds remain 30, 45, and 60 mm per min but the tilt angles are set at 2°, 1°, and 1.75°, respectively. This systematic comparison provides insight into how variations in rotational speed, traverse speed, and tilt angle influence the microstructural characteristics of the composite material.

Post-weld microstructural analysis, as evidenced by the highlighted regions in Figure 4 (yellow circles), confirmimed the presence of silicon carbide (SiC) particles within the nugget zone; however, only a small fraction of these particles exhibit proper metallurgical bonding with the AA5083 matrix. The weak interfacial bonding also indicated by the yellow circles, can be attributed to insufficient heat generation and material flow constraints during friction stir processing (FSP), which limit the full incorporation of SiC particles into the matrix. This inadequate bonding reduces effective load transfer between the reinforcement and the matrix, ultimately compromising tensile strength and ductility [51–55].

A closer examination of secondary phase particle distribution reveals that SiC particles are not uniformly dispersed throughout the nugget zone, and these results are consistent with observations by [56–58]. Instead, regions of agglomeration are observed, where clusters of reinforcement particles accumulate. This nonuniform particle movement creates stress concentration sites that can initiate microcracks, further weakening the composite structure [56,59].

Overall, the images provide insight into the degree of interfacial bonding and particle distribution. In some regions, strong metallurgical bonding between SiC particles and the AA5083 matrix is observed, suggesting effective diffusion at the interface. However, in other areas, gaps and voids exist at the interface, indicating poor adhesion between the matrix and the reinforcement. This suggests that further optimization of FSP parameters, such as multi-pass processing or controlled heat input, may be necessary to achieve a more uniform dispersion and stronger interfacial bonding.

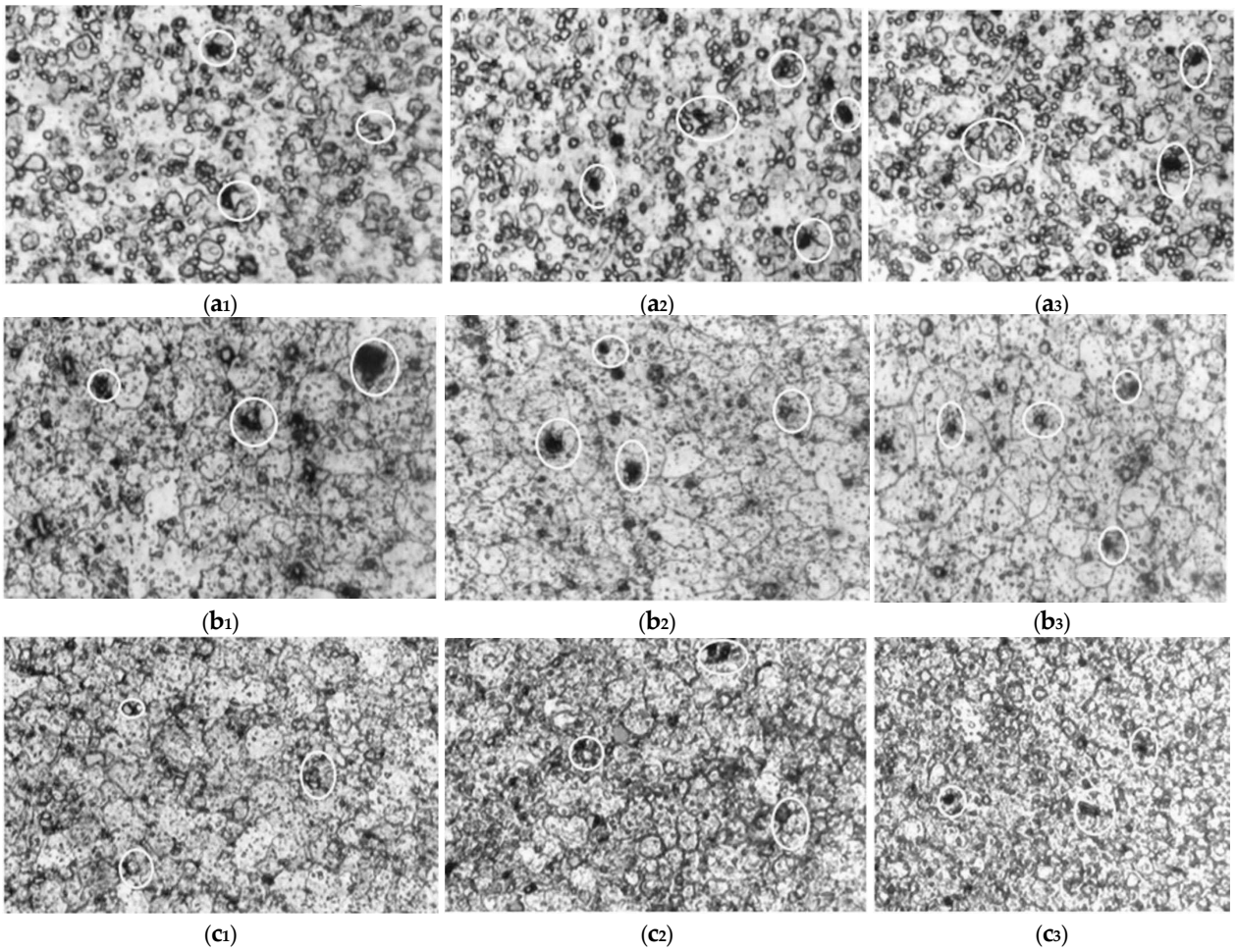


**Figure 4.** AA5083/SiC composite optical microstructures photographed at 20 × 100 μm magnification with a 100 μm scale bar. (**a1–a3**) Microstructures at 600 rev/min with traverse rates of 30 mm per min, 45 mm per min, and 60 mm per min, respectively, and tilt angles of 1°, 1.75°, and 2°. (**b1–b3**) Microstructures at 900 rev/min with traverse rates of 30 mm per min, 45 mm per min, and 60 mm per min, respectively, and tilt angles of 1.75°, 2°, and 1°. (**c1–c3**) Microstructures having traverse rates of 30 mm per min, 45 mm per min, and 60 mm per min at 1200 rev/min with tilt angles of 2°, 1°, and 1.75°, respectively.

### *3.3 Interpretation of Experimental Results*

#### 3.3.1 Signal-to-Noise (S/N) Ratio Analysis

In single-response optimization, Taguchi's method is employed for converting the experiment's result into an evaluation characteristic value for optimal setting analysis. During the operation of any engineering system or process, performance properties are defined as observable responses to the analytical output [60]. To evaluate the effect of each process parameter on these response factors, this study utilized the S/N ratio. The S/N ratio is a key metric in Taguchi's robust design methodology. It provides a quantitative measure of the signal (desired output) relative to the noise (undesirable variations). By maximizing the S/N ratio, engineers can optimize the process to achieve consistent and robust performance. In this study, the "higher the better" equation was selected as the ideal response for all performance properties (HV, PE, and UTS). This characteristic is appropriate when the objective is to maximize the desired output. The specific formula for calculating the signal-to-noise ratio for the "higher the better" characteristic is given in Equation (4) [61,62]:

$$\frac{S}{N} = -10 \log\left(\frac{1}{n}\sum_{i-1}^{3}\frac{1}{y^2}\right) \quad (4)$$

This may be written as follows: y is the response factor at the experiment's *i*-th level, and n is the number of experiment repetitions. Table 6 shows the relationship between the S/N ratios and the mechanical properties test results for the AA5083/SiC composite's parameter settings. The S/N ratio plotted data are shown in Figure 5.

Figure 5a reveals that the highest microhardness (MH) for the AA5083/SiC composite joints was obtained at a tool tilt angle of 2° (Level 3), a tool traverse speed of 45 mm per min (Level 2), and a tool rotational speed of 900 rev/min (Level 2). Furthermore, Figure 5b demonstrates that the maximum percentage elongation was achieved at a tool tilt angle of 2° (Level 3), a tool traverse speed of 30 mm per min (Level 1), and a tool rotational speed of 900 rev/min (Level 2). Notably, this combination of parameters also resulted in the highest ultimate tensile strength, as depicted in Figure 5c. For UTS and PE, the best results were achieved at 900 rpm tool rotational speed, 30 mm per min tool traverse speed, and a 2° tool tilt angle. For MH, a slightly higher traverse speed of 45 mm per min was required at the same rotational speed and tilt angle. These findings align with previous research [63,64] that has demonstrated improved mechanical properties in metal matrix composites by employing a "larger-is-better" strategy for certain processing parameters.

**Table 6.** Experimental results for the AA5083/SiC composite with the relevant S/N ratio.

| TA (°) | RS (rev/min) | TS (mm per min) | MH (HV) | S/N Ratio (HV) | UTS (MPa) | S/N Ratio (UTS) | PE (%) | S/N Ratio (PE) |
|---|---|---|---|---|---|---|---|---|
| 1 | 600 | 30 | 88.05 | 38.895 | 71.5 | 37.086 | 9.88 | 19.895 |
| 1.75 | 600 | 45 | 89.57 | 39.043 | 114 | 41.138 | 11.75 | 21.401 |
| 2 | 600 | 60 | 89.57 | 39.043 | 88 | 38.889 | 11.23 | 21.008 |
| 1.75 | 900 | 30 | 89.39 | 39.026 | 210 | 46.444 | 29.00 | 29.248 |
| 2 | 900 | 45 | 92.98 | 39.368 | 145 | 43.227 | 18.45 | 25.319 |
| 1 | 900 | 60 | 92.95 | 39.365 | 141 | 42.984 | 19.90 | 25.977 |
| 2 | 1200 | 30 | 90.56 | 39.139 | 243 | 47.712 | 29.50 | 29.396 |
| 1 | 1200 | 45 | 91.46 | 39.225 | 132 | 42.412 | 18.70 | 25.437 |
| 1.75 | 1200 | 60 | 89.56 | 39.042 | 121 | 41.656 | 12.08 | 21.641 |

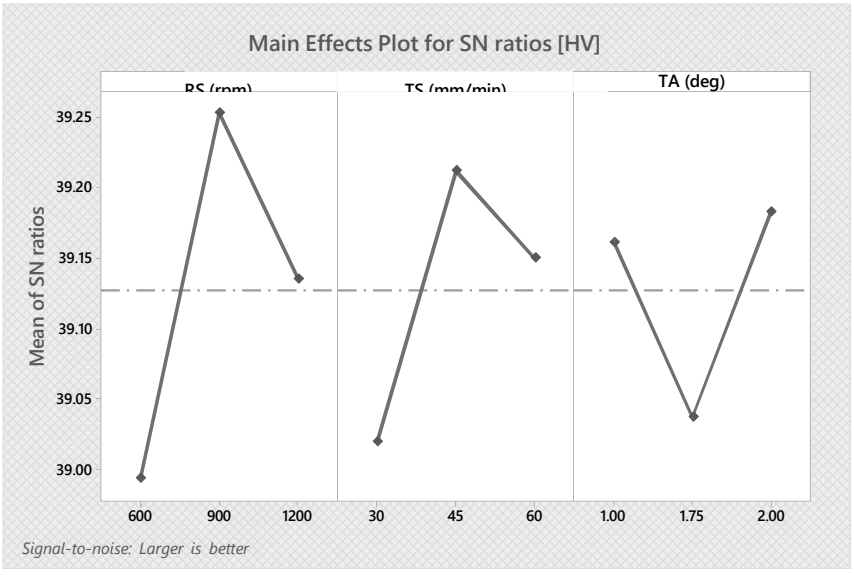


(**a**)

**Figure 5.** *Cont.*

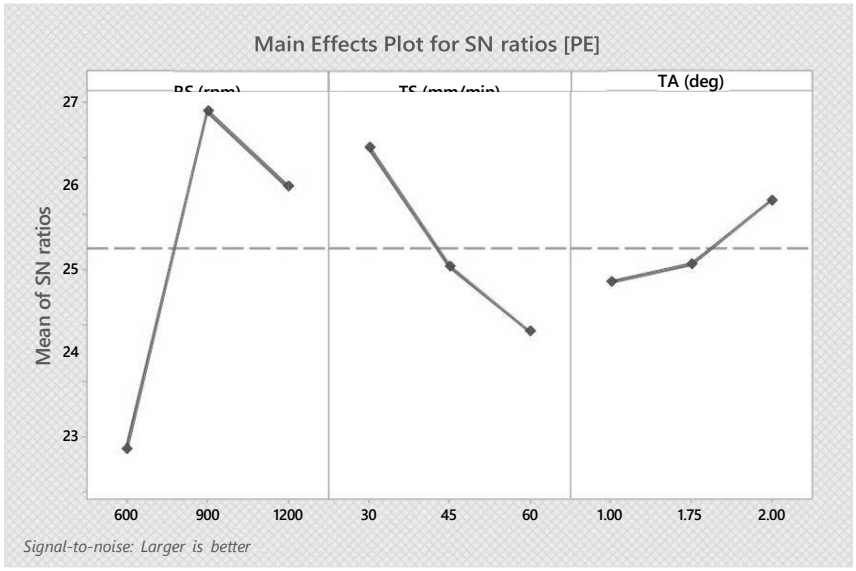


(**b**)

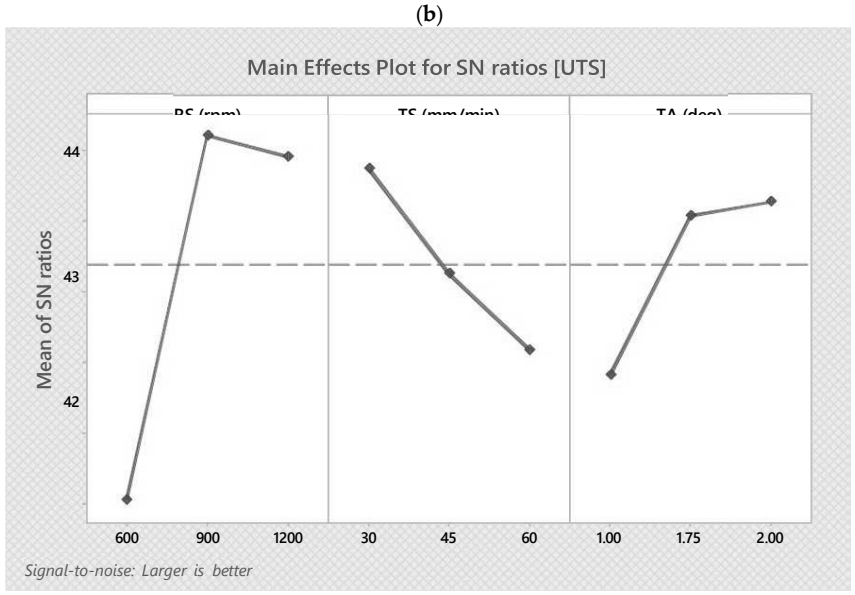


(**c**)

**Figure 5.** AA5083/SiC composite S/N ratio and mean plot: (**a**) Microhardness; (**b**) Percentage elongation; (**c**) Ultimate tensile strength.

### 3.3.2 Determining Optimum Process Parameters and Ranking of Critical Factors

The study used Minitab 18 software to identify the most significant variable influencing the response factor of the manufactured AA5083/SiC composite joint. This program made it possible to determine the mean S/N ratio for each of the three process parame- ter levels. According to the investigation, the most important factor affecting the three mechanical parameters of microhardness (MH), percentage elongation (PE), and ultimate tensile strength (UTS) was rotating speed. This is evident in Table 7, where rotational speed consistently ranks first in significance. Traverse speed consistently ranked second in influence on all three properties, while tilt angle generally exhibited the least (rank 3) influence. These findings strongly suggest that rotational speed has a significant influence on the mechanical properties of the fabricated composites. This is likely attributed to the crucial role of heat generation during FSP, which influences particle distribution and grain refinement within the material [65–67]. The FSP parameters were fine-tuned based on

S/N ratio analysis for each parameter. The results of this investigation showed that a tool tilt angle of 2 degrees, a tool traverse speed of 45 mm per minute, and a tool rotational speed of 900 rev/min were the ideal values for optimizing microhardness (MH). However, a slightly lower traverse speed of 30 mm per minute was needed to achieve maximum ultimate tensile strength (UTS) and percentage elongation (PE) while keeping the tool tilt angle (2 degrees) and rotating speed (900 rev/min) constant.

**Table 7.** Main Effects Response Table for S/N ratio.

| Level | Tilt Angle (°) | Rotational Speed (rev/min) | Traverse Speed (mm per min) |
|---|---|---|---|
| **For UTS** | | | |
| S/N ratio | | | |
| 1 | 40.83 | 39.04 | 43.75 |
| 2 | 43.08 | 44.22 | 42.26 |
| 3 | 43.28 | 43.93 | 41.18 |
| Delta | 2.450 | 5.180 | 2.570 |
| Rank | 3 | 1 | 2 |
| Means | | | |
| 1 | 114.83 | 91.17 | 174.83 |
| 2 | 148.33 | 165.34 | 130.33 |
| 3 | 158.67 | 165.33 | 116.67 |
| Delta | 43.830 | 74.170 | 58.170 |
| Rank | 3 | 1 | 2 |
| **For PE** | | | |
| S/N ratio | | | |
| 1 | 23.77 | 20.77 | 26.18 |
| 2 | 24.10 | 26.85 | 24.05 |
| 3 | 25.24 | 25.49 | 22.88 |
| Delta | 1.470 | 6.080 | 3.300 |
| Rank | 3 | 1 | 2 |
| Means | | | |
| 1 | 16.16 | 10.95 | 22.79 |
| 2 | 17.61 | 22.45 | 16.30 |
| 3 | 19.73 | 20.09 | 14.40 |
| Delta | 3.570 | 11.50 | 8.390 |
| Rank | 3 | 1 | 2 |
| **For HV** | | | |
| S/N ratio | | | |
| 1 | 39.16 | 38.99 | 39.02 |
| 2 | 39.04 | 39.25 | 39.21 |
| 3 | 39.18 | 39.14 | 39.15 |
| Delta | 0.150 | 0.260 | 0.190 |
| Rank | 3 | 1 | 2 |
| Means | | | |
| 1 | 90.82 | 89.06 | 89.33 |
| 2 | 89.51 | 91.77 | 91.34 |
| 3 | 91.04 | 90.53 | 90.69 |
| Delta | 1.530 | 2.710 | 2.000 |
| Rank | 3 | 1 | 2 |

3.3.3 Analysis of Variance (ANOVA)

To determine the statistically significant process parameters, analysis of variance was carried out. Using the percentages and the probability distribution (F-value) of each of the

factors allows the extent of influence of each of the parameters on the output responses to be established. The frequency test is carried out in statistics to assess the significance of parameters, which in turn defines the quality of the properties [68]. The results of the ANOVA for the S/N ratios of percentage elongation, ultimate tensile strength, and microhardness are presented in Tables 8–10, respectively. From the estimated percentages in Table 8, tool rotational speed was found to contribute significantly to UTS at 57.55%, tilt angle contributed 12.58%, and traverse speed contributed 11.32%. The authors also observed some differences between the rankings provided in Table 7 and the percentage contributions in Table 8. This could help address the aforementioned inconsistencies with more specific statistics, specifically confidence intervals and replicate experiments. This means that, when it comes to the choice of methods for analysis, objectivity should be paired with the characteristics of the collected data.

Percentage elongation (PE) depends on tool rotational speed, traverse rate, and tool tilt angle with contribution percentages of 60.36, 16.62, and 3.54 percent, respectively, as seen in Table 9. These contributions are in the same percentages as supported by the F-value analysis. Further, Table 10 demonstrates that the factors—tool rotational speed, traverse rate, and tool tilt angle—significantly influence microhardness. Collectively, these factors account for 93.51% of the observed variations in microhardness, with rotational speed contributing 48.17%, traverse speed contributing 27.54%, and tilt angle contributing 17.78%. According to these findings, the most important element influencing the final material's UTS, PE, and MH is the tool's rotating speed.

Accordingly, other researchers have reported that the tool rotational speed has the most significant influence on the microhardness, which is consistent with this work. These researchers include Chanakyan et al. [66], Syed et al. [67], and Butola et al. [68]. Chanakyan et al. [66], Syed et al. [67], Salehi et al. [69], and Puviyarasan et al. [70] also found that the key element influencing microhardness was the tool's rotational speed. Because of the significant impact that rotating speed has on mechanical characteristics, heat production is essential for promoting grain refining and maintaining particle uniformity. According to ANOVA, it was also shown that rotating speed had the greatest impact on the alloy's UTS, PE, and MH, demonstrating the rotational speed's practical influence on the alloy's mechanical properties. Additionally, in comparison to random error, a parameter that has a larger F-value contributes more significantly to the variance in mechanical properties. A high F-value for rotational speed indicated that it had a significant impact on these properties.

**Table 8.** Factors that affect how much the UTS varies.

| Source | Degree of Freedom (DF) | Seq SS | Adj SS | Adj MS | F-Value | *p*-Value | % Contribution |
|---|---|---|---|---|---|---|---|
| S/N ratio | | | | | | | |
| TA (°) | 2 | 11.110 | 11.108 | 5.5540 | 0.68 | 0.596 | 12.581 |
| RS (rev/min) | 2 | 50.823 | 50.823 | 25.411 | 3.10 | 0.244 | 57.552 |
| TS (mm per min) | 2 | 9.9970 | 9.9970 | 4.9990 | 0.61 | 0.621 | 11.321 |
| Error | 2 | 16.379 | 16.379 | 8.1900 | | | 18.548 |
| Total | 8 | 88.308 | | | | | |
| Means | | | | | | | |
| TA (°) | 2 | 3150 | 3150 | 1575 | 0.73 | 0.579 | 13.109 |
| RS (rev/min) | 2 | 11001 | 11001 | 5501 | 2.54 | 0.282 | 45.782 |
| TS (mm per min) | 2 | 5550 | 5550 | 2775 | 1.28 | 0.438 | 23.097 |
| Error | 2 | 4327 | 4327 | 2163 | | | 18.007 |
| Total | 8 | 24029 | | | | | |

**Table 9.** Factors that affect how much the PE varies.

| Source | Degree of Freedom (DF) | Seq SS | Adj SS | Adj MS | F-Value | *p*-Value | % Contribution |
|---|---|---|---|---|---|---|---|
| S/N ratio | | | | | | | |
| TA (°) | 2 | 3.5830 | 3.5830 | 1.7910 | 0.18 | 0.846 | 3.5378 |
| RS (rev/min) | 2 | 61.127 | 61.127 | 30.563 | 3.10 | 0.244 | 60.357 |
| TS (mm per min) | 2 | 16.831 | 16.831 | 8.4160 | 0.85 | 0.540 | 16.619 |
| Error | 2 | 19.734 | 19.734 | 9.8670 | | | 19.486 |
| Total | 8 | 101.275 | | | | | |
| Means | | | | | | | |
| TA (°) | 2 | 19.300 | 19.300 | 9.6520 | 0.22 | 0.817 | 4.3549 |
| RS (rev/min) | 2 | 221.27 | 221.27 | 110.633 | 2.56 | 0.281 | 49.928 |
| TS (mm per min) | 2 | 116.15 | 116.15 | 58.0760 | 1.34 | 0.427 | 26.208 |
| Error | 2 | 86.450 | 86.450 | 43.2260 | | | 19.507 |
| Total | 8 | 443.18 | | | | | |

**Table 10.** Factors that affect how much the MTS varies.

| Source | Degree of Freedom (DF) | Seq SS | Adj SS | Adj MS | F-Value | *p*-Value | % Contribution |
|---|---|---|---|---|---|---|---|
| S/N ratio | | | | | | | |
| TA (°) | 2 | 0.03729 | 0.03729 | 0.018644 | 2.73 | 0.268 | 17.778 |
| RS (rev/min) | 2 | 0.10103 | 0.10103 | 0.050514 | 7.39 | 0.119 | 48.167 |
| TS (mm per min) | 2 | 0.05777 | 0.05777 | 0.028885 | 4.23 | 0.191 | 27.542 |
| Error | 2 | 0.01367 | 0.01367 | 0.006833 | | | 6.5173 |
| Total | 8 | 0.20975 | | | | | |
| Means | | | | | | | |
| TA (°) | 2 | 4.1130 | 4.1130 | 2.0563 | 2.78 | 0.264 | 17.955 |
| RS (rev/min) | 2 | 11.040 | 11.040 | 5.5198 | 7.47 | 0.118 | 48.195 |
| TS (mm per min) | 2 | 6.2770 | 6.2770 | 3.1384 | 4.25 | 0.191 | 27.402 |
| Error | 2 | 1.4780 | 1.4780 | 0.7391 | | | 6.4522 |
| Total | 8 | 22.907 | | | | | |

Interpretation of ANOVA Data

The amount of overall variance in an experiment that can be attributed to each significant component is shown by the percentage contribution. The ability of each element to reduce variance is demonstrated by this, which is derived from the sum of squares of the major factors. Consequently, by controlling the factor levels with measurement precision, the research can decrease the total spread by the percentage of the contribution [71]. The contribution based on ANOVA is represented in percentage in Figure 6. Rotational speed has a considerable impact on UTS, PE, and MH with a percentage contribution of 58%, 60%, and 48% according to the ANOVA findings of the signal-to-noise ratio displayed in the crosstab. The ranking based on the table and the contribution percentages are also correlated with the F-value analysis. These findings demonstrate the significant impact of tool rotation speed on output reactions. Grain refining and achieving the required particle distribution both benefit from heat production because of the relative significance of rotating speed in microhardness [65–67].

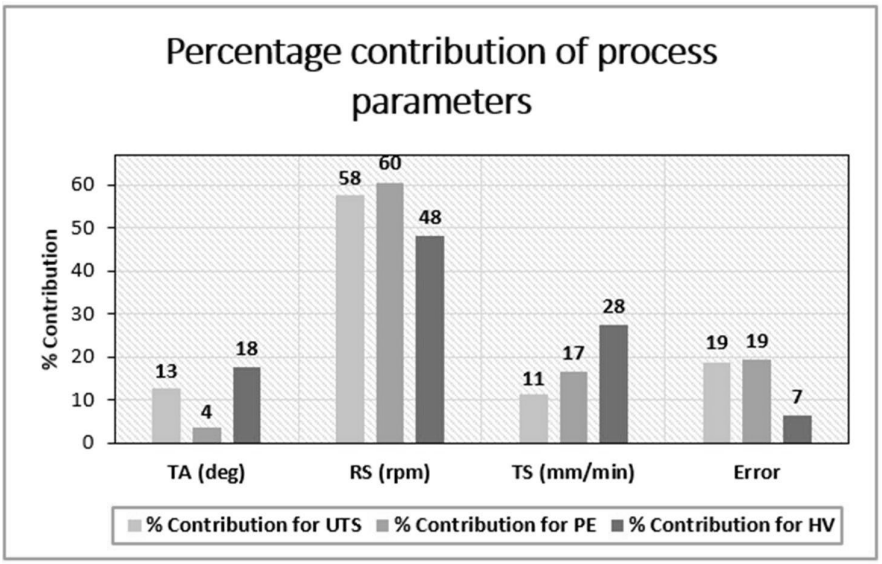


**Figure 6.** Percentage contribution for process parameters.

Normal Probability Plot

To assess the prediction accuracy of models created for AA5083/SiC composites' microhardness (MH), percentage elongation (PE), and ultimate tensile strength (UTS), residual analysis is essential (see Figure 7). Researchers can evaluate the validity and dependability of their models by looking at the residuals, or the disparities between the values predicted by the model and the experimental values. In MH, a well-distributed residual pattern reflects effective hardness predictions, while significant deviations may signal experimental or modeling errors. For PE, randomly scattered residuals suggest accurate ductility predictions, with deviations highlighting biases or unaccounted factors. For UTS, a straight-line pattern in the normal probability plot confirms normality and reliable predictions, while deviations may indicate outliers or model inaccuracies. This analysis ensures model robustness and reliable predictions for critical mechanical properties.

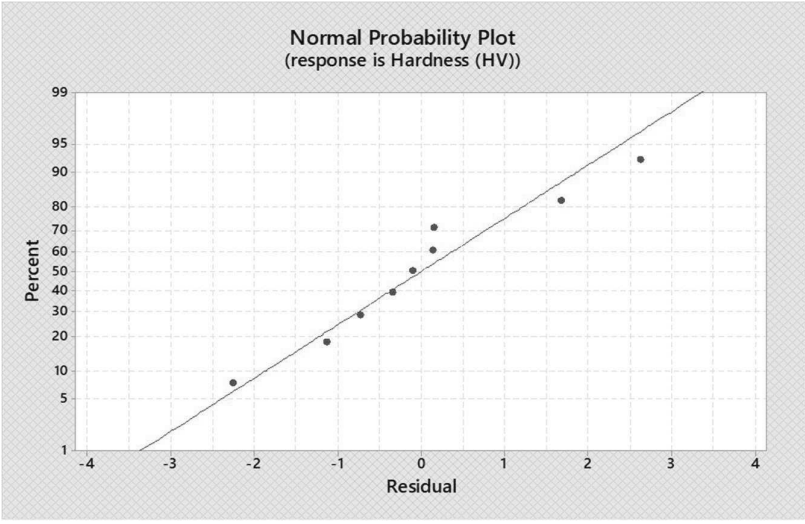


(**a**)

**Figure 7.** *Cont.*

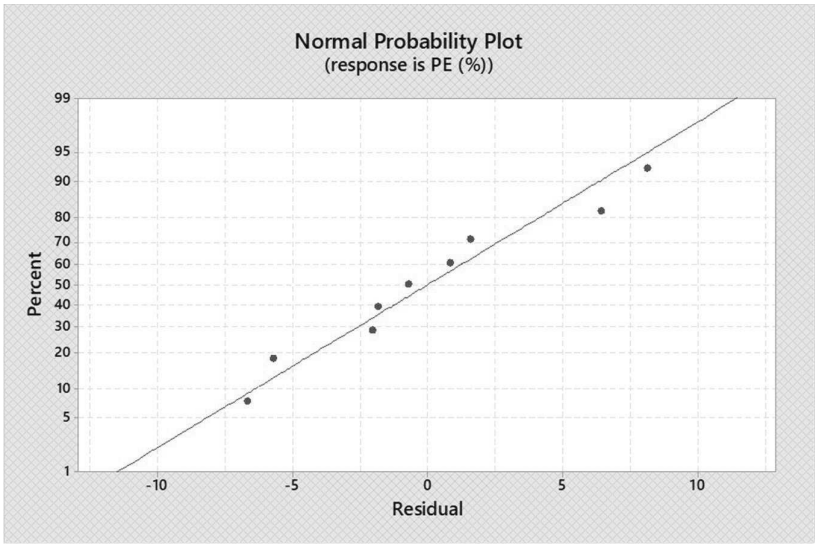


(**b**)

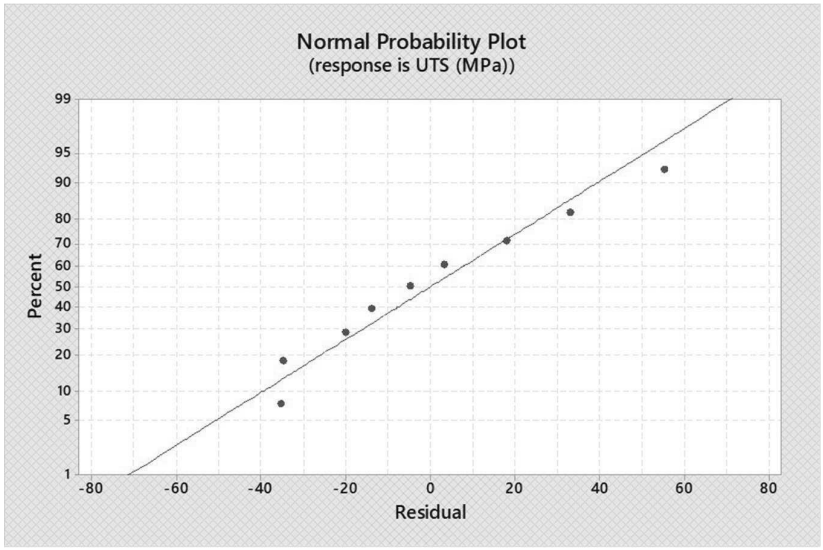


(**c**)

**Figure 7.** Probability Plots; (**a**) Microhardness, (**b**) Percentage elongation, (**c**) Ultimate tensile strength.

In conclusion, the residual analysis conducted for MH, PE, and UTS provides strong evidence for the reliability and validity of the predictive models used in this study. A close alignment of residuals with the assumptions of normality and randomness enhances confidence in the experimental results. Any deviations observed in the residuals provide valuable insights for refining the model, addressing experimental anomalies, and improving the overall predictive accuracy of the research. These results are consistent with earlier research [72–76] that highlighted the use of normal probability plots to guarantee the reliability and validity of statistical models.

*3.4 Confirmation Test*

The identified optimal process parameters-a tool rotational speed of 900 rev/min, a tool traverse speed of 30 mm per min, and a tool tilt angle of 2 degrees [77]-were validated through a series of confirmation tests. Three confirmation tests were conducted on AA5083/SiC composites using these optimal settings. The average UTS obtained in these tests was 275 MPa, with the highest ultimate force recorded at 10,000 N. To investigate

the influence of traverse speed on MH, additional confirmation tests were performed using a tool traverse speed of 45 mm per minute while maintaining a tool rotational speed of 900 rev/min and a tool tilt angle of 2 degrees [77]. Three confirmation tests were also conducted under these conditions. The average UTS in this case was found to be 260 MPa. with the highest ultimate force recorded at 9000 N. All of the obtained average UTS values were higher than the UTS in Table 4 but remained marginally lower than the base material.

Based on average response values, a tool tilt angle of 2°, traverse speed of 30 mm/min, and rotational speed of 900 rpm were identified as optimal for producing AA5083/SiC composites. Confirmation tests validated the initial experimental results, demonstrating improved mechanical properties with these optimized parameters. While the Taguchi method aims to identify the best-performing parameter combination and typically yields improved UTS, achieving values exceeding the base material's strength often requires further refinement. The optimization process, utilizing S/N ratio analysis and ANOVA, pinpoints factor levels positively influencing UTS, and experimental validation at these settings confirms the model's predictive accuracy in achieving enhanced properties.

## 4. Conclusions

Friction stir processing and the Taguchi $L_9$ factorial approach were successfully applied in this work to maximize AMMC fabrication. An aluminum metal matrix composite (AMMC) was effectively created in this study by reinforcing an AA5083 aluminum matrix with silicon carbide particle powder. To maximize the tensile strength and hardness of the final AA5083/SiC composite, the Taguchi approach was utilized to determine the ideal process parameters. The Taguchi approach enabled the following discoveries:

- The ultimate tensile strength of 311 MPa for the base AA5083 material was higher than the greatest experimental tensile strength of 243 MPa for the AA5083/SiC composite. The inclusion of reinforcing silicon carbide particle powder reduced the composite's ductility, even though it showed other mechanical properties that were higher than those of the base material, and this was due to particle agglomeration.
- The base material AA5083's hardness of 93.07 HV was surpassed by the experimental microhardness of the AA5083/SiC composite, which maxed at 94.80 HV. By adding reinforcements, the composite's hardness increased above that of the base material. Grain refinement, particle dispersion, intermetallic particle fracture, and recrystallization are some of the factors that are attributed to the increase.
- According to the investigation, when the AA5083/silicon carbide composite joints were operated at 900 rev/min, 45 mm per minute traverse speed, and a tilt angle of 2 degrees, the greatest microhardness (MH) was generated. However, to maximize both ultimate tensile strength (UTS) and percentage elongation (PE), a slightly lower traverse speed of 30 mm per minute at the same rotational speed and tilt angle is needed.
- According to the ANOVA results of the S/N ratio shown in the crosstab, rotational speed significantly affects UTS, PE, and MH, contributing 58%, 60%, and 48% of the total. These results show that tool rotation speed has a major effect on output responses.
- The experimental design and the range of parameters utilized in this study may limit the generalizability of the developed regression models. However, despite these limitations, the models still provide valuable predictive estimations. Future studies should investigate adding interaction factors to the regression models to better understand the complex relationships between FSP parameters and mechanical properties. Additionally, more sophisticated regression techniques, such as response surface methodology, could be employed to provide more comprehensive and accurate predictions.

## 5. Limitations of the Study

While this study successfully optimized friction stir processing (FSP) parameters for AA5083/SiC composites using the Taguchi $L_9$ method, several limitations must be acknowledged. Firstly, the study focused on single-pass FSP, which may have limited the uniform dispersion of SiC reinforcement particles, leading to agglomeration and weak interfacial bonding in certain regions. A multi-pass approach could further refine the microstructure and improve mechanical properties.

Secondly, the absence of high-magnification SEM analysis of the fractured surfaces limits a deeper understanding of fracture mechanisms, particularly how particle–matrix bonding failure influences mechanical performance. Additionally, this study primarily evaluated tensile strength, microhardness, and elongation, but impact toughness, fatigue strength, and wear resistance were not examined, which are crucial for industrial applications.

Furthermore, while yield strength (YS) and percentage elongation (PE) were included in Table 4, other important performance indicators, such as elastic modulus, were not assessed due to experimental constraints. The elastic modulus is a key parameter for understanding the composite's load-bearing capacity and stiffness, and its absence may limit the comprehensive evaluation of the material's mechanical behavior.

## 6. Future Prospects

Future research should explore multi-pass FSP to enhance particle dispersion and improve mechanical properties. Additionally, incorporating different reinforcement materials, such as hybrid ceramic reinforcements, could be investigated to achieve a better balance of strength, toughness, and wear resistance.

Further studies should also examine the fatigue behavior, corrosion resistance, and tribological performance of the composites to assess their suitability for real-world engineering applications. The effect of postprocessing heat treatments and alternative SiC volume fractions should be explored to optimize the microstructural characteristics further.

Moreover, future work should include elastic modulus measurements through nanoindentation testing or dynamic mechanical analysis (DMA) to provide a complete assessment of the composite's stiffness and energy absorption properties. Additionally, a more detailed fracture mechanics study, including fracture toughness and impact strength, would further enhance the understanding of the material's structural integrity under different loading conditions.

**Author Contributions:** Conceptualization, V.M.; methodology, S.M.; software, O.M.; validation, O.M., V.M. and S.M.; formal analysis, S.M.; investigation, O.M.; resources, V.M.; data curation, S.M. and O.M.; writing original draft, O.M.; writing—review and editing, S.M. and V.M.; visualization, O.M.; supervision, V.M. and S.M.; project administration, V.M. All authors have read and agreed to the published version of the manuscript.

**Funding:** This research received no external funding.

**Data Availability Statement:** The original contributions presented in this study are included in the article. Further inquiries can be directed to the corresponding author.

**Acknowledgments:** Sincere thanks are extended by the authors to the Cape Peninsula University of Technology (CPUT) for kindly granting them unrestricted access to the tools required for this study.

**Conflicts of Interest:** The authors declare no conflicts of interest.

## References


1. Idusuyi, N.; Olayinka, J.I. Dry sliding wear characteristics of aluminium metal matrix composites: A brief overview. *J. Mater. Res. Technol.* **2019**, *8*, 3338–3346. [CrossRef]
2. Senthilkumar, M.; Saravanan, S.D.; Shankar, S. Dry sliding wear and friction behavior of aluminum–rice husk ash composite using Taguchi's technique. *J. Compos. Mater.* **2015**, *49*, 2241–2250. [CrossRef]
3. Reeb, A.; Walter, V.; Schulze, V.; Weidenmann, K.A. Characterization of a hybrid $Al_2O_3$–aluminum matrix composite manufactured via composite extrusion. *J. Compos. Mater.* **2016**, *50*, 1099–1108. [CrossRef]
4. Mistry, J.M.; Gohil, P.P. An overview of diversified reinforcement on aluminum metal matrix composites: Tribological aspects. *Proc. Inst. Mech. Eng. Part J J. Eng. Tribol.* **2017**, *231*, 399–421. [CrossRef]
5. Nathan, S.R.; Suganeswaran, K.; Kumar, S.; Thangavel, P.; Gobinath, V.K. Investigations on microstructure, thermo-mechanical and tribological behavior of graphene oxide reinforced AA7075 surface composites developed via friction stir processing. *J. Manuf. Process.* **2023**, *90*, 139–150. [CrossRef]
6. Gan, W.Y.; Zheng, Z.; Zhang, H.; Tao, P. Evolution of microstructure and hardness of aluminum after friction stir processing. *Trans. Nonferrous Met. Soc. China* **2014**, *24*, 975–981. [CrossRef]
7. Sohn, Y.H.; Patterson, T.; Hofmeister, C.; Kammerer, C.; Mohr, W.; Van Den Bergh, M.; Shaeffer, M.; Seaman, J.; Cho, K. Tailoring microstructure and properties of hierarchical aluminum metal matrix composites through friction stir processing. *JOM* **2012**, *64*, 234–238. [CrossRef]
8. Liu, Z.Y.; Xiao, B.L.; Wang, W.G.; Ma, Z.Y. Singly dispersed carbon nanotube/aluminum composites fabricated by powder metallurgy combined with friction stir processing. *Carbon* **2012**, *50*, 1843–1852. [CrossRef]
9. El Rayes, M.M.; El Danaf, E.A.; Soliman, M.S. High-temperature deformation and enhanced ductility of friction stir processed-7010 Aluminum Alloy. *Mater. Des.* **2011**, *32*, 1916–1922. [CrossRef]
10. Pradeep, S.; Pancholi, V. Effect of microstructural inhomogeneity on superplastic behaviour of multipass friction stir processed aluminium alloy. *Mater. Sci. Eng. A* **2013**, *561*, 78–87. [CrossRef]
11. Borrego, L.P.; Costa, J.D.; Jesus, J.S.; Loureiro, A.R.; Ferreira, J.M. Fatigue life improvement by friction stir processing of 5083 aluminium alloy MIG butt welds. *Theor. Appl. Fract. Mech.* **2014**, *70*, 68–74. [CrossRef]
12. Costa, J.D.M.; Jesus, J.S.; Loureiro, A.; Ferreira, J.A.M.; Borrego, L.P. Fatigue life improvement of mig welded aluminium T-joints by friction stir processing. *Int. J. Fatigue.* **2014**, *61*, 244–254. [CrossRef]
13. Karthikeyan, L.; Senthilkumar, V.S.; Padmanabhan, K.A. On the role of process variables in the friction stir processing of cast aluminum A319 alloy. *Mater. Des.* **2010**, *31*, 761–771. [CrossRef]
14. Mahmoud, T.S. Surface modification of A390 hypereutectic Al–Si cast alloys using friction stir processing. *Surf. Coat. Technol.* **2013**, *228*, 209–220. [CrossRef]
15. Mishra, R.S.; Ma, Z.Y.; Charit, I. Friction stir processing: A novel technique for fabrication of surface composite. *Mater. Sci. Eng. A* **2003**, *341*, 307–310. [CrossRef]
16. Dinaharan, I.; Murugan, N.; Thangarasu, A. Development of empirical relationships for prediction of mechanical and wear properties of AA6082 aluminum matrix composites produced using friction stir processing. *Eng. Sci. Technol. Int. J.* **2016**, *19*, 1132–1144. [CrossRef]
17. Narimani, M.; Lotfi, B.; Sadeghian, Z. Evaluation of the microstructure and wear behaviour of AA6063-B4C/TiB2 mono and hybrid composite layers produced by friction stir processing. *Surf. Coat. Technol.* **2016**, *285*, 1–10. [CrossRef]
18. Selvakumar, S.; Dinaharan, I.; Palanivel, R.; Babu, B.G. Characterization of molybdenum particles reinforced Al6082 aluminum matrix composites with improved ductility produced using friction stir processing. *Mater. Charact.* **2017**, *125*, 13–22. [CrossRef]
19. Khodabakhshi, F.; Gerlich, A.P.; Simchi, A.; Kokabi, A.H. Hot deformation behavior of an aluminum-matrix hybrid nanocomposite fabricated by friction stir processing. *Mater. Sci. Eng. A* **2015**, *626*, 458–466. [CrossRef]
20. Adel Mehraban, F.; Karimzadeh, F.; Abbasi, M.H. Development of surface nanocomposite based on Al-Ni-O ternary system on Al6061 alloy by friction-stir processing and evaluation of its properties. *JOM* **2015**, *67*, 998–1006. [CrossRef]
21. Yadav, D.; Bauri, R. Friction stir processing of Al-TiB 2 in situ composite: Effect on particle distribution, microstructure and properties. *J. Mater. Eng. Perform.* **2015**, *24*, 1116–1124. [CrossRef]
22. Chen, Z.; Li, J.; Borbely, A.; Ji, G.; Zhong, S.Y.; Wu, Y.; Wang, M.L.; Wang, H.W. The effects of nanosized particles on microstructural evolution of an in-situ TiB2/6063Al composite produced by friction stir processing. *Mater. Des.* **2015**, *88*, 999–1007. [CrossRef]
23. Rajan, H.M.; Dinaharan, I.; Ramabalan, S.; Akinlabi, E.T. Influence of friction stir processing on microstructure and properties of AA7075/TiB2 in situ composite. *J. Alloys Compd.* **2016**, *657*, 250–260. [CrossRef]
24. Hangai, Y.; Nakano, Y.; Utsunomiya, T.; Kuwazuru, O.; Yoshikawa, N. Drop weight impact behavior of Al-Si-Cu alloy foam-filled thin-walled steel pipe fabricated by friction stir back extrusion. *J. Mater. Eng. Perform.* **2017**, *26*, 894–900. [CrossRef]
25. Zangabad, P.S.; Khodabakhshi, F.; Simchi, A.; Kokabi, A.H. Fatigue fracture of friction-stir processed Al–$Al_3Ti$–MgO hybrid nanocomposites. *Int. J. Fatigue.* **2016**, *87*, 266–278. [CrossRef]

26. Saini, N.; Dwivedi, D.K.; Jain, P.K.; Singh, H. Surface modification of cast Al-17% Si alloys using friction stir processing. *Procedia Eng.* **2015**, *100*, 1522–1531. [CrossRef]
27. Dolatkhah, A.; Golbabaei, P.; Givi, M.B.; Molaiekiya, F. Investigating effects of process parameters on microstructural and mechanical properties of Al5052/SiC metal matrix composite fabricated via friction stir processing. *Mater. Des.* **2012**, *37*, 458–464. [CrossRef]
28. Prabhakar, D.A.P.; Shettigar, A.K.; Herbert, M.A.; GC, M.P.; Pimenov, D.Y.; Giasin, K.; Prakash, C. A comprehensive review of friction stir techniques in structural materials and alloys: Challenges and trends. *J. Mater. Res. Technol.* **2022**, *20*, 3025–3060. [CrossRef]
29. Yang, Z.; Fan, J.; Liu, Y.; Nie, J.; Yang, Z.; Kang, Y. Strengthening and weakening effects of particles on strength and ductility of SiC particle reinforced Al-Cu-Mg alloys matrix composites. *Materials* **2021**, *14*, 1219. [CrossRef]
30. Ye, J.; Chen, X.; Luo, H.; Zhao, J.; Li, J.; Tan, J.; Yang, H.; Feng, B.; Zheng, K.; Pan, F. Microstructure, mechanical properties and wear resistance of Ti particles reinforced AZ31 magnesium matrix composites. *J. Magnes. Alloy.* **2022**, *10*, 2266–2279. [CrossRef]
31. Kumaravel, S.; Suresh, P. Optimization of friction stir processing parameters to improve mechanical properties and microstructure of Al5083 aluminum alloy reinforced with AlCoCrFeNiSi high-entropy alloy. *Phys. Scr.* **2024**, *99*, 105903.
32. Hang, Z.Y.; Jones, M.E.; Brady, G.W.; Griffiths, R.J.; Garcia, D.; Rauch, H.A.; Cox, C.D.; Hardwick, N. Non-beam-based metal additive manufacturing enabled by additive friction stir deposition. *Scr. Mater.* **2018**, *153*, 122–130.
33. Mohan, R.; Jayadeep, U.B.; Manu, R. CFD modelling of ultra-high rotational speed micro friction stir welding. *J. Manuf. Process.* **2021**, *64*, 1377–1386. [CrossRef]
34. Rana, H.; Badheka, V. Influence of friction stir processing conditions on the manufacturing of Al-Mg-Zn-Cu alloy/boron carbide surface composite. *J. Mater. Process. Technol.* **2018**, *255*, 795–807. [CrossRef]
35. Wang, L.; Jin, J.; Cao, J.; Yang, P.; Peng, Q. Interaction of edge dislocations with graphene nanosheets in graphene/Fe composites. *Crystals* **2018**, *8*, 160. [CrossRef]
36. Zhang, Z.; Urbassek, H.M. Dislocation-based strengthening mechanisms in metal-matrix nanocomposites: A molecular dynamics study of the influence of reinforcement shape in the Al-Si system. *Comput. Mater. Sci.* **2018**, *145*, 109–115. [CrossRef]
37. Mukherjee, I.; Ray, P.K. A review of optimization techniques in metal cutting processes. *CAIE* **2006**, *50*, 15–34. [CrossRef]
38. Besharati-Givi, M.K.; Asadi, P. *Advances in Friction-Stir Welding and Processing*; Woodhead Publishing: Sawston, UK; Elsevier: Amsterdam, The Netherlands, 2014.
39. Siddiquee, A.N.; Pandey, S. Experimental investigation on deformation and wear of WC tool during friction stir welding (FSW) of stainless steel. *Int. J. Adv. Manuf. Technol.* **2014**, *73*, 479–486. [CrossRef]
40. Siddiquee, A.N.; Khan, N.Z. Friction stir welding of austenitic stainless steel: A study on microstructure and effect of parameters on tensile strength. *Mater. Today* **2015**, *2*, 1388–1397. [CrossRef]
41. Zass, K.; Mabuwa, S.; Msomi, V. Introduction of Coal Reinforcing Particles on the Dissimilar FSW AA608/AA5083 Joint via Friction Stir Processing. *Metals* **2023**, *13*, 1981. [CrossRef]
42. *ASTM E8M-04*; Standard Test Methods for Tension Testing of Metallic Materials. ASTM International: West Conshohocken, PA, USA, 2004; pp. 1–24.
43. *ASTM E384-11*; Standard Test Method for Microindentation Hardness of Materials. ASTM International: West Conshohocken, PA, USA, 2011; pp. 1–24. Available online: https://www.astm.org/Standards/E384.htm (accessed on 10 January 2025).
44. Li, Q.; Huang, G.; Cao, Y.; Zhang, C.; He, J.; Jiang, H.; Lin, L.; Liu, Q. Microstructure refinement, strengthening and ductilization mechanisms in Al–Mg–Mn–Er–Zr alloy with high Mn content by friction stir processing. *Mater. Charact.* **2022**, *189*, 111939. [CrossRef]
45. Amra, M.; Ranjbar, K.; Hosseini, S.A. Microstructure and wear performance of Al5083/$CeO_2$/SiC mono and hybrid surface composites fabricated by friction stir processing. *Trans. Nonferrous Met. Soc. China* **2018**, *28*, 866–878. [CrossRef]
46. Faraji, G.; Dastani, O.; Mousavi, S.A.A.A. Effect of process parameters on microstructure and micro-hardness of AZ91/$Al_2O_3$ surface composite produced by FSP. *J. Mater. Eng. Perform.* **2011**, *20*, 1583–1590. [CrossRef]
47. Ayvaz, S.I.; Arslan, D.; Ayvaz, M. Investigation of mechanical and tribological behavior of SiC and B4C reinforced Al-Zn-Mg-Si-Cu alloy matrix surface composites fabricated via friction stir processing. *Mater. Today Commun.* **2022**, *31*, 103419. [CrossRef]
48. Yuvaraj, N.; Aravindan, S. Fabrication of Al5083/B4C surface composite by friction stir processing and its tribological characterization. *J. Mater. Res. Technol.* **2015**, *4*, 398–410. [CrossRef]
49. Srivastava, M.; Rathee, S.; Maheshwari, S.; Siddiquee, A.N. Influence of multiple-passes on microstructure and mechanical properties of Al-Mg/SiC surface composites fabricated via underwater friction stir processing. *Mater. Res. Express.* **2018**, *5*, 066511. [CrossRef]
50. Srivastava, M.; Rathee, S.; Siddiquee, A.N.; Maheshwari, S. Investigation on the effects of silicon carbide and cooling medium during multi-pass FSP of Al-Mg/SiC surface composites. *Silicon* **2019**, *11*, 2149–2157. [CrossRef]

51. Bharathikanna, R.; Elatharasan, G. An investigation on microstructures and mechanical properties of AA1050 in friction stir processing technique. *Adv. Nat. Appl. Sci.* **2017**, *11*, 316–322.
52. Huang, G.; Wu, J.; Hou, W.; Shen, Y. Microstructure, mechanical properties and strengthening mechanism of titanium particle reinforced aluminum matrix composites produced by submerged friction stir processing. *Mater. Sci. Eng. A* **2018**, *734*, 353–363. [CrossRef]
53. Agha Amini Fashami, H.; Bani Mostafa Arab, N.; Hoseinpour Gollo, M.; Nami, B. Numerical and experimental investigation of defects formation during friction stir processing on AZ91. *SN Appl. Sci.* **2021**, *3*, 108. [CrossRef]
54. Habibnia, M.; Shakeri, M.; Nourouzi, S.; Givi, M.B. Microstructural and mechanical properties of friction stir welded 5050 Al alloy and 304 stainless steel plates. *Int. J. Adv. Manuf. Technol.* **2015**, *76*, 819–829. [CrossRef]
55. Zandsalimi, S.; Heidarzadeh, A.; Saeid, T. Dissimilar friction-stir welding of 430 stainless steel and 6061 aluminum alloy: Microstructure and mechanical properties of the joints. *Proc. Inst. Mech. Eng. Part L J. Mater. Des. Appl.* **2019**, *233*, 1791–1801. [CrossRef]
56. Akbari, M.; Ezzati, M.; Asadi, P. Investigation of the effect of tool probe profile on reinforced particles distribution using experimental and CEL approaches. *Int. J. Lightweight Mater. Manuf.* **2022**, *5*, 213–223. [CrossRef]
57. Hamilton, C.; Kopyściański, M.; Senkov, O.; Dymek, S. A coupled thermal/material flow model of friction stir welding applied to Sc-modified aluminum alloys. *Metall. Mater. Trans. A* **2013**, *44*, 1730–1740. [CrossRef]
58. Hamilton, C.; We˛glowski, M.S.; Dymek, S. A simulation of friction-stir processing for temperature and material flow. *Metall. Mater. Trans. B* **2015**, *46*, 1409–1418. [CrossRef]
59. Khan, N.Z.; Siddiquee, A.N.; Khan, Z.A.; Shihab, S.K. Investigations on tunneling and kissing bond defects in FSW joints for dissimilar aluminum alloys. *J. Alloys Compd.* **2015**, *648*, 360–367. [CrossRef]
60. Bozkurt, Y. The optimization of friction stir welding process parameters to achieve maximum tensile strength in polyethylene sheets. *Mater. Des.* **2012**, *35*, 440–445. [CrossRef]
61. Srivastava, M.; Rathee, S.; Maheshwari, S.; Siddiquee, A.N. Optimisation of friction stir processing parameters to fabricate AA6063/SiC surface composites using Taguchi technique. *Int. J. Mater. Prod. Technol.* **2019**, *58*, 16–31. [CrossRef]
62. Ahmadkhaniha, D.; Sohi, M.H.; Zarei-Hanzaki, A.; Bayazid, S.M.; Saba, M. Taguchi optimization of process parameters in friction stir processing of pure Mg. *J. Magnes. Alloy.* **2015**, *3*, 168–172. [CrossRef]
63. Jain, V.K.; Yadav, M.K.; Siddiquee, A.N.; Khan, Z.A. Optimization of friction stir processing parameters for enhanced microhardness of AA5083/Al-Fe in-situ composites via Taguchi technique. *Mater. Sci. Eng. Appl.* **2021**, *1*, 55–61. [CrossRef]
64. Kolli, M.; Naresh, D.S.; Devaraju, A.; Satyanarayana, K. Investigation of mechanical properties in friction stir processing parameters of Cu-TiB2 composite using Taguchi approach. *Int. J. Interact. Des. Manuf.* **2023**, *19*, 153–164. [CrossRef]
65. Muthukrishnan, N.; Davim, J.P. Optimization of machining parameters of Al/SiC-MMC with ANOVA and ANN analysis. *J. Mater. Process. Technol.* **2009**, *209*, 225–232. [CrossRef]
66. Chanakyan, C.; Sivasankar, S.; Meignanamoorthy, M.; Ravichandran, M.; Mohanavel, V.; Alfarraj, S.; Almoallim, H.S.; Manikandan, V.; Isaac JoshuaRamesh Lalvani, J. Optimization of FSP process parameters on AA5052 employing the S/N ratio and ANOVA method. *Adv. Mater. Sci. Eng.* **2021**, *2021*, 6450251. [CrossRef]
67. Syed, K.; Ali, M.A.; Reddy, K.P.K.; Rao, B.N. Analyzing the Influence of Tool Profile on Friction Stir Process with Taguchi Optimization and Tungsten Nano Powder. *Int. J. Veh. Struct. Syst.* **2023**, *15*, 802–807.
68. Butola, R.; Ranganath, M.S.; Murtaza, Q. Fabrication and optimization of AA7075 matrix surface composites using Taguchi technique via friction stir processing (FSP). *Eng. Res. Express* **2019**, *1*, 025015. [CrossRef]
69. Salehi, M.; Saadatmand, M.; Mohandesi, J.A. Optimization of process parameters for producing AA6061/SiC nanocomposites by friction stir processing. *Trans. Nonferrous Met. Soc. China* **2012**, *22*, 1055–1063. [CrossRef]
70. Puviyarasan, M.; Kumar, V.S. Optimization of friction stir process parameters in fabricating AA6061/SiCp composites. *Procedia Eng.* **2012**, *38*, 1094–1103. [CrossRef]
71. Ross, P.J. *Taguchi Techniques for Quality Engineering: Loss Function, Orthogonal Experiments, Parameter and Tolerance Design*; McGraw-Hill: New York, NY, USA, 1998; pp. 1–279.
72. Akinlabi, E.T.; Mahamood, R.M.; Akinlabi, S.A.; Ogunmuyiwa, E. Processing parameters influence on wear resistance behaviour of friction stir processed Al-TiC composites. *Adv. Mater. Sci. Eng.* **2014**, *2014*, 724590. [CrossRef]
73. Swain, P.K.; Mohapatra, K.D.; Das, R.; Sahoo, A.K.; Panda, A. Experimental investigation into characterization and machining of Al+ SiCp nano-composites using coated carbide tool. *Mech. Ind.* **2020**, *21*, 307. [CrossRef]
74. Gunasekaran, J.; Sevvel, P.; Roy, J.V.; Sivaramakrishnan, A. Analysis of sensitivity and formulation of empirical relationship between parameters of FSW process and tensile strength of AZ80A Mg alloy joints. *Mater. Res. Express* **2023**, *10*, 056513. [CrossRef]
75. Gunasekaran, J.; Sevvel, P.; John Solomon, I.; Vasanthe Roy, J. Multi objective optimization of parameters during FSW of AZ80A-AZ31B Mg alloys using grey relational analysis. *J. Mech. Sci. Technol.* **2024**, *38*, 4971–4982. [CrossRef]

76. Adiga, K.; Herbert, M.A.; Rao, S.S.; Shettigar, A.K. Optimization of process parameters for friction stir processing (FSP) of AA8090/boron carbide surface composites. *Weld. World* **2024**, *68*, 2683–2700. [CrossRef]
77. Muribwathoho, O.; Msomi, V.; Mabuwa, S. An Analysis Comparing the Taguchi Method for Optimizing the Process Param-eters of AA5083/Silicon Carbide and AA5083/Coal Composites That Are Fabricated via Friction Stir Processing. *Appl. Sci.* **2024**, *14*, 9616. [CrossRef]